AD-A143 913 APPROXIMATE METHODS FOR OBTAINING THE COMPLEX NATURAL ELECTROMAGNETIC OSC..(U) OHIO STATE UNIV COLUMBUS ELECTROSCIENCE LAB T C LEE ET AL. FEB 84 ESL-710016-16 1/4

UNCLASSIFIED N00014-78-C-0049 F/G 20/3 NL

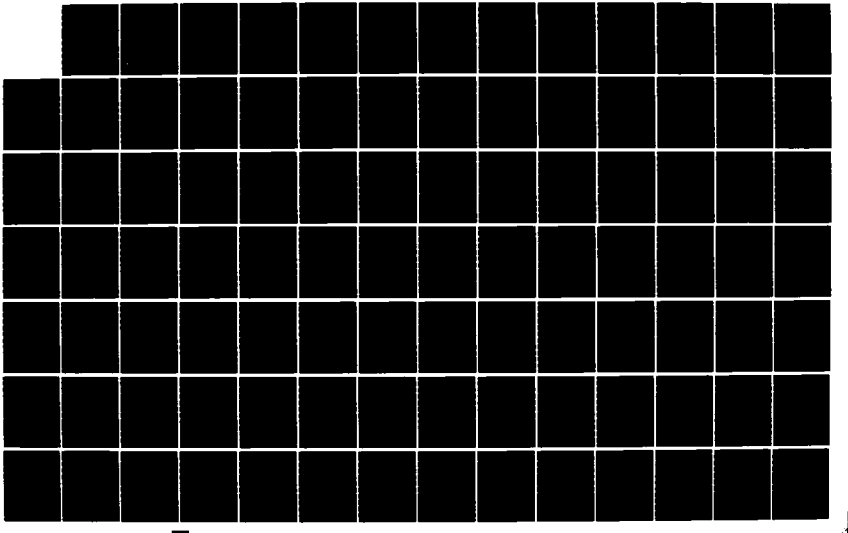

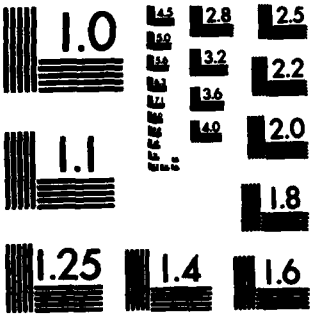

MICROCOPY RESOLUTION TEST CHART
NATIONAL BUREAU OF STANDARDS-1963-A

(12)

OSU

The Ohio State University

APPROXIMATE METHODS FOR OBTAINING THE COMPLEX NATURAL ELECTROMAGNETIC OSCILLATIONS OF AN OBJECT

T.C. Lee
D.L. Moffatt

AD-A143 913

The Ohio State University

ElectroScience Laboratory

Department of Electrical Engineering
Columbus, Ohio 43212

DTIC
ELECTE
AUG 2 1984
S
A

Technical Report 710816-16
Contract No. N00014-78-C-0049
February 1984

This document has been approved for public release and sale; its distribution is unlimited.

DTIC FILE COPY

Department of the Navy
Office of Naval Research
800 N. Quincy Street
Arlington, Virginia 22217

84 06 26 025

NOTICES

When Government drawings, specifications, or other data are used for any purpose other than in connection with a definitely related Government procurement operation, the United States Government thereby incurs no responsibility nor any obligation whatsoever, and the fact that the Government may have formulated, furnished, or in any way supplied the said drawings, specifications, or other data, is not to be regarded by implication or otherwise as in any manner licensing the holder or any other person or corporation, or conveying any rights or permission to manufacture, use, or sell any patented invention that may in any way be related thereto.

50272-101

REPORT DOCUMENTATION PAGE	1. REPORT NO.	2.	3. Recipient's Accession No.

4. Title and Subtitle

APPROXIMATE METHODS FOR OBTAINING THE COMPLEX NATURAL ELECTROMAGNETIC OSCILLATIONS OF AN OBJECT

5. Report Date February 1984

6.

7. Author(s)
T.C. Lee and D.L. Moffatt

8. Performing Organization Rept. No. ESL 710816-16

9. Performing Organization Name and Address

The Ohio State University ElectroScience Laboratory
Department of Electrical Engineering
Columbus, Ohio 43212

10. Project/Task/Work Unit No.

11. Contract(C) or Grant(G) No
(C)
(G) N00014-78-C-0049

12. Sponsoring Organization Name and Address

Department of the Navy, Office of Naval Research
800 North Quincy Street
Arlington, Virginia 22217

13. Type of Report & Period Covered
Technical

14.

15. Supplementary Notes
A portion of the research reported herein was sponsored by Project 714190, Contract #N00014-82-K-0037 between the Office of Naval Research and the Ohio State University Research Foundation.

16. Abstract (Limit: 200 words)

The complex natural resonances (poles) of an object are excitation (aspect and polarization) independent. The primary goal of this dissertation is to develop a rational function approximation (RFA) for use in pole extraction from the measured scattering spectrum data of broadband radar systems. Applications of the RFA are demonstrated for a variety of simple as well as complex objects. The results obtained are compared with those poles extracted using other methods.

To overcome noise problems, two preprocessing techniques--a sum operator and a zero-phase-shift digital filter are developed. The minimum signal-to-noise ratio (additive) is explored such that reliable pole extraction is still feasible. Finally, RFA are applied to the measured data of complex geometric targets (scale models of aircraft).

In addition, the uniform geometrical theory of diffraction (UTD) and equivalent current (EC) have been applied to formulate the resonant modes of a thin circular disc for both broadside and edge-on incidence. An integral equation formulation and numerical search has been applied to a circular thin loop. Poles extracted from these results are compared to those obtained from RFA. The complex natural resonances of a loop are used to generate K-pulse input and response waveforms. These waveforms are, in part, a test of the accuracy of the extracted poles using the methods developed in this report.

17. Document Analysis a. Descriptors

b. Identifiers/Open-Ended Terms

c. COSATI Field/Group

18. Availability Statement	19. Security Class (This Report)	21. No. of Pages
	Unclassified	275
	20. Security Class (This Page) Unclassified	22. Price

(See ANSI-Z39.18) See Instructions on Reverse

OPTIONAL FORM 272 (4-77)
(Formerly NTIS-35)
Department of Commerce

TABLE OF CONTENTS

	Page
LIST OF TABLES.	vii
LIST OF FIGURES	xi
Chapter	
I. INTRODUCTION	1
II. AN OVERVIEW OF RESEARCH IN THE EXTRACTION OF COMPLEX NATURAL RESONANCES.	6
A. Signal Flow Graph.	7
1. Thin Wire Structures	7
2. Solid Structures	8
B. Poles Extraction From the Transient Response--Prony's Method	8
C. Integral Equation and Numerical Search	10
D. Poles Extracted Via the Rational Function Approximants	11
III. RATIONAL FUNCTION APPROXIMATIONS	14
A. Introduction	14
B. Example I: Simulated Sphere Data Using Four Pole-Pairs	19

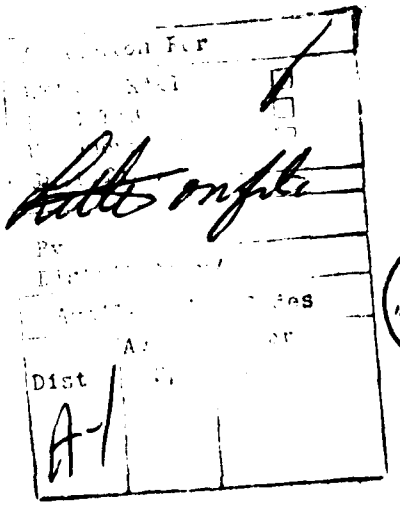

Page

C. Example 2: Simulated Sphere Data Using Six Pole-Pairs 31

D. Example 3: Calculated Backscattering Data for a Conducting Sphere. 35

E. Identification of the True Poles and the Curve Fitting Poles. 41

F. The Selection of Data Points 42

G. Limitation of the System Order M 43

H. Poles Extracted Via a Window Technique 44

I. Additive Noise and Its Effects on Poles Extracted Via Rational Function Approximations 50

J. Preprocessing Techniques 56

1. Preprocessing with Zero-Phase-Shift Digital Filter 56
2. Preprocessing with Sum Operator. 59
3. Preprocessing with Both Digital Filter and Sum Operator 68

K. Brief Summary. 73

IV. LINEAR LEAST SQUARED ERROR SOLUTIONS 76

A. Introduction 76

B. Eigenanalysis. 76

C. Eigenanalysis Via Singular Value Decomposition . . . 78

D. Pseudo-Inverse Method. 83

E. Summary and Discussion 87

V. AN INVESTIGATION OF THE COMPLEX NATURAL RESONANCES OF VARIOUS OBJECTS 88

A. Introduction 88

Page

B. Conducting Sphere 89

1. Analytical Method 89
2. Signal-Flow-Graph Method 89
3. Rational Function Approximation 92

C. Disk 92

1. Introduction 92
2. Broadside Incidence 93
3. Poles of the Disk at Oblique Incidences 104
4. Andrejewski's Magnetic Near Field Data of the Disk Backscattering at Broadside 107
5. Summary 112

D. Wire Scatterers 115

1. Introduction 115
2. Data Sets for Thin Wire and Thick Wire 115

E. Circular Loop 116

1. Introduction 116
2. Integral Equation and Numerical Search 122
3. Rational Function Approximation 125

F. Finite and Semi-Infinite Open Circular Waveguides . . 147

G. Aircraft F104 157

VI. EXTRACTING COMPLEX NATURAL RESONANCES FROM MEASURED DATA 164

A. Introduction 164

B. Amplitude and Phase Plots 165

C. Extracting the Complex Natural Resonance from the Measured Data 184

1. Aircraft A 185
2. Aircraft B 185

Page

D. Impulse Responses of the Aircraft. 190

E. Brief Summary and Discussion 191

VII. CONCLUSIONS. 211

REFERENCES. 217

ADDITIONAL REFERENCES 222

APPENDICES

A. A ZERO-PHASE SHIFT LOWPASS DIGITAL FILTER. 225

B. A SUM OPERATOR 230

C. A COMPARISON OF THE RAYLEIGH-STEVENSON EXPANSION AND THE EXPANSION FROM RFA FOR A DISC AT BROADSIDE 239

D. THE COMPLEX NATURAL RESONANCES OF THE DISC 243

E. THE POLES FOR A CIRCULAR METALLIC DISC AT EDGE-ON INCIDENCE. 255

F. A COMPARISON OF EXACT AND APPROXIMATE BACKSCATTERED FIELDS FOR THE CIRCULAR DISK FOR EDGE-ON INCIDENCE 259

G. A REPRODUCTION OF ANDREJEWSKI'S NEAR FIELD DATA OF THE DISC. 262

H. SOME TRANSIENT RESPONSES 264

I. K-PULSE WAVEFORM FOR THE THIN CIRCULAR LOOP. 269

LIST OF TABLES

Table		Page
3-1.	True Poles and Residues* Used for Generating Sets of Simulated Data	20
3-2.	A Comparison of True Poles and Extracted Poles, True Residues and Extracted Residues for (M,N) as (8,7); Four Pairs of Poles and Residues are Used in the Simulated Data	27
3-3.	A Comparison of True Poles and Extracted Poles, True Residues and Extracted Residues for (M,N) as (20,19); Four Pairs of Poles and Residues are Used in the Calculation of the Simulated Data.	29
3-4.	The Extracted Poles and the Errors Between the Rational Function Fit and the Original Data (Simulated Data Used in Example 1)*.	30
3-5.	A Comparison of True Poles and Extracted Poles True Residues and Extracted Residues for (M,N) as (14,13); 6 Pole-Pairs and Their Corresponding Residues are used in the Generation of Simulated Data	32
3-6.	A Comparison of Exact Poles and Those Extracted* From Calculated Data for Sphere Via Rational Function Approximation.	36
3-7.	A Comparison of True Poles and Poles* Extracted Via Window Technique	46
3-8.	A Comparison of True Poles and Extracted Poles* Using the Rational Function Approximation to the Backscattering Data of Sphere**.	51
3-9.	A Comparison of True Poles and Poles Extracted Using the RFA to the Backscattering Data for a Sphere*.	52

Table		Page
3-10.	Comparison of Exact and Extracted Poles* of Sphere Using the RFA to the Noisy Data for the Sphere**.	54
3-11.	Poles Extracted Via Rational Function Approximation and 10th Order Zero-Phase-Shift Digital Filter* . . .	60
3-12.	Poles Extracted Via Rational Function Approximation and Sum Operator.	69
3-13.	Poles Extracted Via Rational Function Approximation and Sum Operator.	70
3-14.	Poles Extracted Via Rational Function Approximation Using the Digital Filter and the Sum Operator (S/N = 12.35 dB).	74
4-1.	A List of the Singular Values Using Singular Value Decomposition in the RFA for (M,N) as (14,13) to the Calculated Data for the Sphere.	80
4-2.	The Ratio of Two Adjacent Singular Values*.	81
4-3.	A Comparison of the True Poles and the Extracted Poles* Using RFA Model and the Singular Value Decomposition to the Calculated Data (Sphere, Backscatter).	82
4-4.	A Comparison of the True Poles and the Extracted Poles* Using RFA and Pseudo-Inverse Method, i.e., Least Squared Error Without Weight to the Calculated Data (Sphere, Backscatter).	84
5-1.	Poles* of Sphere Extracted Via Analytical Method. . .	90
5-2.	A Comparison of the Pole-Pairs* for a Conducting Sphere Extracted Using Different Methods	91
5-3.	A List of Pole-Pairs* for the Disc Backscattering at Broadside Using the RFA and UTD Approximations. . . .	103
5-4.	A List of Poles for the Disc at Angles Off Broadside Incidence (Backscatter) Using the RFA and Senior's Creeping Wave at Edge-On Incidence	105

Table Page

5-5. A List of Poles for the Disc Using the RFA to the Calculated Data for Different Aspect Angles and Polarizations. The RFA Are Fitted to ka of 0.2 to 6 (30 Samples) 108

5-6. Poles* of Disc Using Senior's Creeping Wave Mode 109

5-7. A Comparison of the Complex Natural Resonances* for a Disc Using RFA to Hodge's Data and Andrejewski's Data (Backscattering for Broadside). 113

5-8. A List of Poles for a Thin-Wire and a Thick-Wire Extracted Using RFA, Integral Equation and Numerical Search and Signal-Flow Graphs for Broadside and 30° Off End-On Excitation (Backscatter). 117

5-9. A List of Poles* (Layer I) of Loops at Three Different Wire to Loop Radius Ratios. The Integral Equation and Numerical Search is Used to Find the Poles 123

5-10. A List of Poles* of a Loop (a/b** = 3.14159E-3) Extracted Using Integral Equation and Numerical Search 126

5-11. A List of Poles of a Loop (a/b* of 3.14159E-3) Extracted Using the RFA and Integral Equation and Numerical Search for Broadside Excitation. 136

5-12. Poles of a Circular Loop at Edge-On Incidence With a/b* of 3.14159E-3 137

5-13. A List of the Poles and the Corresponding Relative Impedance (Znn) for the Loop (a/b* of 3.14159E-3). Note the Impedance (Znn) May Be as High as 1.0 E3 for the Location Slightly Away from the Pole Locations . . . 138

5-14. A List of Poles* of Finite and Semi-Infinite Waveguide Obtained Using the RFA to the Backscattering Calculated Data 148

5-15. The Calculated Data of F104 Aircraft Model* at 1 to 12 MHz 158

5-16. The Dominant Poles* of F 104 Extracted Via the Rational Function Approximant and Prony's Method 161

Table		Page
6-1.	The Complex Natural Resonances* for Commercial Aircraft A Obtained from the Rational Function Approximation to the Measured Data (Backscatter, Vertical Polarization, 1-2 GHz)	186
6-2.	The Complex Natural Resonances* for Commercial Aircraft A Obtained from the Rational Function Approximation to the Measured Data (Backscatter, Vertical Polarization, 2-3 GHz)	187
6-3.	The Complex Natural Resonances* for Commercial Aircraft A Obtained from the Rational Function Approximations to the Measured Data (Backscatter, Horizontal Polarization, 1.5-3 GHz)	188
6-4.	The Complex Natural Resonances* of Aircraft B at 0°, 90°, 135° From Nose-On Incidence for Vertical Polarization.	189
C-1.	A List of the Coefficients of RFA Fitted to the Calculated Backscattering Data for the Disc at Broadside for (M,N) as (14,13)(ka of 0.2 (0.2) 15.2).	241
C-2.	A List of Poles, Zeros, and Residues* Which Correspond to the RFA Coefficients in Table C-1 . . .	241
D-1.	A List of 26 Pole*-Pairs for the A Disc for Broadside Excitation (Backscatter).	252
G-1.	The W_o, ψ_o, ψ_2 Listed in Andrejewski's Dissertation .	263

LIST OF FIGURES

Figure | Page

3-1. The RFA for (M,N) as (8,7) fit to the simulated data using the first four pole-pairs and residues for the sphere. The x's are the data points used for the RFA. The amplitude plot of the RFA (dashed line) gives a good fit to the original amplitude data (solid line). The corresponding phase plot is given in Figure 3-2 22

3-2. The RFA for (M,N) as (8,7) fit to the simulated data using the first four pole-pairs and residues for the sphere. The x's are the data points used for the RFA. The phase plot of the RFA (dashed line) gives a good fit to the original phase data (solid line). The corresponding amplitude plot is given in Figure 3-1 23

3.3. The RFA for (M,N) as (20,19) fit to the simulated data using the first four pole-pairs and residues for the sphere. The x's are the data points used for the RFA. The amplitude plot of the RFA (dashed line) gives a good fit to the original amplitude data (solid line). The corresponding phase plot is given in Figure 3-2 24

3-4. The RFA for (M,N) as (20,19) fit to the simulated data using the first four pole-pairs and residues for the sphere. The x's are the data points used for the RFA. The phase plot of the RFA (dashed line) gives a good fit to the original amplitude data (solid line). The corresponding amplitude plot is given in Figure 3-2 25

3-5. The RFA for (M,N) as (14,13) fit to the simulated data using the first six pole-pairs and residues for the sphere. The x's are the data points used for the RFA. The amplitude plot of the RFA gives a good fit to the original amplitude data (solid line). The corresponding phase plot is given in Figure 3-6 33

Figure Page

3-6. The RFA for (M,N) as (14,13) fit to the simulated data using the first six pole-pairs and residues for the sphere. The x's are the data points used for the RFA. The phase plot of the RFA (dashed line) gives a good fit to the original data (solid line). The corresponding amplitude plot is given in Figure 3-5 34

3-7. The RFA for (M,N) as (14,13) fit to the calculated data for the sphere. The x's are the data points used for the RFA. The amplitude plot of the RFA (dashed line) gives a good fit to the original amplitude data (solid line). The corresponding phase plot is given in Figure 3-8 . . . 37

3-8. The RFA for (M,N) as (14,13) fit to the calculated data for the sphere. The x's are the data points used for the RFA. The phase plot of the RFA (dashed line) gives a good fit to the original amplitude data (solid line). The corresponding amplitude plot is given in Figure 3-7. 38

3-9. The RFA (M,N) as (16,15) fit to the calculated data for the sphere. The x's are the data points used for the RFA. The amplitude plot of the RFA (dashed line) gives a good fit to the original amplitude data (solid line). The corresponding phase data is given in Figure 3-10. . . 39

3-10. The RFA for (M,N) as (16,15) fit to the calculated data for the sphere. The x's are the data points used for the RFA. The phase plot of the RFA (dashed line) gives a good fit to the original phase data (solid line). 40

3-11. The RFA fit to the calculated data for the sphere within the frequency of interest (window I). The x's are the data points used for the RFA. The amplitude plot of the RFA (dashed line) gives a good fit to the original amplitude data (solid line) within the window 47

3-12. The RFA fit to the calculated data for the sphere within the frequency of interest (window II). The x's are the data points used for the RFA. The amplitude plot of the RFA (dashed line) gives a good fit to the original amplitude data (solid line) within the window 48

Figure Page

3-13. The RFA fit to the calculated data for the sphere within the frequency of interest (window III). The x's are the data points used for the RFA. The amplitude plot of the RFA (dashed line) gives a good fit to the original amplitude data (solid line) within the window 49

3-14. The RFA applied to a set of noisy data, where the Gaussian random noise with zero mean and a standard deviation of 0.1 is added to the calculated data for the sphere. The x's are the data points used for the RFA. The amplitude plot of the RFA is plotted as a dashed line (S/N of 18.37 dB). 55

3-15. A comparison of amplitude plots for the calculated data (solid line) and the filtered data (dashed line) for the sphere. The filtered data are obtained by filtering the noisy data (calculated data with additive Gaussian random noise) using a 10th order zero-phase-shift digital filter. The 3 dB cutoff frequency f_c is set to 20 Hz. The signal-to-noise ratio is 12.35 dB before filtering. . 57

3-16. A comparison of the phase plots for the calculated data (solid line) and the filtered data (dashed line) for the sphere. The filtered data are obtained by filtering the noisy data (calculated data with additive Gaussian random noise) using a 10th order zero-phase-digital filter. The signal-to-noise ratio is 12.35 dB before filtering 58

3-17. The sum operator and the RFA applied simultaneouly to the noisy data (solid line) for the sphere, where two Gaussianly distributed random noises have been added to the calculated data for the sphere. The x's are The x's are the data points used for the RAF. The signal-to-noise ratio is 18.37 dB (amplitude plot). . . . 63

3-18. The sum operator and the RFA (dashed line) applied simultaneously to the noisy data (solid line) for the sphere, where two Gaussianly distributed random noises have been added to the calculated data for the sphere. The data points (the x's) are different from those in Figure 3-17. The signal-to-noise ratio is 18.37 dB (amplitude plot). 64

Figure | Page

3-19. The sum operator and the RFA applied simultaneously to the noisy data (solid line) for the sphere, where two Gaussianly distributed random noises have been added to the calculated data for the sphere. The x's are the data points used in the RFA. The signal-to-noise ratio is is 12.35 dB (amplitude plot) 65

3-20. The sum operator and the RFA are applied simultaneously to the noisy data (solid line) for the sphere, where two Gaussianly distributed random noises have been added to the calculated data for the sphere. The selected data points (the x's) used in the RFA are different from those in Figure 3-19. The signal-to-noise ratio is 12.35 dB (amplitude plot) 66

3-21. The sum operator and the RFA (dashed line) applied to the noisy data (solid line) for the sphere, where two Gaussianly distributed random noises have been added to the calculated data for the sphere. Note the selected data points are marked by x's. The signal-to-noise is 6.33 dB (amplitude plot) 67

3-22. The sum operator and the RFA are applied simultaneously to the prefiltered data (solid line) for the sphere. A 10th order zero-phase-shift digital filter is used to prefilter the noisy data, where two Gaussianly distributed random noises have been added to the calculated data for the sphere. The x's are the data points used in the RFA. The original signal-to-noise ratio is 12.35 dB (amplitude plot) 71

3-23. The sum operator and the RFA are applied simultaneously to the prefiltered data (solid line) for the sphere. A 10th order zero-phase-shift digital filter is used to prefilter the noisy data, where two Gaussianly distributed random noises have been added to the calculate data for the sphere. The x's are the data points used in the RFA. The original signal-to-noise ratio is 12.350dB. The data points used are different from those in Figure 3-22 (amplitude plot). 72

4-1. The RFA applied to the calculated data for the sphere in the sense of least squared error without weight. Note twenty complex data points are used (amplitude plot). . . 85

Figure Page

4-2. The RFA applied to the calculated data for the sphere in the sense of least squared error without weight. Note that twenty complex data points are used (phase plot) . . 86

5-1. The coordinate system for a circular metallic disc. . . . 94

5-2. The RFA for (M,N) as (3,2) fit to the backscattering data for the disc at broadside. The x's are the data points used. The solid line is the calculated data and the dotted line is the RFA (amplitude plot). The 3 input samples are in the Rayleigh region and are marked with x's. 95

5-3. The RFA (dashed line) for (M,N) as (14,13) fit to the backscattering calculated data (solid line) for the disc at broadside. The x's are the data points used in the RFA. The last input sample is at ka of 14.8 (amplitude plot) . 97

5-4. The RFA (dashed line) for (M,N) as (14,13) fit to the backscattering calculated data (solid line) for the disc at braodside. The x's are the data points used in the RFA. The last input sample is at ka of 14.8 (phase plot). 98

5-5. The RFA for (M,N) as (18,17) fit to the backscattering data for the disc at broadside. The x's are the data points used. The solid line is the calculated data and the dotted line is the RFA. Note the last input sample of the RFA is at ka of 7.2 (amplitude plot). . . . 99

5-6. A comparison of the poles of a disc extracted using RFA (○) and UTD (Δ) for broadside excitation. 100

5-7. The complex natural resonances of the disc for broadside (○) and edge-on (Δ) incidences 110

5-8. The RFA (dashed line) fit to Andrejewski's data (magnetic near field denoted by the x's) for the disc at broadside. The x's are data points used, and the dashed line is the RFA (amplitude plot). 111

Figure Page

5-9. A comparison of the first 3 pairs of poles of the disc for broadside using RFA to Hodge's calculated data (©) and Andrejewski's data (Δ). Note third pole-pairs using Andrejewski's data is not very close to those using Hodge's data, because Andrejewski's data is truncated at ka of 10 114

5-10. The RFA for (M,N) as (12,11) fit to the backscattering data for the thin-wire with a wire length-to-wire diameter ratio of 2000 at broadside excitation. The x's are the data points used in RFA. The dashed line is the rational function approximation (amplitude plot) 118

5-11. The RFA for (M,N) as (12,11) applied to the backscattering data for the thin-wire with a wire length-to-wire diameter ratio of 2000 at 30° from end-on incidence. The x's are the data points used in RFA. The dashed line is the RFA (amplitude plot) 119

5-12. The RFA for (M,N) as (12,11) applied to the backscattering data for the thick-wire with a wire length (L)-to-wire diameter (D) ratio of 20 for broadside excitation. The x's are the data points used in RFA. The dashed line is the RFA (amplitude plot). The peak in the amplitude of the first resonance can be seen in the RFA, because more data points (50) are reproduced using the coefficients of the RFA 120

5-13. The RFA for (M,N) as (12,11) applied to the backscattering data for the thick-wire for a wire-length (L) to wire diameter (D) ratio of 20 at 30° from end-on incidence. The x's are the data points used in RFA. The dashed line is the RFA (amplitude plot) 121

5-14. The coordinate system for a circular metallic loop. . . . 124

5-15. A plot of the complex natural resonances (layer I) for the loops at different wire to loop radius ratios using the integral equation and numerical search to find the poles 127

5-16. A plot of the poles for a circular loop at the wire radius to the loop radius ratio of 3.14159E-3. The integral equation and numerical search is used to find the poles . 128

Figure Page

5-17. A plot of the poles for a circular loop (a/b of 3.14159E-3). The poles are extracted via the integral equation and numerical search. The number around the location of each pole is the n of Znn. Three types of poles are defined 129

5-18. A plot of the poles for a circular loop (a/b of 3.14159E-3 extracted via the integral equation and numerical search. The number around the location of each pole is the n of Znn. The poles which are extracted from the same Znn are identified by a solid line 130

5-19. The application of RFA for (M,N) as (14,13) to the backscattering data (solid line) for a circular loop at broadside. The wire-radius to the loop radius ratio is 3.14159E-3. The x's are the data points used in the RFA 131

5-20. The RFA (dotted line) fit to the backscattering data (solid line) for the loop at edge-on incidence. a/b is 3.14159E-3, where a is the wire radius and b is the loop radius. The x's are the data points used in RFA 132

5-21. A comparison of the poles extracted using RFA and integral equation and numerical search ("Δ " impedance method, "o" RFA fit) for the loop 139

5-22. The impulse response (with the specular term to be removed) for a loop (backscatter) at broadside. The specular return is seen around the time origin. a/b is 3.14159E-3, where a is the wire radius and b is the loop radius. . . 141

5-23. The impulse response (with the specular return removed) for a loop at broadside (backscatter). a/b is 3.14159E-3, where a is the wire radius and b is the loop radius . . . 142

5-24. A comparison of the impulse response waveforms for a circular loop (a/b is 3.14159E-3) and a circular metallic disc (backscatters). 143

5-25. The ramp response for a loop for broadside excitation . . 144

5-26. The derivative of a short Gaussian pulse response for a loop. (a) is obtained using the convolution of the impulse response and the input short pulse. (b) is calculated using the time domain moment method [36]. Note that wire to the loop radius ratio is 0.00314 in (a). 145

Figure Page

5-27. The individual contribution of each pole-pair and the corresponding residues to the impulse response for a loop backscatter for broadside. 146

5-28. The geometries of finite waveguides with both ends open (a), the rear end shorted (b), and semi-infinite waveguide (c) 149

5-29. The RFA for (M,N) as (14,13) (dashed line) fit to the axial backscattering data (solid line) for the finite waveguide (both ends open) within the window of interest. The x's are data points used in RFA (amplitude plot). . . 150

5-30. The RFA for (M,N) as (14,13) (dashed line) fit to the axial backscattering data (solid line) for the finite waveguide (both ends open) within the window of interest. The x's are the data points used in RFA (phase plot). . . 151

5-31. The RFA for (M,N) as (10,9) (dashed line) fit to the axial backscattering data (solid line) for the finite circular waveguide (the rear end shorted) within the window of interest. The x's are the data points used in RFA (amplitude plot). 152

5-32. The RFA for (M,N) as (10,9) (dashed line) fit to the axial backscattering data (solid line) for the finite circular waveguide (the rear end shorted) within the window of interest. The x's are the data points used in RFA (phase plot) 153

5-33. The RFA for (M,N) as (16,15) (dashed line) fit to the axial back-scattering data (solid line) for a semi-infinite circular waveguide. The x's are the data points used in the RFA. D is the diameter of the circular waveguide (amplitude plot). 154

5-34. The RFA for (M,N) as (16,15) (dashed line) fit to the axial backscattering data (solid line) for a semi-infinite circular waveguide. The x's are the data points used in the RFA. D is the diameter of the circular waveguide (phase plot) 155

5-35. The complex natural resonances for the three cavities.
Δ: finite waveguide (both ends opened)
•: finite waveguide (the rear end opened)
†: semi-infinite waveguide 156

Figure Page

5-36. The scattering coordinate system for the F104 aircraft. Note the stick model here shows the orientation only, not the real model used in the calculation. 159

5-37. The RFA for (M,N) as (12,11) fit to the calculated backscattering data (solid line) for the F104 aircraft at θ of 0°, ϕ of 0° incidence and E_ϕ polarization. The x's are the data points used in the RFA (amplitude plot). 162

5-38. The RFA for (M,N) as (12,11) fit to the calculated backscattering (solid line) for the F104 aircraft at θ of 0°, ϕ of 0° incidence and E_ϕ polarization. The x's are the data points used in the RFA (phase plot). . . 163

6-1. The scattering coordinate system of a transportation aircraft aligned with the fuselage along the x axis (nose in the x direction) with wings in xy plane. 166

6-2. The backscattered amplitude for commercial transportation aircraft A at 0°, 10°, and 20° from nose-on for horizontal polarization. 168

6-3. The backscattered amplitude for commercial transportation aircraft A at 30°, 45°, and 50° from nose-on for horizontal polarization. 169

6-4. The backscattered phase for commercial transportation aircraft A at 0°, 10°, and 20° from nose-on for horizontal polarization. 170

6-5. The backscattered phase for commercial transportation aircraft A at 30°, 45°, and 50° from nose-on for horizontal polarization. 171

6-6. The backscattered amplitude for commercial transportation aircraft A at 0°, 15°, 30° from nose-on for vertical polarization. 172

6-7. The backscattered phase for passenger transportaion aircraft A at 0°, 15°, and 30° from nose-on for vertical polarization. 173

6-8. The backscattered amplitude for the commercial transportation aircraft B at 0°, 30°, and 60° from nose-on for vertical polarization 174

Figure Page

6-9. The backscattered amplitude for commercial transportation aircraft B at 90°, 135°, and 180° from nose-on for vertical polarization. 175

6-10. The backscattered phase for commercial transportation aircraft B at 0°, 30°, and 60° from nose-on for vertical polarization. 176

6-11. The backscattered phase for commercial transportation aircraft B at 90°, 135°, and 180° from nose-on for vertical polarization 177

6-12. A comparison of the backscattering amplitude for the commercial transportation aircraft A at nose-on incidence for horizontal and vertical polarizations 178

6-13. An amplitude plot of the backscattering data for commercial transportation aircraft A at nose-on. The measured data are oversmoothed by a zero-phase-shift digital filter 180

6-14. A phase plot of the backscattering data for commercial transportation aircraft A at nose-on. The measured data are oversmoothed by a zero-phase-shift digital filter. 181

6-15. An Amplitude plot of the backscattering data for commercial transportation aircraft A at nose-on for vertical polarization. The data are oversmoothed by the zero-phase-shift digital filter 182

6-16. A phase plot of the backscattering data for commercial transportation aircraft A at nose-on for vertical polarization. The data are oversmoothed by the zero-phase-shift digital filter 183

6-17. Backscattered impulse response waveform of commercial transportation aircraft A at nose-on incidence for vertical polarization 192

6-18. Backscattered impulse response waveform of commercial transportation aircraft A at 15° from nose-on for vertical polarization. 193

6-19. Backscattered impulse response waveform of commercial transportation aircraft A at nose-on for horizontal polarization. 194

Figure Page

6-20. Backscattered impulse response waveform of commercial transportation aircraft A at 10° from nose-on for horizontal polarization 195

6-21. Backscattered impulse response waveform of commercial transportation aircraft A at 20° from nose-on for horizontal polarization 196

6-22. Backscattered impulse response waveform of commercial transportation aircraft A at 30° from nose-on for horizontal polarization 197

6-23. Backscattered impulse response waveform of commercial transportation aircraft A at 50° from nose-on for horizontal polarization 198

6-24. Backscattered impulse response waveform of commercial transportation aircraft A at 80° from nose-on for horizontal polarization 199

6-25. Backscattered impulse response waveform of commercial transportation aircraft A at 90° from nose-on for horizontal polarization 200

6-26. Backscattered impulse response waveform of commercial transportation aircraft B at nose-on for vertical polarization 201

6-27. Backscattered impulse response waveform of commercial transportation aircraft B at 30° from nose-on for vertical polarization 202

6-28. Backscattered impulse response waveform of commercial transportation aircraft B at 60° from nose-on for vertical polarization 203

6-29. Backscattered impulse response waveform of commercial transportation aircraft B at 90° from nose-on for vertical polarization 204

6-30. Backscattered impulse response waveform of commercial transportation aircraft B at 135° from nose-on for vertical polarization 205

6-31. Backscattered impulse response waveform of commercial transportation aircraft B at 180° from nose-on for vertical polarization 206

Figure Page

6-32. The impulse response of aircraft A at nose-on for horizontal polarization. The whole range is shown here. 209

6-33. The impulse response of aircraft A at 0° aspect angle and horizontal polarization. Note the noise and clutter were filtered out by a lowpass zero-phase-shift digital filter (f_c of 15 Hz). 210

A-1. A block diagram of the 5th order digital filter 229

D-1. The coordinate system for the incident wave diffracted by a half plane 244

D-2. On-axis backscattering from the circular metallic disc. . 247

D-3. The singly, doubly and triply diffracted mechanisms of the the backscattering from the circular metallic disc. . . . 248

D-4. The coordinate system and the higher order ray paths for the disc at angles off broadside excitation 253

F-1. A comparison for the backscattering data for the disc at edge-on incidence (amplitude plot), dotted line--Senior's GTD mode, solid line--Hodge's calculation 260

F-2. A comparison for the backscattering data for the disc at edge-on incidence (phase plot), dotted line-- Senior's analytic mode, solid line--Hodge's calculation . 261

H-1. Impulse response for a loop for edge-on incidence 265

H-2. The ramp response for a loop for edge-on incidence. . . . 266

H-3. The ramp response for a loop for broadside excitation . . 267

H-4. The ramp response waveforms for the disc at 15°, 30°, 45° 60°, 75°, and 90° off broadside incidence (cross polarization) 268

I-1. The K-pulse input spectrum (amplitude plot) generated from Equation (I-1) using the first 10 pole-pairs of the circular loop at edge of incidence (TE mode). The pulse duration is confined to π TAU, where π = 3.14159 and TAU is the loop diameter transit time. Note the spectrum is spread over all the frequency, however, as shown above, the amplitude is small for ka greater than 10. . . 271

Figure Page

I-2. The K-pulse input spectrum (phase plot) generated from (I-1) using 10 pole-pairs for the circular loop (TE mode). The pulse duration at edge-on is confined to π TAU, where π = 3.14159 and TAU is the loop diameter transit time. The data are truncated at ka of 10 because the corresponding amplitude is small for ka greater than 10. 272

I-3. A K-pulse input waveform for a loop for edge-on incidence (TE mode). The ringing is due to the truncation of poles (10 pole-pairs used here). The duration is confined to π TAU, where π is 3.14159 273

I-4. A K-pulse output waveform for a loop for edge-on incidence. The duration is longer than π TAU, where π is 3.14159. This is due to both the truncation of poles and spectrum. 274

CHAPTER I

INTRODUCTION

In future generations of radar systems, the natural electromagnetic oscillations of a radar target may be used to determine the physical properties (size, shape, and composition) of the target. The key to such a possible advance in radar systems is broadband signaling waveforms. Signaling waveforms with low-frequency content give information about the gross size and shape of a target, and waveforms with high-frequency content give a detailed description of isolated parts of the target. The interaction of electromagnetic waves and material objects is best summarized by the canonical response waveforms of the object, i.e., the response waveforms for interrogating signals with impulse, step, and ramp time dependence.

Such a linear system analysis was first introduced for finite objects by Kennaugh and Cosgriff [1] and was later formalized by Kennaugh and Moffatt [2]. The concept of approximating the low-frequency scattering characteristics of an object by rational functions, i.e., complex natural resonances, was first suggested by Kennaugh and Moffatt [2] as

> "Keeping in mind that a distributed-constant representation is exact, it should still be possible to represent the

low-frequency properties of $s^{-2}F_R(s)$ and the corresponding time response [which would be $F_R(t)$] by that of a lumped constant network. In this case, $F_R(t)$ would be approximated by a series of exponential terms, whereas $s^{-2}F_R(s)$ would be the ratio of polynomials rather than the series (8)*."

A rigorous solution to the complex natural resonance idea in analysis known as the singularity expansion method (SEM) has been suggested by Baum [3]. There is much that is correct about this complex natural resonance approach [4,5]; however, Kennaugh [6] has suggested that the one thing that is missing from the SEM is the K-pulse --a time-limited input waveform which produces special time-limited output waveforms. While the main purpose of this dissertation is not to settle this question, a K-pulse response is approximated for simple backscatter (a circular loop for edge-on incidence) by using the complex natural resonances extracted in this dissertation.

Accepting the fact that in many useful situations the transient response waveforms of a scatterer or its corresponding frequency response can be well approximated by lumped parameter models, the purpose of this dissertation is to present various methods for obtaining the complex natural resonances of an object using the model. Of particular interest are methods useful with measured data which are contaminated by noise.

---

* The series (8) referred to above was a Rayleigh-type power series in s.

The complex natural resonances of an object can be obtained analytically if the vector wave equation is separable. For finite objects therefore there are two geometries, spherical, which was treated by Stratton [7], and the thin circular disc [8], which has not yet been studied rigorously from a complex natural resonance viewpoint. The complex natural resonances of all other finite objects must be found by approximate methods. Perhaps the best of these is a quasi-rigorous approach where an integral equation for the object as a scatterer or radiator is developed and then converted to a matrix equation. A numerical search of the complex frequency plane is then used to find the complex natural resonances. Mains and Moffatt [9] used this method to find the complex natural frequencies of bent wires and simple wire airplane models. Unfortunately, complex geometries such as aircraft or ships can only be handled by this approach for small electrical size. For simple geometries, asymptotic theories such as the Uniform Geometrical Theory of Diffraction (UTD) can be used, as by Kennaugh [6], to extract all but the lowest frequency resonances.

For complex geometries in the resonance region the only recourse at this time is measured experimental data at real frequencies. Useful methods for extracting complex natural resonances, therefore, must be applicable to experimental data. Such data are inevitably contaminated by some noise and clutter, which further complicates the extraction problem. The experimental data utilized in this dissertation are frequency domain data. To test time or other domain methods the appropriate data are generated synthetically.

Reviewed briefly in Chapter II of this dissertation are those methods for extracting the complex natural resonances of a scatterer or a radiator which have been suggested and shown to have some success when applied to real or synthetic data. A rational function approximation model is developed in Chapter III. Application of this model to extraction of the poles of sets of simulated data for a conducting sphere are presented. A window technique is developed for the rational fuction approximation. The effects of uncorrelated Gaussian white noise added to the calculated data on the location of extracted poles are demonstrated. A sum operator and a zero-phase-shift digital filter are used to combat noise. An estimate is made of the required signal-to-noise ratio for which the complex natural resonances are still extractable. In Chapter IV, an eigenanalysis model is reviewed, the emphasis being the application of the model using real frequency data. The application of singular value decomposition to eigenanalysis is studied. Presented in Chapter V are comparisons of the complex natural resonances extracted by the models derived in this dissertation with models and methods suggested by others.

A generalized method for extracting a set of complex natural resonances from multiple frequency complex scattering data is described and illustrated in Chapter VI. The scattering data are real data taken from measurements made at the ElectroScience Laboratory and are a true test of the methods and techniques developed. Stressed are the techniques which can be utilized to assure that the correct approximate

order for the system has been obtained as well as actual (as opposed to pattern-fitting) complex natural resonances have been extracted. The desirability of obtaining the same or very similar results using two somewhat different approaches is discussed. It is assumed that the available experimental data are contaminated by noise. For the noise-free case there are a number of techniques by which the proper complex natural resonances can successfully be extracted. An estimate is made, based on the material of this dissertation, as to the required signal-to-noise ratio which must be achieved by the experimental data before extraction of complex natural resonances is feasible.

Conclusions and recommendations based on the research reported in this dissertation are given in Chapter VII. New analytical results for complex natural resonance prediction using asymptotic scattering estimates and first estimates of certain K-pulse waveforms and response are given in the appendices.

CHAPTER II

AN OVERVIEW OF RESEARCH ON THE EXTRACTION OF COMPLEX NATURAL RESONANCES

The complex natural resonances (poles) correspond to the exterior resonant modes of an object [4]. The exterior resonant frequencies are complex, where the real parts account for ray divergence and bending losses, and the imaginary parts account for resonances. These poles are of particular interest in the waveform feature extraction because they are related to the physical characteristics of an object. Furthermore, the complex natural resonances are independent of the target aspect and polarization excitation [9]. These poles may form a minimum set of parameters needed to characterize a target. Research on the extraction of the complex natural resonances has been ongoing for a decade, and many engineering approaches to the complex natural resonances have been established. This chapter summarizes some of the approximate methods discussed in the literature which have been used to extract the complex natural resonances of a radiator or scatterer and have shown some success.

A. SIGNAL FLOW GRAPH

Signal flow graph methods have been used extensively in network analysis, for example, Circuit and System Theory written by Lago and Benningfield. However, the application of the signal-flow-graph concept to electromagnetic scatterers was first suggested by Bagby and Kennaugh [10]. In general there are two kinds of scatterers being studied: thin wire structures such as straight wires, cross wires, wire arcs, circular loops, etc. and solid structures such as spheres, circular cylinders, prolate spheroids, etc. Descriptions of the scattering mechanisms of these two basic structures follow [10].

1. Thin Wire Structures

It is assumed that there are four operations on the current flowing on the wire surface. These are: a) wire path distortion and phase delay, b) wire end and wire junction reflections, c) wire junction transmission and d) wire end radiation and radiation coupling. The parameters associated with these operations are used in the signal-flow graphs to predict the complex natural resonances. For a straight wire, the accuracy of predicted complex natural resonances is very good for very thin wire structure [10], i.e., wires whose length-to-diameter ratios are greater than 1000. However, the accuracy is decreased if the thickness of the wire is increased. Obviously, the formula used for the current distribution should be further modified for thick wires. It is very hard to predict numerically the four scattering mechanisms for

different wire configurations. The application of the signal flow-graph to wire arcs, crossed wires and other complex wire shapes is limited by the accurate values of the scattering mechanisms mentioned above. The complex natural resonances extracted using the signal-flow-graph method may be lacking in accuracy for the reason mentioned above. Nevertheless, the signal graph method yields significant physical insight into the complex natural resonances of an object.

2. Solid Structures

In recent years, the Uniform Geometrical Theory of Diffraction (UTD) has become a very powerful tool for solving such problems as diffraction from a straight or curved wedge, vertex, and/or curved surface. The UTD edge diffraction field and curved surface waves derived by Pathak and Kouyoumjian [11,12] and others have been used to evaluate the complex natural resonances of solid structures such as spheres, prolate spheroids, circular discs, etc., for both transverse electric (TE) and transverse magnetic (TM) modes [10]. The results are fairly close to those obtained from the exact solution (sphere) and from other approximate methods. It is noted that UTD is a high frequency asymptotic approximation and the errors in the poles predicted at low frequencies are due to this high frequency approximation.

B. POLES EXTRACTION FROM THE TRANSIENT RESPONSE-PRONY'S METHOD

Prony's method was originally developed to solve equations which express the relationship between the temperature and the expansion of

water vapor or phenomena defining elastic fluids using experimental data* in 1795 [13]. However, the application of Prony's method to the transient response of electromagnetic radiation or scattering data** to extract poles and residues was first suggested by Van Blaricum in 1976 [14]. In the first application of Prony's method, numerically generated data for the transient current on a thin dipole were used. The resultant poles of the thin dipole were very close to those extracted via a integral equation formulation and numerical search by Tesche [15]. Inspired by this idea, several researchers began studying Prony's method for other scatterers and looking also for solutions to the problems inherent in the Prony process. E.M. Kennaugh suggested the application of an eigenanalysis solution (eigenanalysis was mentioned in [14] but was not exploited) to replace Prony's method; this solution was illustrated by Moffatt, Young, Ksienski et al. [16]. Although the

---

* The equations are of the form:

$$\tau_i = \mu_1\rho_1^{i\Delta x} + \mu_2\rho_2^{i\Delta x} + \mu_3\rho_3^{i\Delta x} + \ldots + \mu_n\rho_n^{i\Delta x}$$

$i = 0, 1, \ldots, M-1$, where μ_j and ρ_j are undetermined constants, Δx is an increment of the variable, M is the total number of observation, τ_i is an observation result of variable at $i\Delta x$.

** The equations dealing with the impulse response of electromagnetic radiation or scattering data are of the form:

$$F_i = R_1 e^{p_1 i\Delta t} + R_2 e^{p_2 i\Delta t} + R_3 e^{p_3 i\Delta t} + \ldots, + R_n e^{p_n i\Delta t}$$

$i = 0, 1, 2, \ldots, M-1$, where A_i, p_i are the residues and poles, M is the total number of the sampled data, Δt is the time increment, F_i is the impulse response at time $i\Delta t$.

complex natural resonances of an object or class of objects can be determined using eigenanalysis, the accuracy is seriously affected by even moderate amounts of noise. Prony's method and many Prony's related methods are summarized in a recent publication [17]. Although Prony's method is a useful tool for extracting the complex natural resonances from transient data, two major problems which occur in the application of Prony's method are: 1) the determination of the system order and 2) the bias problem with noisy data. Many researchers have focused on these two problems [17,18,19] in the past few years, but there is not yet one method which is completely successful.

C. INTEGRAL EQUATION AND NUMERICAL SEARCH

The singularity expansion method [SEM] was first introduced by Baum in 1971 as a technique for solving transient electromagnetic scattering from conducting bodies [3]. Although, it requires a search procedure in conjunction with a space-frequency integral equation formulation, a recent publication showed that the idea of the singularity expansion method can also be applied to a space-time integral equation formulation [20]. In the application of integral equation and numerical search to determine the complex natural resonances, an integral equation for the induced current is derived and reduced to a finite matrix equation using the method of moments. The complex natural resonances are found using an iterative search in the complex wavenumber plane. The complex natural resonances of some simple scatterers were studied using this

method. A thin wire structure was studied by Tesche in 1973 [15]; the prolate spheroid was investigated by Marin in 1974 [21], and the circular loop was done by Blackburn and Wilton in 1978 [22]. The complex natural resonances of some stick models of the Mig19 and F104 were studied by Mains and Moffatt in 1974 [9]. At the Ohio State University, Professor J. H. Richmond's programs for backscattering calculations for the aforementioned airplane models were used. The natural resonances are those complex frequencies which make the admittances in a moment method formulation very large in magnitude. All of these studies showed some success in the extraction of complex natural resonances. However, the search procedure used has the following weaknesses.

1. The search procedure cannot be used for extraction of poles of complex structures for more than moderate electrical sizes.
2. The search procedure is time consuming in machine computing.
3. The search procedure cannot be used to process measured scattering data.

D. POLES EXTRACTED VIA THE RATIONAL FUNCTION APPROXIMANTS

As mentioned in Chapter I, the electromagnetic scattering system can, within some limitations, be modeled as lumped parameter system. The canonical responses of a scatterer are the impulse response, step response, and ramp response. In general the response of a distributed parameter system can first be separated into a forced response as an

aperiodic excitation moves over the object and later a natural response as the excitation moves beyond the body. In this dissertation, the transfer function of the system is approximated by a rational function

$$E(X_i) = \sum_{n=0}^{N} a_n X_i^{n+2} / \left(1 + \sum_{m=1}^{M} b_m X_i^m\right) \quad i = 1, 2, \ldots I , \qquad (2\text{-}3)$$

where X_i is jk_ia (an electrical length), a is a linear dimension of the object, and I is the number of the sampled data points. Thus the phasor response of a system is approximated by the the rational function $E(X_i)$.

The first attempt to extract the complex natural resonances of a scatterer from multiple frequency scattering data was by Moffatt [23] using a rational function approximation to model the transfer function of the target. This approach was largely abandoned with the advent of Prony's method and the improvement of Prony's method--eigenanalysis. In radar applications, with the exception of subsurface radar, the data are recorded using multiple frequency phasor response data [16]; time response waveforms have to be produced synthetically.

The relative advantages of pole extraction in the time and frequency domains are not completely obvious. Assuming that the initial data are measured frequency domain samples, avoiding approximate transforms into the time domain seems desirable. This is clearly true if the data are severely bandlimited and weightings must be used to avoid Gibbs and aliasing difficulties. Also, windowing methods, i.e., examining various portions of the measured spectrum individually, appear somewhat more

direct in the frequency domain. A detailed discussion of the windowing technique is given in Chapter III. The techniques which seek to sequentially extract the most dominant poles are generally not useful because pole-extraction methods are approximate and the errors will be accumulative.

No clearly superior method for complex natural resonances extraction from measured data has emerged in any domain. For this reason alone, a technique utilizing rational function approximants is deserved of some additional study.

CHAPTER III

RATIONAL FUNCTION APPROXIMATIONS

A. INTRODUCTION

As discussed earlier, it is assumed that with the possible limitations mentioned the frequency-dependent electromagnetic scattering by an object can be modeled by a passive linear two-port system with time-invariant parameters. The (normalized) transfer function, which corresponds to the (normalized) impulse response of the system, can be approximated by a rational function in the frequency domain [2]. With such a model the numerator polynomial will be aspect and polarization dependent but the denominator will be excitation invariant.

The rational function model for electromagnetic transfer functions is written initially as

$$E^n(X_i) = \sum_{n=0}^{N} a'_n X_i^{n+2} \Big/ \sum_{m=0}^{M} b'_m X_i^m \quad i = 1, 2, \ldots, I \quad , \qquad (3\text{-}1)$$

where $E^n(X_i)$ (in a phasor form) is a normalized electric or magnetic field at frequency X_i, X_i is $jk_i l$ (an electrical length), l is a linear

dimension of the object and a_n' and b_m' are unknown coefficients*. I is the number of sample data. One of the coefficients in Equation (3-1) is completely arbitrary because the numerator and denominator can be scaled by a common factor without changing the rational function model. The zero order denominator coefficient in Equation (3-1) is chosen to be normalized and accordingly the rational function model (model I) is rewritten as

$$E^n(X_i) = \sum_{n=0}^{N} a_n X_i^{n+2} \Big/ \left(1 + \sum_{m=1}^{M} b_m X_i^m\right) \quad , \qquad (3\text{-}2)$$

where X_i is $jk_i a$ and a is a linear dimension of the object.

It is assumed that the normalized scattered field, E^n, is known at a total of I real ($jk_i l$) frequencies. The proper orders of the denominator and numerator polynominals are unknown, as are the proper frequencies ($jk_i l$) to use where the scattered field is assumed to be known. Note that Equation (3-2) is selected to yield a Rayleigh-type dependence if the scattering data samples include the Rayleigh range. If both sides of Equation (3-2) are multiplied by the denominator polynominal, then I complex or 2I real linear simultaneous equations can be generated. Four cases must be considered when both N and M are allowed to be even or odd. There are N + M + 1 unknown coefficients

---

* For a real physical system, the impulse response (in the time domain) is causal and real. Then the transfer function (in the frequency domain) has the property that $E^n(X^*) = E^{n*}(X)$, where * denotes complex conjugate. With this restriction, the coefficients a_n', b_m' in Equation (3-1) are real.

(a_n, b_m) to be found, and neglecting the underdetermined case these coefficients can be found in an exact or in a least squared error sense depending upon the selection of I. One would anticipate that a least squared error approximation would usually be better. As will be seen, however, an exact solution with or without a preprocessing technique has some advantages over a least-squared error approximation under certain conditions.

To this point, the approximating equations given in Equation (3-2) are no different than those recently given by Brittingham, Miller and Willows [24]. In fact, they are the same as those originally suggested by Moffatt [23]. The idea of using a lumped parameter model to approximate a distributed parameter system goes back to Kennaugh and Moffatt [2]. They suggested such a model for low frequencies in 1965 (see Chapter I), but as is shown in this dissertation the idea can be extended to rather remarkable lengths in terms of higher frequencies.

What makes the the present approach unique, however, is the use of non-harmonically related sampling frequencies. Also, when noisy data are considered, the methods suggested and demonstrated for minimizing the deleterious effects of the noise are felt, to some extent, to be new. The final step in the application of Equation (3-2) is routine once the coefficients in Equation (3-2) are known. The zeros of the denominator polynominal yields the poles of the system, and using the numerator coefficients, Equation (3-2) can be rewritten as a residue series, i.e.,

$$E^n(X) = \sum_{j=1}^{M} R_j/(X-P_j) \quad , \tag{3-3}$$

and

$$E^n(X) = \sum_{n=0}^{N} a_n X^{n+2} / \prod_{j=1}^{M} (X-P_j) \quad , \tag{3-4}$$

where R_j are residues and P_j are poles. Then,

$$R_j = \sum_{n=0}^{N} a_n X^{n+2} / \prod_{\substack{i=1 \\ i\neq j}}^{M} (X-P_i) \Big|_{X = P_j} \quad , \tag{3-5}$$

assuming all poles are simple.

Numerous computer programs are available for the purpose of root extraction. It was found, however, that good results require that double precision must be used with these routines. The residues and poles are in complex conjugate pairs for the transfer function of a linear causal system to yield real time domain responses. It is noted that the complex natural resonances are aspect and polarization independent. However, the residues are aspect and polarization dependent. The complex data $E^n(X_i)$ can be expressed in a phasor form as

$$E^n(X_i) = A(X_i) \angle P(X_i) \quad , \tag{3-6}$$

where $A(X_i)$ is the amplitude and $P(X_i)$ is the phase at frequency of X_i. To measure the error between the rational function approximation and the

original data, the following definitions of amplitude errors (norms) are given:

$$E_{amp}^{av} = \left\{ \frac{1}{I} \sum_{i=1}^{I} |A(jk_i1) - A_{RFA}(jk_i1)|^2 \right\}^{1/2} , \qquad (3\text{-}7)$$

$$E_{amp}^{max} = MAX \{ |A(jk_i1) - A_{RFA}|(jk_i1)| \quad i = 1, 2, \ldots, I \} , \qquad (3\text{-}8)$$

where $A(jk_i1)$ and $A_{RFA}(jk_i1)$ are the original and fitted amplitude at frequency k_i1, and E_{amp}^{av} is the root mean squared error (Euclidean norm) between the fitted amplitude and the original one. The quantity E_{amp}^{max} is defined as the maximum error (infinite norm) between the fitted amplitude and the original one. Similar definitions are used for the phase errors. The dimension of the phase used here is degree.

A "best approximate solution" of a system generally will have different solutions for different choices of the norm. The root mean squared error and the maximun error are calculated in each run using different data sets. From various trials and errors, the least error in the sense of Euclidean norm or infinite norm is selected and the "best" fit is obtained.

In applying the rational function approximants to a set of simulated data, there are a number of parameters which must be chosen before running the program, the orders of the system (M and N) and the selected sample data points. Therefore, to better understand the limitations of the unknown system orders and to gain experience in the

selection of the data points, it is helpful to consider first the simulated real-frequency backscattering data of a conducting sphere where the complex natural resonances and the corresponding residues are well known [7, 25]. Some of the lower order true poles and residues of a conducting sphere (see Table 3-1) [25] are used in Equation (3-9) to generate sets of simulated data.

$$E^S(X) = \sum_{i=1}^{M} \left(\frac{R_i}{X-P_i} + \frac{R_i^*}{X-P_i^*} \right) \quad , \qquad (3\text{-}9)$$

where $E^S(X)$ are the simulated data and R_i, P_i, are poles and residues respectively. X is jkl and X* denotes complex conjugate.

In generating simulated data to test pole extracting procedures, actual poles and actual residues of the sphere were used. Much too often researchers have assumed equal excitation of all poles (a very unrealistic assumption) and correspondingly shown misleading results for particular pole extraction techniques. In principle, the generated simulated waveforms could be exact if many more pole-pairs were used. However even here, great care must be exercised in using residue series summations [26].

B. EXAMPLE 1: SIMULATED SPHERE DATA USING FOUR POLE-PAIRS

In this example, only the first four pairs of poles and the corresponding residues in Table 3-1 are used in Equation (3-9) to generate a set of simulated scattering data. The data are generated in

TABLE 3-1

TRUE POLES AND RESIDUES* USED FOR GENERATING SETS OF SIMULATED DATA

Simulated Poles (true poles of a sphere)	Simulated Residues (true residues of a sphere)
-0.500000+/-j0.866025	-0.0946447-/+0.516674
-0.701964+/-j1.80740	-0.633323 -/+0.0853256
-0.842862+/-j2.75786	-0.0802221+/-j0.733736
-0.954230+/-j3.71478	-0.822075 +/-j0.0767481
-1.04764 +/-j4.57641	-0.0741270-/+j0.901805
-1.12891 +/-j5.64163	-0.0664705+/-j0.223154

* The units of the poles and the residues are in ka, where k is the wavenumber and a is the radius of the sphere.

the real frequency domain from ka of 0.2 to ka of 4 in the increment of 0.02 ka, i.e., 191 data points are generated. Then, a rational function approximant of order (M,N) as (8,7)* is applied to the above set of data. Since there is no Rayleigh region in this set of simulated data, the dependence is taken out from Equation (3-2). Thus, model II is defined as

$$E^n(X_i) = \sum_{n=0}^{N} a_n X_i^n \Big/ \left(1 + \sum_{m=1}^{M} b_m X_i^m\right) i = 1, 2, \ldots, I \quad . \qquad (3\text{-}10)$$

The data points used in the rational function approximant are arbitrary and need not be equally-spaced in frequency. A typical plot of a rational function approximation to the above simulated data is in Figures 3-1 (amplitude) and 3-2 (phase) for (M, N) as (8,7) and in Figures 3-3 (amplitude) and 3-4 (phase) for (M,N) as (20,19)**. As can be seen in the plots, the rational function model with the above system orders fitted all the data points so well that the original and the fitted curves of both amplitude and phase cannot be distinguished in the plots.

---

* M = 8 is the smallest system order for the simulated data using four pole-pairs (eight poles); N of 7, i.e., N of (M-1), is the best choice for the RFA to fit the original data but satisfies Equation (3-9), i.e., the order of the numerator is one order less than that of the denominator.

** The system order M of 20 is chosen because the RFA programs of order higher than 20 are close to the maximum capacity of the computer (VAX 11/780) used in the calculation.

ZEROS		POLES	
real part	imaginary part	real part	imaginary part
-1.648103 X10^{-1}	1.884338 X10^{0}	-9.542384 X10^{-1}	3.714781 X10^{0}
-1.160983 X10^{1}	2.695555 X10^{-7}	-9.542384 X10^{-1}	-3.714782 X10^{0}
-1.648.03 X10^{-1}	-1.884368 X10^{0}	-8.426592 X10^{-1}	2.757888 X10^{0}
-3.808595 X10^{-1}	3.018873 X10^{0}	-8.426592 X10^{-1}	-2.757885 X10^{0}
-3.808589 X10^{-1}	-3.018873 X10^{0}	-7.019529 X10^{-1}	1.807402 X10^{0}
1.298220 X10^{0}	0.000000 X10^{0}	-7.019525 X10^{-1}	-1.807400 X10^{0}
-1.424322 X10^{0}	0.000000 X10^{0}	-5.000001 X10^{-1}	8.660247 X10^{-1}
		-5.000002 X10^{-1}	-8.660249 X10^{-1}

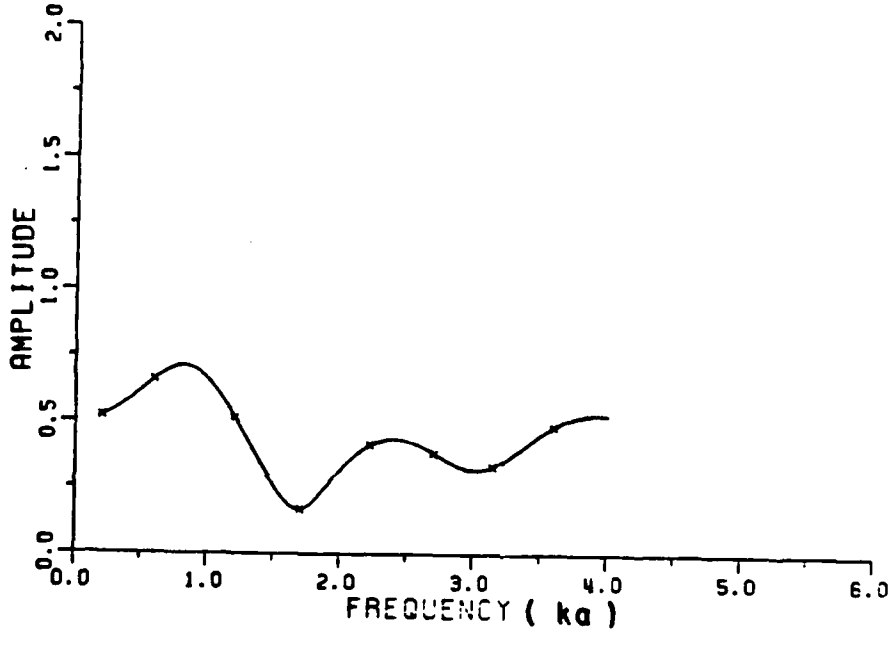

Figure 3-1. The RFA for (M,N) as (8,7) fit to the simulated data using the first four pole-pairs and residues for the sphere. The x's are the data points used for the RFA. The amplitude plot of the RFA (dashed line) gives a good fit to the original amplitude data (solid line). The corresponding phase plot is given in Figure 3-2.

RESIDUES		MAGNITUDE OF RESIDUES
real part	imaginary part	
-8.220891 X10^{-1}	7.675887 X10^{-2}	8.255649 X10^{-1}
-8.220881 X10^{-1}	-7.676030 X10^{-2}	8.256541 X10^{-1}
8.024058 X10^{-2}	7.337325 X10^{-1}	7.381070 X10^{-1}
8.024037 X10^{-2}	-7.337308 X10^{-1}	7.381053 X10^{-1}
6.333205 X10^{-1}	-8.532918 X10^{-2}	6.390430 X10^{-1}
6.333198 X10^{-1}	8.532750 X10^{-2}	6.390421 X10^{-1}
-8.464421 X10^{-2}	-5.166736 X10^{-1}	5.252707 X10^{-1}
-8.464430 X10^{-2}	5.166742 X10^{-1}	5.252712 X10^{-1}

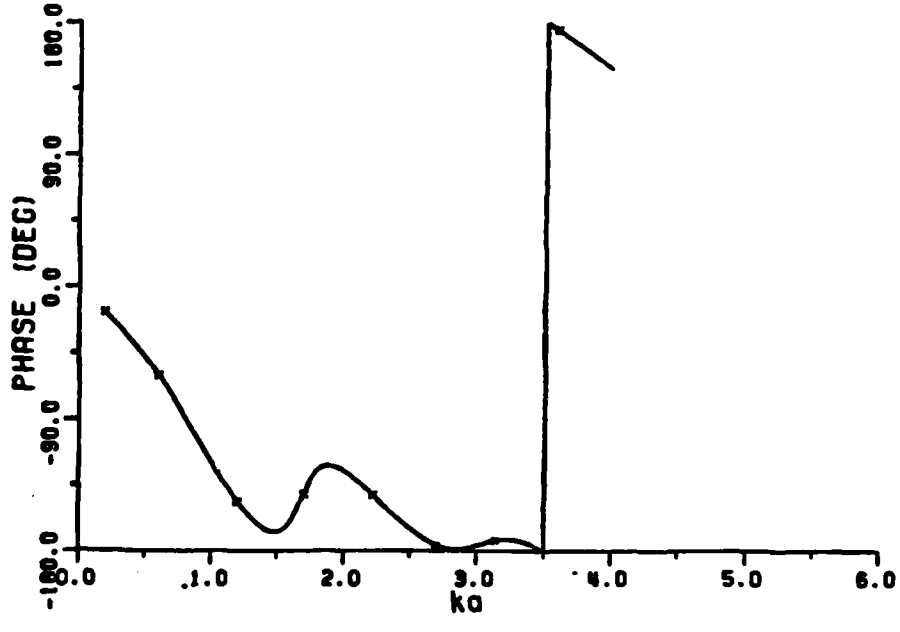

Figure 3-2. The RFA for (M,N) as (8,7) fit to the simulated data using the first four pole-pairs and residues for the sphere. The x's are the data points used for the RFA. The phase plot of the RFA (dashed line) gives a good fit to the original phase data (solid line). The corresponding amplitude plot is given in Figure 3-1.

ZEROS		POLES	
real part	imaginary part	real part	imaginary part
-1.646081 X10^{-1}	1.684404 X10^{0}	-9.542134 X10^{-1}	-3.714774 X10^{0}
-1.161019 X10^{1}	3.401250 X10^{-7}	-9.542189 X10^{-1}	3.714798 X10^{0}
-1.646097 X10^{-1}	-1.684402 X10^{0}	4.301742 X10^{-1}	2.160780 X10^{0}
4.301634 X10^{-1}	2.160790 X10^{0}	4.301637 X10^{-1}	-2.160780 X10^{0}
4.301649 X10^{-1}	-2.160788 X10^{0}	-8.429173 X10^{-1}	2.757886 X10^{0}
-1.424296 X10^{0}	0.000000 X10^{0}	-8.428735 X10^{-1}	-2.757881 X10^{0}
1.298220 X10^{0}	0.000000 X10^{0}	1.800992 X10^{-1}	3.845727 X10^{0}
-3.964923 X10^{-1}	1.865480 X10^{0}	1.800885 X10^{-1}	-3.845716 X10^{0}
-3.964941 X10^{-1}	-1.865483 X10^{0}	1.228633 X10^{-1}	2.979648 X10^{0}
-3.808550 X10^{-1}	3.018866 X10^{0}	1.228256 X10^{-1}	-2.979652 X10^{0}
-3.808586 X10^{-1}	-3.018868 X10^{0}	-3.965272 X10^{-1}	1.865436 X10^{0}
1.800761 X10^{-1}	3.845733 X10^{0}	-3.965224 X10^{-1}	-1.865493 X10^{0}
1.800758 X10^{-1}	-3.845736 X10^{0}	-7.019805 X10^{-1}	1.807431 X10^{0}
1.228364 X10^{-1}	2.979678 X10^{0}	-7.019694 X10^{-1}	-1.807411 X10^{0}
1.228424 X10^{-1}	-2.979674 X10^{0}	2.318138 X10^{-1}	1.513267 X10^{0}
2.318091 X10^{-1}	1.513269 X10^{0}	2.318077 X10^{-1}	-1.513265 X10^{0}
2.318091 X10^{-1}	-1.513268 X10^{0}	-5.000018 X10^{-1}	8.660266 X10^{-1}
1.939628 X10^{-1}	7.806049 X10^{-1}	-5.000018 X10^{-1}	-8.660259 X10^{-1}
1.939629 X10^{-1}	-7.806049 X10^{-1}	1.939628 X10^{-1}	7.806047 X10^{-1}
		1.939628 X10^{-1}	-7.806048 X10^{-1}

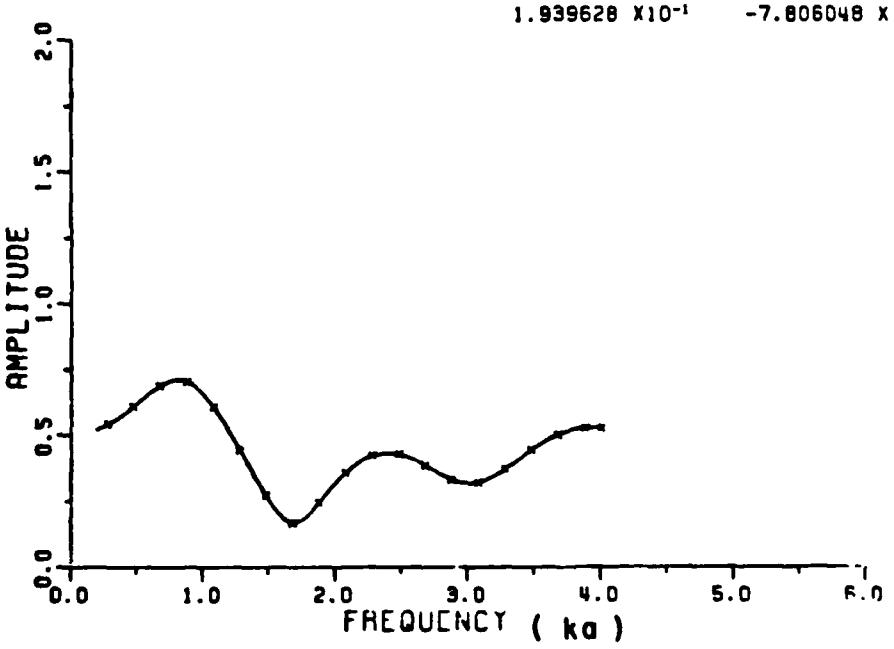

Figure 3-3. The RFA for (M,N) as (20,19) fit to the simulated data using the first four pole-pairs and residues for the sphere. The x's are the data points used for the RFA. The amplitude plot of the RFA (dashed line) gives a good fit to the original amplitude data (solid line). The corresponding phase plot is given in Figure 3-4.

RESIDUES		MAGNITUDE OF RESIDUES
real part	imaginary part	
-8.221192 X10^{-1}	-7.668856 X10^{-2}	8.256884 X10^{-1}
-8.220752 X10^{-1}	7.667348 X10^{-2}	8.256432 X10^{-1}
-2.288067 X10^{-6}	-3.089844 X10^{-7}	2.308835 X10^{-6}
2.298225 X10^{-7}	-1.051067 X10^{-6}	1.075900 X10^{-6}
8.019796 X10^{-2}	7.337992 X10^{-1}	7.381686 X10^{-1}
8.020413 X10^{-2}	-7.338169 X10^{-1}	7.381871 X10^{-1}
-8.347081 X10^{-6}	6.184270 X10^{-6}	1.038840 X10^{-5}
-2.136122 X10^{-6}	-8.898026 X10^{-6}	9.150840 X10^{-6}
-5.328118 X10^{-6}	8.914798 X10^{-6}	1.038569 X10^{-5}
7.058907 X10^{-6}	-8.376256 X10^{-6}	1.095399 X10^{-5}
-5.032626 X10^{-5}	-1.654818 X10^{-5}	5.297712 X10^{-5}
-1.166051 X10^{-5}	-1.975285 X10^{-5}	2.293780 X10^{-5}
6.334225 X10^{-1}	-8.528059 X10^{-2}	6.391376 X10^{-1}
6.333988 X10^{-1}	8.535620 X10^{-2}	6.391242 X10^{-1}
-1.235762 X10^{-6}	-5.211915 X10^{-7}	1.341175 X10^{-6}
-1.016205 X10^{-7}	-6.314587 X10^{-7}	6.395834 X10^{-7}
-9.464732 X10^{-2}	-5.166819 X10^{-1}	5.252793 X10^{-1}
-9.464674 X10^{-2}	5.166803 X10^{-1}	5.252776 X10^{-1}
-6.815718 X10^{-6}	2.013025 X10^{-6}	7.106778 X10^{-6}
-1.554200 X10^{-6}	-3.616981 X10^{-6}	3.936762 X10^{-6}

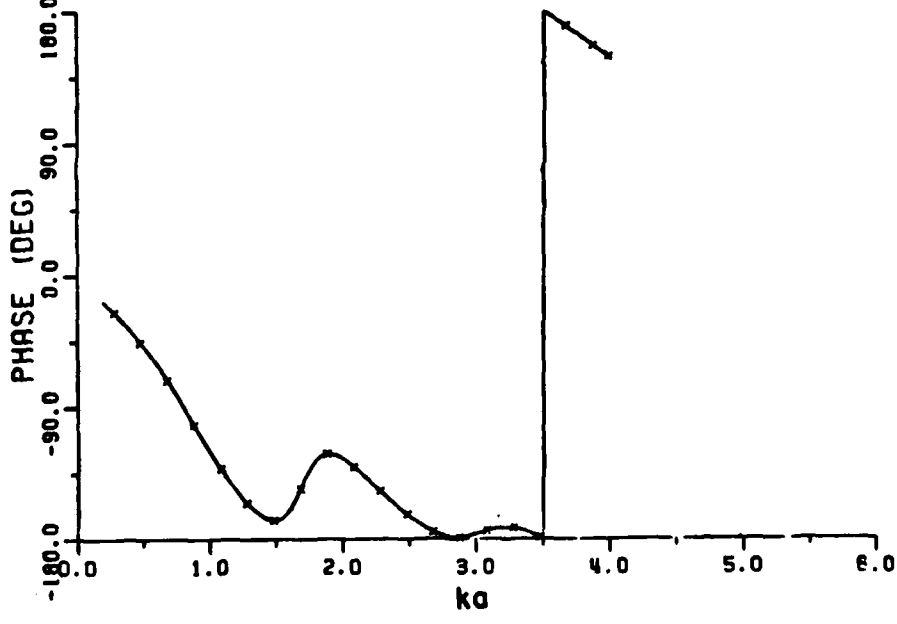

Figure 3-4. The RFA for (M,N) as (20,19) fit to the simulated data using the first four pole-pairs and residues for the sphere. The x's are the data points used for the RFA. The phase plot of the RFA (dashed line) gives a good fit to the original phase data (solid line). The corresponding amplitude plot is given in Figure 3-3.

Besides the original curve (solid line) and the RFA (dotted line), a third one (dashed line) is generated (see Equation (3-9)) using the poles and residues obtained from the RFA. Actually these procedures are routine in the RFA program to check the accuracy of the extracted poles and residues. The approximation is such that only the solid line can be seen in the RFA plots. The zeros, poles, residues and magnitude of residues are listed on the amplitude and phase plots. The advantage of these listings is to see the true poles, curve fitting poles, and the cancellation of poles and zeros before the true poles and residues are deduced. It is noted that only M complex data points are used to solve the linear system equations in the exact sense. The average errors* of the RFA to the above set of simulated data are of the order of 1.E-5 in amplitude and 1.E-4 in the phase (in degrees). The numerical accuracy of the entire rational function program was tested using the data in Example I for various system orders and various input data points. In all cases the programs were found to be very accurate. Therefore, it is assumed that the program can be applied routinely to other scattering data without worrying about numerical errors generated within the program itself.

The poles and the residues extracted via the rational function approximants using different system orders M, N, and different sets of selected data points are listed in Table 3-2 for (M,N) as (8,7) and

---

* Since the data are exact for these poles (residues), only trancation contributes to the errors. Obviously the error is dependent also on the selected sample points.

TABLE 3-2

A COMPARISON OF TRUE POLES AND EXTRACTED POLES, TRUE RESIDUES AND EXTRACTED RESIDUES FOR (M,N) AS (8,7); FOUR PAIRS OF POLES AND RESIDUES* ARE USED IN THE SIMULATED DATA

Poles

True	Extracted	Percentage of Error	
		Real	Imaginary
-0.50000 +/-j0.866025	-0.50000 +/-j0.866025	0.E0	0.E0
-0.701964+/-j1.80740	-0.701962+/-j1.80740	1.04E-4	2.07E-4
-0.842862+/-j2.75786	-0.842859+/-j2.757866	1.03E-4	4.97E-5
-0.954230+/-j3.71478	-0.954238+/-j3.714782	2.08e-4	4.97E-5

Residues

True	Extracted	Percentage of Error	
		Real	Imaginary
-0.0946447+/-j0.516674	-0.094644-/+j0.516674	1.33E-4	0.E0
-0.633323 -/+j0.0853256	0.633320-/+j0.08533	4.76E-4	3.75E-4
0.0802221+/-j0.733736	0.08024 +/-j0.73373	2.42E-3	8.07E-4
-0.822075 +/-j0.07674781	-0.822088+/-j0.07676	1.57E-3	1.48E-3

* The units of the poles and the residues are in ka, where k is the wavenumber and a is the radius of the sphere.

Table 3-3 for (M,N) as (20,19). The maximum and the average discrepancy of the fitted amplitude and the original amplitude, the fitted phase and the original phase are listed in Table 3-4. Obviously, the smaller the maximum amplitude discrepancy or the smaller the average amplitude discrepancy, the closer the fitted curve is to the original one (similarily, for the phase error). Correspondingly, the extracted poles are closer to the original poles. The percentage error (P.E.) is defined for both real part and imaginary part of the extracted poles as

$$\text{P. E. of real part} = \frac{|\text{Real part } (\text{Pole}_{\text{ext.}} - \text{Pole}_{\text{true}})|}{|\text{Pole}_{\text{true}}|} \quad , \qquad (3\text{-}11)$$

$$\text{P. E. of imaginary part} = \frac{|\text{Imag. part}(\text{Pole}_{\text{ext.}} - \text{Pole}_{\text{true}})|}{|\text{Pole}_{\text{true}}|} \quad , \qquad (3\text{-}12)$$

where $\text{Pole}_{\text{ext.}}$ is the extracted pole and $\text{Pole}_{\text{true}}$ is the true pole. Similar definitions are used for the residues. A comparison of extracted poles, the percentage error of extracted poles and the errors of amplitude and phase are also shown in Table 3-4.

As can be seen in Tables 3-2 to 3-4, various system orders of the RFA have been applied to the same data set to see the effect of the system order on the accuracy of the extracting poles. However, no obvious result has been found in this simple simulated example except that the system order should not be less than the number of simulated system poles. For real targets there are an infinite number of

TABLE 3-3

A COMPARISON OF TRUE POLES AND EXTRACTED POLES, TRUE RESIDUES AND EXTRACTED RESIDUES FOR (M,N) AS (20,19); FOUR PAIRS OF POLES AND RESIDUES* ARE USED IN THE CALCULATION OF THE SIMULATED DATA

True Poles	Extracted Poles	Percentage Error real	Percentage Error imaginary
-0.50000 +/-j0.866025	-0.50000+/-j0.86602	0.E0	4.95E-4
-0.701964+/-j1.80740	-0.70196+/-j1.80741	2.06E-4	5.16E-4
-0.842862+/-j2.75786	-0.84283+/-j2.75791	1.11E-3	1.74E-3
-0.954230+/-j3.71478	-0.95421+/-j3.71492	5.22E-4	3.65E-3
	Curve fitting Poles*	Curve-fitting Zeros	
	0.19396+/-j0.78060	-0.19396+/-j0.78060	
	0.23181+/-j1.51326	-0.23181+/-j1.51327	
	-0.39652+/-j1.86546	-0.39649+/-j1.86548	
	0.12284+/-j2.97965	0.12284+/-j2.97967	
	0.18009+/-j3.84572	0.18008+/-j3.84573	
	0.43016+/-j2.16078	0.43016+/-j2.16079	
		Extracted Zeros	
		-0.38086+/-j3.01887	
		-0.16461+/-j1.68440	
		-1.16102+/-j0.	
		1.29822+/-j0.	
		-1.42429+/-j0.	

True Residues	Extracted Residues**	Percentage Error	
-0.0946447-/+j0.516674	-0.09463-/+j0.51668	2.79e-3	1.15E3
0.633323 -/+j0.0853256	0.63332-/+j0.0854	4.76E-4	1.16E-2
0.0802221+/-j0.733736	0.08046+/-j0.7335	3.22E-2	3.197E-2
-0.822075 +/-j0.07674781	0.8219 +/-j0.07706	2.119E-2	3.781E-2

* The units of the poles and the residues are in ka, where k is the wavenumber and a is the radius of the sphere.

** All extracted residues corresponding to the curve-fitting poles are in the order of 1.E-5 or less for both real and imaginary parts.

TABLE 3-4

THE EXTRACTED POLES AND THE ERRORS BETWEEN THE RATIONAL FUNCTION FIT AND THE ORIGINAL DATA (SIMULATED DATA USED IN EXAMPLE 1)*

True poles	RFA Model I M = 14, N = 13	Percentage Error Real Part	Imag. Part
-0.500000+/-J0.866025	-0.50000 +/-J0.866022	0.E0	2.98e-04
-0.70196 +/-J1.80739	-0.7019523+/-J1.80743	6.06E-4	1.55E-3
-0.842849+/-J2.75786	-0.84282 +/-J2.75741	1.457E-3	1.56E-2
-0.954299+/-J3.714787	-0.9648 +/-J3.7253	0.27	0.27

MAX. AMP. ERROR 0.19E-5
AVE. AMP. ERROR 0.2E-6
MAX. PHA. ERROR 0.1068E-3
AVE. PHA. ERROR 0.155E-4

	RFA Model II M = 14, N = 13	Percentage Error Real Part	Imag. Part
	-0.499998+/-J0.86606	2.E-4	3.505E-3
	-0.70196 +/-J1.80738	2.06E-4	1.03E-3
	-0.84295 +/-J2.75778	3.05E-3	2.77E-3
	-0.95515 +/-J3.71550	2.4E-02	1.877E-2

MAX. AMP. ERROR 0.5E-6
AVE. AMP. ERROR 0.1E-6
MAX. PHA. ERROR 0.916E-4
AVE. PHA. ERROR 0.148E-4

	RFA Model I M = 16, N = 15	Percentage Error Real Part	Imag. Part
	-0.499997+/-j0.866023	3.01E-4	1.97E-4
	-0.701981+/-j1.80739	8.76E-4	5.16E-4
	-0.84286 +/-j2.75810	7.03E-5	8.33E-3
	-0.95048 +/-j3.71478	9.78E-2	0.E0

MAX. AMP. ERROR 0.19E-5
AVE. AMP. ERROR 0.2E-6
MAX. PHA. ERROR 0.176E-3
AVE. PHA. ERROR 0.187E-4

* The units of the poles and the residues are in ka, where a is the radius of the sphere and k is the wavenumber.

singularities in the system transfer function. However, over a limited spectral span only a finite number, hopefully small, will contribute significantly.

C. EXAMPLE 2: SIMULATED SPHERE DATA USING SIX POLE-PAIRS

It is well known that there are an infinite number of pole pairs for a scatterer [4]. To generate a set of simulated data similar to the real scattering ones, six pairs of simulated poles and residues (Table 3-1) are used in Equation (3-9). The simulated data (ka of 0.2(0.02),4.) are generated in the same way as that in example 1 except that 2 more pole pairs and the corresponding residues outside the original spectrum are used in Equation (3-9). Once again, the RFA routine is used to extract poles from this set of simulated data. The original data and fitted data are plotted in Figures 3-5 and 3-6. The extracted poles are shown on Table 3-5.

The two highest frequency pole-pairs are not as close to the original ones as as those found in example one because the two pairs of poles outside the original spectrum have some influence on the extracted poles, especially over the higher frequency portion of the spectrum. This is one of the reasons why curve fitting poles are obtained when the rational function approximants are used and the reason why the system order should always be chosen higher than the number of poles actually desired. The number of true poles is known in these simulated data but the number of true poles in a set of calculated data or

TABLE 3-5

A COMPARISON OF TRUE POLES AND EXTRACTED POLES, TRUE RESIDUES AND EXTRACTED RESIDUES FOR (M,N) AS (14,13); 6 POLE-PAIRS AND THEIR CORRESPONDING RESIDUES ARE USED IN THE GENERATION OF SIMULATED DATA

Poles (M = 14, N = 13)*			
True Poles	Extracted Poles	Percentage Error Real	Imaginary
-0.50000 +/-j0.866025	-0.499995+/-j0.866023	5.E-4	1.97E-4
-0.701964+/-j1.80740	-0.70203 +/-j1.80746	3.4E-3	3.1E-3
-0.842862+/-j2.75786	-0.8427 +/-j2.7572	5.62E-3	2.29E-2
-0.954230+/-j3.71478	-0.9689 +/-j3.7213	0.382	0.17

Residues (M = 14, N = 13)			
True Residues	Extracted residues	Percentage Error Real	Imaginary
-0.0946447-/+j0.516674	-0.094641-/+j0.516647	7.05E-4	5.14E-3
0.633323 -/+j0.0853256	0.6337 -/+j0.08573	5.8994E-4	6.328E-2
0.0802221+/-j0.733736	0.07635 +/-j0.7326	0.5246	0.154
-0.822075 +/-j0.07674781	0.924 +/-j0.07676	12.34	6.63E-2

* The units of the poles and the residues are in ka, where k is the wavenumber and a is the radius of the sphere. Also the three pairs of curve fitting poles and the corresponding residues are not shown here.

ZEROS		POLES	
real part	imaginary part	real part	imaginary part
-1.554460 X10^{0}	-4.660380 X10^{0}	-9.600332 X10^{-1}	-5.010544 X10^{0}
-1.554460 X10^{0}	4.660381 X10^{0}	-9.601137 X10^{-1}	5.010547 X10^{0}
5.117474 X10^{0}	5.204235 X10^{-8}	-1.248494 X10^{0}	4.339105 X10^{0}
-2.650605 X10^{-1}	2.755748 X10^{0}	-1.248550 X10^{0}	-4.339154 X10^{0}
-2.650607 X10^{-1}	-2.755748 X10^{0}	-9.688541 X10^{-1}	3.721324 X10^{0}
-4.807194 X10^{-1}	4.064566 X10^{0}	-9.688918 X10^{-1}	-3.721268 X10^{0}
-4.807195 X10^{-1}	-4.064566 X10^{0}	-8.427192 X10^{-1}	2.757222 X10^{0}
-1.496857 X10^{0}	1.609424 X10^{0}	-8.427510 X10^{-1}	-2.757230 X10^{0}
-1.496857 X10^{0}	-1.609423 X10^{0}	-7.020343 X10^{-1}	1.807463 X10^{0}
-3.923506 X10^{0}	4.256098 X10^{-7}	-7.020302 X10^{-1}	-1.807463 X10^{0}
-2.119843 X10^{0}	-8.165484 X10^{-7}	-1.493493 X10^{0}	1.613342 X10^{0}
-1.174672 X10^{-1}	-1.462692 X10^{0}	-1.493492 X10^{0}	-1.613345 X10^{0}
-1.174674 X10^{-1}	1.462892 X10^{0}	-4.999944 X10^{-1}	8.660237 X10^{-1}
		-4.999948 X10^{-1}	-8.660234 X10^{-1}

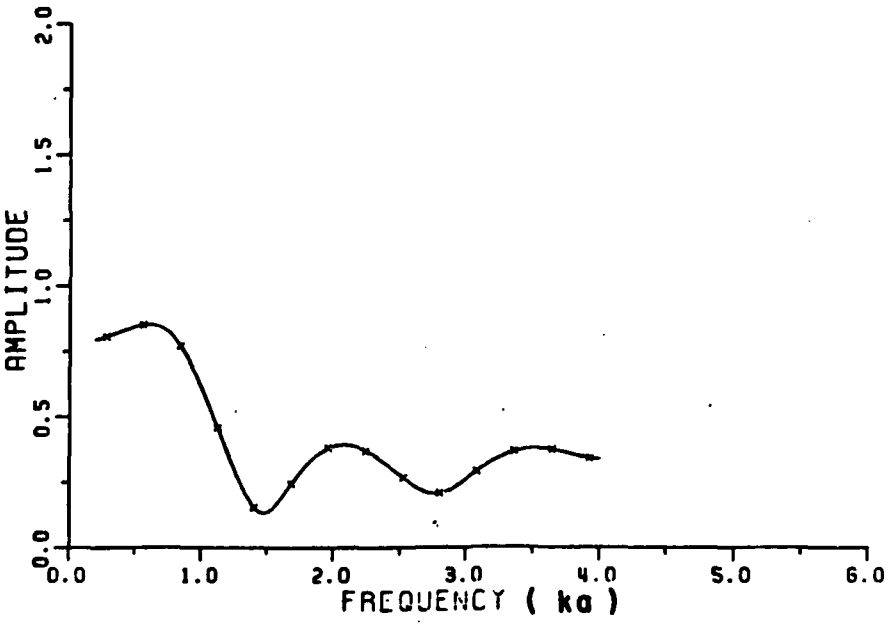

Figure 3-5. The RFA for (M,N) as (14,13) fit to the simulated data using the first six pole-pairs and residues for the sphere. The x's are the data points used for the RFA. The amplitude plot of the RFA gives a good fit to the original data (solid line). The corresponding phase plot is given in Figure 3-6.

RESIDUES		MAGNITUDE OF RESIDUES
real part	imaginary part	
-5.778155 X10^{-1}	2.186992 X10^{-1}	6.179124 X10^{-1}
-5.779323 X10^{-1}	-2.186572 X10^{-1}	6.179132 X10^{-1}
5.521024 X10^{-1}	-4.324758 X10^{-1}	7.013219 X10^{-1}
5.519400 X10^{-1}	4.323715 X10^{-1}	7.011297 X10^{-1}
-9.241735 X10^{-1}	7.633334 X10^{-2}	9.273205 X10^{-1}
-9.240150 X10^{-1}	-7.621012 X10^{-2}	9.271525 X10^{-1}
7.636612 X10^{-2}	7.326234 X10^{-1}	7.365927 X10^{-1}
7.635854 X10^{-2}	-7.326953 X10^{-1}	7.366634 X10^{-1}
6.337088 X10^{-1}	-8.572482 X10^{-2}	6.394807 X10^{-1}
6.337043 X10^{-1}	8.573312 X10^{-2}	6.394774 X10^{-1}
-3.499669 X10^{-3}	-3.834912 X10^{-3}	5.191747 X10^{-3}
-3.501096 X10^{-3}	3.837290 X10^{-3}	5.194465 X10^{-3}
-9.464147 X10^{-2}	-5.166474 X10^{-1}	5.252443 X10^{-1}
-9.464074 X10^{-2}	5.166478 X10^{-1}	5.252445 X10^{-1}

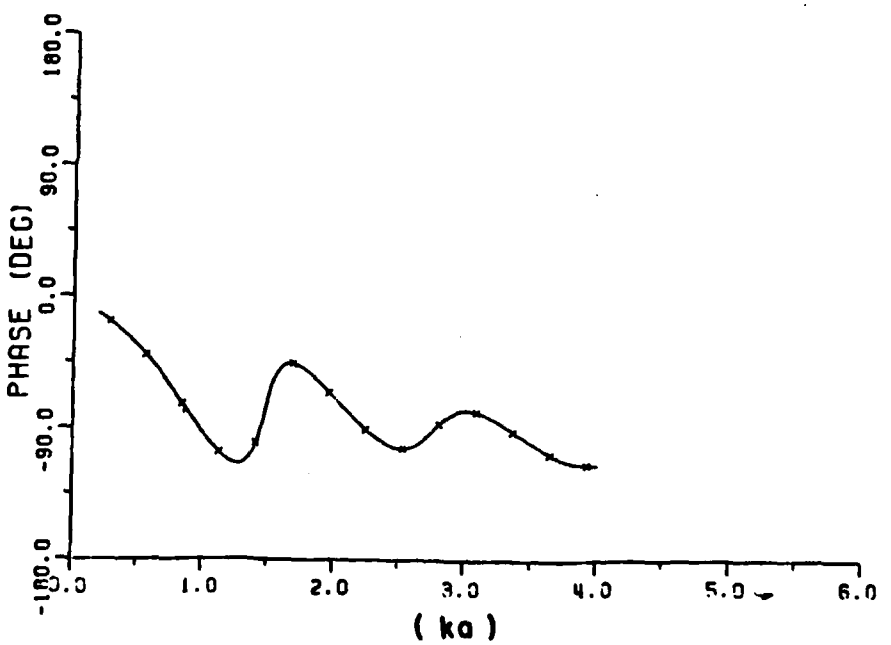

Figure 3-6. The RFA for (M,N) as (14,13) fit to the simulated data using the first six pole-pairs and residues for the sphere. The x's are the data points used for the RFA. The phase plot of the RFA (dashed line) gives a good fit to the original data (solid line). The corresponding amplitude plot is given in Figure 3-5.

measured data is unknown. A detailed discussion on the determination of the system order is given in a later section.

D. EXAMPLE 3: CALCULATED BACKSCATTERING DATA FOR A CONDUCTING SPHERE

The spectrum of a conducting sphere [27] used to test rational function approximants is from ka of 0.2 to ka of 4 in the increment of 0.02 ka, i.e., 191 data points are available. To test the rational function approximation in application to this set of calculated data, M is set to be the number of poles where the imaginary parts are within the given spectrum first. As discussed before, the extracted poles are not accurate if the system order M is less than the number of true poles. However, a better result can be obtained if the system order is set around twice the number of the true poles in the system.*

After the polynomial orders (M and N) are selected for testing, different sets of data points are used and the defined errors in amplitude and phase are calculated. Table 3-6 is a comparison of the extracted poles and their percent errors. Figures 3-7 to 3-10 are plots of the rational function fit under two different sets of (M,N) ((14,13) and (16,15)). Obviously, the original curve and the fitted curve agree so well that they cannot be distinguished in the plots of both amplitude and phase. However, the results fit better for (M,N) as (14,13). If different sets of selected data points are used for the RFA, the results

---

* Basically, the extra orders (the orders which are higher than the number of true poles) are required for the curve fittings although the curve-fitting poles have no physical meaning.

TABLE 3-6

A COMPARISON OF EXACT POLES AND THOSE EXTRACTED* FROM CALCULATED DATA FOR SPHERE VIA RATIONAL FUNCTION APPROXIMATION

True Poles	Extracted Poles M = 14, N = 13	Percentage Error Real Part	Imag. Part
-0.50000 +/-j0.866025	-0.500000+/-j0.86662	0.E00	5.95E-2
-0.701964+/-j1.80740	-0.70193 +/-j1.8028	1.75E-3	0.237
-0.842862+/-j2.75786	-0.84244 +/-j2.76213	1.463E-2	0.148
-0.95423 +/-j3.71478	-0.9175 +/-j3.6829	0.9576	0.8312
	M = 16, N = 15 (exact fit)		
	-0.50087+/-j0.86575	8.7E-2	2.75E-2
	-0.71008+/-j1.79815	0.42E0	0.48E0
	-0.84535+/-j2.76718	8.63E-2	0.32E0
	-0.9076 +/-j3.69581	1.22E0	0.49E0

* The units of the poles are in ka, where k is the wavenumber, a is the sphere radius.

ZEROS		POLES	
real part	imaginary part	real part	imaginary part
9.481741 X10^{1}	2.824622 X10^{-7}	-7.592796 X10^{-1}	4.427872 X10^{0}
-1.405259 X10^{0}	-5.480211 X10^{0}	-7.592834 X10^{-1}	-4.427870 X10^{0}
-1.405260 X10^{0}	5.480212 X10^{0}	-9.175043 X10^{-1}	-3.682917 X10^{0}
-2.986803 X10^{-1}	-4.152524 X10^{0}	-9.175143 X10^{-1}	3.682912 X10^{0}
-2.986795 X10^{-1}	4.152524 X10^{0}	-8.424441 X10^{-1}	-2.762127 X10^{0}
-2.298278 X10^{-1}	-2.949347 X10^{0}	-8.424373 X10^{-1}	2.762136 X10^{0}
-2.298284 X10^{-1}	2.949347 X10^{0}	-7.019316 X10^{-1}	-1.802941 X10^{0}
-1.392493 X10^{-1}	-1.740495 X10^{0}	-7.019265 X10^{-1}	1.802834 X10^{0}
-1.392492 X10^{-1}	1.740496 X10^{0}	-7.112110 X10^{-1}	-1.218378 X10^{0}
-1.231829 X10^{0}	-7.873954 X10^{-1}	-7.112207 X10^{-1}	1.218378 X10^{0}
-1.231829 X10^{0}	7.873953 X10^{-1}	-1.340053 X10^{0}	-5.872938 X10^{-6}
-7.211325 X10^{-1}	-1.209984 X10^{0}	-1.116686 X10^{0}	5.496470 X10^{-6}
-7.211317 X10^{-1}	1.209983 X10^{0}	-4.999974 X10^{-1}	-8.666176 X10^{-1}
		-4.999950 X10^{-1}	8.666194 X10^{-1}

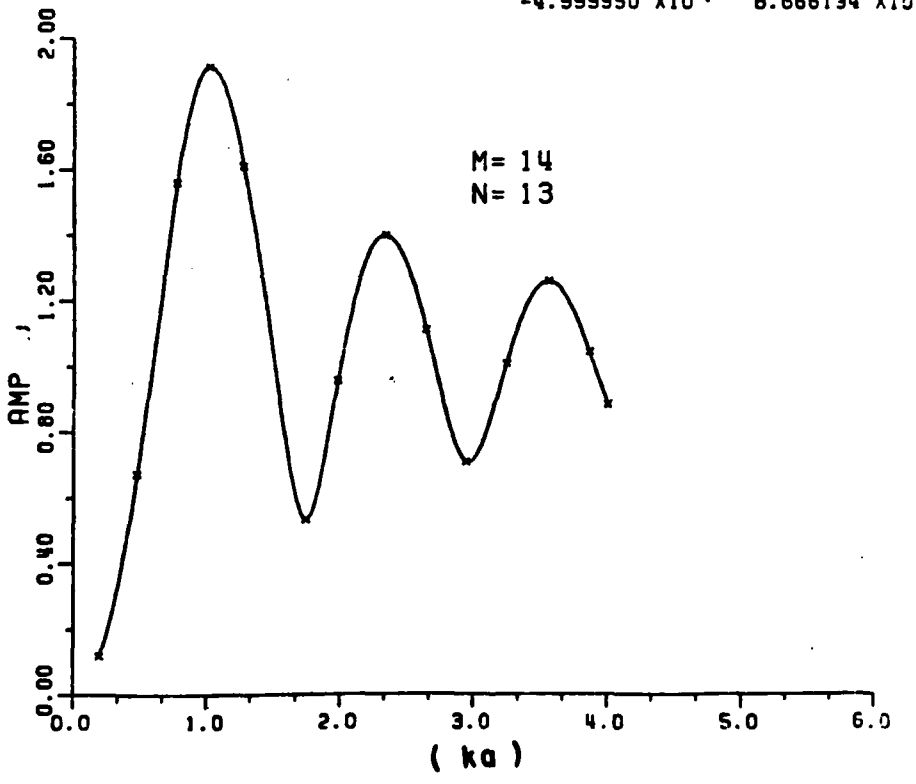

Figure 3-7. The RFA for (M,N) as (14,13) fit to the calculated data for the sphere. The x's are the data points used for the RFA. The amplitude plot of the RFA (dashed line) gives a good fit to the original amplitude data (solid line). The corresponding phase plot is given in Figure 3-8.

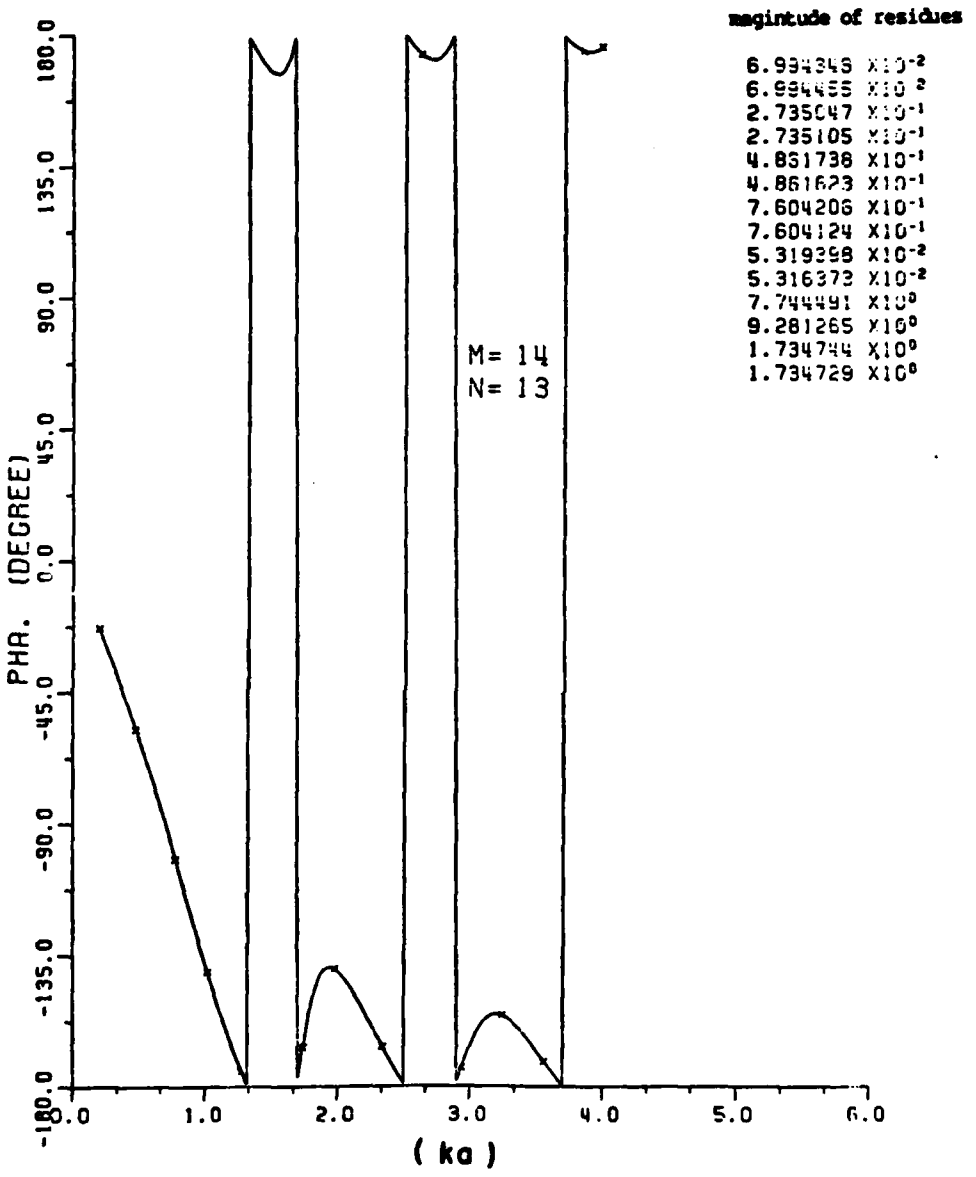

Figure 3-8. The RFA for (M,N) as (14,13) fit to the calculated data for the sphere. The x's are the data points used for the RFA. The phase plot of the RFA (dashed line) gives a good fit to the original phase data (solid line). The corresponding amplitude plot is given in Figure 3-7.

ZEROS		POLES	
real part	imaginary part	real part	imaginary part
7.102981 X10^{1}	-2.992931 X10^{-7}	-7.439583 X10^{-1}	4.469733 X10^{0}
-1.245875 X10^{0}	-5.475637 X10^{0}	-7.439592 X10^{-1}	-4.469731 X10^{0}
-1.245875 X10^{0}	5.475638 X10^{0}	-9.076006 X10^{-1}	-3.695808 X10^{0}
-2.984059 X10^{-1}	-4.153725 X10^{0}	-9.076023 X10^{-1}	3.695809 X10^{0}
-2.984064 X10^{-1}	4.153725 X10^{0}	-8.453510 X10^{-1}	-2.767184 X10^{0}
-2.298105 X10^{-1}	-2.949361 X10^{0}	-8.453512 X10^{-1}	2.767176 X10^{0}
-2.298093 X10^{-1}	2.949361 X10^{0}	-3.238230 X10^{-1}	-1.962551 X10^{0}
-3.241807 X10^{-1}	-1.962527 X10^{0}	-3.238292 X10^{-1}	1.962556 X10^{0}
-3.241827 X10^{-1}	1.962527 X10^{0}	-7.100863 X10^{-1}	-1.798145 X10^{0}
-1.392796 X10^{-1}	-1.740481 X10^{0}	-7.100788 X10^{-1}	1.798145 X10^{0}
-1.392783 X10^{-1}	1.740481 X10^{0}	-5.008748 X10^{-1}	-8.657454 X10^{-1}
-1.147611 X10^{0}	-6.916483 X10^{-1}	-5.008749 X10^{-1}	8.657455 X10^{-1}
-1.147611 X10^{0}	6.916483 X10^{-1}	1.961218 X10^{0}	0.000000 X10^{0}
1.961505 X10^{0}	0.000000 X10^{0}	8.258358 X10^{-2}	0.000000 X10^{0}
8.258108 X10^{-2}	0.000000 X10^{0}	-1.108586 X10^{0}	2.115911 X10^{-1}
		-1.108586 X10^{0}	-2.115911 X10^{-1}

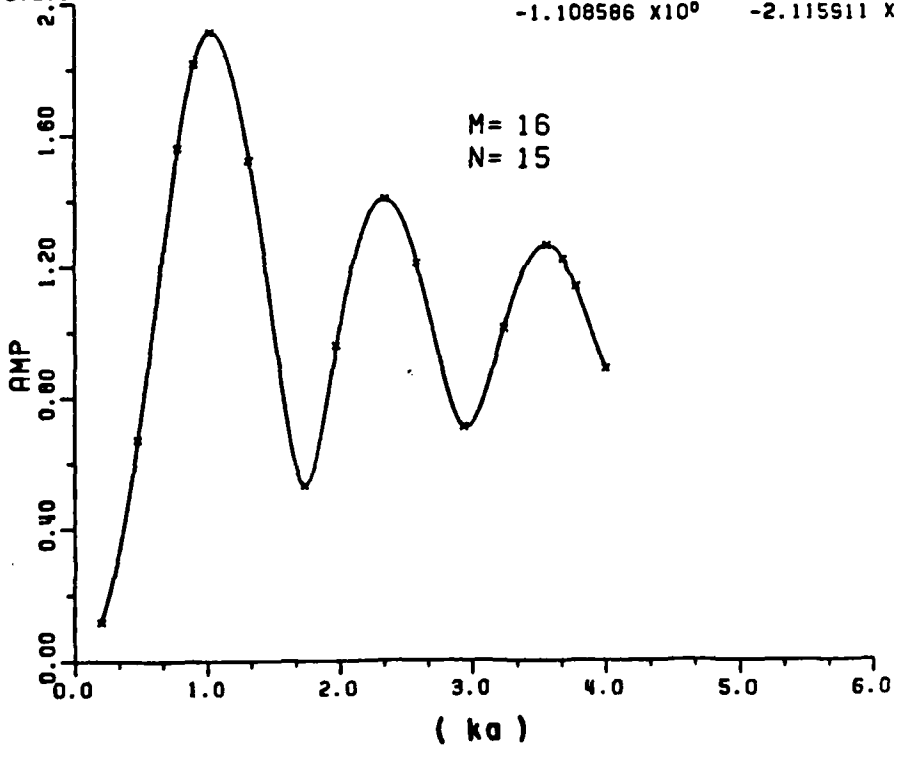

Figure 3-9. The RFA (M,N) as (16,15) fit to the calculated data for the sphere. The x's are the data points used for the RFA. The amplitude plot of the RFA (dashed line) gives a good fit to the original amplitude data (solid line). The corresponding phase data is given in Figure 3-10.

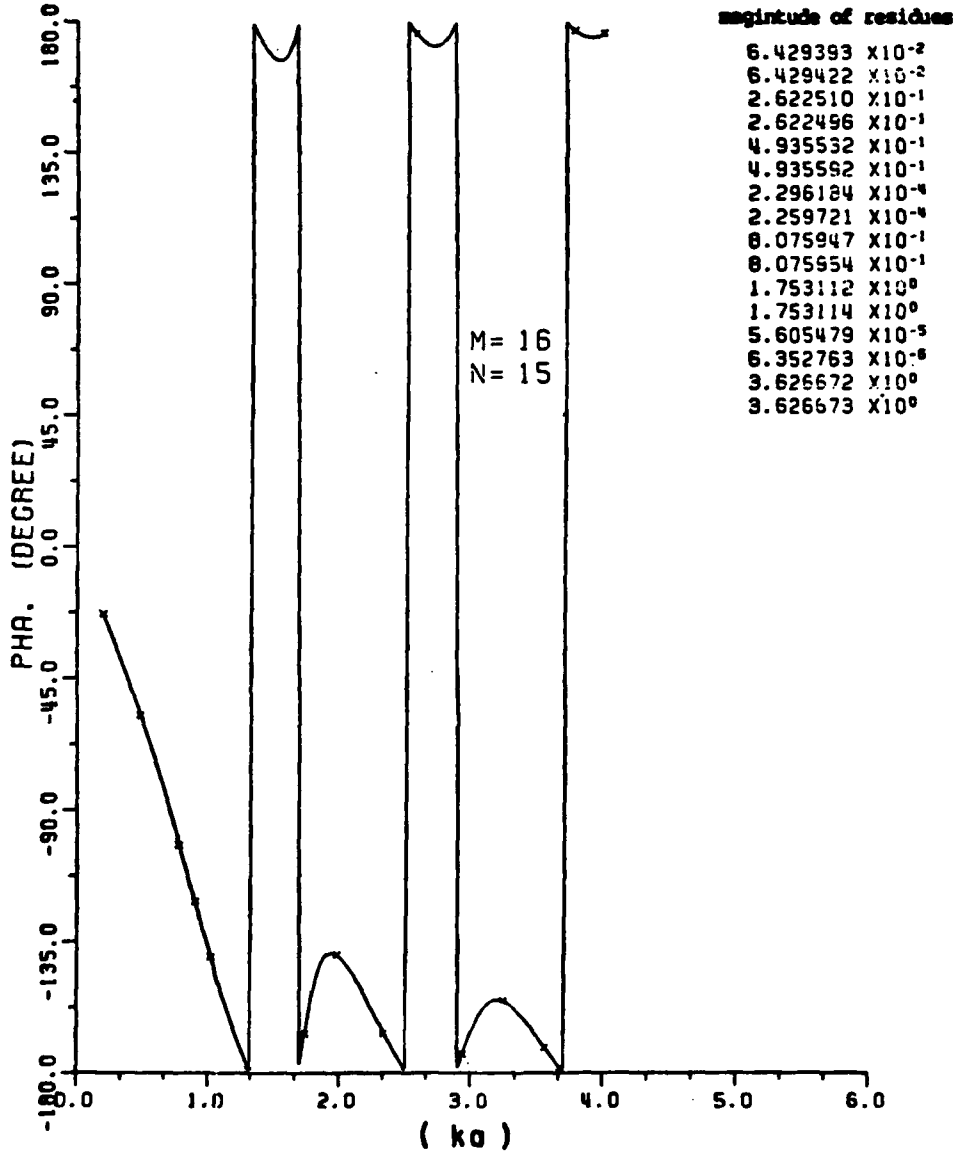

Figure 3-10. The RFA for (M,N) as (16,15) fit to the calculated data for the sphere. The x's are the data points used for the RFA. The phase plot of the RFA (dashed line) gives a good fit to the original phase data (solid line).

may differ somewhat, but they are still within the same order of accuracy.

E. IDENTIFICATION OF THE TRUE POLES AND THE CURVE FITTING POLES

With proper use of rational function approximants, the polynomial order required is always higher than the number of true poles. Therefore, the following rules are used to help to identify the true extracted poles and curve fitting poles in any test.

1. Pole locations found which are in the right half plane are assumed to be curve-fitting poles. Clearly, right-half plane poles would make the transient response unstable.

2. Poles whose corresponding residues are relatively small compared to others obtained with that test are assumed to be curve-fitting poles. The reason is that the pole-pairs having very small residues contribute little to the time domain response or to the frequency domain response. Models with higher orders have too much detail about the data. The fine detail of the data may be due to the numerical errors from the machine computation or from using a less perfect model in the original data calculation.

3. Poles which can be approximately cancelled by zeroes are curve fitting poles. This type of cancellation is due to the polynomial orders, M and N, being overdetermined (too large) both in the denominator and numerator.

4. Poles which have only a real part or whose real parts are very large compared with other extracted poles are assumed to be curve fitting poles. Poles with large negative real parts make the corresponding transient response decay so quickly that they make little contribution in the total transient response.

Therefore, all of the above poles are assumed to be due to noise or errors in the original data and are classified as curve fitting poles. It is true that poles with only real parts exist for certain targets, the conducting sphere is an example. A real pole showing consistently for numerous tests would be reexamined.

F. THE SELECTION OF DATA POINTS

If the matrix equations are solved in the exact sense, the number of data points used ((M+N+1)/2) or ((M+N)/2+1) is limited by the number of unknowns (M+N+1). Equally spaced interpolation may or may not yield the best fit for a rational function approximation. On the other hand, data points sampled at relative maxima and minima of amplitude are always a good choice for the best fit. This is deduced from observations of the applications of the rational function approximants to numerous sets of scattering data. Furthermore, in most cases, one additive data point chosen between the adjacent relative maximum and minimum is helpful in making the error smaller.

Although there is no general proof, the following technique is used and works reasonably well. The amplitude and phase error at all the

data points must be computed. For points where the error is large, the sample points are moved closer together; and where the local error is small, the samples are moved farther apart. With this new choice of sample points, the process is repeated until the error is as small as possible and is distributed evenly.

If the matrix equation is solved in a least squared error sense, there is no limitation on the number of data points used in solving an overdetermined system. (However, the sampling rate has been shown to be related to the accuracy of the extracted poles using the least squared error solutions in Prony's Method [28].) The application of least squared error solutions to pole estimation in the frequency domain using the RFA will be shown in Chapter IV.

G. LIMITATION OF THE SYSTEM ORDER M

For a large system order (for example, M greater than 20), the rational function approximant program may fail due to overflows in the computer during the computation. The machine used in this application, VAX 11/780, has a capacity in the range of 0.29 E-38 to 1.7 E+38 for floating point numbers in double precision. In our applications, the overflow happens in the subroutine Dpolyrt (a zero-searching routine) during its calculation of zeros, if M is roughly greater than 20. It seems that the overflow or ill-conditioning never happens in the subroutine Crout (a modification of Gauss reduction to solve a set of linear system equations) as long as M is roughly less than 20 if the VAX

11/780 machine is used. Therefore the parameter M is always taken to be less than 20.

H. POLES EXTRACTED VIA A WINDOW TECHNIQUE

In some situations the data available may be, 1) from too large a spectral span to be covered with one rational function approximation, 2) without low-frequency content due to difficulties in measurement, or 3) inaccurate over the low frequency portion if calculated data are being used because of an inherent limitation of the method, e.g., Uniform Geometrical Theory of Diffraction (UTD). Thus, a window technique (rectangular window) has been developed for extracting poles in the above situations.

This rectangular window is generated simply by taking sample points over a band limited region of the spectrum. Then the RFA is fitted accurately over only that region and the extracted poles (whose imaginary component falls in the appropriate range) are accurate. Model II given below is used in the window technique.

$$E^n(X_i) = \sum_{n=0}^{N} a_n X_i^n \,/1 + \sum_{m=1}^{M} b_m X_i^m \qquad i = 1, 2, \ldots, I \,. \qquad (3\text{-}13)$$

where now an X_i^2 in the numerator is taken out since there is no Rayleigh region. It is noted that due to a truncation of data on both sides of the window, the lowest and highest frequency of oscillation poles extracted via this technique are not very accurate. However, the rest within the window are still very close to the true poles.

Plots using this window technique applied to the backscattering data of a conducting sphere are shown in Figures 3-11 to 3-13. These plots show that curves within the window fit well both in amplitude and phase. In Table 3-7, the first two pairs of poles are extracted via window I (ka of 0.36 to 2.4), the third and fourth pairs of poles are extracted via window II (ka of 2.1 to 4.2) and the last two pairs of poles are from window III (ka of 3.9 to 5.9). Obviously, as the windows move to higher frequencies, the percentage errors are still in the same order. The rational function model is inherently more accurate at low frequencies than at high frequencies. This was initially suggested by Kennaugh and Moffatt [2] who noted that for a distributed parameter system a lumped parameter approximation can best be utilized where the scattering or radiation properties of the object are essentially global, i.e., not dominated by portions of the object. A more subtle distinction is made by examination of the K-pulse [6] which notes something missing from the singularity expansion method [SEM].

The width of the window is chosen such that at least three pairs of poles are covered in the spectrum. The first and the last pair of poles are deleted because the truncation of data makes these poles inaccurate. Also note that the poles extracted using one RFA over the whole spectral span (one window) have almost the same order of accuracy as those extracted using three RFA and three overlapped windows over the

TABLE 3-7

A COMPARISON OF TRUE POLES AND POLES* EXTRACTED VIA WINDOW TECHNIQUE

Exact Poles of Sphere	Poles Extracted via RFA & Windows (Three) Technique		Percentage Error	
			Real Part	Imag. Part
-0.500000+/-j0.866025 3.80E-2 7.50E-3	-0.5003+/-j0.86610 (WI)**			
-0.701964+/-j1.80740	-0.7086+/-j1.8133	(WI)	0.342	0.304
-0.842862+/-j2.75786	-0.8766+/-j2.7483	(WII)	1.17	0.332
-0.954230+/-j3.71478	-0.9277+/-j3.7388	(WII)	0.692	0.626
-1.04764 +/-j4.67641	-0.9996+/-j4.6191	(WIII)	1.002	1.196
-1.12891 +/-j5.64163	-1.1338+/-j5.5328	(WIII)	8.50E-2	1.891

* The units of the poles are in ka, where k is the wavenumber and a is the sphere radius.

** WI denotes window I.

ZEROS		POLES	
real part	imaginary part	real part	imaginary part
-3.899521 X10^{0}	1.231749 X10^{1}	6.432034 X10^{-2}	2.067850 X10^{0}
-3.899521 X10^{0}	-1.231748 X10^{1}	6.431817 X10^{-2}	-2.067850 X10^{0}
-2.715040 X10^{-1}	2.945970 X10^{0}	-6.786652 X10^{-1}	2.729713 X10^{0}
-2.715048 X10^{-1}	-2.945968 X10^{0}	-6.786652 X10^{-1}	-2.729713 X10^{0}
-1.392566 X10^{-1}	1.740500 X10^{0}	-7.085919 X10^{-1}	1.813268 X10^{0}
-1.392551 X10^{-1}	-1.740499 X10^{0}	-7.085877 X10^{-1}	-1.813269 X10^{0}
6.431926 X10^{-2}	2.067845 X10^{0}	-1.957764 X10^{0}	7.542527 X10^{-1}
-1.091773 X10^{0}	-8.239071 X10^{-1}	-1.957765 X10^{0}	-7.542531 X10^{-1}
-1.091773 X10^{0}	8.239073 X10^{-1}	-4.355239 X10^{-2}	8.663692 X10^{-1}
6.431857 X10^{-2}	-2.067848 X10^{0}	-4.355229 X10^{-2}	-8.663692 X10^{-1}
-4.355227 X10^{-2}	8.663695 X10^{-1}	-1.072975 X10^{0}	4.295478 X10^{-7}
-4.355223 X10^{-2}	-8.663696 X10^{-1}	4.499001 X10^{-2}	0.000000 X10^{0}
4.498780 X10^{-2}	0.000000 X10^{0}	-5.003769 X10^{-1}	-8.661069 X10^{-1}
0.000000 X10^{0}	0.000000 X10^{0}	-5.003762 X10^{-1}	8.661074 X10^{-1}
0.000000 X10^{0}	0.000000 X10^{0}		

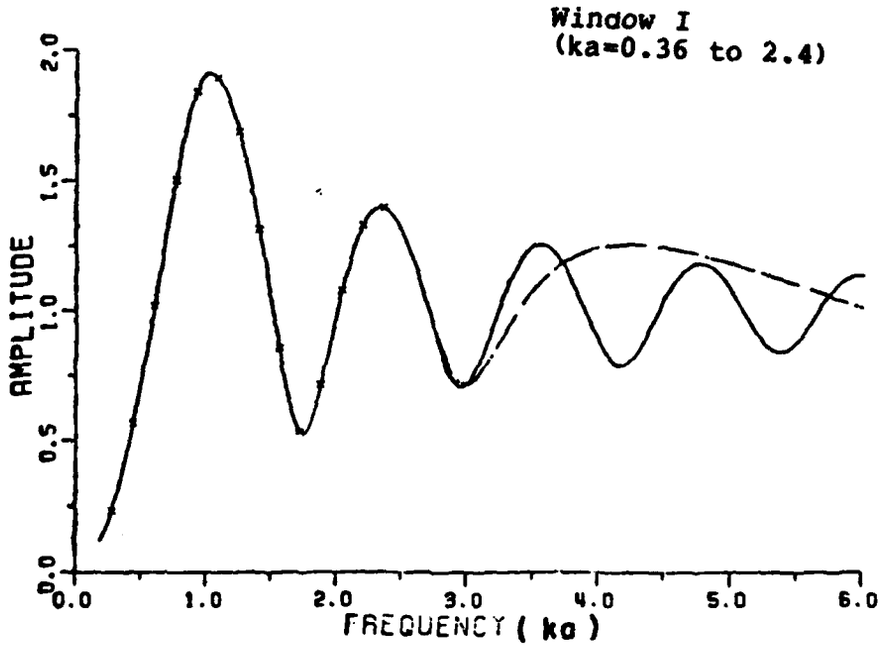

Figure 3-11. The RFA fit to the calculated data for the sphere within the frequency of interest (window I). The x's are the data points used for the RFA. The amplitude plot of the RFA (dashed line) gives a good fit to the original amplitude data (solid line) within the window.

ZEROS		POLES	
real part	imaginary part	real part	imaginary part
-8.253189 X10^{-1}	5.583209 X10^{0}	-7.9[illegible]205 X10^{-1}	-4.601527 X10^{0}
-8.253201 X10^{-1}	-5.583209 X10^{0}	-2.175642 X10^{1}	1.068570 X10^{-7}
-1.406261 X10^{-1}	1.744352 X10^{0}	-7.[illegible]4286 X10^{-1}	4.601523 X10^{0}
-1.406267 X10^{-1}	-1.744350 X10^{0}	5.605201 X10^{-2}	-3.662331 X10^{0}
5.606160 X10^{-2}	3.662305 X10^{0}	5.604627 X10^{-2}	3.662330 X10^{0}
5.604859 X10^{-2}	-3.662317 X10^{0}	-9.277147 X10^{-1}	-3.738780 X10^{0}
-2.298664 X10^{-1}	2.949363 X10^{0}	-9.276904 X10^{-1}	3.738779 X10^{0}
-3.002870 X10^{-1}	-4.155033 X10^{0}	-8.766138 X10^{-1}	-2.748281 X10^{0}
-3.002915 X10^{-1}	4.155044 X10^{0}	-8.766202 X10^{-1}	2.748300 X10^{0}
-5.548292 X10^{-1}	2.616053 X10^{0}	-5.556495 X10^{-1}	-2.619283 X10^{0}
-5.548392 X10^{-1}	-2.616055 X10^{0}	-5.556539 X10^{-1}	2.619272 X10^{0}
-2.298464 X10^{-1}	-2.949357 X10^{0}	-6.738217 X10^{-1}	-1.718931 X10^{0}
3.944065 X10^{-1}	0.000000 X10^{0}	-6.738215 X10^{-1}	1.718931 X10^{0}
		-1.268861 X10^{0}	0.000000 X10^{0}

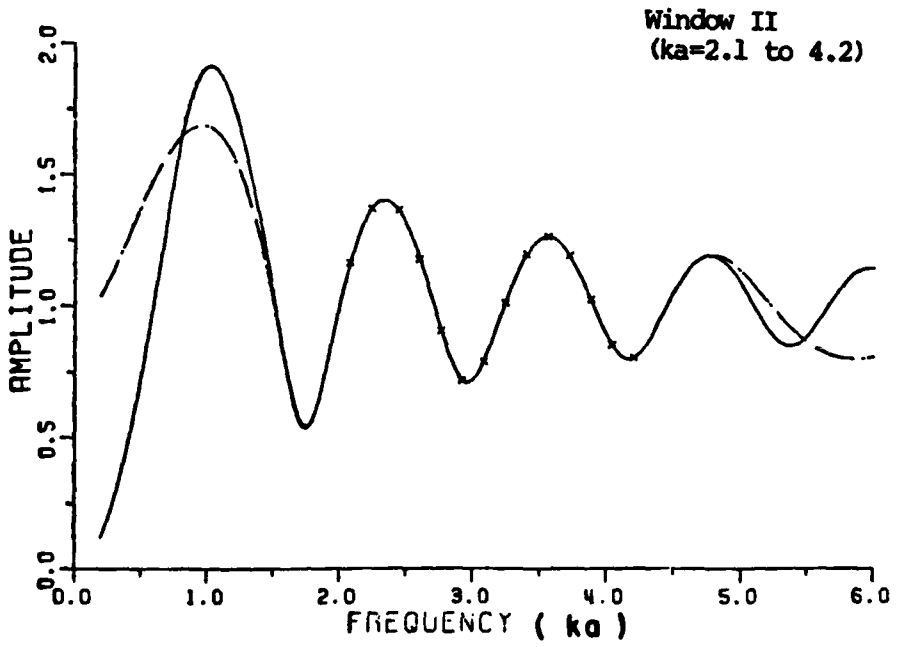

Figure 3-12. The RFA fit to the calculated data for the sphere within the frequency of interest (window II). The x's are the data points used for the RFA. The amplitude plot of the RFA (dashed line) gives a good fit to the original amplitude data (solid line) within the window.

ZEROS		POLES	
real part	imaginary part	real part	imaginary part
1.052375 X10^{1}	1.225268 X10^{-7}	-9.887772 X10^{-1}	6.255781 X10^{0}
-5.331648 X10^{-1}	2.530583 X10^{0}	-9.888250 X10^{-1}	-6.255767 X10^{0}
-5.331650 X10^{-1}	-2.530582 X10^{0}	-2.607428 X10^{-1}	4.512208 X10^{0}
-3.008935 X10^{-1}	4.154336 X10^{0}	-2.809372 X10^{-1}	-4.512212 X10^{0}
-3.008314 X10^{-1}	-4.154304 X10^{0}	-1.133977 X10^{0}	5.532900 X10^{0}
-2.808144 X10^{-1}	4.512299 X10^{0}	-1.133761 X10^{0}	-5.532757 X10^{0}
-2.809772 X10^{-1}	-4.512367 X10^{0}	7.619740 X10^{0}	3.131265 X10^{-6}
-4.571337 X10^{-1}	6.586211 X10^{0}	-4.553929 X10^{0}	0.000000 X10^{0}
-4.571332 X10^{-1}	-6.586199 X10^{0}	-9.996915 X10^{-1}	4.618969 X10^{0}
1.137515 X10^{-1}	5.100268 X10^{0}	-9.995255 X10^{-1}	-4.619159 X10^{0}
1.137699 X10^{-1}	-5.100148 X10^{0}	1.137866 X10^{-1}	5.100226 X10^{0}
-3.544716 X10^{-1}	5.360181 X10^{0}	1.137701 X10^{-1}	-5.100145 X10^{0}
-3.543896 X10^{-1}	-5.360293 X10^{0}	-7.591943 X10^{-1}	3.695371 X10^{0}
		-7.592175 X10^{-1}	-3.695393 X10^{0}

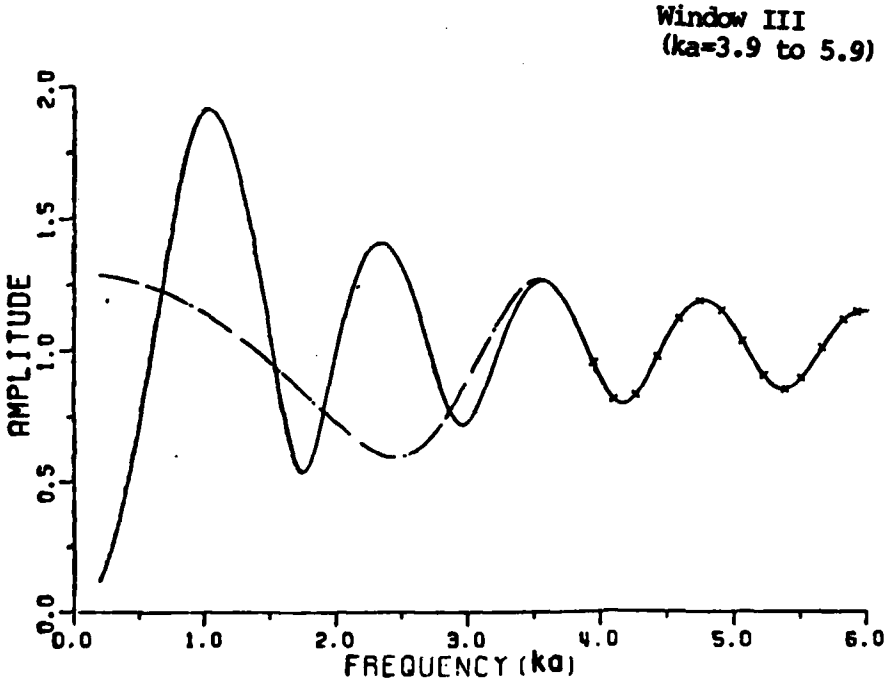

Figure 3-13. The RFA fit to the calculated data for the sphere within the frequency of interest (window III). The x's are the data points used for the RFA. The amplitude plot of the RFA (dashed line) gives a good fit to the original amplitude data (solid line) within the window.

whole spectral span. The detail of this application to some experimental data will be demonstrated in a later chapter.

I. ADDITIVE NOISE AND ITS EFFECTS ON POLES EXTRACTED VIA RATIONAL FUNCTION APPROXIMATIONS

Up to this point, the rational function approximation has been applied to extract the complex natural resonances from sets of noiseless data. However, in any measured system noise, clutter and uncertainty are inevitable. Two types of pseudo-noise are considered in this section. One type is simply the calculated data rounded to the kth decimal. The other type is an uncorrelated Gaussian* white noise added to the calculated data. For the first test, both the real and imaginary part of the calculated sphere data are rounded to the kth decimal.

The rational function routine is applied to these sets of data with system order for (M,N) as (14,13). This set of system orders is chosen because the system with these orders works reasonable well (see Figures 3-7 and 3-8) for eight poles in the spectrum, i.e., about twice the number of poles. For a general problem, an estimate of the number of poles can be obtained from the measured amplitude spectrum. Tables 3-8 to 3-9 show comparisons of extracted poles from data rounded to the 2nd, and to the 1st decimal respectively. Obviously, as k decreases, the extracted poles move away from the true ones.

---

* The Gaussian random number generating subroutine-Gauss in IBM Scientific Subroutine Package (SSP) is used.

TABLE 3-8

A COMPARISON OF TRUE POLES AND EXTRACTED POLES*
USING THE RATIONAL FUNCTION APPROXIMATION TO THE BACKSCATTERING
DATA OF SPHERE**

True Poles	Extracted (M = 16, N = 15)	Percentage of Error Real Part	Imag. Part
-0.50000 +/-j0.866025	-0.5398+/-j0.80699	3.98	5.903
-0.701964+/-j1.80740	-0.8233+/-j1.8558	6.257	2.496
-0.842862+/-j2.75786	-1.0036+/-j2.8927	5.574	4.676
-0.954230+/-j3.71478	-0.9817+/-j3.7629	0.716	1.254
	(M = 14, N = 13)	Real part	Imag. Part
	-0.5196+/-j0.8159	1.96	5.01
	-0.7721+/-j1.8882	3.617	4.167
	-0.9394+/-j3.1347	3.348	13.07
	-1.4014+/-j3.5855	11.65	3.37

* The units of the poles are in ka, where k is the wavenumber and a is the sphere radius.

** The data were rounded to 2nd decimal.

TABLE 3-9

A COMPARISON OF TRUE POLES AND POLES EXTRACTED
USING THE RFA TO THE BACKSCATTERING DATA FOR A SPHERE*

True Pole	Extracted Poles (M = 16, N = 15)	Percentage of Error Real Part	Imag. Part
-0.500000+/-j0.866025	-0.4525+/-j1.012	4.75	14.59
-0.701964+/-j1.80740	-0.4898+/-j2.009	10.94	10.39
-0.842862+/-j2.75786	-0.3040+/-j3.2430	18.69	16.82
-0.954230+/-j3.71478	not located		

(M = 22, N = 21)	Real Part	Imag. Part
-0.415 +/-j0.8779	8.5	1.148
-0.5548+/-j1.7920	7.59	0.794
-0.5674+/-j2.6454	9.55	3.899
-0.4200+/-j3.7250	13.93	0.266

* The data were rounded to 1st decimal.

The second type of noise is uncorrelated Gaussian random noise with zero mean and σ standard deviation. Two uncorrelated Gaussian random processes with a zero mean and a standard deviation of σ which are generated from two different seeds are added to the real and imaginary parts respectively of the calculated data for the sphere. The signal-to-noise ratio is defined as

$$S/N(dB) = 10\log\left[\left[\sum_{i=1}^{N} \tilde{A}^2(X_i)/N\right]/2\sigma^2\right] \quad , \tag{3.14}$$

where $\tilde{A}(X_i)$ is the amplitude of signal at frequency X_i, and N is the total number of samples used.

These noisy data are fitted by the rational function in the exact sense. Figure 3-14 is a typical example of rational function fit to the noisy data, where the noise level is σ of 1.E-1. The extracted poles under different noise levels are listed in Table 3-10. It is easy to see that the discrepancies between the extracted poles and the true poles are increased as the noise level is increased. Furthermore, the rational function approximants may fail to extract the complex natural resonances at all when the S/N is below 20 dB or so. Based on the above characteristics of noise effects, several preprocessing techniques will be used to preprocess the noisy data. These preprocessing techniques are described and are applied to several sets of noisy data for the sphere in the following section.

TABLE 3-10

COMPARISON OF EXACT AND EXTRACTED POLES* OF SPHERE
USING THE RFA TO THE NOISY DATA FOR THE SPHERE**

True Poles	Poles Extracted via RFA (in the exact sense) σ=2.E-2(Run 1)	σ=2.E-2(Run 2)	σ=1.E-1
-0.500000+/-j0.866025	-0.5362 +/-j0.9616	-0.4386+/-j0.80129	-0.439 +/-j0.5497
-0.701964+/-j1.80740	-0.4745 +/-j1.9577	-0.6482+/-j1.8509	-0.295 +/-j1.6033
-0.842862+/-j2.75786	-0.38518+/-j2.643	-0.9795+/-j2.7384	-0.2574+/-j2.784
-0.954230+/-j3.71478	-0.4745 +/-j3.538	-0.6285+/-j3.5081	not located

Run 1 and 2 used different data points.

* The units of the poles are in ka, where k is the wavenumber and a is the sphere radius.

** Two Gaussian white noise generator (using two different seeds) with standard deviation σ are added to the backscattering data for the sphere. The signal to noise ratio corresponding to σ of 1.E-1 is 18.37 dB.

ZEROS		POLES	
real part	imaginary part	real part	imaginary part
1.743265 X10^{-1}	-4.388152 X10^{0}	7.303770 X10^{-1}	-4.743851 X10^{0}
1.743264 X10^{-1}	4.388153 X10^{0}	7.303767 X10^{-1}	4.743851 X10^{0}
4.742387 X10^{0}	-9.[illegible] X10^{-8}	-2.573951 X10^{-1}	2.783871 X10^{0}
-1.297361 X10^{-1}	2.858775 X10^{0}	-2.573951 X10^{-1}	-2.783872 X10^{0}
-1.297366 X10^{-1}	-2.858775 X10^{0}	2.618428 X10^{-1}	1.985825 X10^{0}
2.637822 X10^{-1}	2.071921 X10^{0}	2.618425 X10^{-1}	-1.985824 X10^{0}
2.637830 X10^{-1}	-2.071921 X10^{0}	-2.958908 X10^{-1}	1.603305 X10^{0}
-7.899303 X10^{-2}	1.656142 X10^{0}	-2.958907 X10^{-1}	-1.603305 X10^{0}
-7.899350 X10^{-2}	-1.656141 X10^{0}	1.766671 X10^{-1}	5.731889 X10^{-1}
1.589571 X10^{-1}	6.249202 X10^{-1}	1.766671 X10^{-1}	-5.731888 X10^{-1}
1.589571 X10^{-1}	-6.249202 X10^{-1}	3.757455 X10^{-2}	1.000217 X10^{0}
4.683138 X10^{-2}	1.011262 X10^{0}	3.757453 X10^{-2}	-1.000217 X10^{0}
4.683141 X10^{-2}	-1.011262 X10^{0}	-4.389232 X10^{-1}	5.497194 X10^{-1}
		-4.389232 X10^{-1}	-5.497194 X10^{-1}

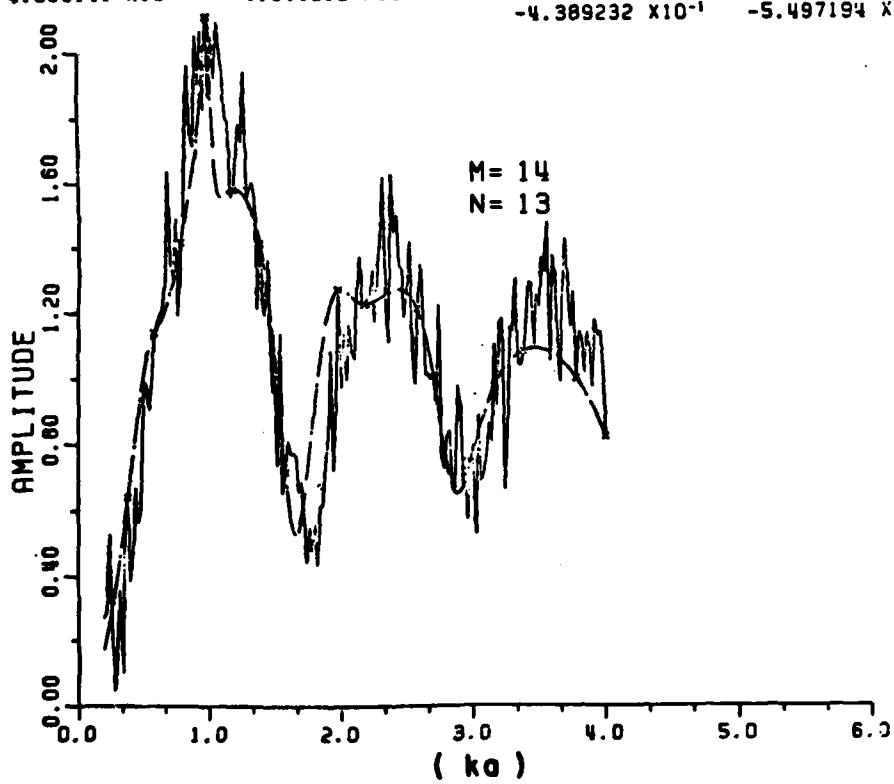

Figure 3-14. The RFA applied to a set of noisy data, where the Gaussian random noise with zero mean and a standard deviation of 0.1 is added to the calculated data for the sphere. The x's are the data points used for the RFA. The amplitude plot of the RFA is plotted as a dashed line (S/N of 18.37 dB).

J. PREPROCESSING TECHNIQUES

1. Preprocessing With Zero-Phase-Shift Digital Filter

In general, a digital filter is defined in the z-domain as

$$H(z) = \sum_{i=1}^{N} a_n z^{-i} / (1 + \sum_{i=1}^{M} b_i z^{-i}) \quad , \tag{3-15}$$

where a_i and b_i are coefficients which determine the behavior of the filter. Emphasized in this section is the design of a high order (10) lowpass digital filter with zero-phase-shift, where the 3 dB cutoff frequency is movable. The Butterworth approximation is used because it is a maximally-flat amplitude approximation. In order to obtain a 10th order zero phase shift digital filter, a 5th order lowpass Butterworth digital filter is designed first. Then, a complex conjugate filter $H^*(z)$ is cascaded to H(z). Thus, the total filter $H^T(z)$ is a 10th order lowpass filter with zero phase shift.

$$H^T(z) = H(z) \cdot H^*(z) = |H(z)|^2 \quad 0° \quad . \tag{3.16}$$

The details of the zero phase shift digital filter and its implementation are described in Appendix A. Comparisons of the filtered data with a 12.35 dB S/N (see Figure 3-20 for the noisy waveform) and the original noiseless data are plotted in Figures 3-15 (amplitude) and 3-16 (phase). The 3 dB cutoff frequency f_c is set at 20* Hz, the RFA are applied to the filtered data. The extracted poles and the percent

---

* Corresponding to 6.29 TAU (diameter transit time) of the impulse response (see Appendix A).

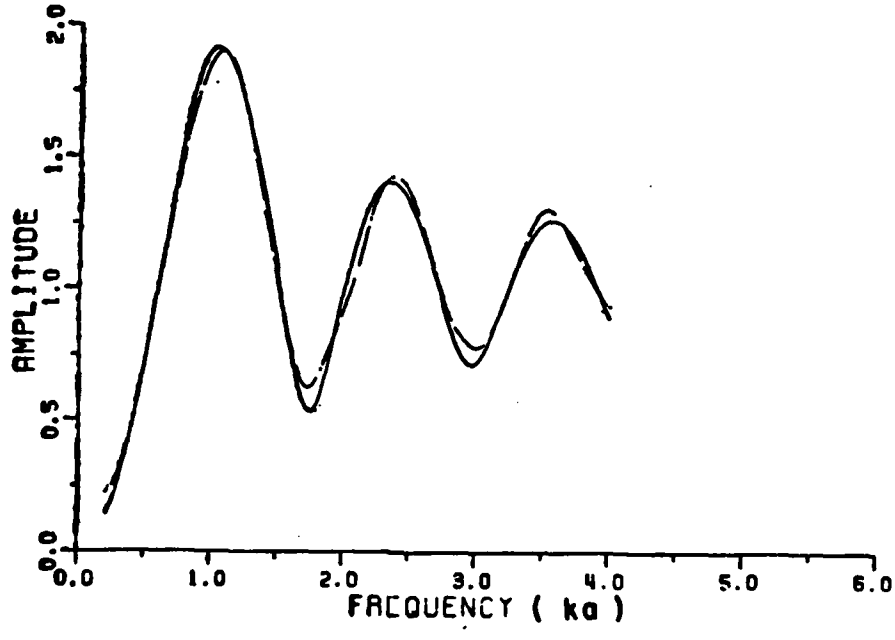

Figure 3-15. A comparison of amplitude plots for the calculated data (solid line) and the filtered data (dashed line) for the sphere. The filtered data are obtained by filtering the noisy data (calculated data with additive Gaussian random noise) using a 10th order zero-phase-shift digital filter. The 3 dB cutoff frequency f_c is set to 20 Hz. The signal-to-noise ratio is 12.35 dB before filtering.

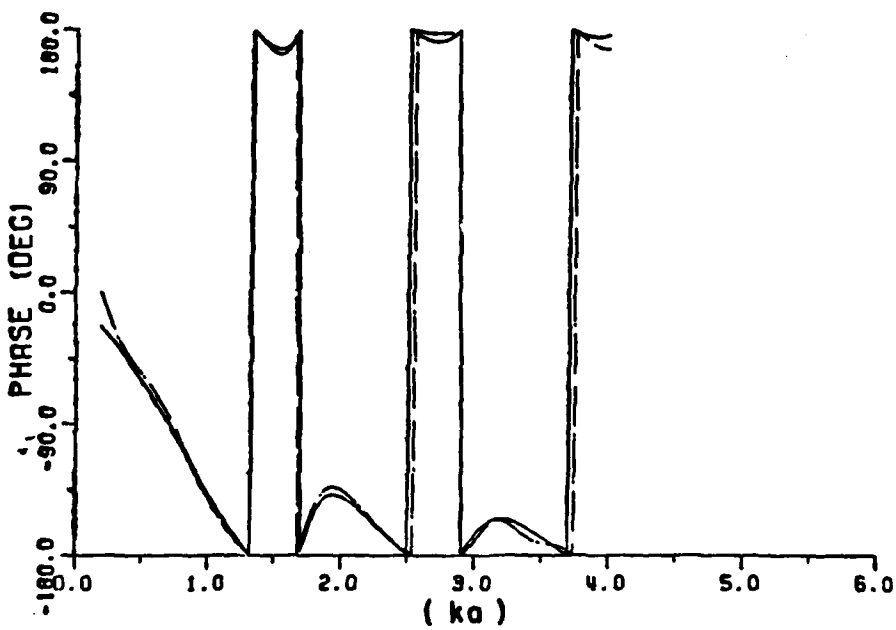

Figure 3-16. A comparison of the phase plots for the calculated data (solid line) and the filtered data (dashed line) for the sphere. The filtered data are obtained by filtering the noisy data (calculated data with additive Gaussian random noise) using a 10th order zero-phase-digital filter. The signal-to-noise ratio is 12.35 dB before filtering.

errors are shown in Table 3-11. Note that the extracted poles are 15 percent in error in the real part and 10 percent in error in the imaginary part. Therefore, the minimum signal-to-noise ratio which can be tolerated is about 15 dB.

2. Preprocessing With Sum Operator

After some initial manipulation the technique in using the rational function approximation is to solve the matrix equation AX = B, where A is an mxn matrix, B is an mx1 matrix, and X is an nx1 unknown column matrix. It has been shown that the least squared error method is very sensitive to noise and has no guarantee of convergence if an iterative search is used [25]. As will be shown in Chapter IV , there are some advantages to solving the matrix equation in an exact sense rather than solving it in a least squared error sense. However, there are many data points which contain useful information and are corrupted by noise to a certain extent but are unused.

To extract better poles from a set of additive noise data, a major effort is to reduce the effect of noise to a minimun. The intention here is to use the row echelon algorithms (which are used in Gauss elimination) for an overdetermined matrix equation to reduce N rows to one, i.e., N linear system equations can be scaled arbitrarily (say 1/N) and added together. A detailed description of the sum operator is shown in Appendix B. It is expected that the noise in each element of the matrix equation is reduced by a factor of about 1/N. Assuming that $\tilde{X}(t)$ is an arbitrary stationary random process with mean $\bar{X}$ and variance σ,

TABLE 3-11

POLES EXTRACTED VIA RATIONAL FUNCTION APPROXIMATION AND 10th ORDER ZERO-PHASE-SHIFT DIGITAL FILTER.*

Extracted Poles*	Percentage of Error	
	Real	Imaginary
Run 1		
-0.415 ± j 0.802	8.50	6.40
-0.364 ± j 1.526	17.43	14.51
-0.361 ± j 2.744	16.71	0.48
-0.307 ± j 3.738	16.88	0.61
Run 2		
-0.637 ± j 0.798	13.7	6.80
-0.752 ± j 1.716	2.58	4.71
-0.529 ± j 2.982	10.88	7.77
Average		
-0.526 ± j 0.800	2.6	6.60
-0.558 ± j 1.621	7.42	9.61
-0.418 ± j 2.863	14.73	3.65

* The original signal-to-noise ratio: 12.35 dB. The 3 dB cut-off frequency is set at f_c of 20 Hz.

** The units of the extracted poles are in ka, where k is the the wavenumber and a is the sphere radius.

then the following statistics* are true:

$$E\left(\sum_{i=1}^{N} \tilde{X}_i/N\right) = \bar{X} \quad , \tag{3-17}$$

$$V\left(\sum_{i=1}^{N} \tilde{X}_i/N\right) = \sigma^2/N \quad , \tag{3-18}$$

where E and V are the expected value and the variance respectively, N is the number of samples. Thus, the variance of the noise is reduced by a factor of 1/N.

The rational function approximant with the sum operator was defined in this study (see Appendix B). The sum operations are made in the matrix equation formed by the RFA instead of in the sampled data. Then the sum operator and RFA are applied simultaneously to a set of calculated sphere data, where two Gaussian white noise processes generated with two different seeds are added to the real and imaginary parts respectively. It is noted that there is a tradeoff between the noise reduction factor and the number of samples (N) used for the sum operation. The noise term in each element of matrix A' (see Appendix B) is enlarged by a factor X_i^M, where X_i is jk_ia, M is a system order. If the N sampled frequencies $X_1, X_2, \ldots X_N$ used for a group summation are assumed to be close to each other, i.e.,

$$X_1 \cong X_2 \cong X_3 \ldots \cong X_N \quad , \tag{3-19}$$

---

* John Neter and William Wasserman, Applied Linear Statistical Models, Richard D. Irwin, Inc. Homewood, Illinois, 1974.

where ≅ means for almost equal to, then the noise reduction factor is 1/N based on Equations (3-17) and (3-18). However, if the number of samples used in the group summation N is large and Equation (3-19) is no longer true, then the additive noise reduction factor is no more a factor of 1/N. Nevertheless, too many samples as well as too few samples in the group of sum operations still reduce the additive noise significantly. Note the sum operator developed here does not reduce any of the signal itself. In other words, the sum operator can be applied to a noiseless matrix equation, the solutions with or without a sum operator are exactly the same.

The manipulation of a sum operator in the elements of the matrix equation is definitely better than that in the sampled data because the sum operator defined here does not reduce the signal at all. It should be noted that there is an optimal N so that the noise can be reduced as much as possible. However, the search of the optimal N is beyond the scope of this dissertation. The number of samples (N) used in the group summation is set optionally at 10 in this dissertation.

The plots shown in Figures 3-17 and 3-18 (for S/N as 18.37 dB), Figures 3-19 and 3-20 (for S/N as 12.35 dB), and Figure 3-21 (for S/N as 6.33 dB) are amplitude plots of the original noisy data (solid line) and of the fitted curve via sum operator in the rational function fit (dashed line). Various sets of data points are selected from the first two noisy data sets (S/N of 18.37 dB and 12.35 dB) respectively (see Figures 3-17 to 3-20) and then the rational function approximations and

ZEROS		POLES	
real part	imaginary part	real part	imaginary part
-3.219773×10^{-1}	3.919755×10^{0}	-4.253798×10^{-1}	-3.732206×10^{0}
-3.219773×10^{-1}	-3.919754×10^{0}	-4.253798×10^{-1}	3.732207×10^{0}
6.431612×10^{0}	-1.699179×10^{-7}	-3.655697×10^{-2}	1.531806×10^{0}
-2.219895×10^{-1}	2.944112×10^{0}	-3.655697×10^{-2}	-1.531806×10^{0}
1.821979×10^{0}	1.547945×10^{-7}	-6.737158×10^{-1}	2.779822×10^{0}
-2.219896×10^{-1}	-2.944112×10^{0}	-6.737154×10^{-1}	-2.779823×10^{0}
-3.208515×10^{-2}	1.533100×10^{0}	-5.817472×10^{-1}	1.858214×10^{0}
-1.476556×10^{-1}	-1.774589×10^{0}	-5.817479×10^{-1}	-1.858213×10^{0}
-1.476556×10^{-1}	1.774589×10^{0}	1.027473×10^{0}	4.635614×10^{-1}
-3.208522×10^{-2}	-1.533100×10^{0}	1.027473×10^{0}	-4.635614×10^{-1}
7.666940×10^{-1}	2.491958×10^{-8}	-3.738658×10^{-1}	7.643278×10^{-1}
-3.946160×10^{-2}	5.912038×10^{-1}	-3.738658×10^{-1}	-7.643277×10^{-1}
-3.946162×10^{-2}	-5.912037×10^{-1}	-4.594510×10^{-2}	5.751686×10^{-1}
		-4.594509×10^{-2}	-5.751686×10^{-1}

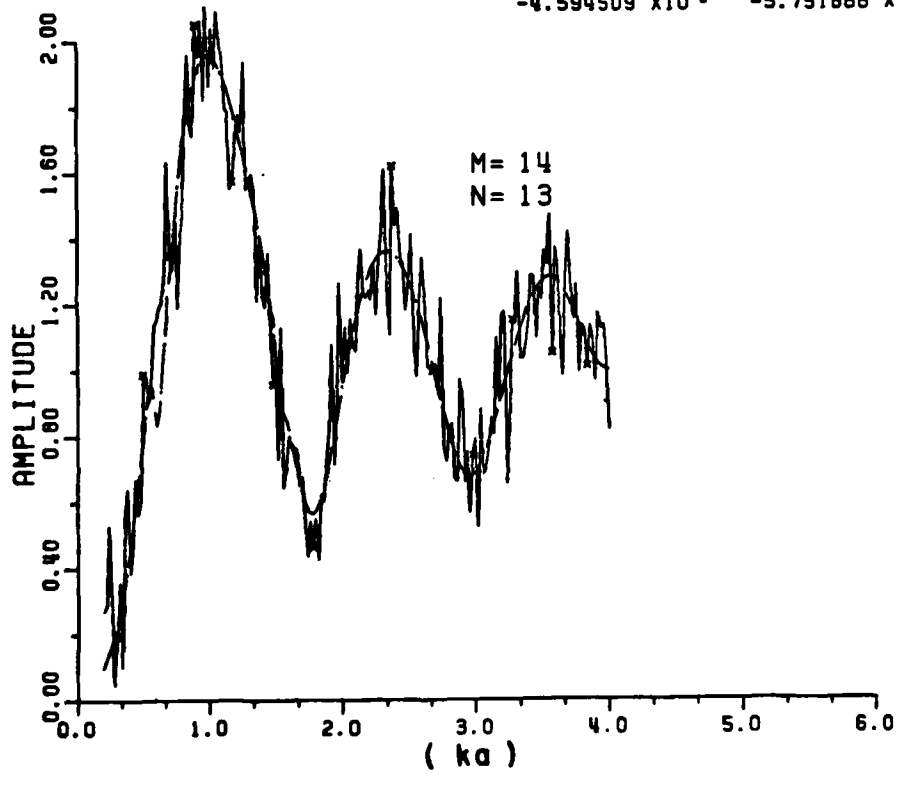

Figure 3-17. The sum operator and the RFA applied simultaneouly to the noisy data (solid line) for the sphere, where two Gaussianly distributed random noises have been added to the calculated data for the sphere. The x's are the data points used for the RAF. The signal-to-noise ratio is 18.37 dB (amplitude plot).

ZEROS		POLES	
real part	imaginary part	real part	imaginary part
-3.565937 X10^{-1}	3.827230 X10^{0}	-3.379839 X10^{-1}	-3.664120 X10^{0}
-3.565940 X10^{-1}	-3.827229 X10^{0}	-3.379840 X10^{-1}	3.664121 X10^{0}
1.365961 X10^{1}	9.720143 X10^{-6}	-4.970016 X10^{-1}	2.700610 X10^{0}
-1.423162 X10^{-1}	1.737466 X10^{0}	-4.970010 X10^{-1}	-2.700612 X10^{0}
-1.423170 X10^{-1}	-1.737466 X10^{0}	-5.806524 X10^{-1}	1.662031 X10^{0}
-2.169326 X10^{-1}	2.926950 X10^{0}	-5.806546 X10^{-1}	-1.662031 X10^{0}
-2.169321 X10^{-1}	-2.926951 X10^{0}	2.277019 X10^{-2}	1.933210 X10^{0}
2.582912 X10^{-2}	1.928497 X10^{0}	2.277154 X10^{-2}	-1.933208 X10^{0}
2.582965 X10^{-2}	-1.928495 X10^{0}	3.023073 X10^{-1}	9.037622 X10^{-1}
3.236114 X10^{-1}	8.902832 X10^{-1}	3.023072 X10^{-1}	-9.037621 X10^{-1}
3.236115 X10^{-1}	-8.902832 X10^{-1}	-4.046820 X10^{-1}	7.592254 X10^{-1}
-6.531780 X10^{-2}	5.028517 X10^{-1}	-4.046819 X10^{-1}	-7.592252 X10^{-1}
-6.531781 X10^{-2}	-5.028517 X10^{-1}	-6.057431 X10^{-2}	4.921674 X10^{-1}
		-6.057430 X10^{-2}	-4.921674 X10^{-1}

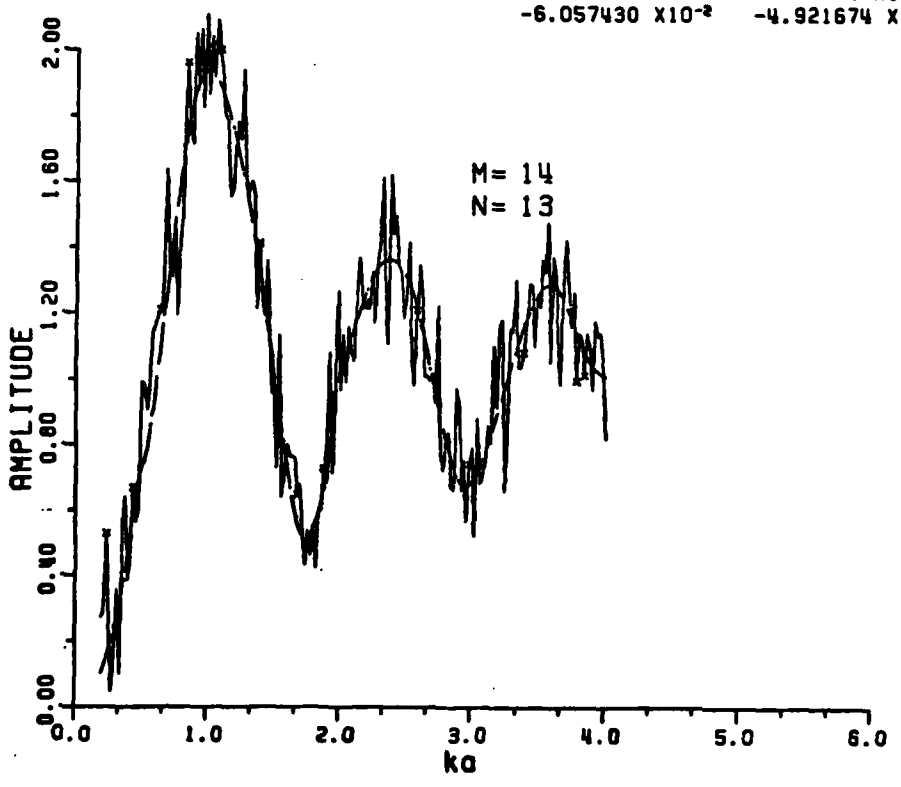

Figure 3-18. The sum operator and the RFA (dashed line) applied simultaneously to the noisy data (solid line) for the sphere, where two Gaussianly distributed random noises have been added to the calculated data for the sphere. The data points (the x's) are different from those in Figure 3-17. The signal-to-noise ratio is 18.37 dB (amplitude plot).

ZEROS		POLES	
real part	imaginary part	real part	imaginary part
1.081960 X10^{2}	4.800438 X10^{-8}	-1.827604 X10^{-1}	-2.271206 X10^{0}
-2.904986 X10^{-1}	3.742679 X10^{0}	-1.827607 X10^{-1}	2.271209 X10^{0}
-2.904985 X10^{-1}	-3.742680 X10^{0}	-2.455365 X10^{-1}	3.693741 X10^{0}
-8.098942 X10^{-2}	1.704530 X10^{0}	-2.455355 X10^{-1}	-3.693737 X10^{0}
-8.098953 X10^{-2}	-1.704530 X10^{0}	-2.300199 X10^{-1}	1.680228 X10^{0}
-1.217338 X10^{-1}	3.014067 X10^{0}	-2.300196 X10^{-1}	-1.680228 X10^{0}
-1.217337 X10^{-1}	-3.014064 X10^{0}	-2.053640 X10^{-1}	3.038413 X10^{0}
-2.488049 X10^{-1}	2.221688 X10^{0}	-2.053654 X10^{-1}	-3.038419 X10^{0}
-2.488050 X10^{-1}	-2.221689 X10^{0}	-2.988714 X10^{-1}	8.643417 X10^{-1}
1.486414 X10^{-1}	9.304325 X10^{-1}	-2.988714 X10^{-1}	-8.643419 X10^{-1}
1.486414 X10^{-1}	-9.304325 X10^{-1}	1.570321 X10^{-1}	9.405675 X10^{-1}
-9.588260 X10^{-1}	0.000000 X10^{0}	1.570319 X10^{-1}	-9.405675 X10^{-1}
1.980077 X10^{-1}	0.000000 X10^{0}	7.316114 X10^{-2}	0.000000 X10^{0}
		-2.193302 X10^{-1}	0.000000 X10^{0}

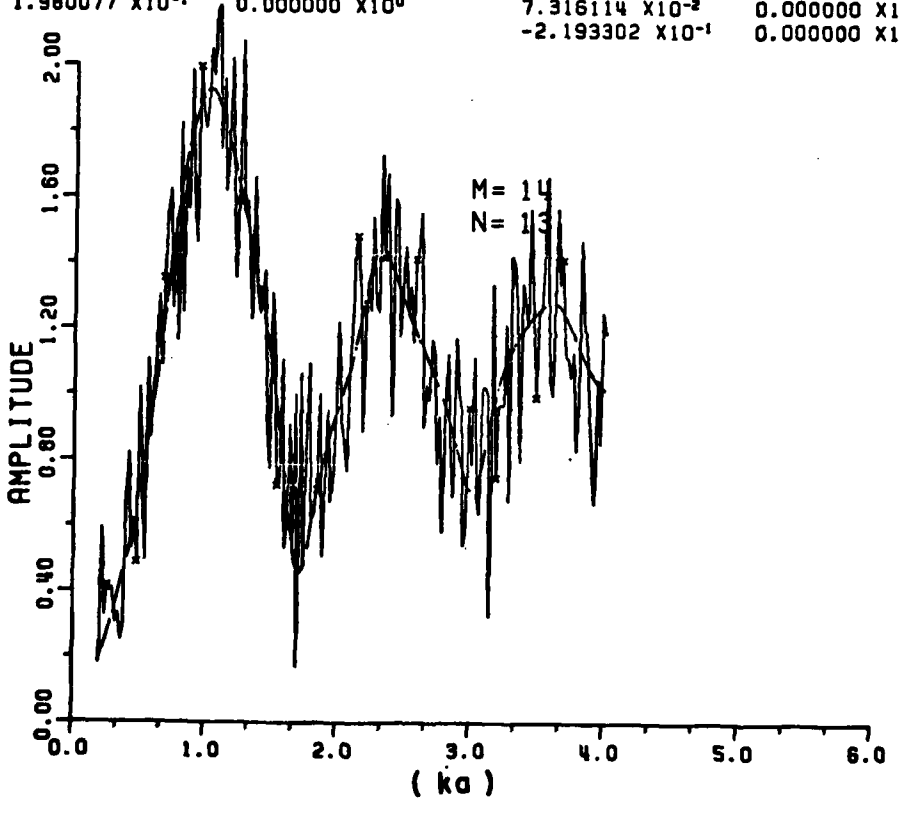

Figure 3-19. The sum operator and the RFA applied simultaneously to the noisy data (solid line) for the sphere, where two Gaussianly distributed random noises have been added to the calculated data for the sphere. The x's are the data points used in the RFA. The signal-to-noise ratio is is 12.35 dB (amplitude plot).

ZEROS		POLES	
real part	imaginary part	real part	imaginary part
-3.349424 X10^{-1}	4.029986 X10^{0}	-4.473662 X10^{-1}	3.654730 X10^{0}
-3.349426 X10^{-1}	-4.029986 X10^{0}	-4.473668 X10^{-1}	-3.654730 X10^{0}
4.367680 X10^{0}	-6.755852 X10^{-6}	-5.323102 X10^{-1}	2.515733 X10^{0}
-2.862792 X10^{-1}	2.953559 X10^{0}	-5.323086 X10^{-1}	-2.515732 X10^{0}
-2.862786 X10^{-1}	-2.953558 X10^{0}	8.773348 X10^{-1}	1.274611 X10^{0}
-2.949375 X10^{-1}	2.207569 X10^{0}	8.773348 X10^{-1}	-1.274611 X10^{0}
-2.949378 X10^{-1}	-2.207569 X10^{0}	-4.695184 X10^{-1}	9.854268 X10^{-1}
1.106047 X10^{0}	1.018864 X10^{0}	-4.695184 X10^{-1}	-9.854268 X10^{-1}
1.106047 X10^{0}	-1.018864 X10^{0}	-3.457155 X10^{0}	1.709516 X10^{-7}
-1.825088 X10^{-1}	1.741428 X10^{0}	-1.325123 X10^{0}	-4.895301 X10^{-8}
-1.825089 X10^{-1}	-1.741428 X10^{0}	-2.530140 X10^{-1}	2.160017 X10^{0}
7.945538 X10^{-1}	0.000000 X10^{0}	-2.530149 X10^{-1}	-2.160018 X10^{0}
-3.656569 X10^{-2}	0.000000 X10^{0}	3.928344 X10^{-1}	0.000000 X10^{0}
		2.568311 X10^{-2}	0.000000 X10^{0}

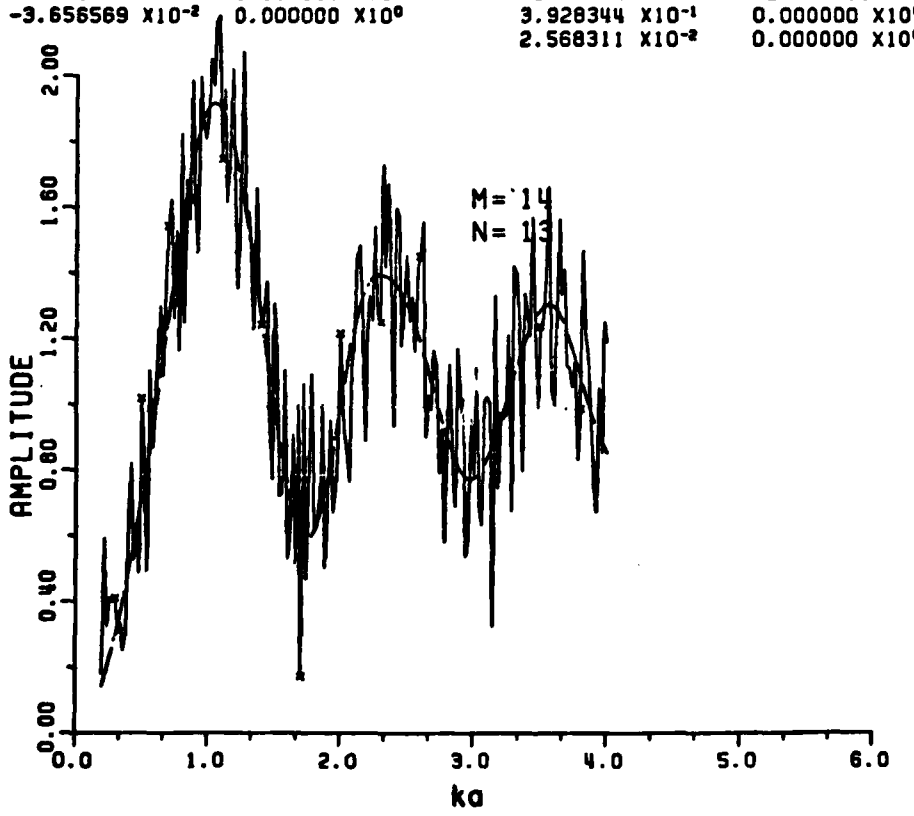

Figure 3-20. The sum operator and the RFA are applied simultaneously to the noisy data (solid line) for the sphere, where two Gaussianly distributed random noises have been added to the calculated data for the sphere. The selected data points (the x's) used in the RFA are different from those in Figure 3-19. The signal-to-noise ratio is 12.35 dB (amplitude plot).

ZEROS		POLES	
real part	imaginary part	real part	imaginary part
2.049101 X10^{-1}	4.335937 X10^{0}	-5.839402 X10^{-1}	3.974244 X10^{0}
2.049097 X10^{-1}	-4.335997 X10^{0}	-5.839413 X10^{-1}	-3.974245 X10^{0}
-5.922597 X10^{-1}	-2.936402 X10^{0}	1.128287 X10^{-1}	3.221825 X10^{0}
1.120957 X10^{-1}	3.183171 X10^{0}	1.128301 X10^{-1}	-3.221824 X10^{0}
1.120980 X10^{-1}	-3.183171 X10^{0}	-1.193190 X10^{0}	1.773633 X10^{-8}
-5.922577 X10^{-1}	2.936402 X10^{0}	7.068751 X10^{-1}	1.398300 X10^{-1}
-1.287708 X10^{-1}	-2.019105 X10^{0}	-1.734394 X10^{-1}	-1.903291 X10^{0}
-1.287712 X10^{-1}	2.019106 X10^{0}	-1.734400 X10^{-1}	1.903291 X10^{0}
-1.142900 X10^{-1}	-1.736789 X10^{0}	-2.742092 X10^{-1}	-2.153199 X10^{0}
-1.142897 X10^{-1}	1.736790 X10^{0}	-2.742084 X10^{-1}	2.153200 X10^{0}
4.971141 X10^{-1}	-6.120666 X10^{-1}	-4.187900 X10^{-1}	9.177913 X10^{-1}
4.971141 X10^{-1}	6.120666 X10^{-1}	-4.187900 X10^{-1}	-9.177913 X10^{-1}
-7.871488 X10^{-2}	0.000000 X10^{0}	7.068751 X10^{-1}	-1.398300 X10^{-1}
		6.276282 X10^{-3}	0.000000 X10^{0}

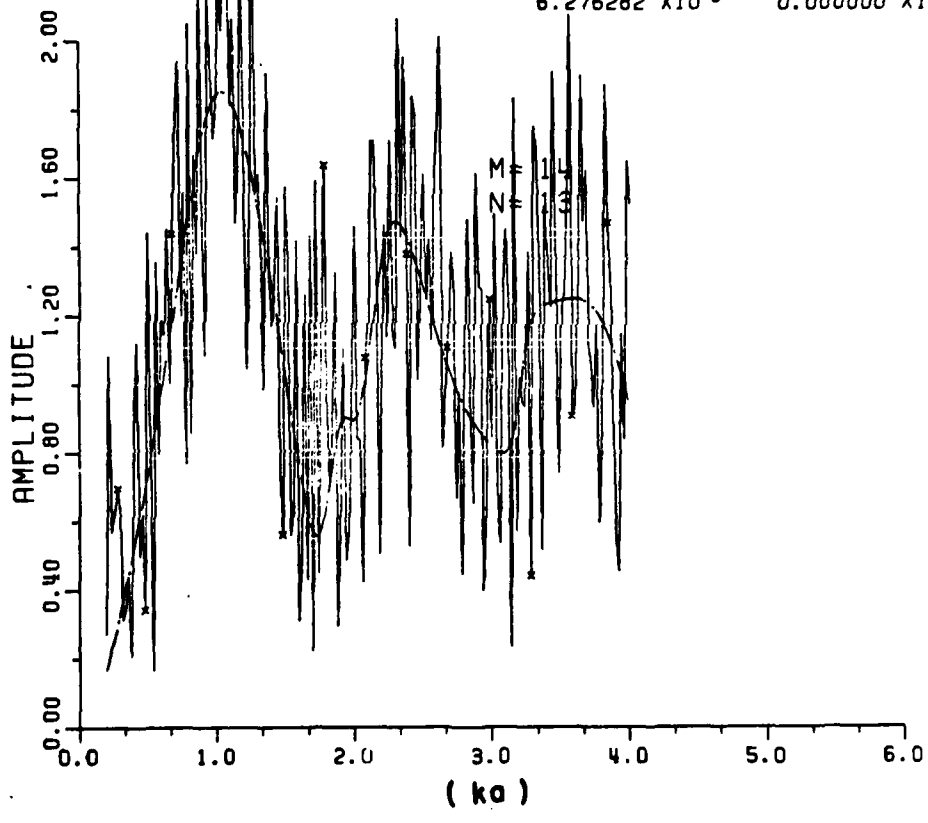

Figure 3-21. The sum operator and the RFA (dashed line) applied to the noisy data (solid line) for the sphere, where two Gaussianly distributed random noises have been added to the calculated data for the sphere. Note the selected data points are marked by x's. The signal-to-noise is 6.33 dB (amplitude plot).

the sum operators are simultaneously used to form system matrix equations. The extracted poles are listed in Tables 3-12 and 3-13.

Averaged, the real part has 13.64 percent error and the imaginary part 4.81 percent error for the S/N at 12.35 dB. For a S/N of 18.37 dB, the real part has 10.5 percent error and the imaginary part 2.4 percent error. The percentage error is 18.25 percent for the real part and 9.6 percent for the imaginary part for a S/N of 6.33 dB. The corresponding amplitude plot using a sum operator is shown in Figure 3-21 for S/N ratio of 6.33 dB. The imaginary parts have been improved more than the real part using the sum operator. The fact that the real parts of the poles are very sensitive to noise is is well known in the extraction of poles from the transient response waveforms.

3. *Preprocessing with Both Digital Filter and Sum Operator*

The functions of both digital filter and sum operator have been discussed in the two preceeding sections. In order to extract the complex natural resonances individually from a set of noisy data, the two techniques are used sequentially. In the beginning, the original data are preprocessed with a 10th order digital filter with the 3 dB cutoff frequency f_c. Then, the rational function approximant with sum operator is applied to the prefiltered data for a f_c of 20 Hz.* Two examples are shown in Figures 3-22 and 3-23, where the amplitude of the

---

* The same reason for an f_c of 20 Hz is given in Section J of this Chapter.

TABLE 3-12

POLES EXTRACTED VIA RATIONAL FUNCTION APPROXIMATION AND SUM OPERATOR

Extracted Poles* S/N=18.37 dB (σ=1.E-1)	Percentage Error Real	Imaginary
Run 1 (Figure 3-17)		
-0.373+/-J0.764	12.7	10.2
-0.5817+/-J1.8582	6.20	2.62
-0.6737+/-J2.7798	5.87	0.76
-0.4253+/-J3.7322	13.79	0.454
Run 2 (Figure 3-18)		
-0.4047+/-J0.7592	9.53	10.68
-0.5807+/-J1.6620	6.25	7.499
-0.4970+/-J2.7006	11.99	1.985
-0.3379+/-J3.6641	16.07	1.321
Run 3		
-0.353+/-J0.8167	14.7	4.932
-0.564+/-J1.873	7.12	3.383
-0.6478+/-J2.7828	6.76	0.865
-0.3852+/-J3.7031	14.84	0.305
Average Poles		
-0.3769+/-J0.78	12.31	8.6
-0.5755+/-J1.798	6.52	0.485
-0.6062+/-J2.7562	8.21	0.057
-0.3828+/-J3.700	14.90	0.385

* The units of the poles are in ka, where k is the wavenumber and a is the sphere radius.

TABLE 3-13

POLES EXTRACTED VIA RATIONAL FUNCTION APPROXIMATION AND SUM OPERATOR.

Extracted Poles S/N=12.35 dB (σ=2E-1)	Percentage of Error Real	Imaginary
Run 1 (Figure 3-19)		
-0.2989+/-J0.8643	20.11	0.17
-0.2300+/-J1.6802	24.34	6.56
-0.1827+/-J2.2712	22.89	16.88
-0.2455+/-J3.6937	18.48	0.55
Run 2 (Figure 3-20)		
-0.4695+/-J0.9854	3.05	11.94
-0.2530+/-J2.160	23.15	18.19
-0.5323+/-J2.5157	10.77	8.397
-0.4474+/-J3.6547	13.21	1.57
Run 3		
-0.4571+/-J0.9676	4.29	10.16
-0.4727+/-J2.088	11.82	14.47
-0.2651+/-J3.296	20.03	18.66
-0.1739+/-J3.674	20.34	1.063
Average Poles		
-0.405 +/-J0.9391	9.5	7.307
-0.318 +/-J1.976	19.80	8.70
-0.3267+/-J2.6943	17.90	2.20
-0.2889+/-J3.674	17.35	1.06

S/N = 6.33 dB Extracted Poles	Percentage of Error Real	Imaginary
(Figure 3-21)		
-0.418 ±j 0.9177	16.4	5.9
-0.173 ±j 1.903	27.3	4.93
-0.274 ±j 2.153	19.7	20.97
-0.584 ±j 3.974	9.6	6.78
Average	18.25	9.65

* The units are ka, where a is the sphere radius.

ZEROS		POLES	
real part	imaginary part	real part	imaginary part
-1.297710 X10^{-1}	1.702045 X10^{0}	-2.461260 X10^{-1}	-3.587156 X10^{0}
-1.319606 X10^{1}	-2.038285 X10^{-7}	-2.461263 X10^{-1}	3.587155 X10^{0}
-1.297717 X10^{-1}	-1.702046 X10^{0}	-4.458549 X10^{-1}	1.730457 X10^{0}
-2.053497 X10^{-1}	2.880495 X10^{0}	-4.458572 X10^{-1}	-1.730457 X10^{0}
-2.053504 X10^{-1}	-2.880494 X10^{0}	-1.234172 X10^{-1}	1.991303 X10^{0}
-3.680136 X10^{-1}	3.633183 X10^{0}	-1.234140 X10^{-1}	-1.991303 X10^{0}
-3.680132 X10^{-1}	-3.633184 X10^{0}	-3.213453 X10^{-1}	2.783686 X10^{0}
-1.025977 X10^{-1}	1.974989 X10^{0}	-3.213464 X10^{-1}	-2.783684 X10^{0}
-1.025967 X10^{-1}	-1.974990 X10^{0}	2.431422 X10^{-1}	9.107757 X10^{-1}
2.281609 X10^{-1}	9.023890 X10^{-1}	2.431422 X10^{-1}	-9.107756 X10^{-1}
2.281609 X10^{-1}	-9.023890 X10^{-1}	-5.314038 X10^{-1}	9.264346 X10^{-1}
-6.721890 X10^{0}	0.000000 X10^{0}	-5.314038 X10^{-1}	-9.264344 X10^{-1}
4.925702 X10^{-2}	0.000000 X10^{0}	-5.990435 X10^{-1}	0.000000 X10^{0}
		-6.941624 X10^{-2}	0.000000 X10^{0}

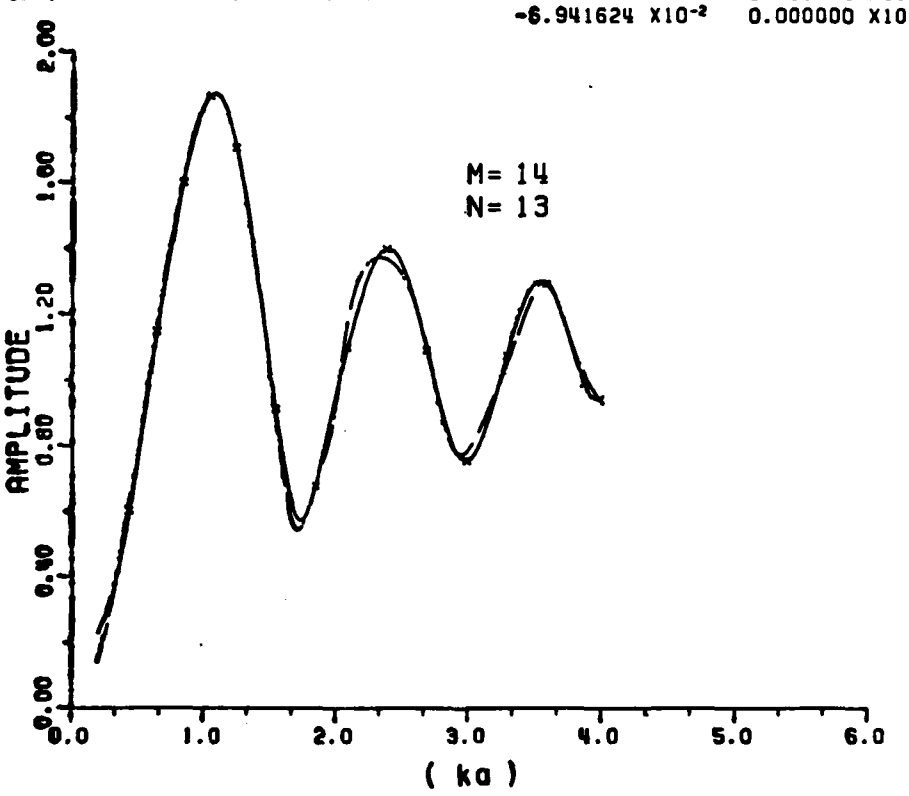

Figure 3-22. The sum operator and the RFA are applied simultaneously to the prefiltered data (solid line) for the sphere. A 10th order zero-phase-shift digital filter is used to prefilter the noisy data, where two Gaussianly distributed random noises have been added to the calculated data for the sphere. The x's are the data points used in the RFA. The original signal-to-noise ratio is 12.35 dB (amplitude plot).

ZEROS		POLES	
real part	imaginary part	real part	imaginary part
5.268377 X10^{-1}	-4.215118 X10^{0}	2.598235 X10^{-1}	3.555334 X10^{0}
5.268342 X10^{-1}	4.215117 X10^{0}	-2.891078 X10^{1}	1.675003 X10^{-7}
3.341878 X10^{-1}	-3.560440 X10^{0}	-5.651634 X10^{-1}	-3.001400 X10^{0}
3.341935 X10^{-1}	3.560446 X10^{0}	-5.651639 X10^{-1}	3.001400 X10^{0}
6.448721 X10^{-2}	-2.162105 X10^{0}	2.598231 X10^{-1}	-3.555334 X10^{0}
6.449073 X10^{-2}	2.162104 X10^{0}	2.228815 X10^{0}	-1.807314 X10^{-8}
1.299975 X10^{0}	3.582260 X10^{-8}	-6.639862 X10^{-1}	1.790383 X10^{0}
-1.320187 X10^{-1}	-1.725456 X10^{0}	-6.639862 X10^{-1}	-1.790383 X10^{0}
-1.320197 X10^{-1}	1.725456 X10^{0}	7.460998 X10^{-2}	2.163905 X10^{0}
-2.254793 X10^{-1}	-2.962519 X10^{0}	7.460988 X10^{-2}	-2.163905 X10^{0}
-2.254843 X10^{-1}	2.962516 X10^{0}	-5.681291 X10^{-1}	9.150119 X10^{-1}
9.240991 X10^{-2}	7.802422 X10^{-1}	-5.681291 X10^{-1}	-9.150119 X10^{-1}
9.240987 X10^{-2}	-7.802422 X10^{-1}	9.447543 X10^{-2}	7.768920 X10^{-1}
-1.207707 X10^{0}	0.000000 X10^{0}	9.447547 X10^{-2}	-7.768919 X10^{-1}
2.[illegible]3516 X10^{-1}	0.000000 X10^{0}	-5.287395 X10^{-1}	0.000000 X10^{0}
		2.576995 X10^{-2}	0.000000 X10^{0}

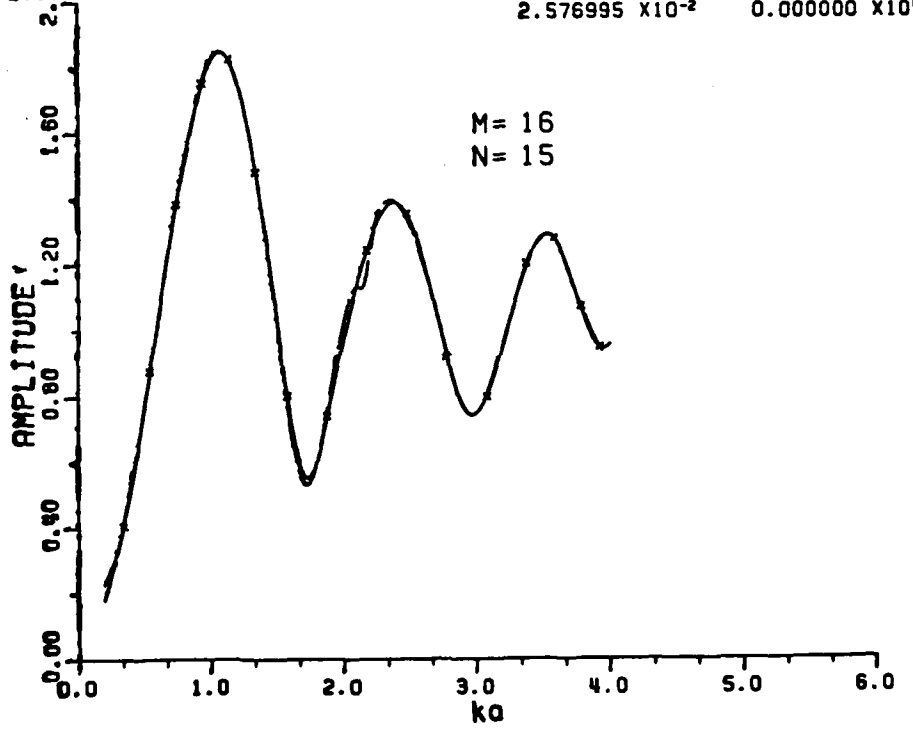

Figure 3-23. The sum operator and the RFA are applied simultaneously to the prefiltered data (solid line) for the sphere. A 10th order zero-phase-shift digital filter is used to prefilter the noisy data, where two Gaussianly distributed random noises have been added to the calculate data for the sphere. The x's are the data points used in the RFA. The original signal-to-noise ratio is 12.35 dB. The data points used are different from those in Figure 3-22 (amplitude plot).

AD-A143 913 APPROXIMATE METHODS FOR OBTAINING THE COMPLEX NATURAL ELECTROMAGNETIC OSC..(U) OHIO STATE UNIV COLUMBUS ELECTROSCIENCE LAB T C LEE ET AL. FEB 84 ESL-710816-16 2/4

UNCLASSIFIED N00014-78-C-0049 F/G 20/3 NL

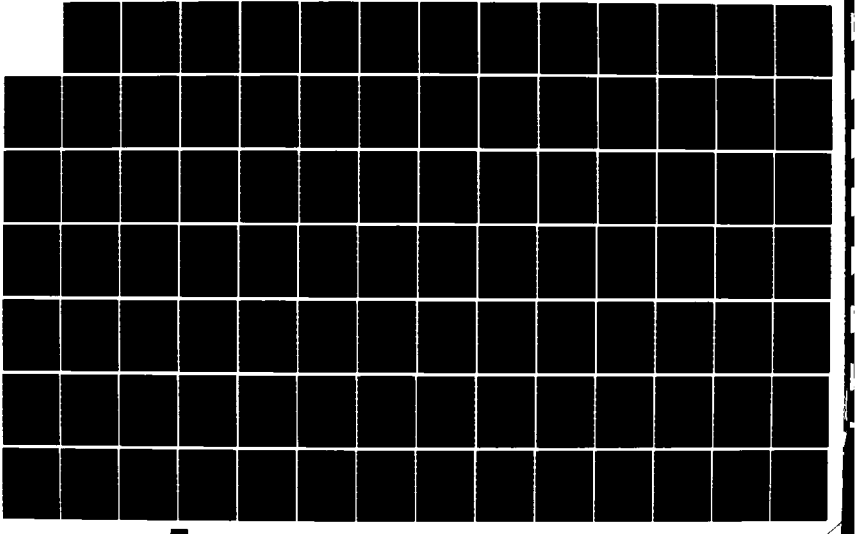

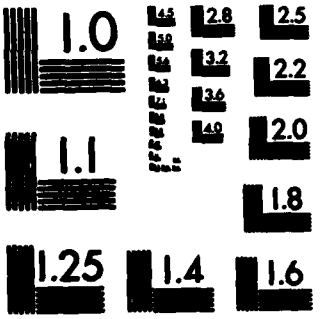

MICROCOPY RESOLUTION TEST CHART
NATIONAL BUREAU OF STANDARDS-1963-A

filtered data (solid line) and the fitted curve using sum operator (dashed line) in the rational function are plotted. The extracted poles are listed in Table 3-14. It has been shown (see Table 3-14) that the first three pole-pairs are much improved using the digital filter and sum operator sequentially. However, the fourth pole-pairs may not be located at all because both digital filter and sum operator are using only one sided information to predict or to smooth the data around the high frequency end (due to the truncation of data there). The smoothed data near the high-frequency end are therefore not accurate.

K. BRIEF SUMMARY

In this chapter, rational function approximants have been defined, developed and applied to noiseless and noisy data for a conducting sphere. Two major problems, critical points in any system identification, are the system order and the noise problem. Inherently, the system order is not a very critical point in the rational function fit as long as the system order M is not less than the true poles desired. In fact the system order can be roughly determined from the amplitude curve resonances, i.e., the order of the system is roughly determined by the number of peaks in the amplitude data. However, some curve fitting poles and some true poles should also be counted although they are not seen clearly in the amplitude peaks (if there are interferences from different scattering mechanisms).

TABLE 3-14

POLES EXTRACTED VIA RATIONAL FUNCTION APPROXIMATION
USING THE DIGITAL FILTER AND THE SUM OPERATOR (S/N = 12.35 dB)

Poles* Extracted via Digital Filter and Sum Operator for (M,N) as (16,15)	Percentage Error Real	Imaginary
Run 1 (Figure 3.22) M=14, N=13		
-0.531+/-j0.926	3.10	6.037
-0.446+/-j1.730	13.21	3.992
-0.321+/-j2.784	18.08	0.893
-0.246+/-j3.587	18.46	3.33
Run 2 (Figure 3.23)		
-0.568+/-j0.915	6.8	4.89
-0.664+/-j1.790	1.96	0.89
-0.565+/-j3.001	9.63	8.43
Run 3		
-0.392+/-j0.927	10.8	6.10
-0.455+/-j1.927	12.73	6.17
-0.453+/-j3.0[illegible]	13.52	11.17
Run 4		
-0.568+/-j0.8235	6.80	4.25
-0.789+/-j1.538	4.49	13.89
-0.455+/-j2.902	13.45	4.99
Average		
-0.515+/-j0.897	1.499	3.097
-0.589+/-j1.759	5.826	2.455
-0.429+/-j2.923	14.35	5.72

* The units of the poles are in ka, where k is the wavenumber and a is the sphere radius.

As far as the noise problem is concerned, a high-order digital filter has been developed to prefilter the additive noise and a sum operator is used in the rational function fit to reduce both the additive and multiplicative noise. As shown in this chapter, the poles still can be extracted and identified for a S/N ratio at 12.35 dB*, if a 10th order zero-phase-shift digital filter and a sum operator are used. Although the study in this chapter is limited to the computer generated additive Gaussian white noise. Chapter VI will present an extension of using the 10th order zero-phase-shift digital filter and RFA to the measured data using the reflectivity measurement facility at the ElectroScience Laboratory.

---

* Although there is an example of S/N of 6.33 dB (Figure 3-21); however, the percentage error is relatively high (see Table 3-13).

CHAPTER IV

LINEAR LEAST SQUARED ERROR SOLUTIONS

A. INTRODUCTION

It was shown in Chapter III that the RFA with preprocessing can extract the complex natural resonances reasonably well when the signal is contaminated by additive noise. It would appear that the RFA applied in a least squared error sense might fit the data better. In this chapter several techniques using least squared error solutions are investigated.

B. EIGENANALYSIS

An imhomogeneous system of linear equations

$$AX = E \quad , \tag{4-1}$$

where A is a real m x (n+1) data matrix of rank (n+1) and X and E are (n+1) and m rows column vectors, respectively, is an overdetermined system if m > (n+1). The components of X are unknown coefficients and E is the error, assumed small. The squared error is

$$X^T A^T A X = E^T E \quad , \tag{4-2}$$

where Y^T means the transpose of Y.

There are N+2 ways to solve the matrix equation [16]. However, the solution with the constraint

$$\sum_{i=0}^{n} |a_i|^2 = 1 \quad , \tag{4-3}$$

the eigenanalysis method [16] , is the solution to the min max problems and yields the minimum total squared error.

Eigenanlysis has been used to minimize the total squared error of the matrix equation (Equation (4-1)) and has shown some success in simple simulated cases [16]. In addition, noise remains a serious problem. The following procedures are used to solve the matrix equation given by Equation (4-1).

1. Find the eigenvalues of A^TA first.
2. Find the eigenvector which corresponds to the smallest eigenvalue, this is the minimum total squared error.
3. The eigenvector corresponding to the smallest eigenvalue is the solution X of the matrix equation in the sense that the sum of the residuals squared is minimized.

Several efforts have been made to extract the complex natural resonances from rational function approximants via eigenanalysis. The results are not good even for a relatively low system order for (M,N) as (6,5) and noiseless data. With noisy data, the result is even worse. Assuming no mistake in theory, the error must be due to

numerical calculation, in particular, the calculation of the eigenvalues. This will be clear in the next section on singular decomposition where it is shown that better results can be obtained.

C. EIGENANALYSIS VIA SINGULAR VALUE DECOMPOSITION

Given a real m x (n+1) matrix A with m > (n+1), the matrix A can be decomposed into the following form.

$$A = U\Sigma V^T \quad , \tag{4-4.1}$$

where

$$U^TU = VV^T = V^TV = I_{(n+1)} \ , \tag{4-4.2}$$

and

$$\Sigma = \text{diag}(\sigma_1, \ldots, \sigma_{(n+1)}). \tag{4-4.3}$$

The matrix U is an mxn matrix consisting of n orthonormalized eignevectors associated with the n largest eigenvalues of AA^T. The matrix V is an (n+1) x (n+1) matrix consisting of the (n+1) orthonormalized eigenvectors of A^TA and the diagonal elements of Σ are the non-negative square roots of the eigenvalues of A^TA which are called singular values. It is assumed that

$$\sigma_1 > \sigma_2 > \sigma_3 > \ldots > \sigma_{(n+1)} > 0 \quad . \tag{4-4.4}$$

If the rank of A is r and r is less than (n+1), then

$$\sigma_{r+1} = \sigma_{r+2} = \ldots, \sigma_{(n+1)} = 0 \quad . \tag{4-4.5}$$

The decomposition of matrix A in Equation (4-4.1) is called singular value decomposition (SVD). To compute the singular value decomposition of a given matrix A, Householder transformations and a QR algorithm are used in the literature.* The advantage in solving least squared error problems using SVD** is that there is no necessity to compute A^TA, which may involve unnecessary numerical inaccuracies.

Singular value decomposition routines are available in the literature.*** An application of the singular value decomposition to find the complex natural resonances from the calculated data for a sphere is presented in Table 4-1 and Table 4-3. Table 4-1 is a list of singular values for the rational function fit to the sphere data for (M,N) as (14,13) and I as 20 (20 data points). Table 4-2 is a list of the ratio of two adjacent singular values. Table 4-3 is a list of the extracted poles from the sphere backscattering data via SVD.

The smallest singualar value is of the order of 0.01. The ratios of two adjacent singular values are all in the order of 100 to 10, i.e., no sudden change occurs. Thus there is no clue for finding the system order via the ratio of two adjacent singular values although the

---

* G.H. Gould and C. Reinsch, "Singular Value Decomposition and Least Squares Solutions", Numerical Mathematics 14, p. 403-420, 1970.

** The eigenvector of A^TA which corresponds to the smallest singular value of A is the solution of the unknown matrix X in Equation (4-1).

***C.L. Lawson and R. J. Hanson, Solving Least Squares Problems, Englewood Cliffs, N. J., Prentice-Hall, 1974.

TABLE 4-1

A LIST OF THE SINGULAR VALUES USING SINGULAR VALUE DECOMPOSITION IN THE RFA for (M,N) as (14,13) TO THE CALCULATED DATA FOR THE SPHERE

M= 14 N= 13
DATA POINT USED = 20 INCREMENT= 10

THE	1	SINGULAR VALUE IS	0.1213032E+10
THE	2	SINGULAR VALUE IS	0.4227007E+09
THE	3	SINGULAR VALUE IS	0.2762580E+08
THE	4	SINGULAR VALUE IS	0.1471489E+08
THE	5	SINGULAR VALUE IS	0.1902102E+07
THE	6	SINGULAR VALUE IS	0.9058594E+06
THE	7	SINGULAR VALUE IS	0.7508329E+05
THE	8	SINGULAR VALUE IS	0.3740441E+05
THE	9	SINGULAR VALUE IS	0.1346613E+05
THE	10	SINGULAR VALUE IS	0.8894107E+04
THE	11	SINGULAR VALUE IS	0.8768583E+03
THE	12	SINGULAR VALUE IS	0.3870276E+03
THE	13	SINGULAR VALUE IS	0.1275254E+03
THE	14	SINGULAR VALUE IS	0.8262138E+02
THE	15	SINGULAR VALUE IS	0.4379275E+02
THE	16	SINGULAR VALUE IS	0.2039347E+02
THE	17	SINGULAR VALUE IS	0.1570983E+02
THE	18	SINGULAR VALUE IS	0.4903873E+01
THE	19	SINGULAR VALUE IS	0.4777973E+01
THE	20	SINGULAR VALUE IS	0.2413255E+01
THE	21	SINGULAR VALUE IS	0.1353038E+01
THE	22	SINGULAR VALUE IS	0.3440572E+00
THE	23	SINGULAR VALUE IS	0.2936901E+00
THE	24	SINGULAR VALUE IS	0.1810666E+00
THE	25	SINGULAR VALUE IS	0.8229814E-01
THE	26	SINGULAR VALUE IS	0.6865017E-01
THE	27	SINGULAR VALUE IS	0.1388225E-01
THE	28	SINGULAR VALUE IS	0.6414558E-02
THE	29	SINGULAR VALUE IS	0.2125495E-02

TABLE 4-2

THE RATIO OF TWO ADJACENT SINGULAR VALUES*

THE	1TH	SINGULAR VALUE OVER THE	2	TH	0.286972E+01
THE	2TH	SINGULAR VALUE OVER THE	3	TH	0.153009E+02
THE	3TH	SINGULAR VALUE OVER THE	4	TH	0.187740E+01
THE	4TH	SINGULAR VALUE OVER THE	5	TH	0.773612E+01
THE	5TH	SINGULAR VALUE OVER THE	6	TH	0.209978E+01
THE	6TH	SINGULAR VALUE OVER THE	7	TH	0.120647E+02
THE	7TH	SINGULAR VALUE OVER THE	8	TH	0.200734E+01
THE	8TH	SINGULAR VALUE OVER THE	9	TH	0.277767E+01
THE	9TH	SINGULAR VALUE OVER THE	10	TH	0.151405E+01
THE	10TH	SINGULAR VALUE OVER THE	11	TH	0.101432E+02
THE	11TH	SINGULAR VALUE OVER THE	12	TH	0.226562E+01
THE	12TH	SINGULAR VALUE OVER THE	13	TH	0.303491E+01
THE	13TH	SINGULAR VALUE OVER THE	14	TH	0.154349E+01
THE	14TH	SINGULAR VALUE OVER THE	15	TH	0.188664E+01
THE	15TH	SINGULAR VALUE OVER THE	16	TH	0.214739E+01
THE	16TH	SINGULAR VALUE OVER THE	17	TH	0.129813E+01
THE	17TH	SINGULAR VALUE OVER THE	18	TH	0.320356E+01
THE	18TH	SINGULAR VALUE OVER THE	19	TH	0.102635E+01
THE	19TH	SINGULAR VALUE OVER THE	20	TH	0.197989E+01
THE	20TH	SINGULAR VALUE OVER THE	21	TH	0.178358E+01
THE	21TH	SINGULAR VALUE OVER THE	22	TH	0.393260E+01
THE	22TH	SINGULAR VALUE OVER THE	23	TH	0.117150E+01
THE	23TH	SINGULAR VALUE OVER THE	24	TH	0.162200E+01
THE	24TH	SINGULAR VALUE OVER THE	25	TH	0.220013E+01
THE	25TH	SINGULAR VALUE OVER THE	26	TH	0.119880E+01
THE	26TH	SINGULAR VALUE OVER THE	27	TH	0.494517E+01
THE	27TH	SINGULAR VALUE OVER THE	28	TH	0.216418E+01
THE	28TH	SINGULAR VALUE OVER THE	29	TH	0.301791E+01

* The singular values in Table 4-1 were used.

* The singular values in Table 4-1 were used.

TABLE 4-3

A COMPARISON OF THE TRUE POLES AND THE EXTRACTED POLES*
USING RFA MODEL AND THE SINGULAR VALUE DECOMPOSITION TO
THE CALCULATED DATA (SPHERE, BACKSCATTER)

True Poles	Extracted Poles	Percentage of Error	
		real	imaginary
-0.500000+/-j0.8660250	-0.501176+/- j0.8552016	0.1176	1.082337
-0.701964+/-j1.80740	-0.7111590+/-j1.806740	0.4742292	0.0034
-0.842862+/-j2.75786	-0.8363640+/-j2.76490	0.2253303	0.2441246
-0.954230+/-j3.714780	-0.9193100+/-j3.67700	0.9104712	1.166823

* The units of the poles are in ka, where k is the wavenumber and a is the sphere radius.

extracted poles are very close to the true ones. The application of singular value decomposition to noisy data fails even for small additive noise. It was disappointing to learn that zero phase-shift digital filter effected no improvement in the extraction of poles via singular value decomposition of the filtered data.

D. PSEUDO-INVERSE METHOD

Instead of forming a matrix equation such as Equation (4-1), where E is an error matrix for an overdetermined system, the other simple way of forming a matrix equation from the RFA is similar to that of exact determined systems in Chapter III, i.e.,

$$AX = B, \tag{4-5.1}$$

where A is an mxn matrix with m>n, X is a nx1 unknown matrix, B is a mx1 matrix and the elements in B are the real and imaginary parts of the complex data points. Then the easiest way to solve this equation is to perform a a pseudo-inverse as

$$A^TAX = A^TB \quad , \tag{4-5.2}$$

where A^T is the transpose of A. In fact this method is also known as a least squared error solution without weight in mathematics. The application of this solution to the calculated data for a sphere are given in Figures 4-1 (amplitude) and 4-2 (phase). Note that twenty complex data points are used in this overdetermined system for (M,N) as (14,13) (28 unknowns). Table 4-4 is a comparison of the true poles and

TABLE 4-4

A COMPARISON OF THE TRUE POLES AND THE EXTRACTED POLES*
USING RFA AND PSEUDO-INVERSE METHOD, i.e., LEAST SQUARED ERROR
WITHOUT WEIGHT TO THE CALCULATED DATA (SPHERE, BACKSCATTER)

True Poles	Extracted Poles	Percentage of Error real	Percentage of Error imaginary
-0.500000+/-j0.8660250	-0.5043270+/-j0.8679600	0.4327	0.1935
-0.701964+/-j1.80740	-0.70266 +/-j1.79561	0.03589	0.6081
-0.842862+/-j2.75786	-0.84936 +/-j2.76335	0.2253	0.1903
-0.95423+/-j3.71478	-0.92042 +/-j3.70323	0.8815	0.30115

* The units of the poles are in ka, where k is the wavenumber and a is the sphere radius.

ZEROS		POLES	
6.078589 X10^{1}	-2.917712 X10^{-7}	-9.204194 X10^{-1}	3.703229 X10^{0}
-1.391740 X10^{-1}	1.740449 X10^{0}	-9.204198 X10^{-1}	-3.703230 X10^{0}
-1.391742 X10^{-1}	-1.740449 X10^{0}	-8.493635 X10^{-1}	2.763350 X10^{0}
-1.200745 X10^{0}	5.580223 X10^{0}	-8.493635 X10^{-1}	-2.763350 X10^{0}
-1.200746 X10^{0}	-5.580222 X10^{0}	-7.026555 X10^{-1}	1.795610 X10^{0}
-2.992245 X10^{-1}	4.153576 X10^{0}	-7.026555 X10^{-1}	-1.795610 X10^{0}
-2.992242 X10^{-1}	-4.153576 X10^{0}	1.717934 X10^{0}	1.087607 X10^{0}
1.718133 X10^{0}	1.087670 X10^{0}	1.717934 X10^{0}	-1.087607 X10^{0}
1.718133 X10^{0}	-1.087670 X10^{0}	-7.769776 X10^{-1}	4.480850 X10^{0}
-2.298296 X10^{-1}	2.949380 X10^{0}	-7.769775 X10^{-1}	-4.480848 X10^{0}
-2.298291 X10^{-1}	-2.949379 X10^{0}	-5.043270 X10^{-1}	8.679571 X10^{-1}
-1.296468 X10^{0}	8.343870 X10^{-1}	-5.043270 X10^{-1}	-8.679572 X10^{-1}
-1.296468 X10^{0}	-8.343870 X10^{-1}	-1.756604 X10^{0}	0.000000 X10^{0}
0.000000 X10^{0}	0.000000 X10^{0}	-1.029366 X10^{0}	0.000000 X10^{0}
0.000000 X10^{0}	0.000000 X10^{0}		

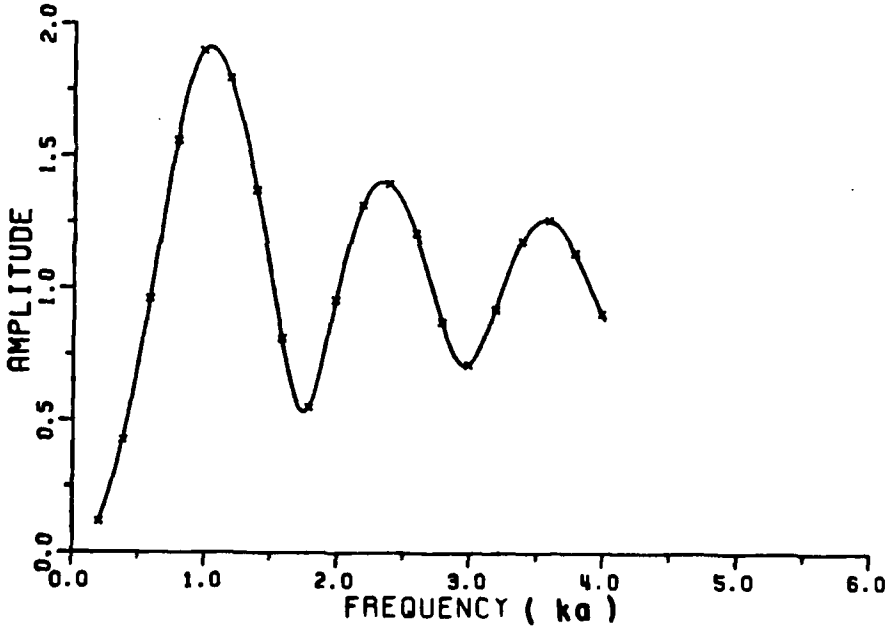

Figure 4-1. The RFA applied to the calculated data for the sphere in the sense of least squared error without weight. Note twenty complex data points are used (amplitude plot).

RESI.		MAG. OF RESI.
-2.885144 X10^{0}	2.949349 X10^{0}	4.125859 X10^{0}
-2.885145 X10^{0}	-2.949358 X10^{0}	4.125867 X10^{0}
2.151874 X10^{0}	3.669074 X10^{0}	4.253547 X10^{0}
2.151874 X10^{0}	-3.669073 X10^{0}	4.253546 X10^{0}
2.868279 X10^{0}	-3.122501 X10^{-1}	2.885225 X10^{0}
2.868279 X10^{0}	3.122519 X10^{-1}	2.885225 X10^{0}
1.489154 X10^{-4}	7.516474 X10^{-5}	1.668099 X10^{-4}
1.489154 X10^{-4}	-7.516477 X10^{-5}	1.668099 X10^{-4}
-9.326031 X10^{-1}	-1.218709 X10^{0}	1.534601 X10^{0}
-9.326016 X10^{-1}	1.218716 X10^{0}	1.534606 X10^{0}
-3.001210 X10^{-2}	-1.810827 X10^{0}	1.811076 X10^{0}
-3.001225 X10^{-2}	1.810827 X10^{0}	1.811076 X10^{0}
8.312219 X10^{0}	1.113897 X10^{-6}	8.312219 X10^{0}
-4.417518 X10^{0}	-3.929819 X10^{-7}	4.417519 X10^{0}

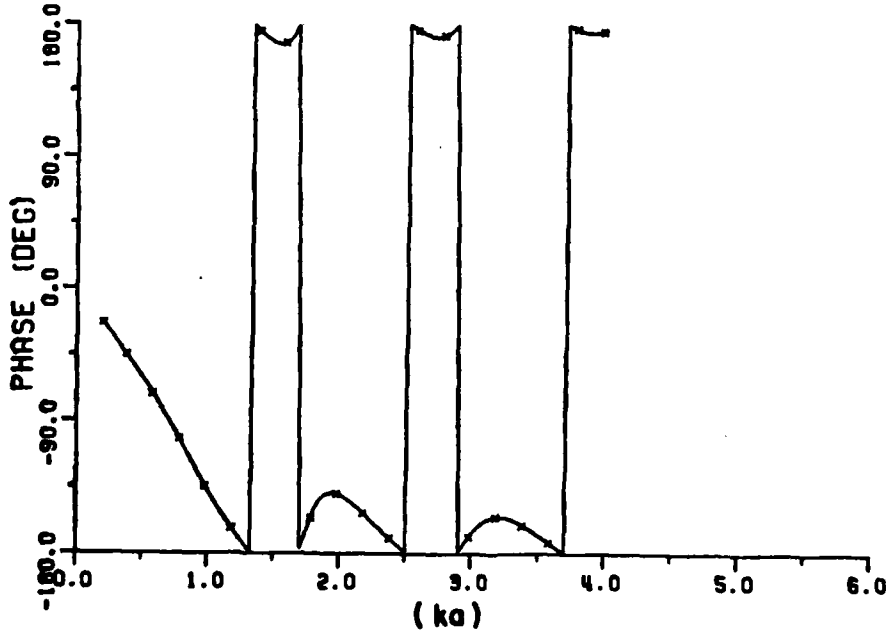

Figure 4-2. The RFA applied to the calculated data for the sphere in the sense of least squared error without weight. Note that twenty complex data points are used (phase plot).

the extracted poles using this method. The extracted poles are very close to the true ones in the noiseless situation.

The intentions to use more data points have been made but the results are even worse due to the numerical errors in the computation of large matrix. An attempt to extract poles using the pseudo-inverse method from sets of noisy data fails even for small additive noise, e.g., signal to noise ratio at 30 dB. Without doubt the bias problem is serious in this method as well as the other two methods mentioned earlier.

E. SUMMARY

All techniques discussed in this chapter concerned methods for solving the matrix equation in the least squared error sense. They are eigenanalysis using the eigenvalues or singular values and a pseudo-inverse method. The eigenanalysis using singular values works well if there is no noise; however, the method generally fails even for slightly noisy data. Eigenanalysis would appear to be the best of these unweighted solutions. The anticipation of better fits from least squared error solutions using more data points is not true due to the accumulation of numerical errors and the bias problem.

CHAPTER V

AN INVESTIGATION OF THE COMPLEX NATURAL RESONANCES OF VARIOUS OBJECTS

A. INTRODUCTION

It was shown in Chapter III that the RFA could be applied successfully, for pole extraction, to the calculated data for the sphere with or without additive noise. Furthermore, it was shown in Chapter IV that the RFA used for pole extraction in a least squared error sense were very sensitive to noise. An approximate method which can be utilized to extract the complex natural resonances of a particular target may or may not be precisely applicable to other targets. Therefore, various sets of backscattering data for different targets should be tested to see the general applicability of the method. In this chapter, the complex natural resonances of some simple* conducting scatterers such as a circular disc, loop, thin wire, finite circular waveguide, semi-infinite circular wave-guide, and one stick model of a F104 aircraft are extracted via the rational function approximations

---

* Applications to geometrically complex targets are given in Chapter VI (measured data).

(RFA) in the exact sense. The results (poles) are compared in some cases with those obtained using different approximate or exact (sphere) methods. The approximate methods (in addition to RFA) which were used in this study are the Uniform Geometrical Theory of Diffraction (UTD) [11] for a disc and an integral equation formulation and numerical search for a loop.

B. CONDUCTING SPHERE

1. Analytical Method

For convenience, the first few complex natural resonances of a conducting sphere as taken from Stratton are listed again in Table 5-1 for both the transverse electric (TE) and the transverse magnetic (TM) modes. Both TE and TM modes are excited at the same time. The oscillations of the electric mode are independent of the magnetic mode oscillations.

2. Signal-Flow-Graph Method

Using the differential attenuation and phase shift of a surface wave on a spherical surface given by Pathak and Kouyoumjian [11,12], Kennaugh [10] derived two characteristic equations for a geodesic path around the sphere. The roots of these two equations are the poles of the sphere. The first 4 pole-pairs for the electric mode via signal-flow graphs [10] and rational function approximation are compared in Table 5-2. The low order poles extracted via the rational function

TABLE 5-1

POLES* OF SPHERE EXTRACTED VIA ANALYTICAL METHOD

Electric Mode	Magnetic Mode
-1.60+/-j0.	-1. +/-j0.
-0.50+/-j0.86	-1.5 +/-j0.86
-2.17+/-j0.87	
-0.70+/-j1.81	-2.26+/-j0
-0.83+/-j2.77	-1.87+/-j1.75

* The units of the poles are in ka, where k is the wavenumber and a is the sphere radius.

TABLE 5-2

A COMPARISON OF THE POLE-PAIRS* FOR A
CONDUCTING SPHERE EXTRACTED USING DIFFERENT METHODS

True Poles [25]	Signal Flow Graphs	Rational Function
-0.50000 +/-j0.86025	-0.4968+/-j0.8759	-0.49999+/-j0.8666
-0.701964+/-j1.80740	-0.7008+/-j1.8130	-0.7019 +/-j1.8028
-0.842862+/-j2.75786	-0.8422+/-j2.7618	-0.8424 +/-j2.7621
-0.954230+/-j3.71478	-0.9538+/-j3.7178	-0.9175 +/-j3.6829

* The units of the poles are in ka, where k is the wavenumber and a is the sphere radius.

approximants are more accurate than those extracted via the signal-flow-graph method but the asymptotic approach obtains the high frequency poles with greater accuracy.

3. Rational Function Approximation

The results of applying the rational function approximations to the backscattering data of sphere [27] have been shown in Figures 3-7 and 3-8 for a system order for (M,N) as (14,13). Fourteen data points (marked by x's) are used in the RFA in the exact sense. A comparison of the true poles [25] and those extracted via the rational function approximations and the signal-flow-graph approach are listed in Table 5-2. The data used for the rational function approximant are from ka of 0.2 to ka of 4, i.e., the data are truncated at ka of 4. Therefore, it is not surprising that the real part of the last pole-pair is not as accurate as the others.

C. DISC

1. Introduction

The diffraction of a plane electromagnetic wave by a thin, circular, metallic disc remained unsolved until the rigorous solution obtained by Meixner and Andrejewski in 1950*. The disc is treated

---

* J. Meixner and W. Andrejwski, "A Rigorous Theory on the Diffraction of Plane Electromagnetic Waves by a Perfectly Conducting Circular Disc and by a Circular Aperature in a Perfectly Conducting Plane Sheet," Aner. der Phys., Vol. 7, p. 157, 1950.

as a limiting surface in an oblate spheroidal coordinate system using an eigenfunction solution. Numerical results of fourteen discrete frequencies were subsequently obtained by Andrejewski in 1952 [30]. Flammer [31] derived another solution using oblate spheroidal vector wave functions in 1953. Hodge [32] presented Meixner's solution in in terms of the notation introduced by Flammer [31] and the far field amplitude and phase scattering data (ka of 0.2(0.2)15.2) for plane wave incidence at broadside were calculated using his development of an efficient method of computing the spheroidal eigenvalues [32]. Using Hodge's computer programs, J. L. Li of the ElectroScience Laboratory at The Ohio State University compiled the backscattering data (ka of 0.2(0.2) 10.) of the disc at angles off broadside incidence (θ of 15°(15°)90°) for the incident electric field in both θ and ϕ polarizations (see Figure 5-1). The results of applying the RFA to these sets of data and UTD approximations to the resonant modes of the disc are presented in the following section.

2. Broadside Incidence

Rational function approximants have been developed and applied to the calculated backscattering data of a circular disc. The data sets are in the range of ka of 0.2 to ka of 15.2 for broadside incidence. Cases with both the incident electric field and the incident magnetic field parallel to the plane of the disc are included. These data sets are fitted with the rational function approximants in the exact sense.

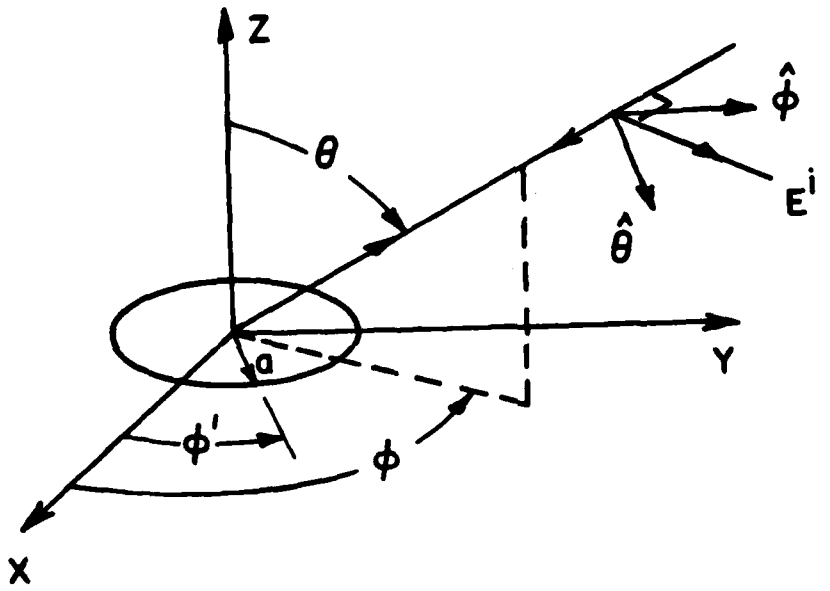

Figure 5-1. The coordinate system for a circular metallic disc.

ZEROS		POLES	
real part	imaginary part	real part	imaginary part
-1.825366×10^{0}	6.735340×10^{-1}	-4.896136×10^{-1}	-1.229665×10^{0}
-1.825368×10^{0}	-6.735328×10^{-1}	-2.466722×10^{0}	1.036491×10^{-7}
		-4.896136×10^{-1}	1.229665×10^{0}

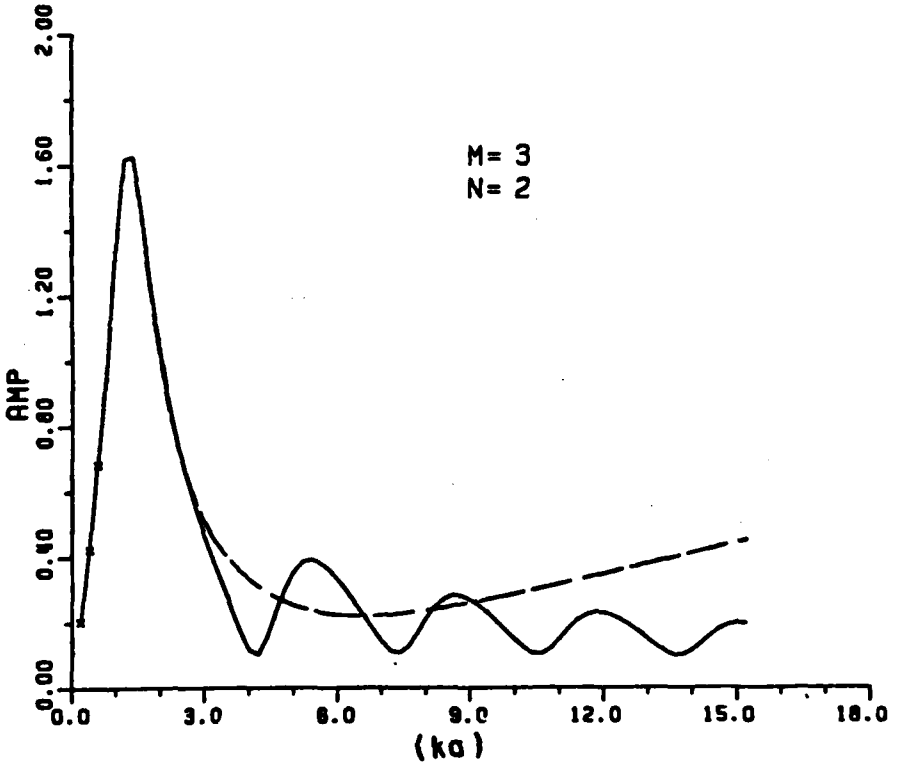

Figure 5-2. The RFA for (M,N) as (3,2) fit to the backscattering data for the disc at broadside. The x's are the data points used. The solid line is the calculated data and the dotted line is the RFA (amplitude plot). The 3 input samples are in the Rayleigh region and are marked with x's.

Figures 5-3 through 5-6 show several examples of applying the rational function approximation (RFA) program to the real frequency data of the disc for plane wave incidence at broadside. Appendix C gives a detailed list of the coefficients of the RFA using system order for (M,N) as (14,13) (Table C-1) and the corresponding zeros, poles and residues (Table C-2) by applying RFA to the disc backscattering data at broadside for plane wave excitation. Note the coefficients of the RFA at higher orders become smaller and smaller. In order to estimate the accuracy of the rational function coefficients for the disc backscattering data for a plane wave incidence at broadside, a long division of the rational function approximant with the coefficients listed in Table C-1 was performed with the result in the form of

$$E^{n}(X) = \sum_{n=1}^{k} c_n X^{n+1} \quad , \qquad (5\text{-}1)$$

where X is jka and a is the radius of the disc, is shown in Equation (C-1). It approximates closely the result in Equation (C-2), the low frequency approximation given by Boersma* (see Appendix C). Figure 5-3, which is similar to that obtained by D.B. Hodge, is the RFA to the first resonant region [33]. The order (M,N) for the system as (3,2), i.e., only three input samples (marked with x's in Figure 5-2) are used in the RFA. Figure 5-3 and 5-4 are excellent fits of the RFA to the entire data region with a system order of (M,N) as (14,13). Poles, zeros, and

---

* Boersma, J., "Boundary Value Problems in Diffraction Theory and Lifting Surface Theory," Thesis, Groninger, Holland, 1964.

ZEROS		POLES	
real	imaginary part	real part	imaginary part
-3.937129 X10⁰	1.977370 X10¹	-4.025044 X10⁰	2.001848 X10¹
-3.937129 X10⁰	-1.977369 X10¹	-4.025046 X10⁰	-2.001847 X10¹
-1.281795 X10⁰	-1.434566 X10¹	-1.284660 X10⁰	-1.440915 X10¹
-1.281795 X10⁰	1.434566 X10¹	-1.284662 X10⁰	1.440913 X10¹
-1.241245 X10⁰	-1.119711 X10¹	-1.241248 X10⁰	-1.128542 X10¹
-1.241246 X10⁰	1.119711 X10¹	-1.241250 X10⁰	1.128544 X10¹
-1.162094 X10⁰	-7.982498 X10⁰	-1.163499 X10⁰	-8.106087 X10⁰
-1.162093 X10⁰	7.982495 X10⁰	-1.163497 X10⁰	8.106080 X10⁰
-1.524350 X10⁰	-1.553103 X10⁰	-4.906894 X10⁻¹	-1.231033 X10⁰
-1.524349 X10⁰	1.553103 X10⁰	-4.906893 X10⁻¹	1.231033 X10⁰
-1.035533 X10⁰	-4.666735 X10⁰	-1.045793 X10⁰	-4.873465 X10⁰
-1.035535 X10⁰	4.666736 X10⁰	-1.045794 X10⁰	4.873467 X10⁰
-2.109441 X10⁰	0.000000 X10⁰	-1.589850 X10⁰	-1.757181 X10⁰
		-1.589850 X10⁰	1.757181 X10⁰

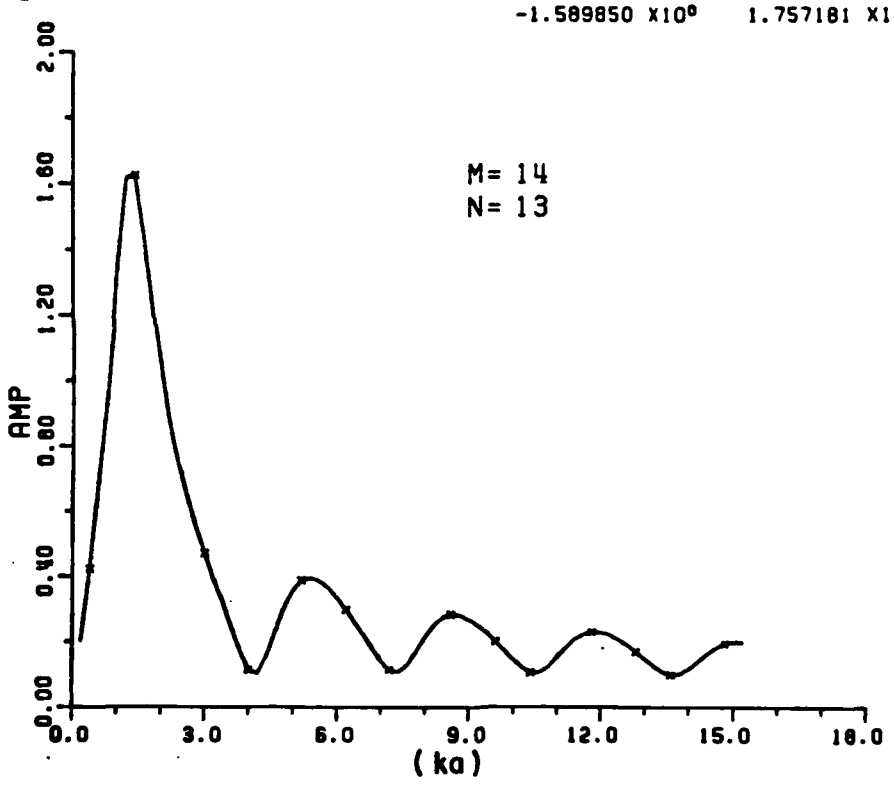

Figure 5-3. The RFA (dashed line) for (M,N) as (14,13) fit to the backscattering calculated data (solid line) for the disc at broadside. The x's are the data points used in the RFA. The last input sample is at ka of 14.8 (amplitude plot).

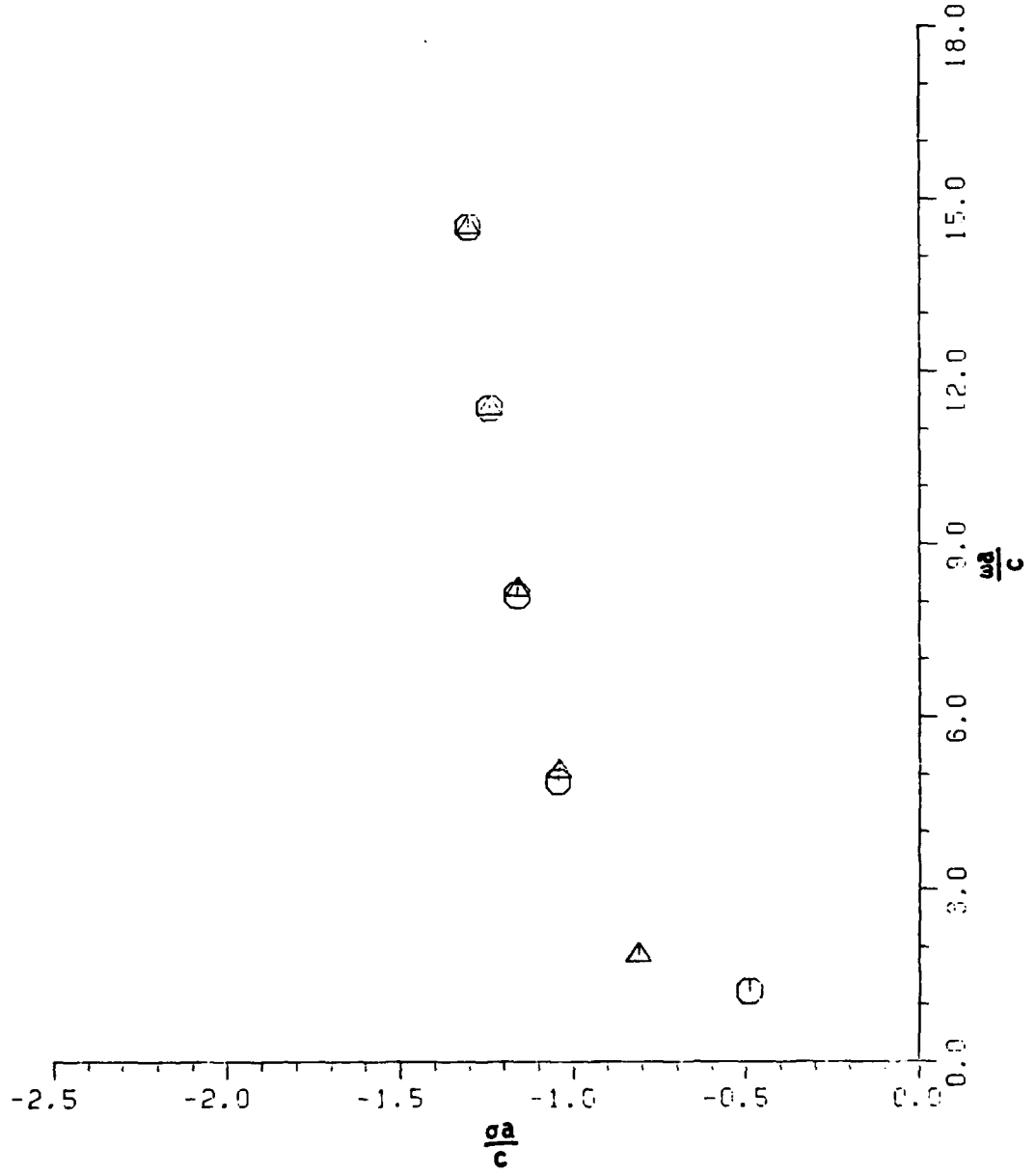

Figure 5-6. A comparison of the poles of a disc extracted using RFA (○) and UTD (Δ) for broadside excitation.

ZEROS		POLES	
real part	imaginary part	real part	imaginary part
-4.588581 X10⁰	9.540524 X10⁰	-5.136516 X10⁰	-9.729803 X10⁰
-4.588586 X10⁰	-9.540520 X10⁰	-5.136525 X10⁰	9.729801 X10⁰
-1.147251 X10⁰	8.001202 X10⁰	6.064494 X10⁻³	4.090105 X10⁰
-1.147256 X10⁰	-8.001204 X10⁰	6.071571 X10⁻³	4.090107 X10⁰
-2.959823 X10⁰	5.158536 X10⁰	-3.006657 X10⁰	-5.328921 X10⁰
6.072063 X10⁻³	-4.090106 X10⁰	-3.006629 X10⁰	5.328900 X10⁰
6.071192 X10⁻³	4.090109 X10⁰	-1.135383 X10⁰	8.119683 X10⁰
-2.959807 X10⁰	-5.158528 X10⁰	-1.135389 X10⁰	-8.119688 X10⁰
-1.045099 X10⁰	4.680569 X10⁰	-1.043285 X10⁰	-4.888601 X10⁰
-1.010567 X10⁰	-1.927570 X10⁰	-1.043308 X10⁰	4.888618 X10⁰
-1.010567 X10⁰	1.927570 X10⁰	-2.209201 X10⁰	-1.656605 X10⁰
-1.045106 X10⁰	-4.680579 X10⁰	-2.209198 X10⁰	1.656607 X10⁰
6.973723 X10⁻¹	0.000000 X10⁰	-1.010578 X10⁰	-1.927627 X10⁰
-1.840615 X10⁰	-1.046664 X10⁰	-1.010577 X10⁰	1.927627 X10⁰
-1.840615 X10⁰	1.046664 X10⁰	-4.917520 X10⁻¹	-1.228591 X10⁰
-3.252002 X10⁰	0.000000 X10⁰	-4.917522 X10⁻¹	1.228591 X10⁰
-1.443699 X10⁻¹	0.000000 X10⁰	6.973706 X10⁻¹	0.000000 X10⁰
		-1.443693 X10⁻¹	0.000000 X10⁰

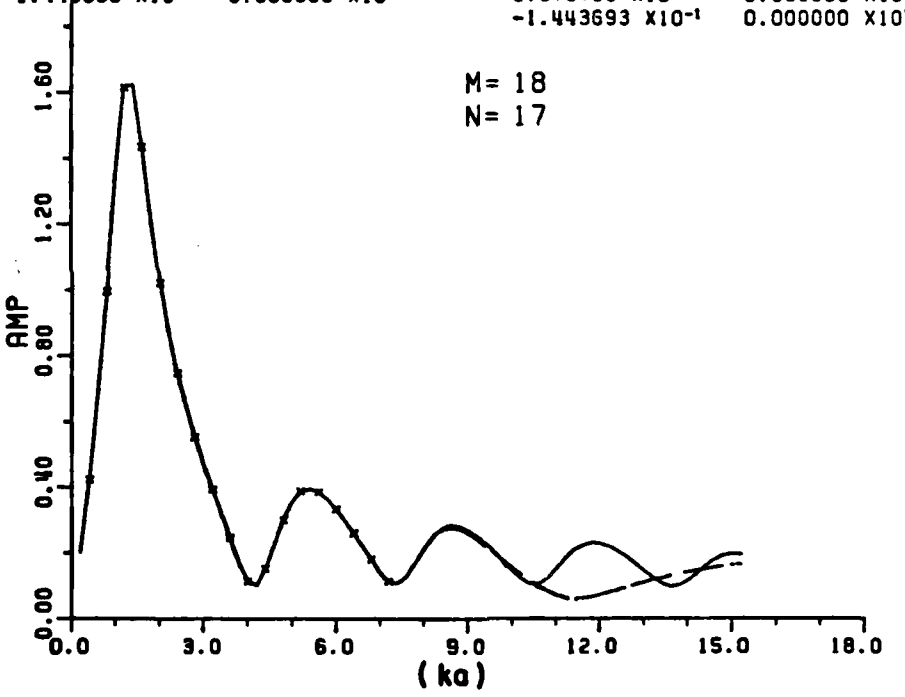

Figure 5-5. The RFA for (M,N) as (18,17) fit to the backscattering data for the disc at broadside. The x's are the data points used. The solid line is the calculated data and the dotted line is the RFA. Note the last input sample of the RFA is at ka of 7.2 (amplitude plot).

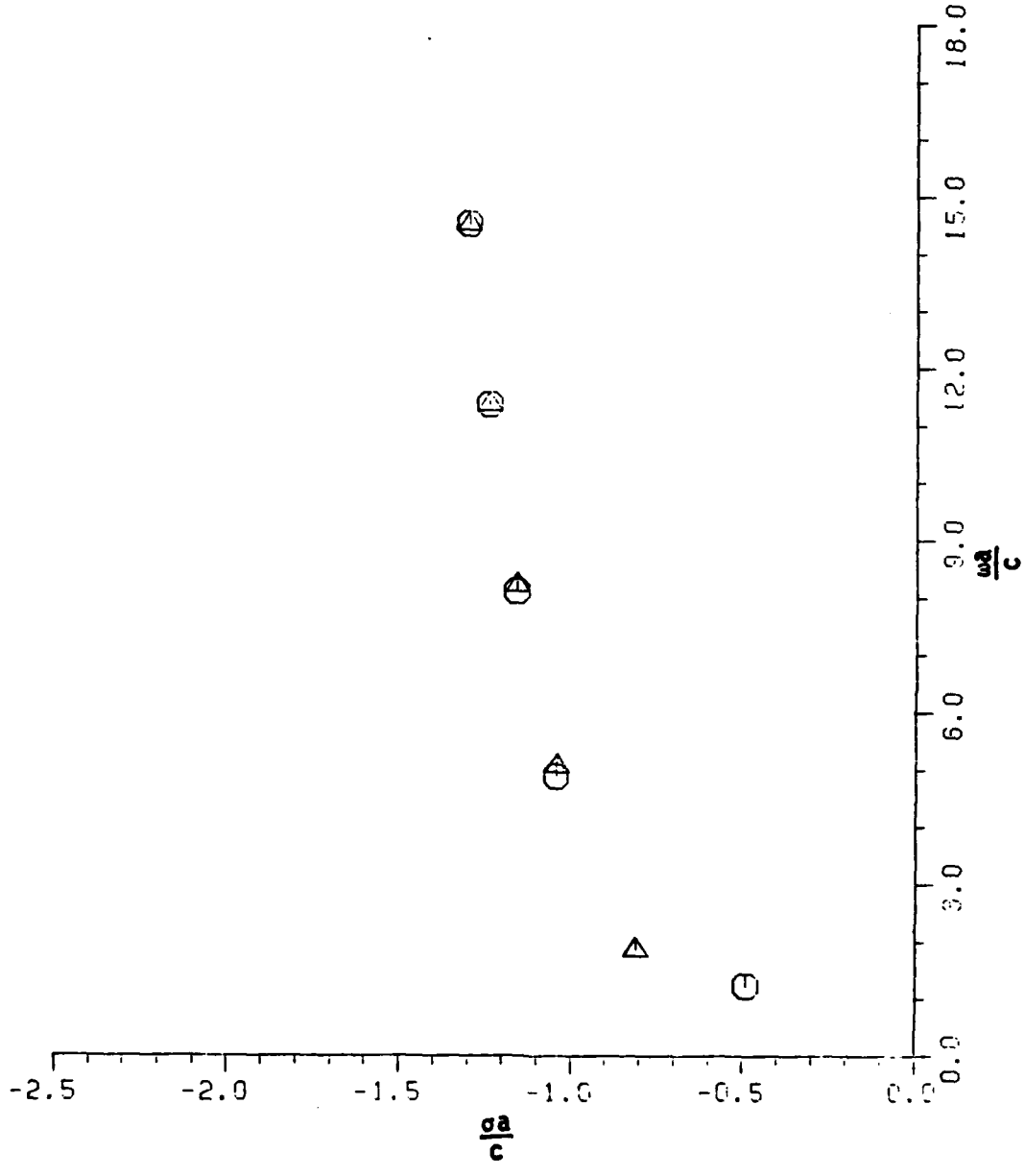

Figure 5-6. A comparison of the poles of a disc extracted using RFA (○) and UTD (△) for broadside excitation.

residues are all shown in the amplitude and phase plots in Figures 5-3 and 5-4. With a system order at M of 14, 7 pole-pairs are extracted. However, only 5 out of these 7 pole-pairs are the true system poles (see the criteria in Chapter III).

The result shown in Figures 5-5 is to extract more poles from a shorter frequency range to see if secondary dominant poles may appear. Unfortunately, the poles of the second layer are too weakly excited to be extracted via RFA using these real frequency data. However, as was discussed in Chapter III, the overdetermined system order does not influence the extraction of the real physical poles. In addition, the UTD [11] and an Equivalent Current approach (EC) [29] can be used to predict the complex natural resonances of the disc at broadside. A detailed description is given in Appendix D. A list of the poles extracted via the RFA and those via the UTD method for the disc at broadside are presented in Table 5-3. Figure 5-6 is a comparison of poles of disc for broadside using RFA and UTD. The poles of string I in Table 5-3 from the RFA are an edge diffraction mode. The one pole pair of the string II in Table 5-3 is the lowest frequency pole of the creeping wave mode. This can be identified because the imaginary part is around ka of 1, i.e., $2\pi a$ of λ. The poles of the disc at broadside from these two methods are very close to each other except for the two lowest frequency pole-pairs. It is known that UTD will not properly

predict low frequency poles because it is an asymptotic high frequency approximation. The oscillatory parts of the poles (string I) occur in increments of around ka of 3 (which is very close to π, i.e., 2a of λ), because the diameter (2a) should be close to (n + 1/2) wavelength at the resonances of the edge diffraction at broadside. A list of the first 26 pole-pairs for the disc at broadside excitation (edge diffraction mode) is shown in Appendix D. Note the first three low frequency pole-pairs come from the rational function approximation to the backscattering calculated data for the disc at broadside. The higher order poles for broadside excitation are obtained using UTD approximation. The UTD Equivalent Currrent Concept (EC) [29] has been used because of the caustic field. A detailed discussion is presented in Appendix D. From the UTD approximation for broadside excitation, it has been shown (see Appendix D) that the equivalent current of more than the second order diffraction (included) forms a geometric series. Obviously, this is the edge diffraction mode. However, the first order diffraction which is dominant and is not included in the geometric series forms the lowest resonant mode of the disc. The first order equivalent current on the rim is shown in Equations (D-2) and (D-3) of Appendix D. Apparently, both the equivalent electric and magnetic currents have only one period of variation on the rim, i.e., $2\pi a$ of λ. Therefore, the imaginary part of the poles (-0.49+/-j1.21) is around one unit of ka, where a is the radius of the disc and k is the wavenumber.

TABLE 5-3

A LIST OF POLE-PAIRS* FOR THE DISC BACKSCATTERING AT BROADSIDE USING THE RFA AND UTD APPROXIMATIONS

	RFA		UTD method
	String I	String II	
1.	-2.22+/-j1.656	-0.49+/-j1.23	
2.	-1.04+/-j4.87		-1.04 +/-j5.0542
3.	-1.16+/-j8.10		-1.1616+/-j8.2116
4.	-1.24+/-j11.28		-1.2418+/-j11.3611
5.	-1.27+/-j14.4		-1.3024+/-j14.5075

* All poles are in units of ka, where a is the radius of disc and k is the wavenumber.

3. Poles of the Disc at Oblique Incidences

Here the RFA is applied to the calculated backscattering data of the disc at θ of (15° (15°) 90°) with $\hat{\phi}$ polarization (electric field parallel to the disc). The angle θ is measured from broadside incidence. The first dominant pole-pair (see Table 5-4) is exactly the same as that obtained at broadside,i.e., 0.49+/-j1.23. However, there are more poles extracted in this string at oblique incidence (instead of only 0.49+/-j1.23 for the broadside excitation). The oscillatory parts of this string have an increment of approximately one ka unit. Obviously, the dominant string of poles (edge diffraction mode) at broadside is not strongly excited for off-broadside incidences. A calculation of the caustic distances for waves multiply diffracted at Q_1, Q_2 (see Figure D-4) is presented in Appendix D. The caustic distance for the N^{th} order diffraction is

$$\rho_N = \frac{-a(1+2N\sin\theta)}{1+2(N+1)\sin\theta} \quad . \qquad (5\text{-}2)$$

Obviously, the caustic distances of each multiple diffraction is not the same at oblique incidences. There is no way to form a geometrical series at angles off-broadside incidence. However, the caustic distances are the same for all diffractions at broadside (theta of 0 degrees). Actually the caustic distances are -a for any order of diffraction at broadside. Therefore, the resonant modes are not the same for broadside and angles off-broadside incidence.

TABLE 5-4

A LIST OF POLES* FOR THE DISC AT ANGLES OFF BROADSIDE INCIDENCE (BACKSCATTER) USING THE RFA AND SENIOR'S CREEPING WAVE AT EDGE-ON INCIDENCE

Rational Function Approximation

θ=15°	θ=30°	
-0.49+/-j1.23	-0.49+/-j1.23	
-0.64+/-j2.33	-0.61+/-j2.32	
-1.38+/-j3.3	-1.39+/-j3.71	
-0.98+/-j4.82	-0.95+/-j4.52	
θ=45°	**θ=60°**	**θ=90°**
-0.492+/-j1.23	-0.49 +/-j1.23	-0.49 +/-j1.23
-0.62 +/-j2.32	-0.687+/-j2.31	-0.614+/-j2.31
-0.66+/-j3.20	-0.71+/-j3.39	-0.688+/-j3.36
-0.67+/-j4.22	-0.74+/-j4.40	-0.763+/-j4.42
	-0.83+/-j5.43	-0.848+/-j5.40
	-1.04+/-j6.43	-0.925+/-j6.42
	-0.92+/-j7.43	-1.08 +/-j7.43
	-0.99+/-j8.50	-1.27 +/-j8.53

Senior's creeping wave mode

θ=90°
-0.506+/-j1.23
-0.603+/-j2.28
-0.675+/-j3.33
-0.733+/-j4.37
-0.78 +/-j5.40
-0.83 +/-j6.43
-0.87 +/-j7.46
-0.90 +/-j8.48
-0.94 +/-j9.50
-0.97 +/-j10.52
.
.
.

* The units of poles are in ka, where k is the wavenumber and a is the radius of the disc.

The creeping wave around the rim of the disc is not an easy problem. Two papers [34,35] which specifically deal with the creeping wave on the rim of the disc can be found in the literature. In this study, the creeping wave formula developed using both the Geometrical Theory of Diffraction (GTD) and measured technique in [34] is used. After some manipulation, the normalized electric field (i.e., the squared root of the normalized Radar Cross Section (RCS), the RCS normalized to the area of the disc) is

$$E_{cw}^{\eta} = 2(1 - \frac{\gamma}{\pi}) \mu^{-1/2} \mu^{-1/3} e^{j^{5\pi/6}} \exp[-\pi\mu + \frac{\pi}{2} \mu^{1/3}] \quad , \qquad (5\text{-}3)$$

where γ is 0.8π (actually a trial value), μ is jka, and a is the radius of the disc (see Appendix E). The complex natural resonances are obtained by imposing a selfconsistent condition on the creeping waves which revolve around the rim of the disc, i.e., after one revolution these fields should exhibit phase coherence with the fields at the starting points. Consequently, the zeros of the following equation (see Appendix E) are the poles of the creeping mode of the disc.

$$e^{\pi \mu^{1/3} - 2\pi\mu} = 1 \quad , \qquad (5\text{-}4)$$

where μ is jka and a is the radius of the disc. A list of the dominant string of poles at angles off broadside incidence extracted from RFA and those extracted via Senior's creeping wave mode [34] are listed in

Table 5-4. The details of the extraction of poles using Senior's creeping wave mode are presented in Appendix E. A comparison of the scattering by the disc at edge-on incidence between Senior's analytical method and Hodge's calculated data is presented in Appendix F.

Table 5-5 is a list of poles using the RFA to the calculated data for the disc at several aspect angles (0°(15°)90°) and two polarizations ($\hat{\theta}$ and $\hat{\phi}$), the natural resonances are indeed independent of the incidence and the field polarization. For angles off-broadside incidence, it is the creeping wave mode which is dominant for resonance. A detailed list of the first 30 pole-pairs of the disc using Senior's creeping wave formula for edge-on excitation is shown in Table 5-6. Figure 5-7 is a plot of the poles of the disc for broadside using RFA to the calculated data, and the poles of creeping wave mode using Senior's analytical method. This set of poles (Figure 5-7) may be used to generate a K-pulse waveform [6] for the backscattering of the disc.

4. Andrejewski's Magnetic Near Field Data of the Disc Backscattering at Broadside

In Andrejewski's dissertation [30], fourteen normalized scattered magnetic field data points for the disc backscattering at broadside were plotted in the complex plane. Here, the normalized magnetic scattering data at these 14 points are reproduced at ka of 0.5(0.5),4. and ka of 4.(1.),10. Details of the calculation are shown in Appendix G. These data are shown fitted with a RFA in Figure 5-8. The extracted

TABLE 5-5

A LIST OF POLES* FOR THE DISC USING THE RFA TO THE CALCULATED DATA FOR DIFFERENT ASPECT ANGLES AND POLARIZATIONS. THE RFA ARE FITTED TO ka of 0.2 to 6 (30 SAMPLES)

	Rational Function Approximation poles			
$\hat{\phi}$ Polarization	P1	P2	P3	P4
0.	-0.49+/-J1.23	-1.04+/-J4.87	-1.16+/-J8.10	-1.24+/-J11.28
15.	-0.49+/-J1.23	-0.64+/-J2.33	-1.38+/-J3.30	-0.98+/-J4.82
30.	-0.49+/-J1.23	-0.61+/-J2.32	-1.39+/-J3.71	-0.95+/-J4.52
45.	-0.49+/-J1.23	-0.62+/-J2.32	-0.67+/-J3.40	-0.75+/-J4.30
60.	-0.49+/-J1.23	-0.63+/-J2.30	-0.97+/-J3.80	
75.	-0.49+/-J1.25	-0.61+/-2.33	-0.73+/-J3.35	-0.67+/-J4.50
90.	-0.49+/-J1.23	-0.60+/-J2.31	-0.74+/-J3.42	-0.65+/-J4.28
$\hat{\theta}$ Polarization				
15.	-0.49+/-J1.22	-0.64+/-J2.27	-1.08+/-J3.30	-0.82+/-J5.02
30.	-0.49+/-J1.23	-0.62+/-J2.33	-1.23+/-J3.52	-0.94+/-J4.57
45.	-0.49+/-J1.23	-0.64+/-J2.34	-0.87+/-J2.90	-0.86+/-J4.80
60.	-0.49+/-J1.23	-0.62+/-J2.32	-0.65+/-J3.21	-1.52+/-J5.40
75.	-0.49+/-J1.23	-0.63+/-J2.32	-0.64+/-J3.24	-1.26+/-J5.80

* The units of poles are in ka, where a is the radius of the disc and k is the wavenumber.

TABLE 5-6

POLES* OF DISC USING SENIOR'S CREEPING WAVE MODE

n	Poles
1.	(-0.5057350,±1.208781)
2.	(-0.6030402,±2.282039)
3.	(-0.6746498,±3.331739)
4.	(-0.7328901,±4.370643)
5.	(-0.7826892,±5.403155)
6.	(-0.8265909,±6.431364)
7.	(-0.8660754,±7.456467)
8.	(-0.9021299,±8.479179)
9.	(-0.9354153,±9.499999)
10.	(-0.9664097,±10.51928)
11.	(-0.9954736,±11.53727)
12.	(-1.022884,±12.55416)
13.	(-1.048859,±13.57012)
14.	(-1.073574,±14.58525)
15.	(-1.097172,±15.59966)
16.	(-1.119781,±16.61343)
17.	(-1.141471,±17.62662)
18.	(-1.162356,±18.63929)
19.	(-1.182501,±19.65149)
20.	(-1.201968,±20.66326)
21.	(-1.220811,±21.67463)
22.	(-1.239077,±22.68564)
23.	(-1.256811,±23.69632)
24.	(-1.274049,±24.70668)
25.	(-1.290820,±25.71675)
26.	(-1.307164,±26.72656)
27.	(-1.323088,±27.73611)
28.	(-1.338675,±28.74543)
29.	(-1.353844,±29.75452)
30.	(-1.368698,±30.76340)

* Units of ka, where a is the radius of the disc.

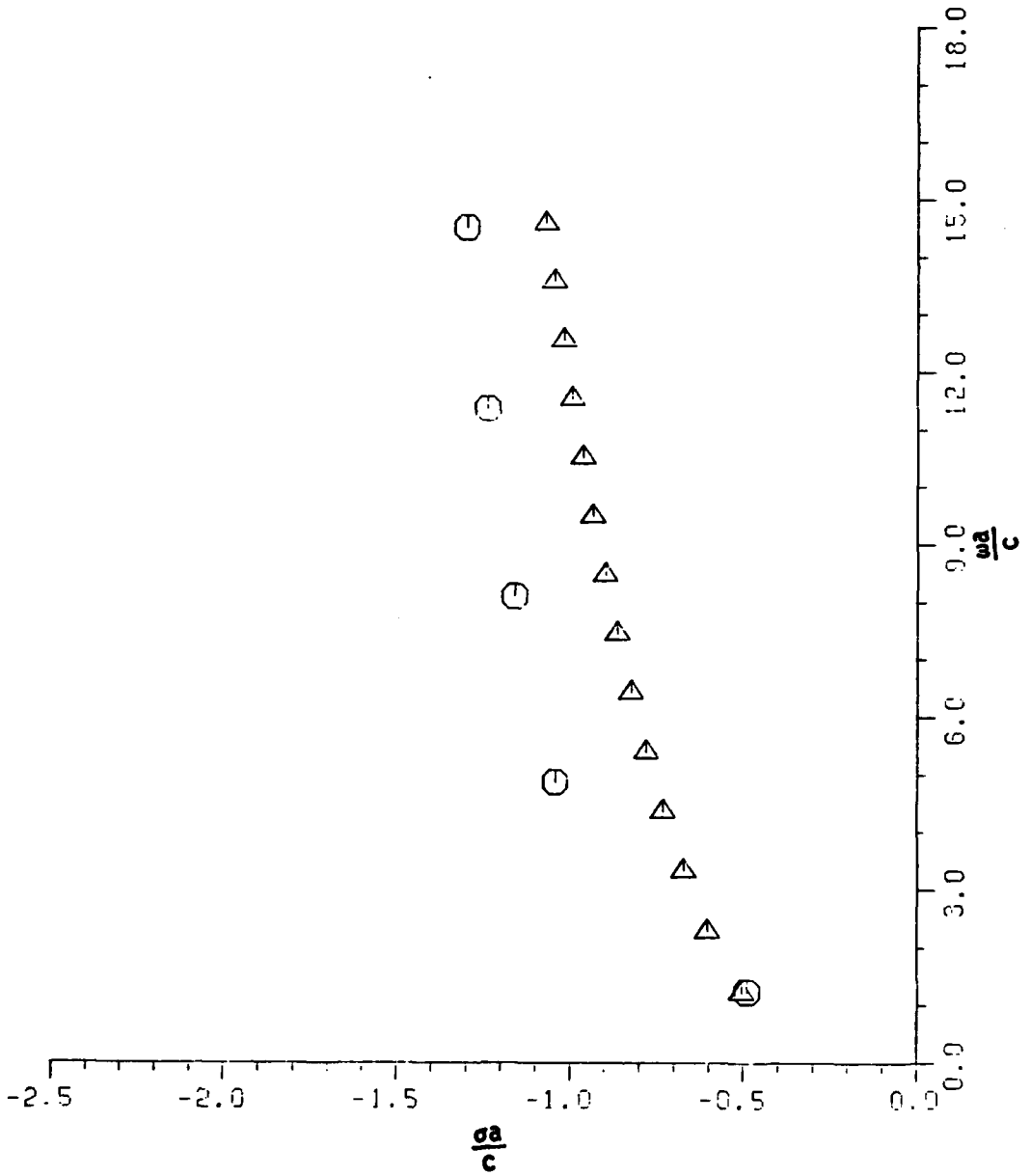

Figure 5-7. The complex natural resonances of the disc for broadside (○) and edge-on (△) incidences.

ZEROS		POLES	
real part	imaginary part	real part	imaginary part
2.891695 X10^{0}	-9.270621 X10^{0}	-1.377459 X10^{0}	8.142751 X10^{0}
-1.567997 X10^{0}	8.248971 X10^{0}	-1.377460 X10^{0}	-8.142750 X10^{0}
2.891695 X10^{0}	9.270620 X10^{0}	1.636559 X10^{-1}	3.654007 X10^{0}
-1.567997 X10^{0}	-8.248970 X10^{0}	1.636552 X10^{-1}	-3.654007 X10^{0}
1.656605 X10^{-1}	3.658574 X10^{0}	-9.978924 X10^{-1}	4.624791 X10^{0}
-8.031586 X10^{-1}	-4.618158 X10^{0}	-9.978915 X10^{-1}	-4.624790 X10^{0}
-8.031594 X10^{-1}	4.618159 X10^{0}	2.872097 X10^{0}	9.213258 X10^{0}
1.656599 X10^{-1}	-3.658573 X10^{0}	2.872098 X10^{0}	-9.213258 X10^{0}
-4.460859 X10^{-1}	1.821242 X10^{0}	-4.655014 X10^{-1}	-1.841690 X10^{0}
-9.592589 X10^{-1}	-1.450546 X10^{0}	-4.655015 X10^{-1}	1.841690 X10^{0}
-9.592589 X10^{-1}	1.450546 X10^{0}	-5.474505 X10^{-1}	1.190756 X10^{0}
-4.460861 X10^{-1}	-1.821242 X10^{0}	-5.474505 X10^{-1}	-1.190756 X10^{0}
5.666817 X10^{-1}	0.000000 X10^{0}	7.992367 X10^{-9}	1.023446 X10^{-1}
		7.992368 X10^{-9}	-1.023446 X10^{-1}

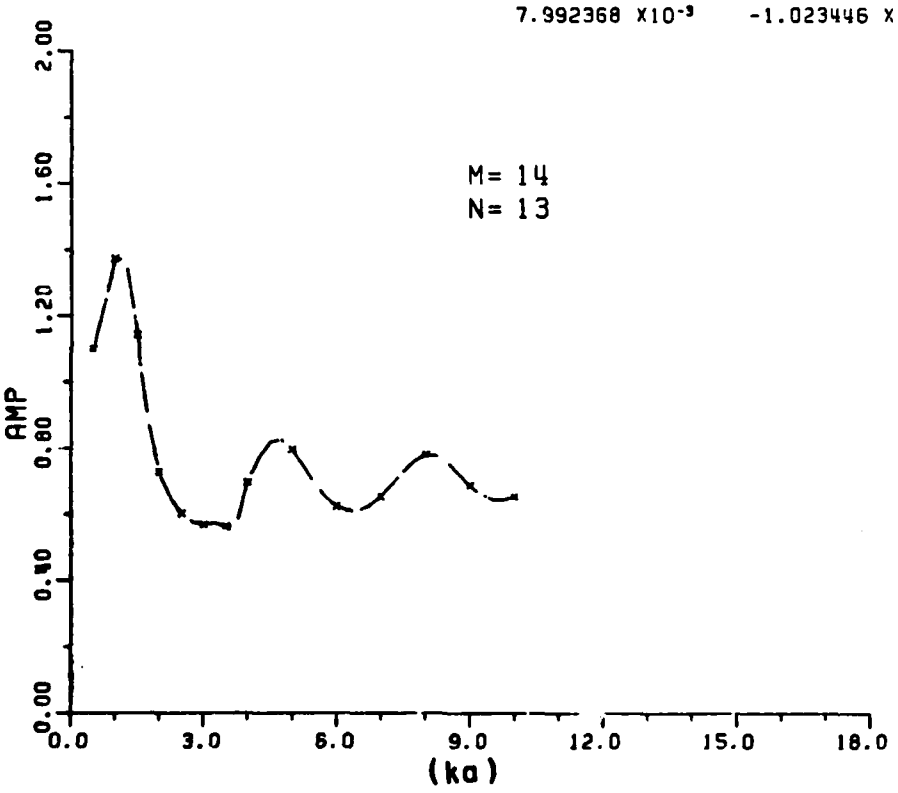

Figure 5-8. The RFA (dashed line) fit to Andrejewski's data (magnetic near field denoted by the x's) for the disc at broadside. The x's are data points used, and the dashed line is the RFA (amplitude plot).

poles are listed in Table 5-7. The resultant poles are very close to those obtained from the RFA to Hodge's data for the disc (electric field), also given in Table 5-7 and plotted in Figure 5-9. The great discrepancy of the third pole-pairs is due to the truncation in Andrejewski's data at ka of 10. The extracted complex natural resonances, are accurate using the RFA both for electric far field or magnetic near field.

5. Summary

Two strings of poles for backscattering from discs have been found. One is the resonant mode due to the multiple diffraction at the edges (rim) of the disc, the other is the creeping wave mode formed by the wave creeping around the circumference of the disc. For broadside incidence, the dominant string of poles is the edge diffraction mode. Simultaneously, the creeping wave mode also exists. However, only the first pole-pair of the creeping wave mode can be extracted by RFA at broadside incidence. A detailed discussion is presented in Appendix D. The extracted poles are independent of the angle of incidence and polarization (see Table 5-5). This conclusion comes from applying the RFA to the calculated data for the disc at angles off broadside excitation.

TABLE 5-7

A COMPARISON OF THE COMPLEX NATURAL RESONANCES* FOR A DISC USING RFA TO HODGE'S DATA AND ANDREJEWSKI'S DATA (BACKSCATTERING FOR BROADSIDE)

RFA to Hodge's Data (Electric Far Field)	RFA to Andrejewski's Data (Magnetic Near Field)
-0.49+/-J1.23	-0.547+/-j1.19
-1.04+/-j4.87	-0.998+/-j4.62
-1.16+/-j8.10	-1.38 +/-j8.14
-1.24+/-j11.28	data up to ka=10.
-1.27+/-j14.4	
data up to ka=15.2	

* The units of the poles are in ka, where k is the wavenumber and a is the disc radius.

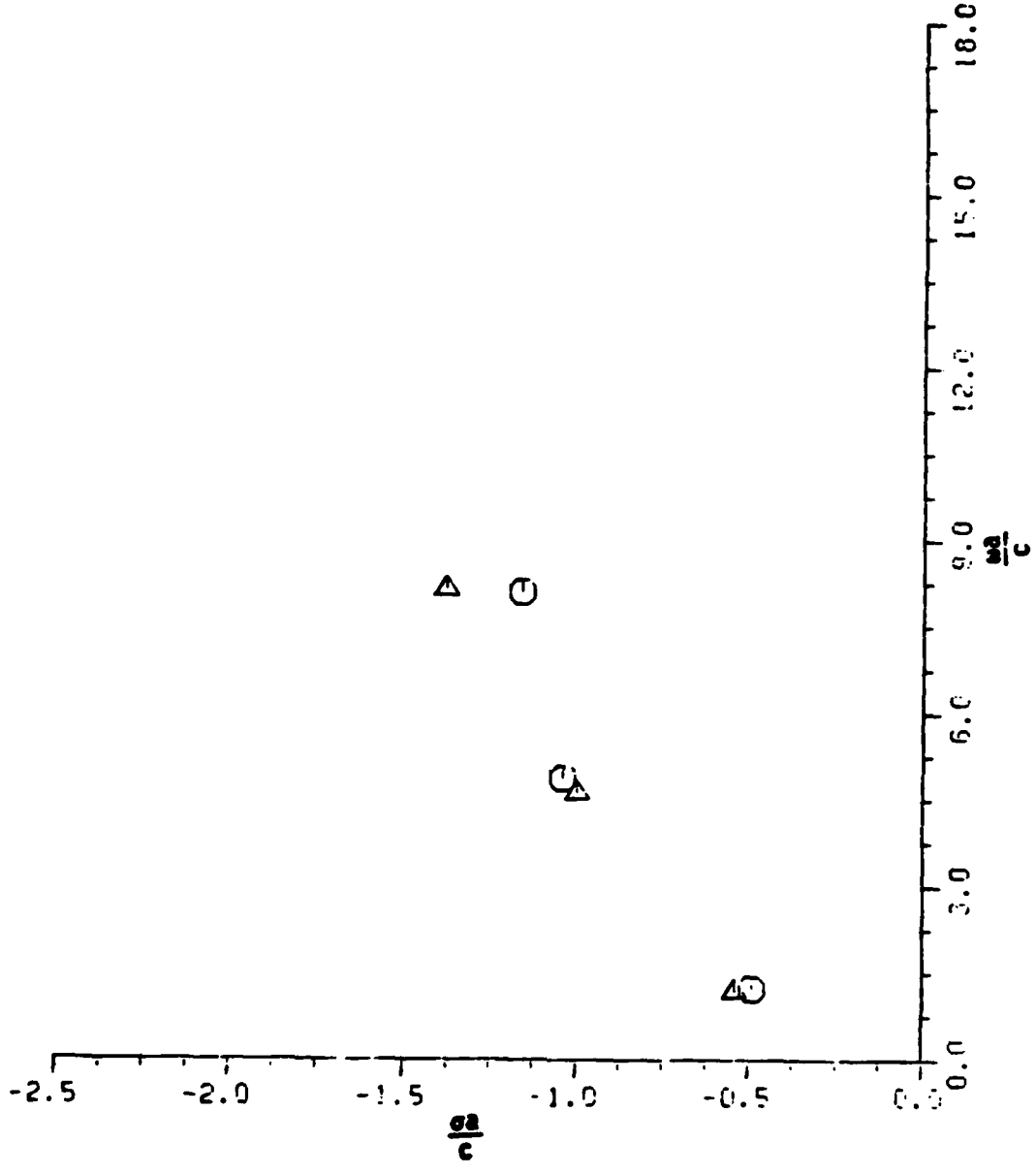

Figure 5-9. A comparison of the first 3 pairs of poles of the disc for broadside using RFA to Hodge's calculated data (⊙) and Andrejewski's data (Δ). Note third pole-pairs using Andrejewski's data is not very close to those using Hodge's data, because Andrejewski's data is truncated at ka of 10.

D. WIRE SCATTERERS

1. Introduction

The electromagnetic resonances of thin wire scatterers have been studied for a long time [15]. Kennaugh solved the problem using a signal-flow-graph method [10]. The results were compared with those from an impedance method by Richmond* with excellent agreement. Since the poles of the thin wire scatterers are well known and they may be the basic building elements for more complex targets, it is wise to apply the rational function approximations to the thin wire scatterers and compare the results with the known poles.

2. Data Sets For Thin Wire and Thick Wire

Computed values of backscattering (and bistatic scattering as well as induced current distributions) for thin wire and thick wire** were made in 1964, using a program developed by J. Richmond, for L/λ from 0.1 to 1.4 at the increment of 0.1 (14 data points) for plane wave incidences at broadside and 30° from end-on. (L is the wire length and D is the wire diameter.) These sets of phasor signals were fitted with RFA using system orders for (M,N) as (12,11) , i.e., 12 out of the 14 data points were used in the approximations. The selection of the data

---

* J.H. Richmond,"Digital computer solutions of the rigious equations for scattering problems", IEEE, v. 57, pp. 796-804, August 1965.

** The wire length (L) to wire diameter (D) ratio are 20 and 2000 for thick wire and thin wire respectively.

points is very arbitrary; however, the set of data points which can yield a smooth interpolation is used because there are some errors in the data sets. These errors may be due to numerical calculation or imperfect modelling. The amplitude plots of the fits to the thin wire scatterers are shown in Figures 5-10 to 5-13 for both broadside and 30° from end-on incidence. Fifty data points are reproduced in Figure 5-10 to 5-13 using the coefficients of the RFA fitted to the 14 samples of the wire scatterers in each case. These are good examples of using the RFA for complex data interpolation as well as pole extraction. The pole-pairs extracted via the RFA and those extracted via other methods are listed in Table 5-8. As is well known, at broadside incidence only even modes are excited. However, for 30° off broadside, both even and odd modes are excited.

E. CIRCULAR LOOP

1. Introduction

Complex natural resonances of a circular metallic loop are extracted using a space-frequency integral equation and numerical computation. Then, the backscattering data for the loop were generated for broadside incidence (ka of 0.2(0.2)10.) and for edge-on incidence (ka of 0.2(0.04)5.2). Using these sets of data, poles were extracted by applying the RFA to the calculated data and the results are compared with those obtained from the integral equation formulation.

TABLE 5-8

A LIST OF POLES FOR A THIN-WIRE AND A THICK-WIRE EXTRACTED USING RFA, INTEGRAL EQUATION AND NUMERICAL SEARCH AND SIGNAL-FLOW GRAPHS FOR BROADSIDE AND 30° OFF END-ON EXCITATION (BACKSCATTER)

	Poles*	
Richmond L/D=2000	Rational Function Approximants L/D=2000 Broadside	Theta=30°
-0.0128+/-J0.2398	-0.0128+/-J0.239	-0.0128+/-J0.2399
-0.0175+/-J0.4881		-0.0174+/-J0.4884
-0.0208+/-J0.7366	-0.018+/-J0.743	-0.01998+/-J0.735
-0.0234+/-J0.9854		
-0.0255+/-J1.2344		
-0.0273+/-J1.4835		
		-0.48588+/-J0.2825
Signal Flow Graphs L/D=2000 (Bagby and Kennaugh)		
-0.0123+/-j0.2389		
-0.0172+/-j0.4872		
-0.0204+/-j0.7360		
-0.0229+/-j0.9850		
-0.0249+/-j1.2341		
-0.0266+/-j1.4834		
	Rational Function Approximants L/D=20 Broadside	Theta=30°.
	-0.03086+/-J0.2149	-0.03015+/-J0.21495
		-0.04958+/-J0.4469
	-0.052128+/-J0.677	-0.05349+/-J0.6887

* L is the wire length, D is the wire diameter, and a is $\frac{L}{4\pi}$; the units of the poles are in ka, where k is the wavenumber.

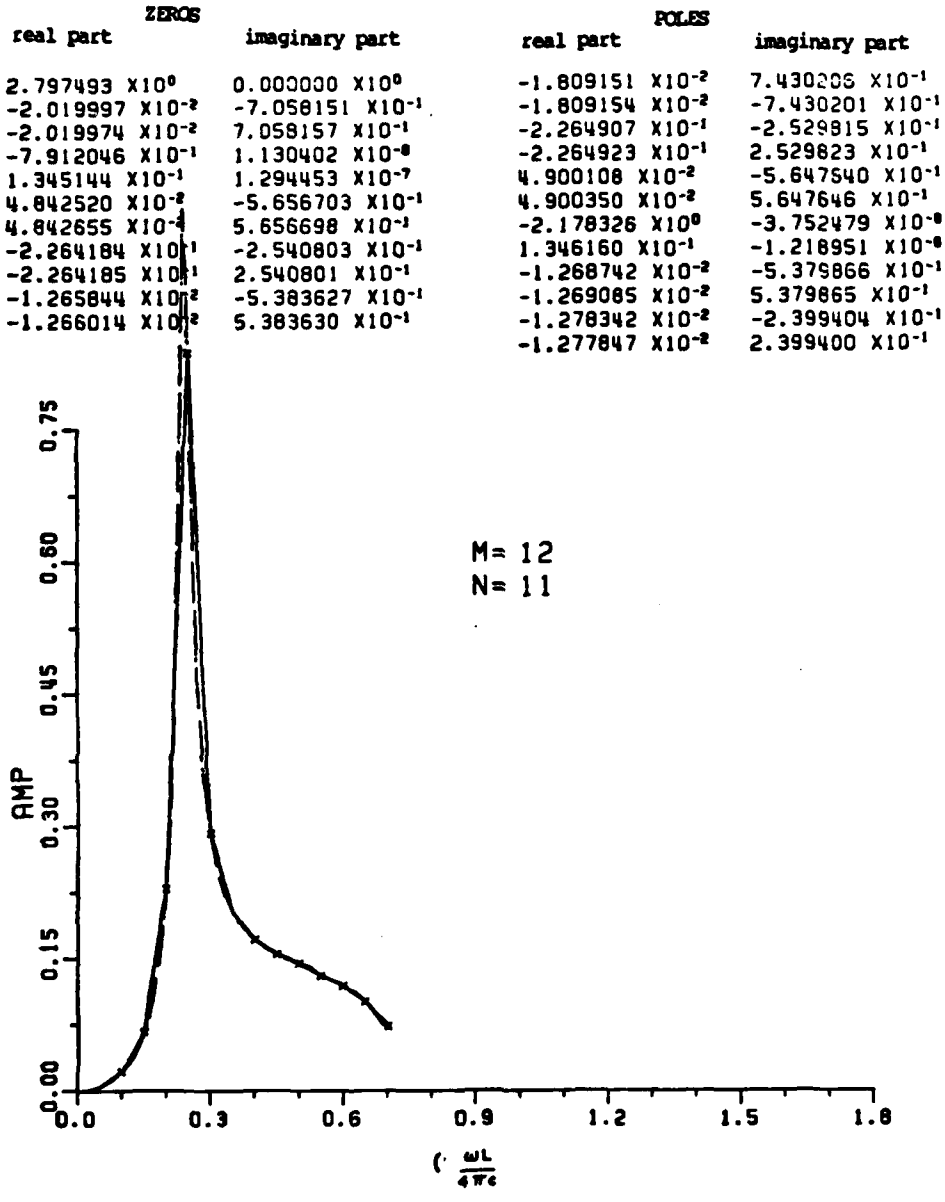

Figure 5-10. The RFA for (M,N) as (12,11) fit to the backscattering data for the thin-wire with a wire length-to-wire diameter ratio of 2000 at broadside excitation. The x's are the data points used in RFA. The dashed line is the rational function approximation (amplitude plot).

ZEROS		POLES	
real part	imaginary part	real part	imaginary part
-2.546238 X10^{-1}	-6.539576 X10^{-1}	-1.998074 X10^{-2}	-7.350499 X10^{-1}
-9.533646 X10^{0}	-3.646274 X10^{-8}	-1.998077 X10^{-2}	7.350500 X10^{-1}
-2.546237 X10^{-1}	6.539577 X10^{-1}	-4.858857 X10^{-1}	-2.825011 X10^{-1}
2.111327 X10^{-1}	-6.525048 X10^{-1}	-4.858856 X10^{-1}	2.825012 X10^{-1}
2.111327 X10^{-1}	6.525049 X10^{-1}	-1.743243 X10^{-2}	-4.883759 X10^{-1}
-2.025455 X10^{-1}	-3.511854 X10^{-1}	-1.743243 X10^{-2}	4.883759 X10^{-1}
-2.025456 X10^{-1}	3.511855 X10^{-1}	2.984970 X10^{-1}	-1.605218 X10^{-8}
3.379026 X10^{-1}	1.344978 X10^{-8}	7.617970 X10^{-2}	0.000000 X10^{0}
7.571635 X10^{-2}	-2.210319 X10^{-8}	-1.277893 X10^{-2}	-2.399448 X10^{-1}
1.715105 X10^{-1}	-3.619670 X10^{-1}	-1.277893 X10^{-2}	2.399449 X10^{-1}
1.715105 X10^{-1}	3.619670 X10^{-1}	4.003515 X10^{-1}	-3.509493 X10^{-1}
		4.003515 X10^{-1}	3.509493 X10^{-1}

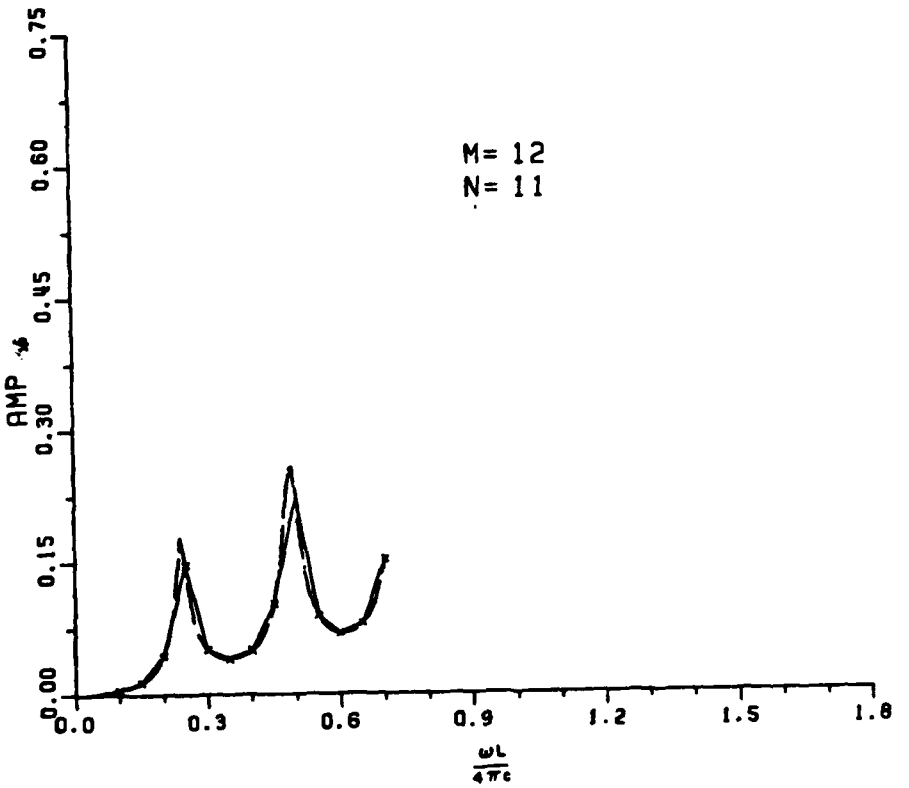

Figure 5-11. The RFA for (M,N) as (12,11) applied to the backscattering data for the thin-wire with a wire length-to-wire diameter ratio of 2000 at 30° from end-on incidence. The x's are the data points used in RFA. The dashed line is the RFA (amplitude plot).

ZEROS		POLES	
real part	imaginary part	real part	imaginary part
-5.116426 X10^{-2}	-6.485783 X10^{-1}	-5.212809 X10^{-2}	6.766320 X10^{-1}
-9.013577 X10^{-1}	0.000000 X10^{0}	-5.212819 X10^{-2}	-6.766923 X10^{-1}
-5.116372 X10^{-2}	6.485785 X10^{-1}	2.499298 X10^{-3}	-6.060710 X10^{-1}
2.341402 X10^{-3}	-6.060614 X10^{-1}	2.498520 X10^{-3}	6.060717 X10^{-1}
2.340881 X10^{-3}	6.060612 X10^{-1}	6.291840 X10^{-2}	4.658803 X10^{-5}
6.967597 X10^{-2}	-1.418668 X10^{-7}	-2.378055 X10^{-2}	-5.614741 X10^{-5}
-2.588707 X10^{-2}	1.967807 X10^{-7}	4.086252 X10^{-4}	-3.625245 X10^{-1}
3.569557 X10^{-4}	-3.625974 X10^{-1}	4.136693 X10^{-4}	3.625232 X10^{-1}
3.569557 X10^{-4}	3.625974 X10^{-1}	3.880811 X10^{-3}	-1.396824 X10^{-1}
3.929780 X10^{-3}	-1.381514 X10^{-1}	3.839670 X10^{-3}	1.396930 X10^{-1}
3.929780 X10^{-3}	1.381514 X10^{-1}	-3.086281 X10^{-2}	-2.148990 X10^{-1}
		-3.086281 X10^{-2}	2.148990 X10^{-1}

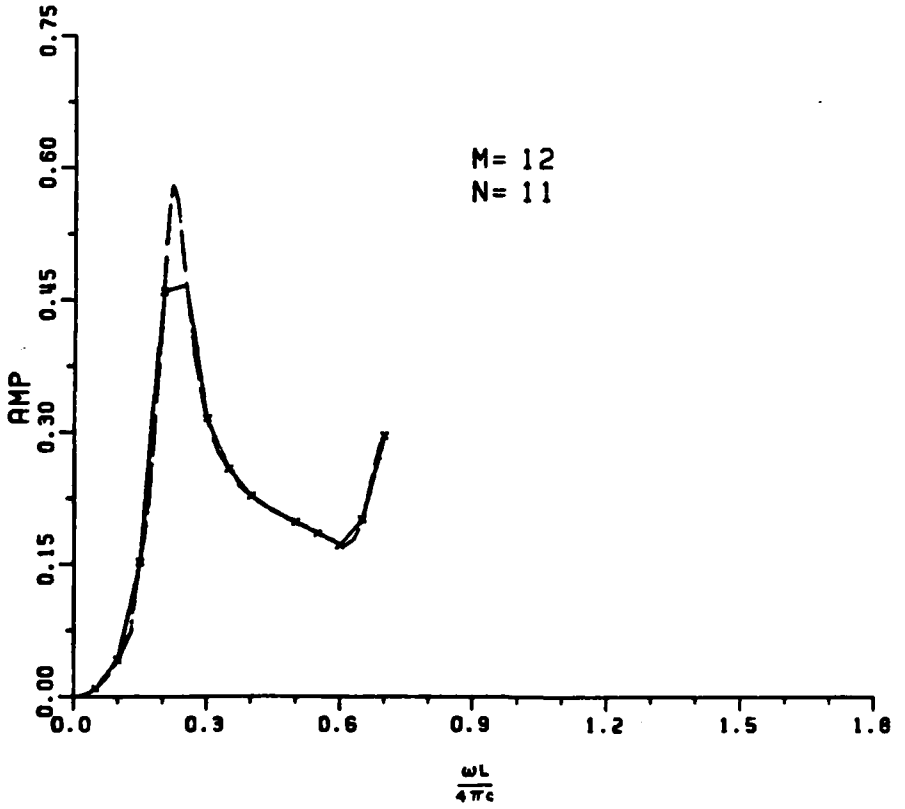

Figure 5-12. The RFA for (M,N) as (12,11) applied to the backscattering data for the thick-wire with a wire length (L)-to-wire diameter (D) ratio of 20 for broadside excitation. The x's are the data points used in RFA. The dashed line is the RFA (amplitude plot). The peak in the amplitude of the first resonance can be seen in the RFA, because more data points (50) are reproduced using the coefficients of the RFA.

ZEROS		POLES	
real part	imaginary part	real part	imaginary part
3.071277 X10^{-1}	-7.692284 X10^{-1}	-5.349543 X10^{-2}	6.886654 X10^{-1}
-2.350138 X10^{-1}	3.546965 X10^{-1}	-5.349545 X10^{-2}	-6.886654 X10^{-1}
3.071278 X10^{-1}	7.692285 X10^{-1}	-1.854181 X10^{-1}	0.000000 X10^{0}
-2.350139 X10^{-1}	-3.546966 X10^{-1}	2.253988 X10^{-1}	-2.921569 X10^{-8}
5.090303 X10^{-9}	1.412906 X10^{-1}	5.561443 X10^{-2}	-4.874077 X10^{-1}
6.131346 X10^{-2}	-4.964998 X10^{-1}	5.561443 X10^{-2}	4.874077 X10^{-1}
6.131326 X10^{-2}	4.964998 X10^{-1}	-4.957892 X10^{-2}	-4.469082 X10^{-1}
5.090288 X10^{-9}	-1.412905 X10^{-1}	-4.957892 X10^{-2}	4.469083 X10^{-1}
-2.970992 X10^{-1}	2.042244 X10^{-8}	5.332153 X10^{-9}	-1.429911 X10^{-1}
1.822763 X10^{-1}	-3.731297 X10^{-1}	5.332153 X10^{-9}	1.429911 X10^{-1}
1.822763 X10^{-1}	3.731297 X10^{-1}	-3.014495 X10^{-2}	-2.149508 X10^{-1}
		-3.014495 X10^{-2}	2.149509 X10^{-1}

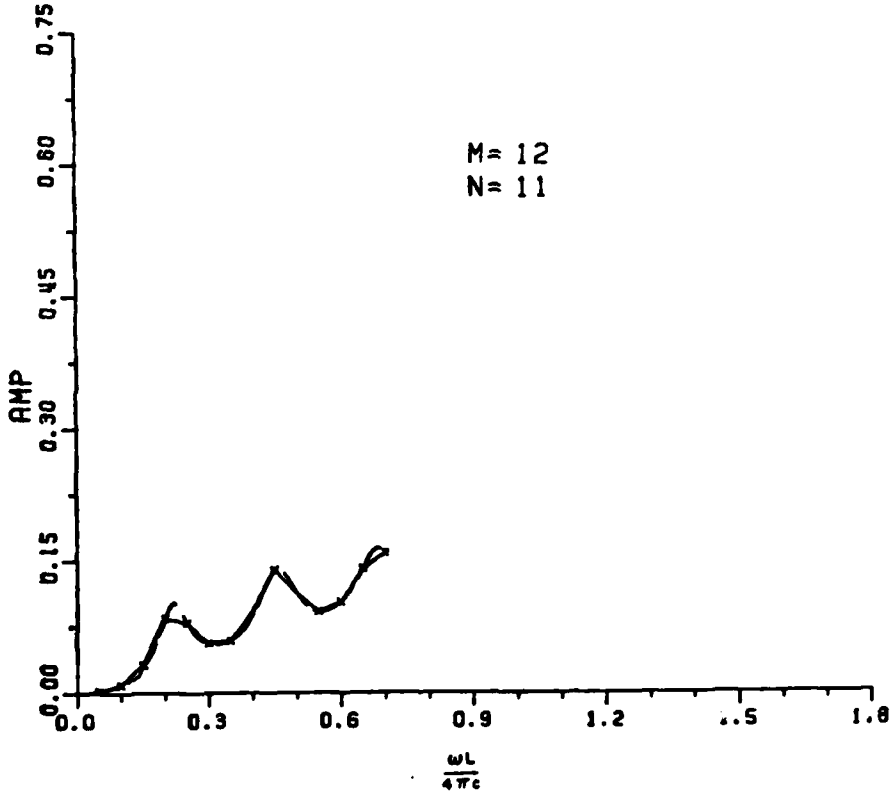

Figure 5-13. The RFA for (M,N) as (12,11) applied to the backscattering data for the thick-wire for a wire-length (L) to wire diameter (D) ratio of 20 at 30° from end-on incidence. The x's are the data points used in RFA. The dashed line is the RFA (amplitude plot).

2. Integral Equation and Numerical Search

Because of the rotational symmetry of the circular loop (Figure 5-14), the induced currents $I(\phi)$ can be expressed in terms of $I_n e^{jn\phi}$, where I_n are constants. Using Harrington's* impedance matrix formulation for the circular loop

$$Z_{mn} = 0 \quad (m \neq n) \quad , \tag{5-5}$$

and

$$Z_{nn} = j\pi nkb \left[\frac{1}{2} K_{n-1} + \frac{1}{2} K_{n+1} - \left(\frac{n}{kb}\right)^2 K_n\right] \quad , \tag{5-6}$$

where

$$K_n = \frac{1}{2\pi} \int_0^{2\pi} \frac{e^{-jkb\sqrt{4\sin^2 \frac{\phi}{2} + \left(\frac{a}{b}\right)^2}}}{\left[4\sin^2 \frac{\phi}{2} + \left(\frac{a}{b}\right)^2\right]^{\frac{1}{2}}} e^{-jn\phi} \, d\phi \quad . \tag{5-7}$$

A program was written to find the zeros of Znn in Equation (5-6) using Muller's method of iteration and Simpson's rule of integration. All poles found with this program are consistent with those found in [22]. Table 5-9 is a list of poles of the first layer** at different wire to loop ratios. A plot of those poles (Table 5-9) is shown in

---

* R.F. Harrington, Field Computation by Moment Method, New York, Macmillan, 1968.

** The classification of Layers are shown in Figure 5-17.

TABLE 5-9

A LIST OF POLES* (LAYER I) OF LOOPS AT THREE DIFFERENT WIRE TO LOOP RADIUS RATIOS. THE INTEGRAL EQUATION AND NUMERICAL SEARCH IS USED TO FIND THE POLES.

	Poles		
a/b	(.5E-3) x π	(2.E-3) x π	(1.E-3) x π
	-.109 +/-J1.0485	-0.086 +/-J1.04	-0.073317+/-J1.03822
	-.164 +/-J2.066	-0.125 +/-J2.058	-0.10591 +/-J2.05176
	-.2085 +/-J3.079	-0.1562+/-J3.068	-0.130826+/-J3.06151
	-.248 +/-J4.085	-0.1825+/-J4.078	-0.151932+/-J4.06949
	-.2845 +/-J5.095	-0.2068+/-J5.06	-0.17066 +/-J5.0764
	-.3185 +/-J6.11	-0.2288+/-J6.09	-0.187729+/-J6.0826

* The units of the poles are in kb, where k is the wavenumber and b is the loop radius. (π is 3.14159 and a is the wire radius.)

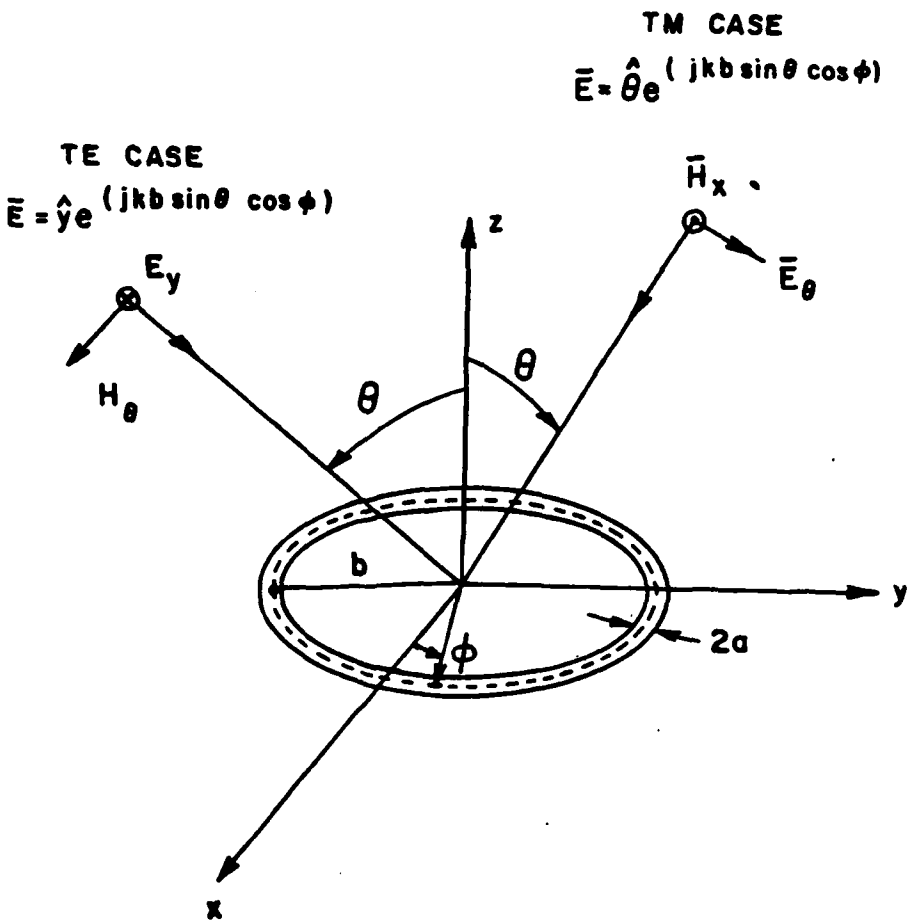

Figure 5-14. The coordinate system for a circular metallic loop.

Figure 5-15. Figure 5-16 is a plot of poles for wire radius to the loop radius ratio of 3.14159E-3.

The numbers shown with the locations of poles in Figure 5-17 are n's of Znn. The poles in Figure 5-17 are divided into layers. Table 5-10 is a list of poles for the circular loop via integral equation and numerical search at wire radius to the loop radius ratio of 3.14159E-3. Figure 5-18 is a plot of all poles showing constant n results in Znn. From the result of applying RFA to the backscattering data for the loop, it will be seen that layer I poles are found at edge-on incidence and layer II poles are found at broadside (also the first one of layer I). Layer III poles are not found using RFA approach either at broadside or at edge-on incidence. However, this does not mean that they are not there.

3. Rational Function Approximation

The backscatter of the loop for broadside and edge-on (TE case) incidence (Figures 5-19 and 5-20) were calculated using Kouyoumjian's equations in his report*. The backscatter of both broadside and edge-on incidence are shown in Figures 5-19 and 5-20 individually.

The variational method has been used to determine the radar cross section (RCS) of a perfectly-conducting, thin, circular loop by R.G.

---

* R.G. Kouyoumjian, "The Backscattering from a circular loop (antenna)," Bulletin No. 162, The Ohio State University, The Engineering Experiment Station, November 1956.

TABLE 5-10

A LIST OF POLES* OF A LOOP (a/b** of 3.14159E-3) EXTRACTED USING INTEGRAL EQUATION AND NUMERICAL SEARCH

Poles		
layer 1	layer 3	layer 2
		-0.073317+/-J1.03822
-0. +/-J0.	-1.48611 +/-J0.	-1.47916 +/-J1.54327
-0.073317+/-J1.03822	-1.47916 +/-J1.54327	-1.25879 +/-J5.0763
-0.105910+/-J2.05177	-1.6727 +/-J2.76692	-1.31026 +/-J8.3208
-0.130827+/-J3.06151	-1.82195 +/-J3.90846	-1.34771 +/-J11.5139
-0.15193 +/-J4.06950	-1.9425 +/-J5.01545	
-0.170661+/-J5.0769	-2.048715+/-J6.10285	
-0.187729+/-J6.0826		
-0.203555+/-J7.0883	layer 4	
	-2.15481+/-J0.	
	-2.70814+/-J1.0550	
	-3.12022+/-J2.05139	
	-3.45635+/-J3.02946	
	-3.74378+/-J3.99996	
	-3.99684+/-J4.96701	
	layer 5	
	-3.50331+/-J0.	
	-4.10168+/-J0.97958	
	-4.59325+/-J1.93514	
	-5.0157 +/-J2.88079	
	layer 6	
	-4.84712+/-J0.	
	-5.4633 +/-J0.94868	
	-5.9950 +/-J1.88392	
	-6.4665 +/-J2.81279	
	-6.8921 +/-J3.73865	
	layer 7	
	-6.1859+/-J0.	
	-6.817 +/-J0.93148	
	-7.3681+/-J1.85427	

* The units of the poles are in kb, where k is the wavenumber and b is the loop radius.

** a is the wire radius.

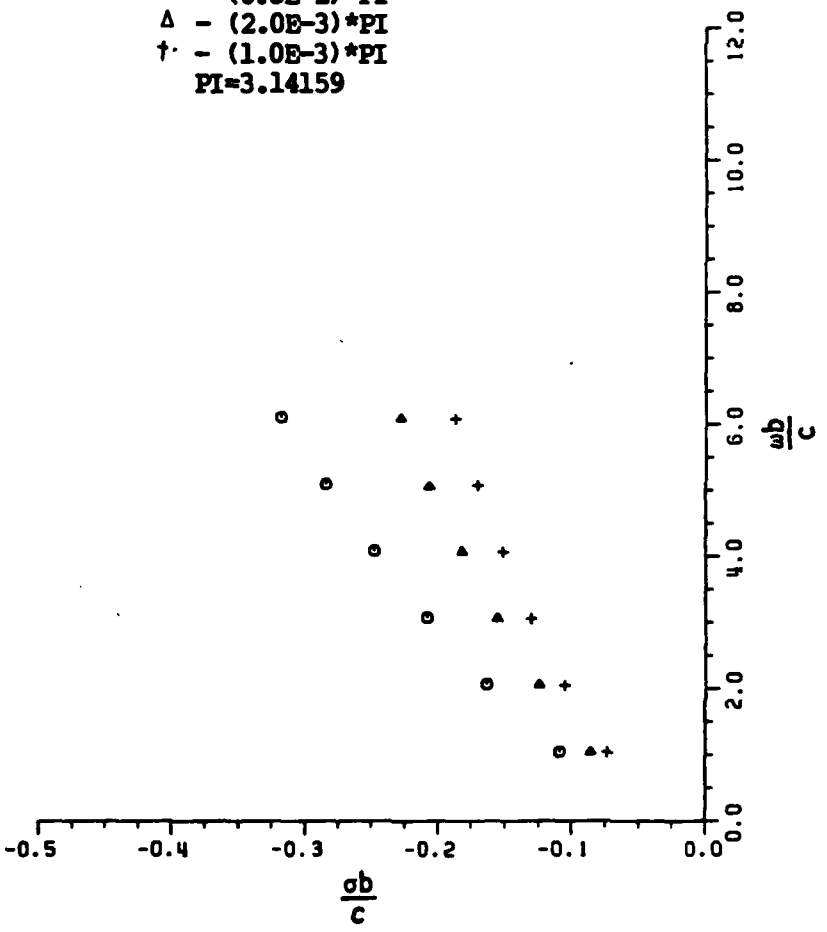

Figure 5-15. A plot of the complex natural resonances (layer I) for the loops at different wire to loop radius ratios using the integral equation and numerical search to find the poles.

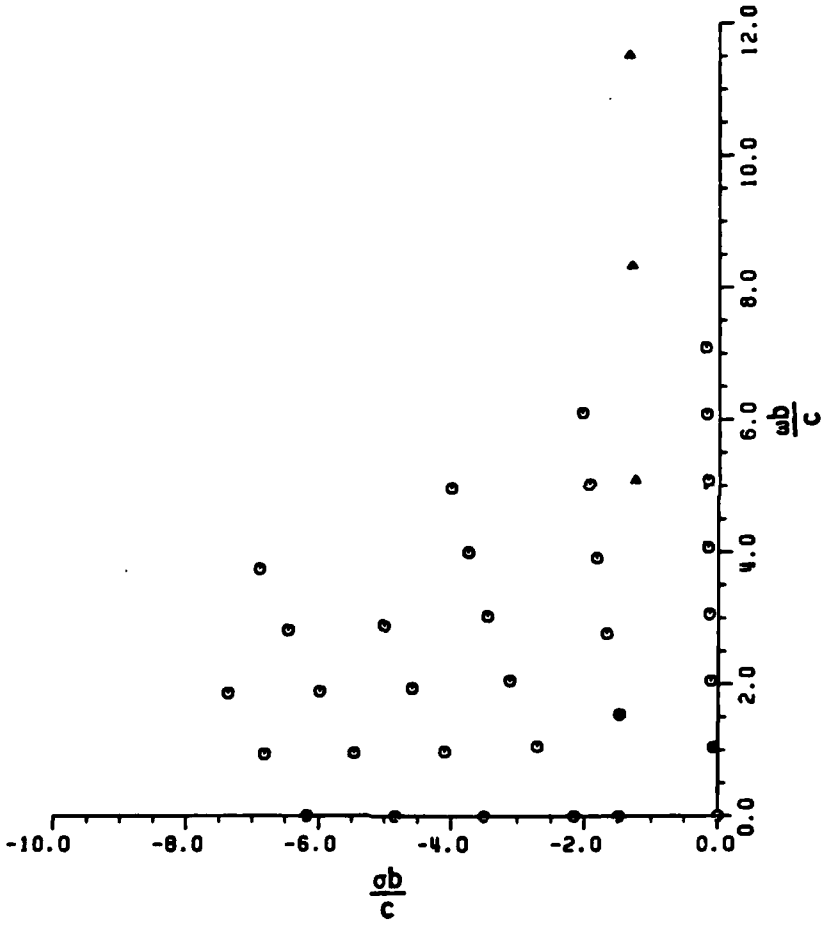

Figure 5-16. A plot of the poles for a circular loop at the wire radius to the loop radius ratio of 3.14159E-3. The integral equation and numerical search is used to find the poles.

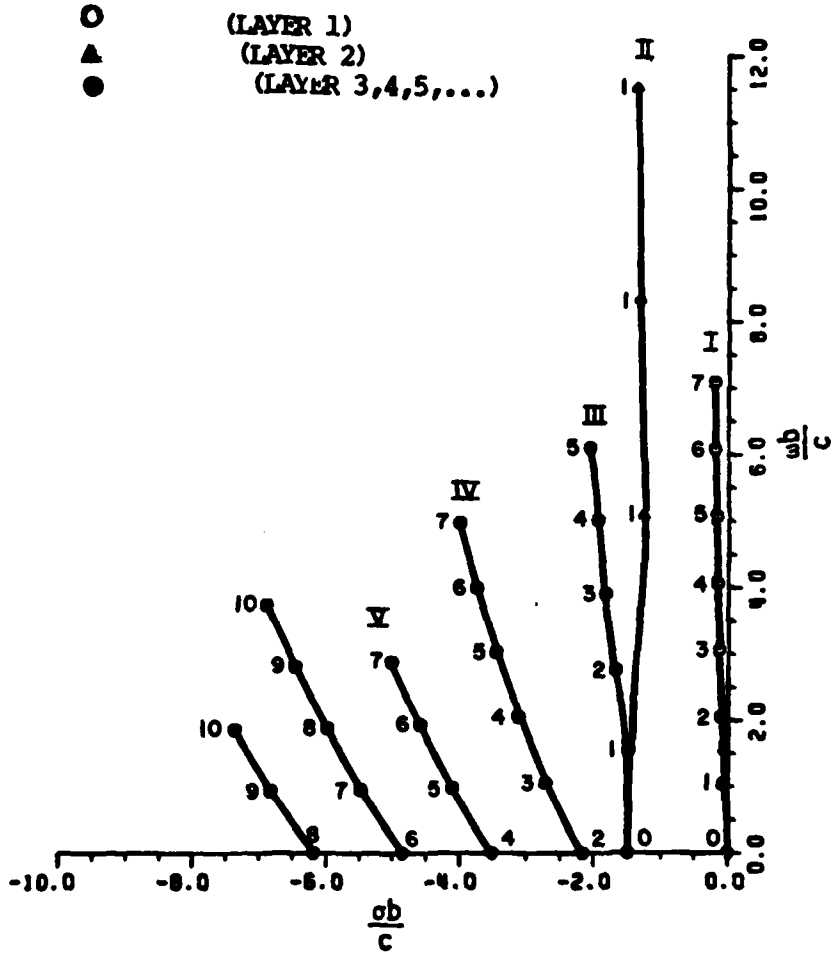

Figure 5-17. A plot of the poles for a circular loop (a/b of 3.14159E-3). The poles are extracted via the integral equation and numerical search. The number around the location of each pole is the n of Znn. Three types of poles are defined.

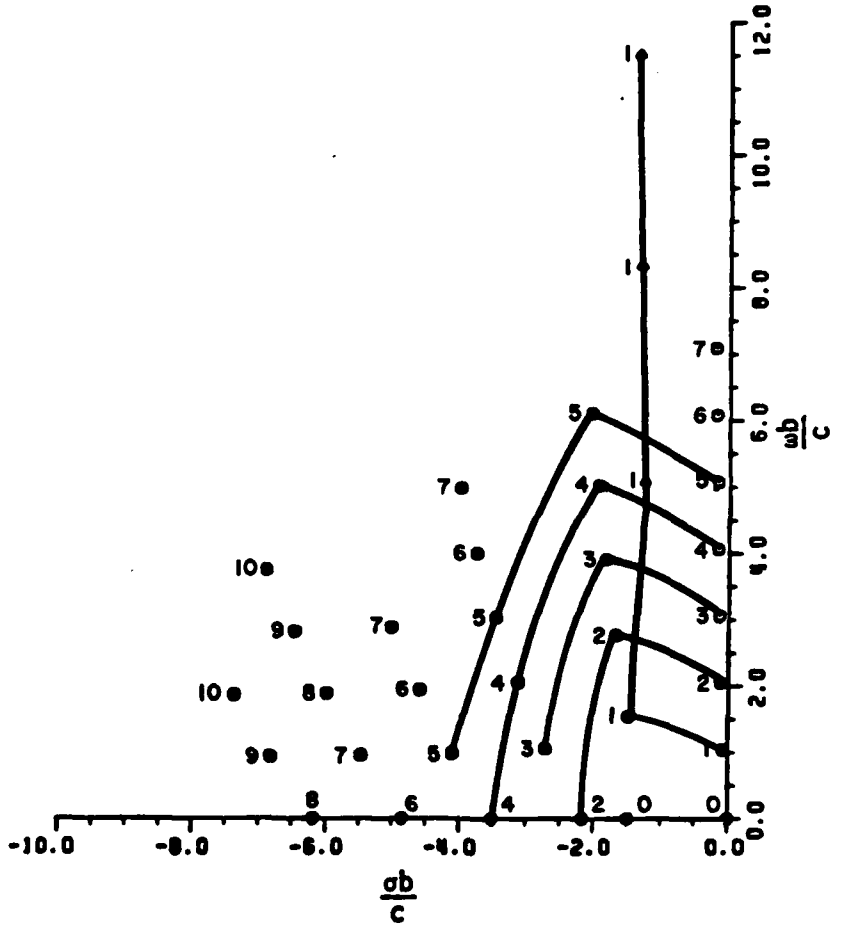

Figure 5-18. A plot of the poles for a circular loop (a/b of 3.14159E-3 extracted via the integral equation and numerical search. The number around the location of each pole is the n of Znn. The poles which are extracted from the same Znn are identified by a solid line.

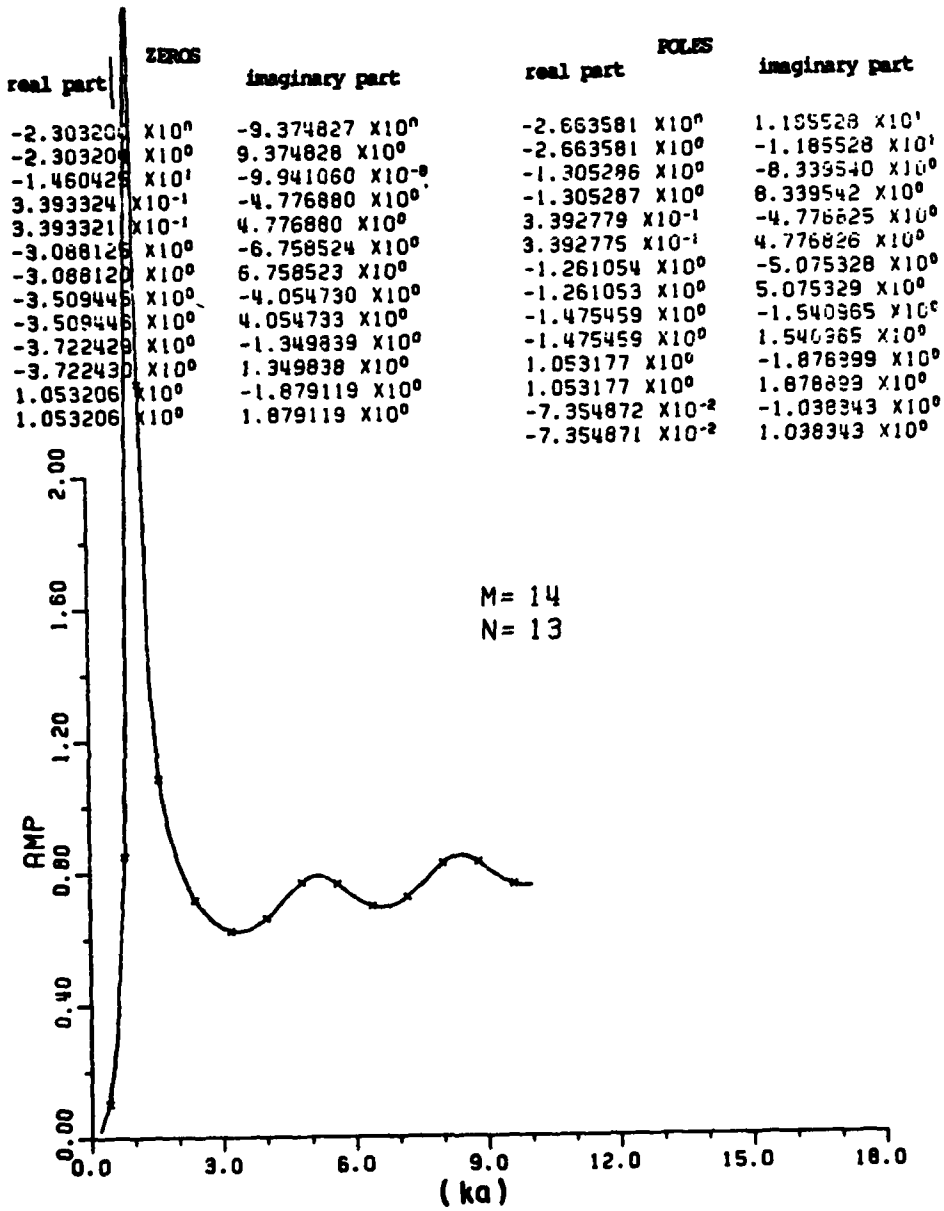

Figure 5-19. The application of RFA for (M,N) as (14,13) to the backscattering data (solid line) for a circular loop at broadside. The wire-radius to the loop radius ratio is 3.14159E-3. The x's are the data points used in the RFA.

ZEROS		POLES	
real part	imaginary part	real part	imaginary part
9.093257 X10^{-2}	-5.338513 X10^{0}	-1.979718 X10^{-1}	5.082444 X10^{0}
9.092996 X10^{-2}	5.339510 X10^{0}	-1.879747 X10^{-1}	-5.082443 X10^{0}
5.557376 X10^{0}	-1.985174 X10^{-7}	1.695386 X10^{0}	-3.992643 X10^{0}
2.304666 X10^{-1}	-2.801795 X10^{0}	1.695886 X10^{0}	3.992648 X10^{0}
2.305836 X10^{-1}	2.801810 X10^{0}	-1.770321 X10^{0}	-2.026050 X10^{0}
2.628924 X10^{-1}	-4.102598 X10^{0}	-1.770321 X10^{0}	2.026049 X10^{0}
2.629014 X10^{-1}	4.102255 X10^{0}	2.154596 X10^{0}	-1.912053 X10^{0}
-6.038113 X10^{-1}	-4.266512 X10^{0}	2.154596 X10^{0}	1.912053 X10^{0}
-6.038865 X10^{-1}	4.266473 X10^{0}	1.713832 X10^{-5}	-3.099755 X10^{0}
9.612989 X10^{-4}	-4.199132 X10^{0}	-1.671175 X10^{-5}	3.099739 X10^{0}
1.132204 X10^{-3}	4.199545 X10^{0}	-2.487884 X10^{0}	0.000000 X10^{0}
-4.710483 X10^{-1}	-2.833646 X10^{0}	2.269944 X10^{0}	-1.590563 X10^{-8}
-4.710157 X10^{-1}	2.833650 X10^{0}	-1.314712 X10^{-1}	-3.061251 X10^{0}
1.764213 X10^{-4}	-3.100153 X10^{0}	-1.314476 X10^{-1}	3.061272 X10^{0}
-5.329429 X10^{-5}	3.100109 X10^{0}	-1.527180 X10^{-1}	-4.072685 X10^{0}
-1.693506 X10^{-1}	-1.693563 X10^{0}	-1.526632 X10^{-1}	4.072699 X10^{0}
-1.543495 X10^{-1}	1.693558 X10^{0}	2.571348 X10^{-5}	-4.202686 X10^{0}
5.254009 X10^{-3}	-1.414843 X10^{0}	-2.154853 X10^{-5}	4.202674 X10^{0}
5.254717 X10^{-3}	1.414845 X10^{0}	-1.061955 X10^{-1}	-2.051208 X10^{0}
		-1.061953 X10^{-1}	2.051209 X10^{0}
M= 27		2.350814 X10^{-2}	-1.038382 X10^{0}
N= 27		2.350816 X10^{-2}	1.038382 X10^{0}

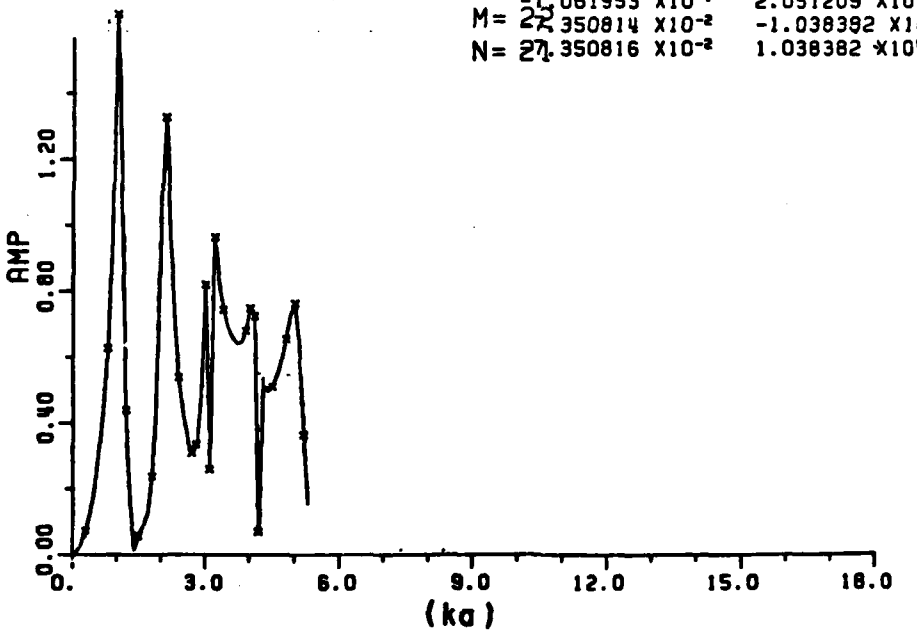

Figure 5-20. The RFA (dotted line) fit to the backscattering data (solid line) for the loop at edge-on incidence. a/b is 3.14159E-3, where a is the wire radius and b is the loop radius. The x's are the data points used in RFA.

Kouyoumjian at the Ohio State University. The equivalent source of the scattered field is approximated by the current

$$I(\phi) = \sum_{n=0}^{\infty} (c_n \cos n\phi + d_n \sin n\phi) \quad , \tag{5-9}$$

where $I(\phi)$ is assumed to flow parallel with the axis of the wire. Good agreement between the calculated (broadside and edge-on) and measured values were obtained. More data points are necessary to test the RFA. Therefore, the following formula were used to calculate additional backscattering data (TE case) in this study.

$$E^n(kb) = 2\,2\,\pi(kb)^2 \left| \frac{J_1^2(kb\sin\theta)}{k^2b^2K_1(kb,\frac{a}{b})} \right.$$

$$\left. + \sum_{n=1}^{\infty} (-1)^n \frac{\sum_{n=1}^{\infty} [Jn-1(kbsin\theta) - Jn+1(kbsin\theta)]^2}{k^2b^2[K_{n-1}(kb, \frac{a}{b}) + K_{n+1}(kb, \frac{a}{b})] - 2n^2K_n(kb, \frac{a}{b})} \right| \tag{5-10}$$

and at broadside

$$E^n(kb) = \frac{2\,2\pi(kb)^2}{|k^2b^2[K_0(kb,\Delta) + K2\,(kb,\Delta] - 2K1(kb,\Delta|^2} \tag{5-11}$$

where $\Delta=a/b$, and

$$K_n(kb,\frac{a}{b}) = \int_0^{\pi} \frac{\cos n\phi \exp\{-ikb[4\sin^2\frac{\phi}{2} + (\frac{a}{b})^2]^{1/2}\}}{[2\sin^2\frac{\phi}{2} + \frac{1}{2}(\frac{a}{b})^2]^{1/2}} d\phi \qquad (5\text{-}12)$$

E^n is the normalized backscattered amplitude and phase, i.e., the squared root of the normalized (πa^2) RCS, and J_n is the Bessel function of the first kind and order n.

The backscattering data for the loop at broadside and edge-on (TE case) incidences were calculated using Equations (5-10) to (5-12). It is noted that the K_n of Equation (5-12) were integrated by Simpson's rule for 5000 points in $[0,\pi]$. Also, three unequal subsections were divided in $[0,\pi]$, i.e., more data points were put in the steepest region of K_n. Thus, more accuracy of K_n can be reached without much more effort in the integration. Fifty data points (kb of 0.2(0.2)50) were calculated using the Equation (5-11) for the broadside excitation.

More effort is involved in the calculation of backscattering data for the loop at edge-on incidence. There is a summation of an infinite series in Equation (5-10). The infinite series was truncated at the point where five more successive terms made little contribution to the total sum at that point. Thus, the backscattering data of the loop at edge-on incidence were calculated at ka of 0.2(0.1)10. Figures 5-19 and 5-20 show the application of the RFA to the backscattering data for the loop at broadside and edge-on respectively (amplitude plots).

The RFA is not only an excellent approximation in finding the complex natural resonances but is also a good approach for complex data interpolation. Here is a good example of using the RFA for the data interpolation because the calculated data are very expensive and time-consuming to obtain. For broadside excitation the dominant string of poles was extracted using RFA (Figure 5-19). Table 5-11 is a list of poles (layer I) at broadside via the integral equation (using numerical search) and RFA. It is interesting to note that all of these poles are the same as those searched at Z_{11} via the integral equation and numerical search. From the RFA viewpoint, only one pair of poles (the lowest frequency ones) belong to layer I. The rest belong to layer II.

The pole-pairs of a loop at broadside are similar to the pole-pairs of a disc at broadside. For edge-on incidence (Figure 5-20), the dominant string of poles is shown on Table 5-12. They belong to the family Z11, Z22, Z33, ..., etc. respectively. This string of poles has the same spacing in the imaginary (oscillatory) part as that of creeping wave mode of disc.

Some of the pole-loci of a loop are similar to those of a disc, because some of the scattering mechanisms are the same. One is due to the creeping wave around the circumference of the scatterer, the other is due to the multiple diffractions of the thin wire (diffractions across the center of the loop). A Table of 25 pole-pairs of the first layer via the integral equation and numerical search are also shown in Table 5-13. Figure 5-21 is a comparison of the poles extracted using RFA and integral equation with numerical search for the loop.

TABLE 5-11

A LIST OF POLES OF A LOOP (a/b* of 3.14159E-3) EXTRACTED USING THE RFA AND INTEGRAL EQUATION AND NUMERICAL SEARCH FOR BROADSIDE EXCITATION.

Poles	
Integral Equation and Numerical Search	Rational Function Approximation
Layer I	
-0.073317+/-J1.03822	-0.073548+/-J1.03834
Layer II	
-1.47916+/-J1.54327	-1.475459+/-J1.540965
-1.25879+/-J5.0763	-1.261053+/-J5.07532
-1.31026+/-J8.3208	-1.305286+/-J8.33954
-1.34771+/-11.5139	

* The units of the poles are kb, where k is the wavenumber, b is the loop radius, and a is the wire radius.

TABLE 5-12

POLES OF A CIRCULAR LOOP AT EDGE-ON INCIDENCE WITH a/b* of 3.14159E-3

Integral Equation and Numerical Search	Rational Function Approximant
Layer I	
-0.73317E-1+/-J1.03822	-0.7354E-1+/-J1.03834
-1.05310E-1+/-J2.05176	-1.0628E-1+/-J2.0515
-1.30826E-1+/-J3.06151	-1.308 E-1+/-J3.06
Layer II	
-1.47546+/-J1.540965	-1.62 +/-J1.69

* The units of the poles are kb, where k is the wavenumber, b is the loop radius, and a is the wire radius.

TABLE 5-13

A LIST OF THE POLES AND THE CORRESPONDING RELATIVE IMPEDANCE (Znn) FOR THE LOOP (a/b* of 3.14159E-3). THE IMPEDANCE (Znn) MAY BE AS HIGH AS 1.0 E3 FOR THE LOCATION SLIGHTLY AWAY FROM THE POLE LOCATIONS.

N	POLES(2kb)	Z (NN)
0	(0.,0)	1.78470E-5
1	(-1.46634E-1,±2.07644)	1.13116E-4
2	(-2.11820E-1,±4.10353)	3.79588E-4
3	(-2.61653E-1,±6.12302)	3.21737E-4
4	(-3.03864E-1,±8.13899)	6.98320E-4
5	(-3.41321E-1,±10.1528)	5.67344E-4
6	(-3.75458E-1,±12.1652)	2.01817E-5
7	(-4.07110E-1,±14.1765)	3.44889E-4
8	(-4.36814E-1,±16.1869)	7.87555E-4
9	(-4.64939E-1,±18.1967)	2.44959E-5
10	(-4.91752E-1,±20.2058)	7.70241E-4
11	(-5.17453E-1,±22.2145)	7.71799E-4
12	(-5.42195E-1,±24.2228)	6.32431E-4
13	(-5.66101E-1,±26.2307)	7.59797E-4
14	(-5.89269E-1,±28.2382)	9.36263E-4
15	(-6.11779E-1,±30.2455)	3.61295E-5
16	(-6.33699E-1,±32.2525)	1.81433E-3
17	(-6.55086E-1,±34.2593)	8.89091E-4
18	(-6.75987E-1,±36.2658)	5.91972E-4
19	(-6.96445E-1,±38.2722)	5.83594E-4
20	(-7.16494E-1,±40.2783)	8.52026E-5

* The units of the poles are 2kb, where k is the wvaenumber and b is the loop radius. (a is the wire radius.)

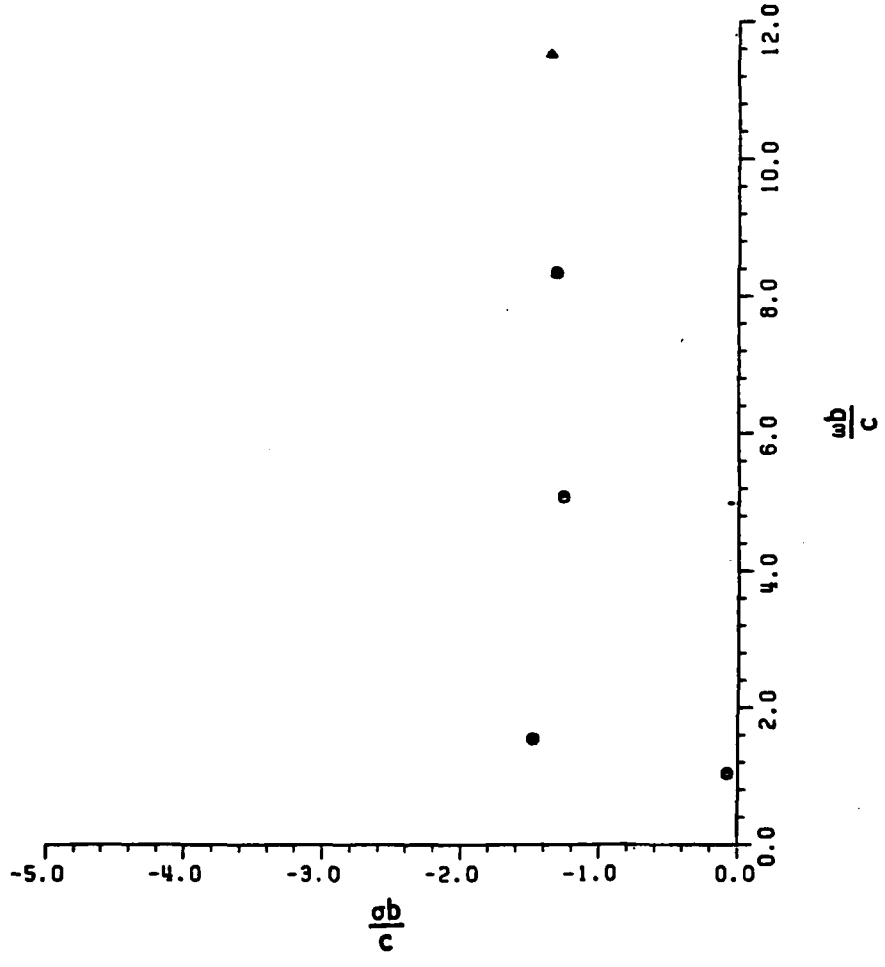

Figure 5-21. A comparison of the poles extracted using RFA and integral equation and numerical search ("Δ " impedance method, "o" RFA fit) for the loop.

From the backscattering data of a loop for broadside incidence, an impulse response in the time domain (Figure 5-22) can be found using an inverse Fourier transform of the data. Figure 5-23 is a plot of the impulse response of the loop for broadside where the specular return of the waveform has been removed. Figure 5-24 is a comparison of the impulse response waveforms for a loop and a disc. Obviously, the loop is a high Q scatter compared to the disc. Figure 5-25 is a ramp response of the loop using the first 10 harmonics for Fourier synthesis. The duration of the response is longer than 15 TAU (2b/c, i.e., the loop diameter transit time) although the plot only shows up to 15 TAU. Landt and Miller have calculated the short pulse response of a loop (the derivative of a Gaussian pulse) using a time domain approach (space-time integral equation). The convolution of the impulse response obtained here with a short pulse yields a result very similar to that of Landt and Miller's short pulse response [36]. A comparison is shown in Figure 5-26.

A plot of the individual contribution of each pole-pair and the corresponding residues of the impulse response for a loop (backscatter) at broadside is shown in Figure 5-27. More transient response waveforms for the loop at broadside and edge-on incidence are shown in Appendix H. The dominant string of poles of a loop at edge on incidence belong to layer I (see Figure 5-17). Only one pole belonging to layer II was found using a RFA. Other poles were too weakly excited for extraction using RFA.

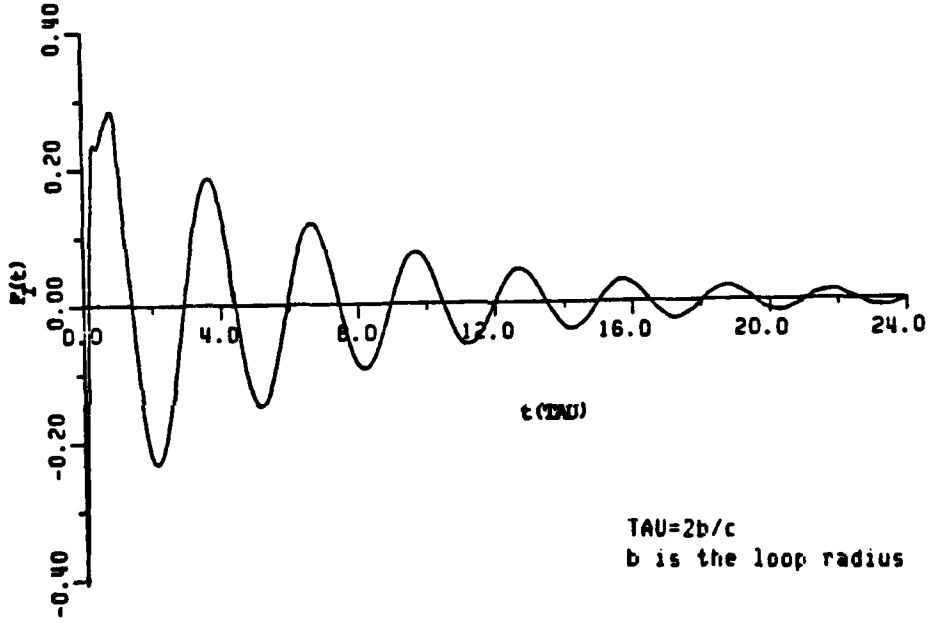

Figure 5-22. The impulse response (with the specular term to be removed) for a loop (backscatter) at broadside. The specular return is seen around the time origin. a/b is 3.14159E-3, where a is the wire radius and b is the loop radius.

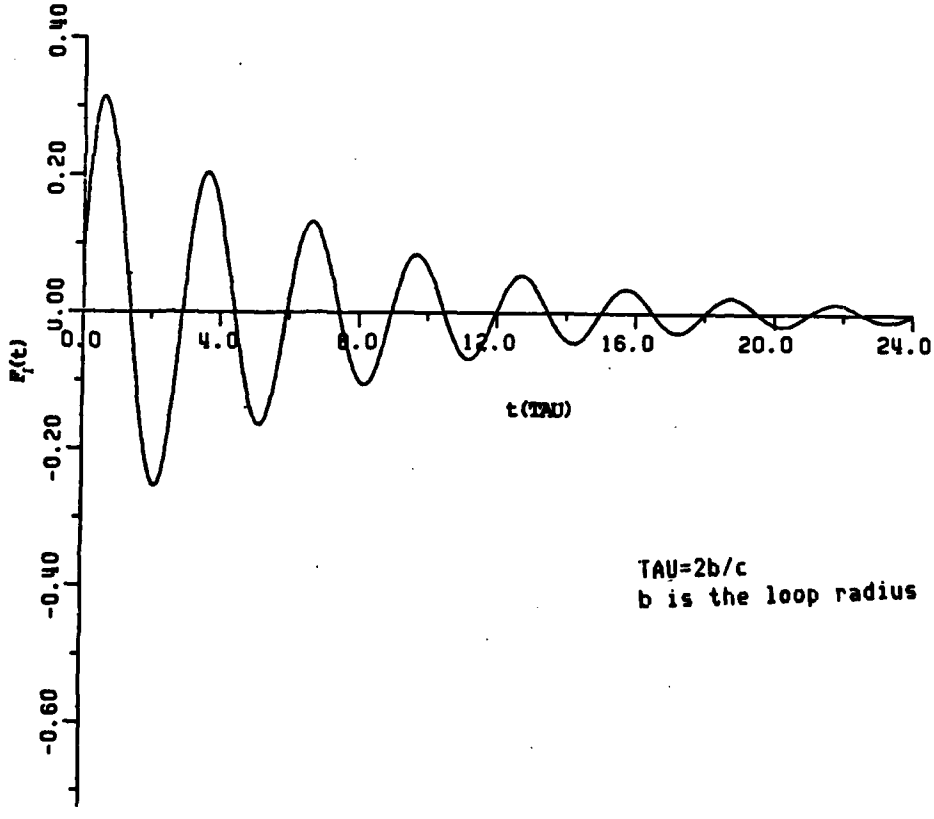

Figure 5-23. The impulse response (with the specular return removed) for a loop at broadside (backscatter). a/b is 3.14159E-3, where a is the wire radius and b is the loop radius.

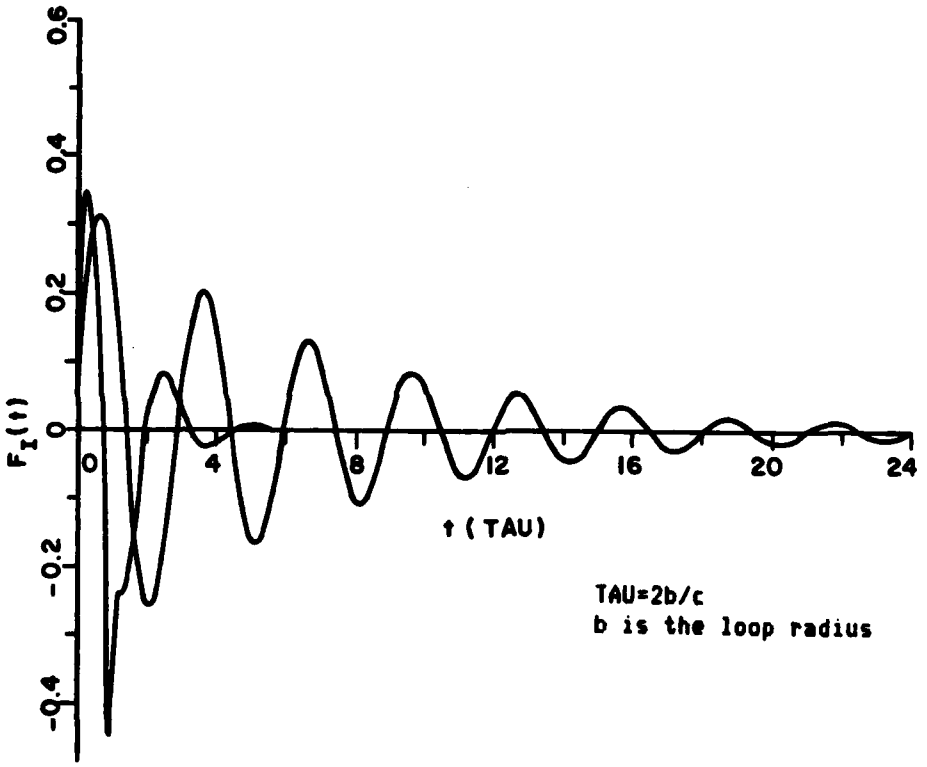

Figure 5-24. A comparison of the impulse response waveforms for a circular loop (a/b is 3.14159E-3) and a circular metallic disc (backscatters).

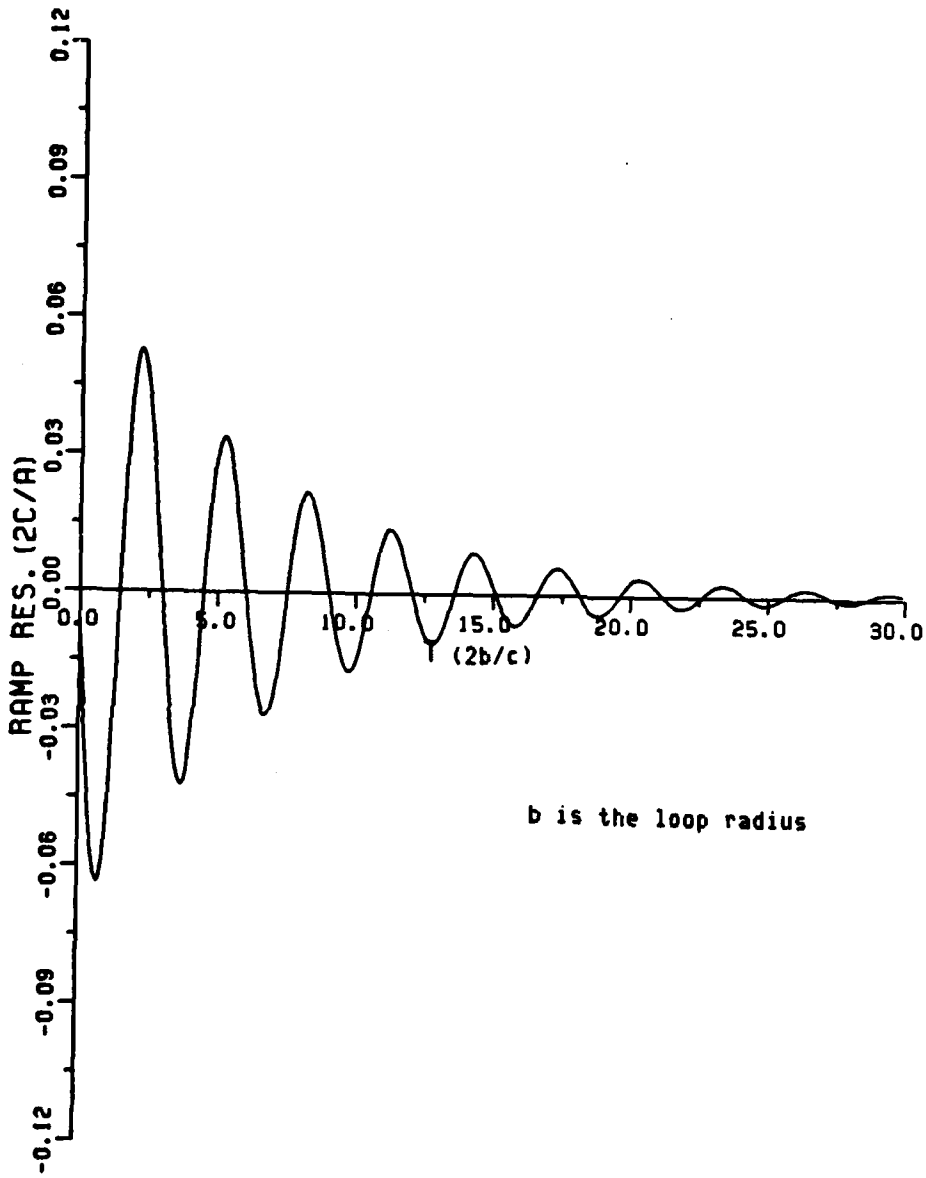

Figure 5-25. The ramp response for a loop for broadside excitation.

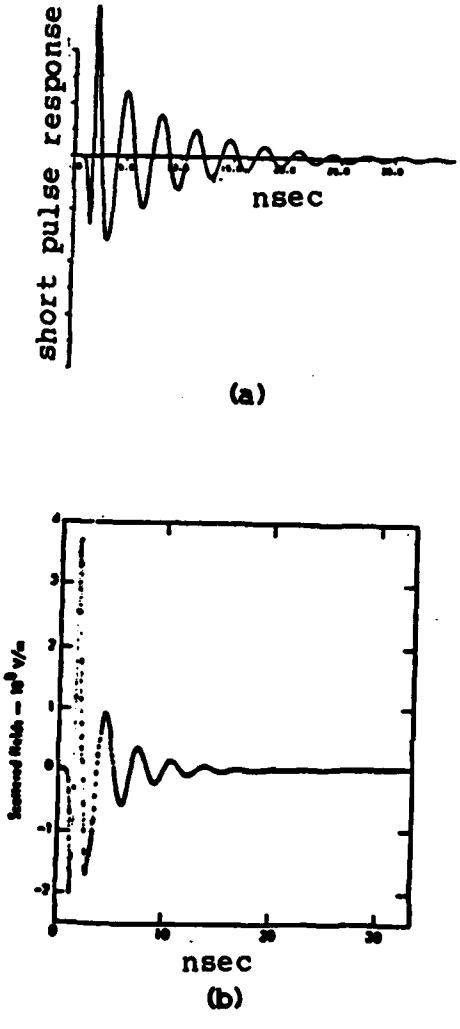

Figure 5-26. The derivative of a short Gaussian pulse response for a loop. (a) is obtained using the convolution of the impulse response and the input short pulse. (b) is calculated using the time domain moment method [36]. Note that wire to the loop radius ratio is 0.00314 in (a).

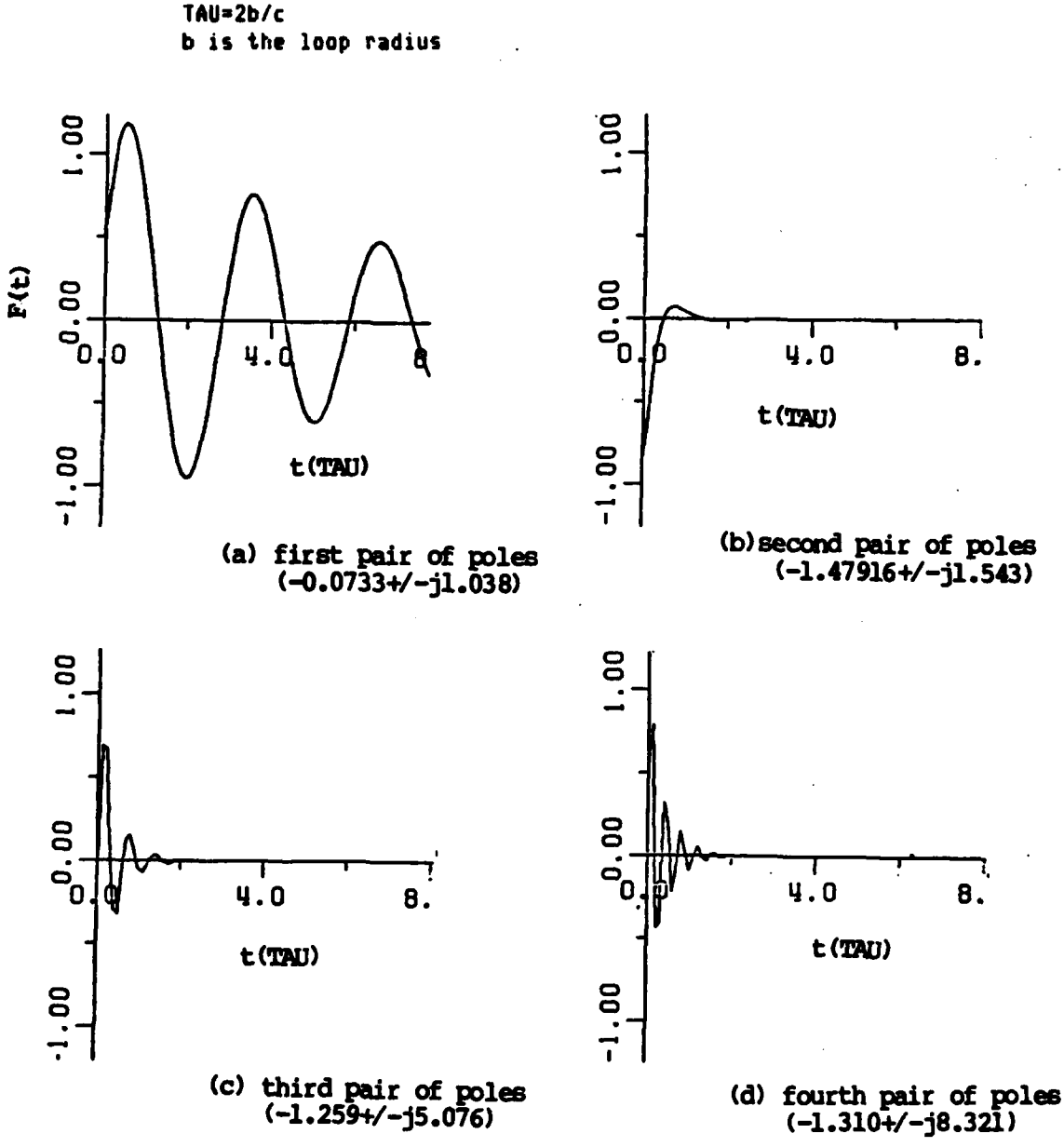

Figure 5-27. The individual contribution of each pole-pair and the corresponding residues to the impulse response for a loop backscatter for broadside.

F. FINITE AND SEMI-INFINITE OPEN CIRCULAR WAVEGUIDES

The frequency domain axial backscattering for the semi-infinite* circular waveguide has been studied and computed, in the resonance region, using exact Wiener-Hopf solution by Johnson and Moffatt [37]. Later, a UTD approximation was done by Huang [38]. Axial backscatter from finite circular waveguides** with the far end shorted or opened have been computed using the UTD approximation, and a comparison has been made to a moment method solution [38, 39]. Geometrical descriptions of the finite and semi-infinite waveguides are shown in Figure 5-28.

Figures 5-29 to 5-34 show plots of RFA fits to portions of the scattering data in the frequency domain obtained using a moment method solution. Table 5-14 is a list of poles extracted from RFA and the window technique developed in Chapter III for these three objects. Figure 5-35 is a plot of the extracted poles for the three geometries. Note that the poles of the finite open waveguides are very close for both the far end shorted or opened, and definitely more pole-strings exist for the the finite waveguides than for the the semi-infinite guide because of

---

* For the semi-infinite circular waveguide the data are D/λ of 01(.01).7 from Johnson and Moffatt's exact solution. The data D/λ of 1.(.01)2.6 are the GTD high frequency approximation. The rest of the data are fitted and predicted by the rational function approximation. D is the diameter of the waveguide.

** For the finite circular waveguide with the far end shorted or opened the data D/λ of .01(.01)1.20 are from Huang's UTD solution. D is the the diameter of the waveguide.

TABLE 5-14

A LIST OF POLES* OF FINITE AND SEMI-INFINITE WAVEGUIDE OBTAINED USING THE RFA TO THE BACKSCATTERING CALCULATED DATA.

Finite Waveguide The Rear End Open	Finite Waveguide Both Ends Open	Semi-infinite Waveguide
-0.22+/-j0.54	-0.22+/-j0.55	
-0.20+/-j0.82	-0.21+/-j0.82	
-0.21+/-j1.06	-0.19+/-j1.04	
-0.19+/-j1.29	-0.16+/-j1.28	-0.95+/-j1.36
-0.15+/-j1.51	-0.13+/-j1.53	
-0.19+/-j1.63	-0.17+/-j1.62	-0.33+/-j1.79
-0.10+/-j1.81	-0.11+/-j1.90	
-0.02+/-j2.08	-0.01+/-j2.05	
-0.05+/-j2.22	-0.10+/-j2.21	
-0.08+/-j2.42	-0.17+/-j2.45	
-0.30+/-j2.57	-0.47+/-j2.57	
-0.10+/-j2.64	-0.22+/-j2.69	
-0.13+/-j2.88	-0.31+/-j2.82	
-0.13+/-j3.04	-0.21+/-j3.04	
-0.11+/-j3.14	-0.20+/-j3.14	
-0.13+/-j3.26	-0.19+/-j3.24	-0.40+/-j3.31
		-0.86+/-j4.95
		-0.80+/-j6.14
		-0.53+/-j7.89

* The poles are in the units of ka, where a is the radius of the circular waveguide and k is the wavenumber.

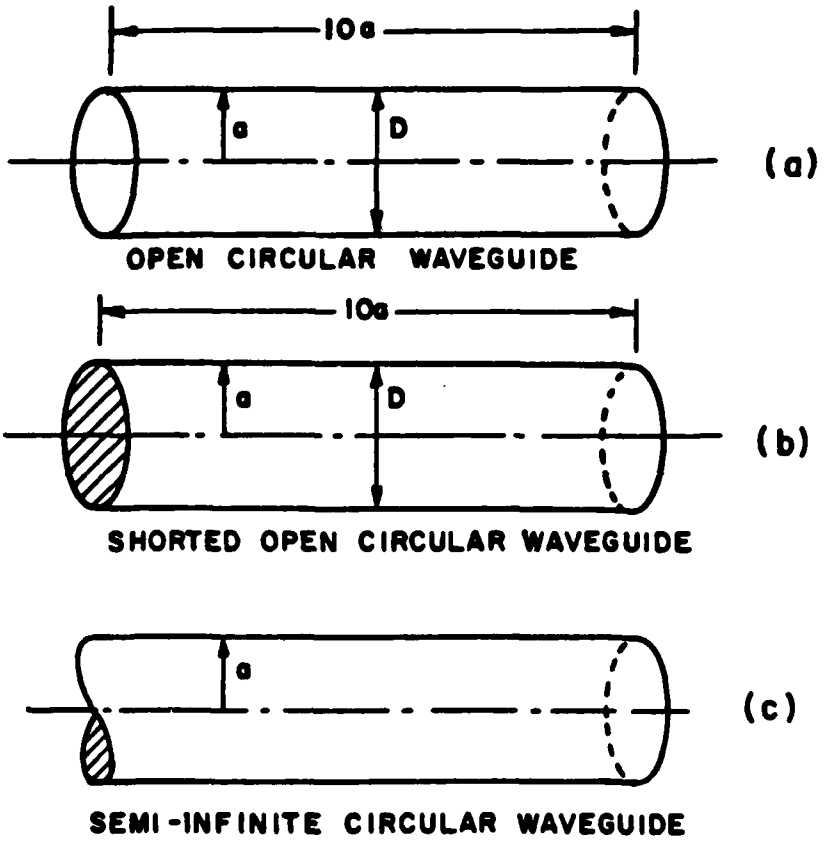

Figure 5-28. The geometries of finite waveguides with both ends open (a), the rear end shorted (b), and semi-infinite waveguide (c).

ZEROS		POLES	
-8.144565×10^{-2}	-1.340101×10^{0}	-1.620145×10^{-1}	1.080560×10^{0}
-8.144583×10^{-2}	1.340101×10^{0}	-1.620296×10^{-1}	-1.080546×10^{0}
-2.172532×10^{-3}	-1.248706×10^{0}	-6.577510×10^{-2}	1.358820×10^{0}
-2.172588×10^{-3}	1.248706×10^{0}	-6.575880×10^{-2}	-1.358909×10^{0}
3.279553×10^{-3}	-9.392838×10^{-1}	-1.069637×10^{-1}	1.272292×10^{0}
3.284794×10^{-3}	9.392836×10^{-1}	-1.069825×10^{-1}	-1.272317×10^{0}
2.984661×10^{-2}	-9.170457×10^{-1}	2.892429×10^{-2}	9.150275×10^{-1}
2.984142×10^{-2}	9.170455×10^{-1}	2.893159×10^{-2}	-9.150392×10^{-1}
1.371537×10^{-1}	-1.843840×10^{-8}	-1.775159×10^{-1}	8.749970×10^{-1}
3.261737×10^{-3}	6.291685×10^{-1}	-1.775075×10^{-1}	-8.749830×10^{-1}
3.261563×10^{-3}	-6.291680×10^{-1}	-1.577187×10^{-1}	6.847922×10^{-1}
-3.695567×10^{-2}	5.250802×10^{-1}	-1.577168×10^{-1}	-6.847945×10^{-1}
-3.695567×10^{-2}	-5.250802×10^{-1}	-2.964783×10^{-2}	5.443450×10^{-1}
		-2.964783×10^{-2}	-5.443449×10^{-1}

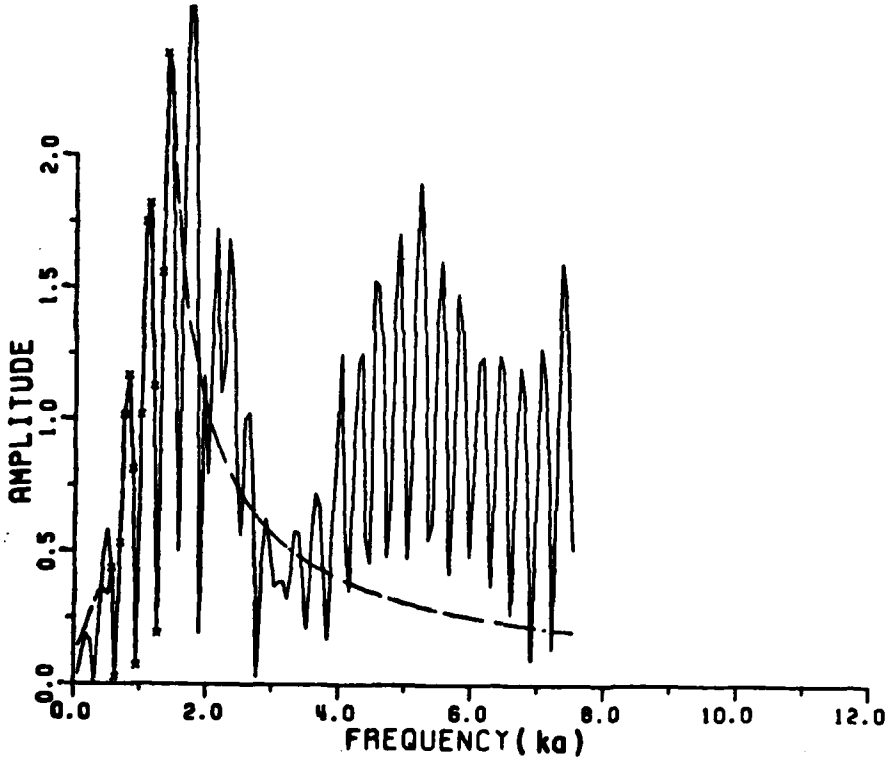

Figure 5-29. The RFA for (M,N) as (14,13) (dashed line) fit to the axial backscattering data (solid line) for the finite waveguide (both ends open) within the window of interest. The x's are data points used in RFA (amplitude plot).

RESI.		MAG. OF RESI.
-2.771144 X10^{-1}	-1.029103 X10^{0}	1.065761 X10^{0}
-2.771955 X10^{-1}	1.029058 X10^{0}	1.065738 X10^{0}
2.077066 X10^{-3}	-8.397622 X10^{-2}	8.400190 X10^{-2}
2.050872 X10^{-3}	8.398229 X10^{-2}	8.400733 X10^{-2}
3.065995 X10^{-1}	-8.593742 X10^{-2}	3.184156 X10^{-1}
3.065877 X10^{-1}	8.601199 X10^{-2}	3.184244 X10^{-1}
-1.174388 X10^{-4}	8.171567 X10^{-4}	8.255525 X10^{-4}
-1.174537 X10^{-4}	-8.118793 X10^{-4}	8.203314 X10^{-4}
-1.002066 X10^{0}	3.211600 X10^{-1}	1.052274 X10^{0}
-1.001975 X10^{0}	-3.211975 X10^{-1}	1.052199 X10^{0}
2.313904 X10^{-1}	3.538857 X10^{-1}	4.228198 X10^{-1}
2.314184 X10^{-1}	-3.538886 X10^{-1}	4.228376 X10^{-1}
-8.438090 X10^{-4}	-9.041017 X10^{-3}	9.080308 X10^{-3}
-8.438079 X10^{-4}	9.041057 X10^{-3}	9.080348 X10^{-3}

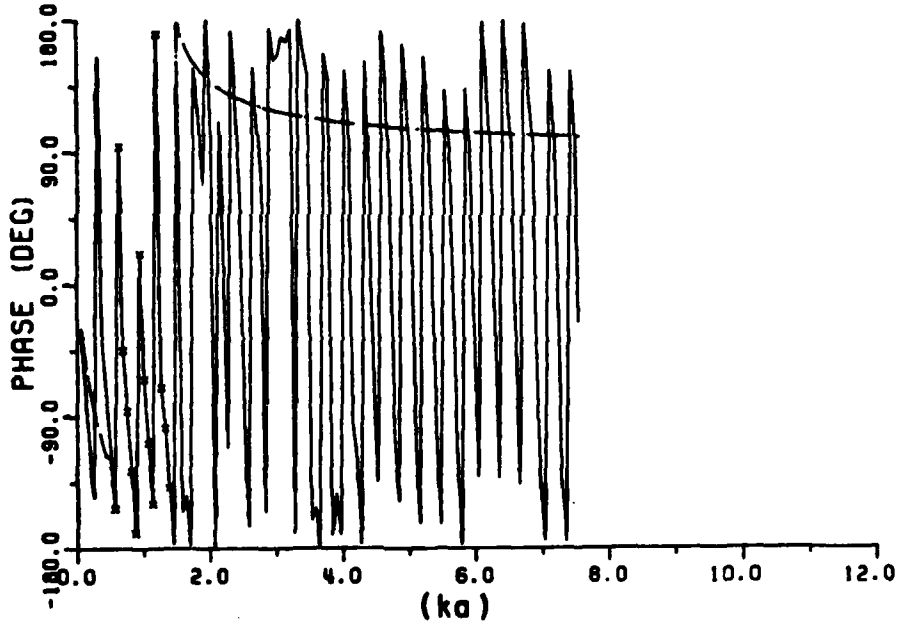

Figure 5-30. The RFA for (M,N) as (14,13) (dashed line) fit to the axial backscattering data (solid line) for the finite waveguide (both ends open) within the window of interest. The x's are the data points used in RFA (phase plot).

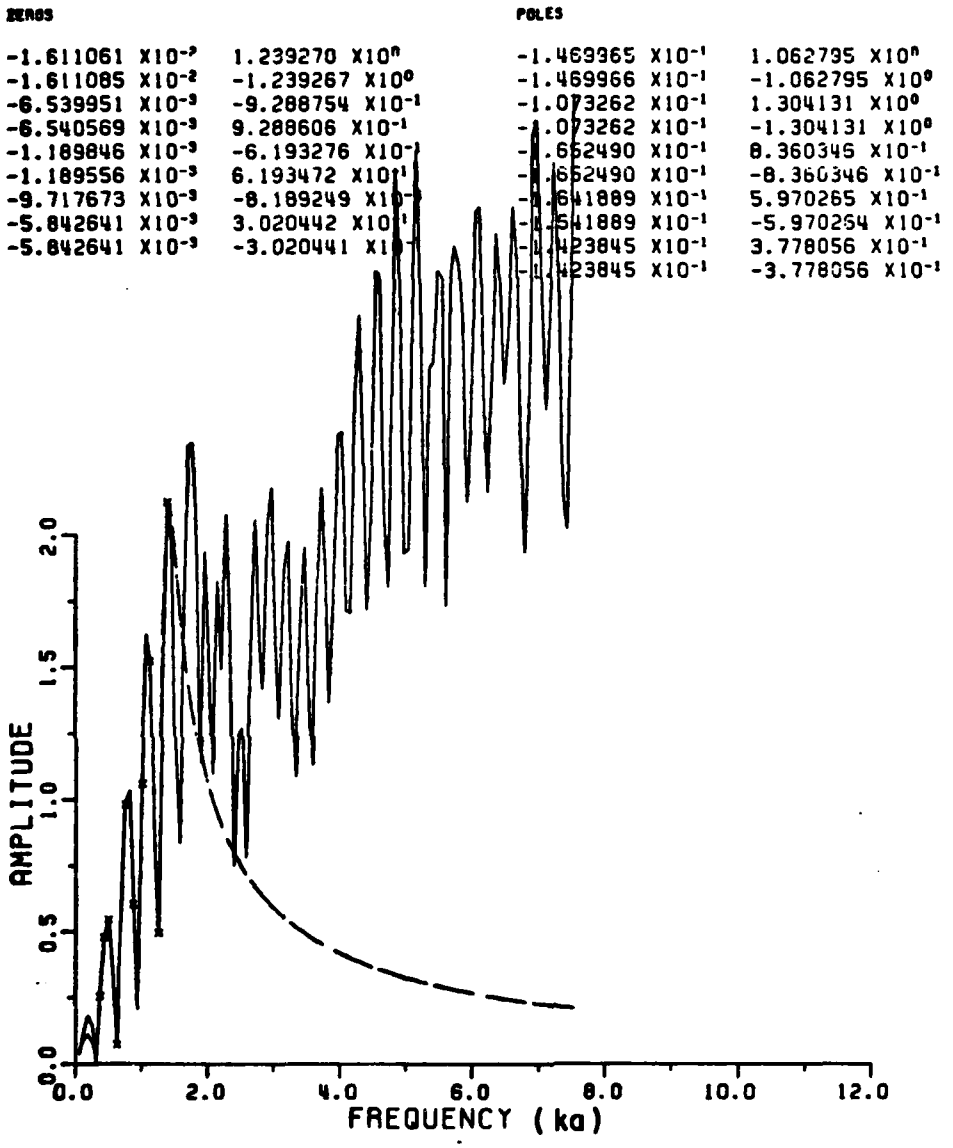

Figure 5-31. The RFA for (M,N) as (10,9) (dashed line) fit to the axial backscattering data (solid line) for the finite circular waveguide (the rear end shorted) within the window of interest. The x's are the data points used in RFA (amplitude plot).

RESI.		MAG. OF RESI.
-1.210182 X10^{-1}	-6.648830 X10^{-1}	6.758068 X10^{-1}
-1.210183 X10^{-1}	6.648833 X10^{-1}	6.758071 X10^{-1}
2.115404 X10^{-1}	-2.661929 X10^{-1}	3.400118 X10^{-1}
2.115404 X10^{-1}	2.661928 X10^{-1}	3.400117 X10^{-1}
-6.885370 X10^{-1}	-1.626539 X10^{-1}	7.074882 X10^{-1}
-6.885370 X10^{-1}	1.626538 X10^{-1}	7.074882 X10^{-1}
-2.693191 X10^{-1}	3.510494 X10^{-1}	4.424574 X10^{-1}
-2.693191 X10^{-1}	-3.510494 X10^{-1}	4.424574 X10^{-1}
8.821848 X10^{-2}	1.138946 X10^{-1}	1.440642 X10^{-1}
8.821848 X10^{-2}	-1.138946 X10^{-1}	1.440642 X10^{-1}

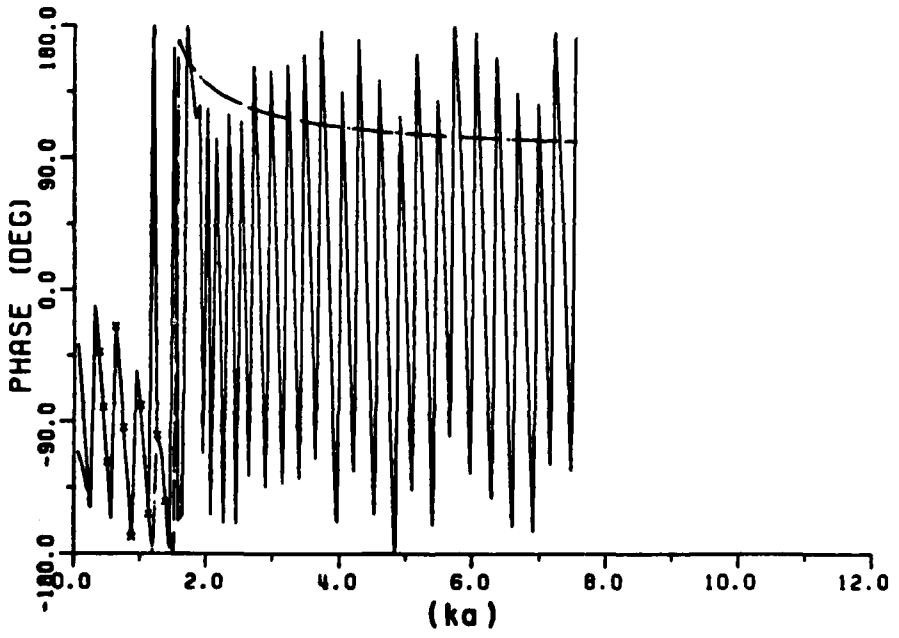

Figure 5-32. The RFA for (M,N) as (10,9) (dashed line) fit to the axial backscattering data (solid line) for the finite circular waveguide (the rear end shorted) within the window of interest. The x's are the data points used in RFA (phase plot).

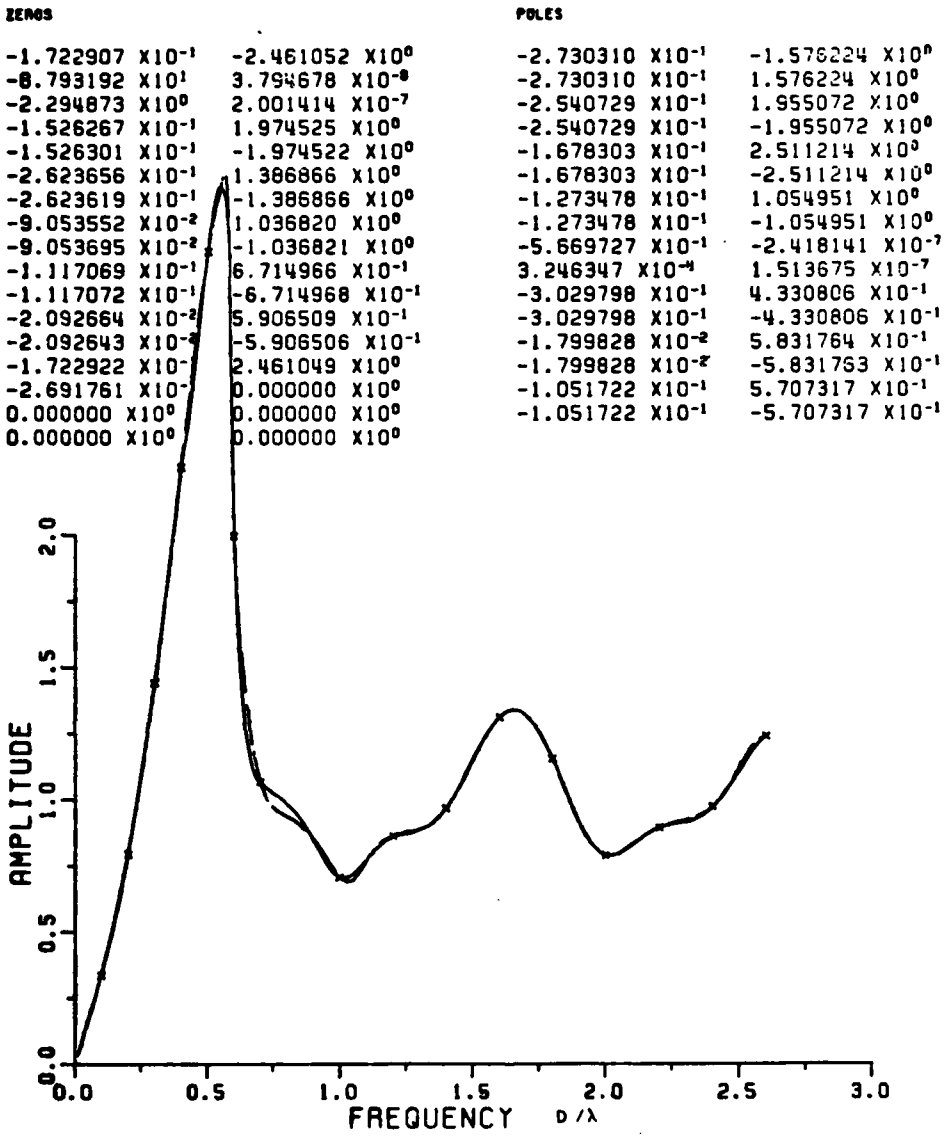

Figure 5-33. The RFA for (M,N) as (16,15) (dashed line) fit to the axial back-scattering data (solid line) for a semi-infinite circular waveguide. The x's are the data points used in the RFA. D is the diameter of the circular waveguide (amplitude plot).

RESI.		MAG. OF RESI.
-1.361640×10^{-1}	2.084748×10^{-1}	2.490028×10^{-1}
-1.361640×10^{-1}	-2.084747×10^{-1}	2.490027×10^{-1}
1.526774×10^{-1}	-2.473606×10^{-2}	1.543682×10^{-1}
1.526774×10^{-1}	2.473607×10^{-2}	1.546682×10^{-1}
-1.157496×10^{-2}	-5.531275×10^{-2}	5.651089×10^{-2}
-1.157496×10^{-2}	5.531276×10^{-2}	5.651089×10^{-2}
2.859424×10^{-2}	-2.654425×10^{-2}	3.901574×10^{-2}
2.859425×10^{-2}	2.654425×10^{-2}	3.901574×10^{-2}
-8.525676×10^{-1}	-2.328665×10^{-7}	8.525676×10^{-1}
-3.311520×10^{-7}	0.000000×10^{0}	3.311522×10^{-7}
8.385943×10^{-2}	-8.539180×10^{-1}	8.580259×10^{-1}
8.386019×10^{-2}	8.539183×10^{-1}	8.580262×10^{-1}
3.106215×10^{-3}	2.172073×10^{-2}	2.194171×10^{-2}
3.106204×10^{-3}	-2.172073×10^{-2}	2.194171×10^{-2}
-1.246465×10^{-1}	2.208890×10^{-1}	2.536310×10^{-1}
-1.246466×10^{-1}	-2.208889×10^{-1}	2.536310×10^{-1}

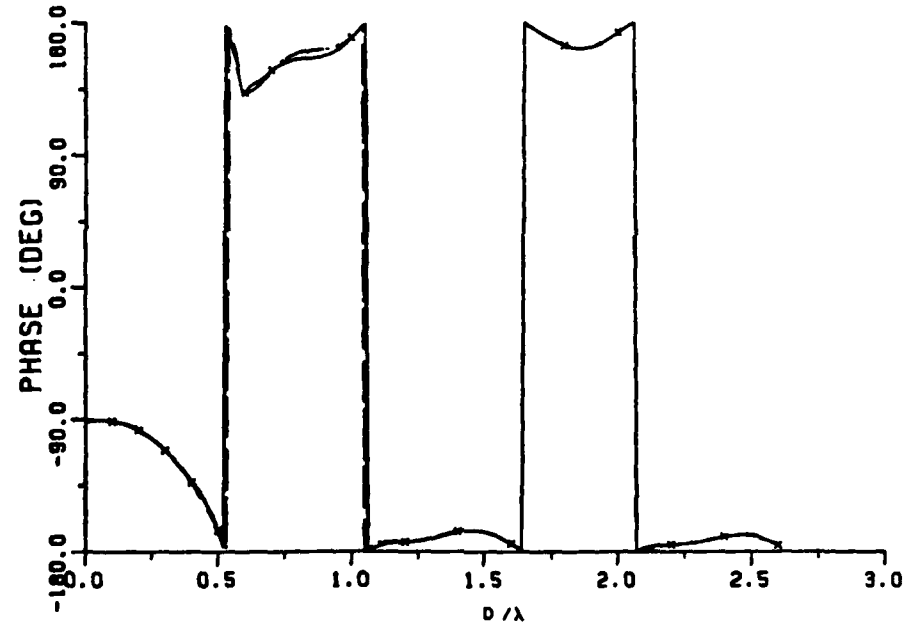

Figure 5-34. The RFA for (M,N) as (16,15) (dashed line) fit to the axial backscattering data (solid line) for a semi-infinite circular waveguide. The x's are the data points used in the RFA. D is the diameter of the circular waveguide (phase plot).

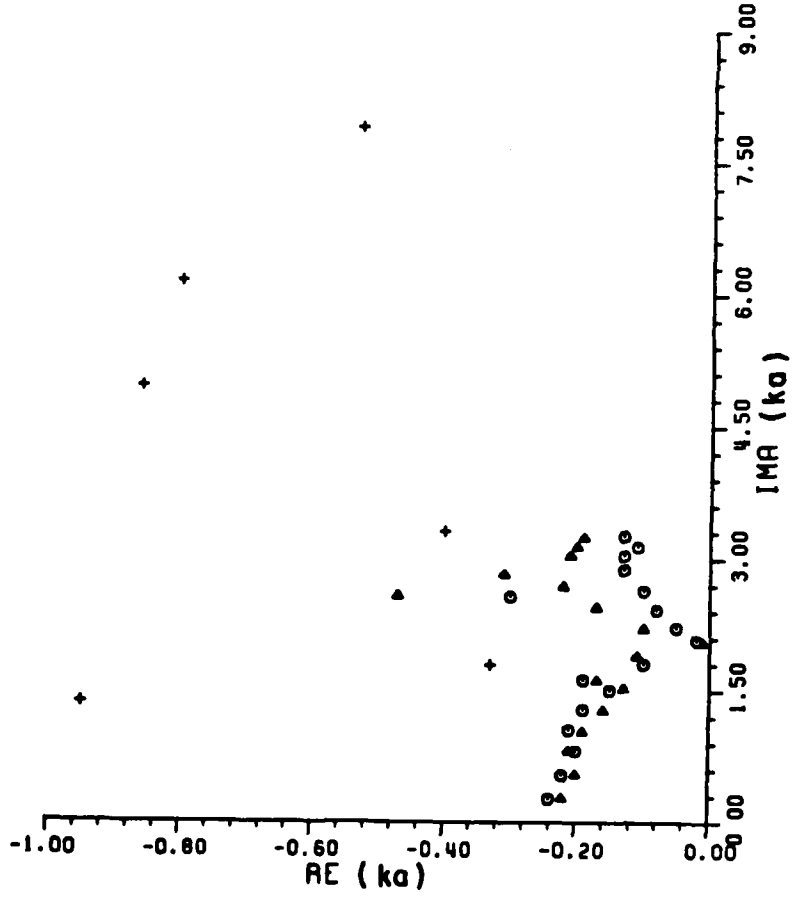

Figure 5-35. The complex natural resonances for the three cavities.
Δ: finite waveguide (both ends opened)
∘: finite waveguide (the rear end opened)
†: semi-infinite waveguide.

basically dipole-type modes. This can be seen either in the plot of poles in Figure 5-35 or in Table 5-14.

The complex natural resonances of finite waveguides and semi-infinite waveguide are compared Figure 5-35. The complex natural resonances are very close for the finite waveguides with the far end opened or closed (as least in the interesting spectrum used for the RFA). The major resonant modes (dipole modes) of the finite guides are nearly the same as can be seen in either Figure 5-35 or Table 5-14. The edge diffraction and rim creeping modes are dominant for the semi-infinite waveguide and the dipole modes are dominant for the finite waveguide. However, the scattering mechanisms due to the front rim for any of the open waveguides are the same for all three cavities.

The window technique was used with the RFA to the calculated data for the finite waveguides, therefore the poles due to the resonant modes from the front rim were missed for both finite waveguides. If the rim resonances were to be extracted, a very wide window could be needed.

G. AIRCRAFT F104

Table 5-15 shows calculated data for the F104 aircraft. (A stick model obtained at the ElectroScience Laboratory by E. Lin [40].) The simplest wire-grid airplane model utilizing 8 wire segments was used in the claculation. The stick model shown in Figure 5-36 is not the wire grid model used by E. Lin; it only shows the orientation. This set of low frequency backscattered data at θ of 0° and ϕ of 0° for horizontal

TABLE 5-15

THE CALCULATED DATA OF F104 AIRCRAFT MODEL*
AT 1 to 12 MHz

"Aspect" θ=0° , ϕ=0°, E_ϕ polarization

Frequency(MHZ)	Normalized Echo Signal
1	.010591-j0.001060
2	.044214-j0.009941
3	.107527-j0.025901
4	.186288-j.061203
5	.281474-j.119757
6	.390186-j.208745
7	.508891-j.337996
8	.632569-j.522298
9	.751477-j.783962
10	.843199-j1.163223
11	.842512-j1.698540
12	.612234-j2.427848

* The fuselage length is 16.69 m and the wing length is 6.68 m.

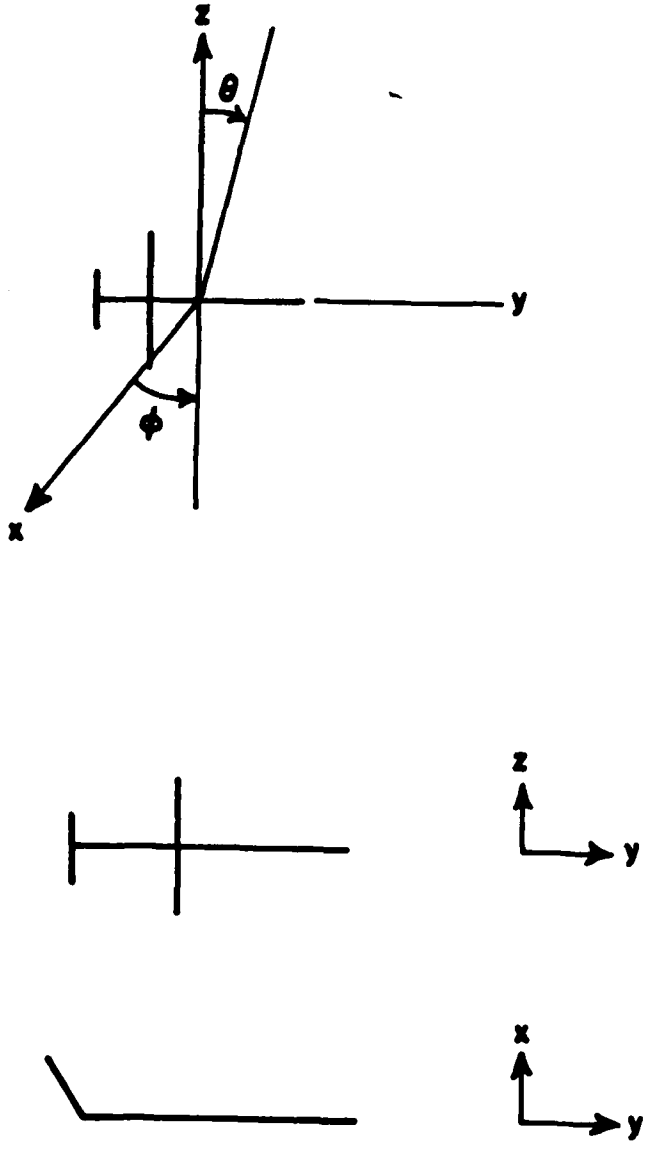

Figure 5-36. The scattering coordinate system for the F104 aircraft. Note the stick model here shows the orientation only, not the real model used in the calculation.

($\hat{\phi}$) polarization as fitted by the rational functional approximant is shown in Figures 5-37 and 5-38.

An extracted pole is listed in Table 5-16 and is compared with that found by Moffatt and Chuang [41] using Prony's method for the same data. The reason that only one pole-pair was extracted is that the data points available were limited to the Rayleigh region. Basically, the wire model used for the aircraft is really a very simple one in the calculations for these data. This example shows that complex natural resonances can sometimes still be extracted even if the imaginary parts of the poles are outside the spectrum of the available data.

TABLE 5-16

THE DOMINANT POLES* OF F104 EXTRACTED VIA
THE RATIONAL FUNCTION APPROXIMANT AND PRONY'S METHOD

Rational Function	Prony's Method (Moffatt & Chuang)
-0.475+/-j2.526	-0.545+/-j2.62

* The units of the poles are ka, where k is the wavenumber and a is one half length of the fuselage.

ZEROS		POLES	
1.132191 X10^{1}	8.300330 X10^{-8}	-4.339201 X10^{-2}	-1.675431 X10^{0}
-5.545548 X10^{0}	1.008805 X10^{-7}	-4.339204 X10^{-2}	1.675431 X10^{0}
-4.344727 X10^{-2}	1.675284 X10^{0}	-4.745941 X10^{-1}	2.526204 X10^{0}
-4.344720 X10^{-2}	-1.675284 X10^{0}	-4.745941 X10^{-1}	-2.526204 X10^{0}
1.364852 X10^{0}	1.251919 X10^{0}	1.370123 X10^{0}	1.079320 X10^{0}
1.364852 X10^{0}	-1.251919 X10^{0}	1.370123 X10^{0}	-1.079920 X10^{0}
-6.809875 X10^{-2}	3.810629 X10^{-1}	-7.083014 X10^{-2}	3.831476 X10^{-1}
-6.809875 X10^{-2}	-3.810629 X10^{-1}	-7.083017 X10^{-2}	-3.831476 X10^{-1}
-3.621376 X10^{-1}	0.000000 X10^{0}	-1.879245 X10^{0}	0.000000 X10^{0}
1.144872 X10^{-1}	2.691892 X10^{-1}	-3.816374 X10^{-1}	-2.350757 X10^{-9}
1.144872 X10^{-1}	-2.691892 X10^{-1}	1.183461 X10^{-1}	3.002626 X10^{-1}
0.000000 X10^{0}	0.000000 X10^{0}	1.183461 X10^{-1}	-3.002525 X10^{-1}
0.000000 X10^{0}	0.000000 X10^{0}		

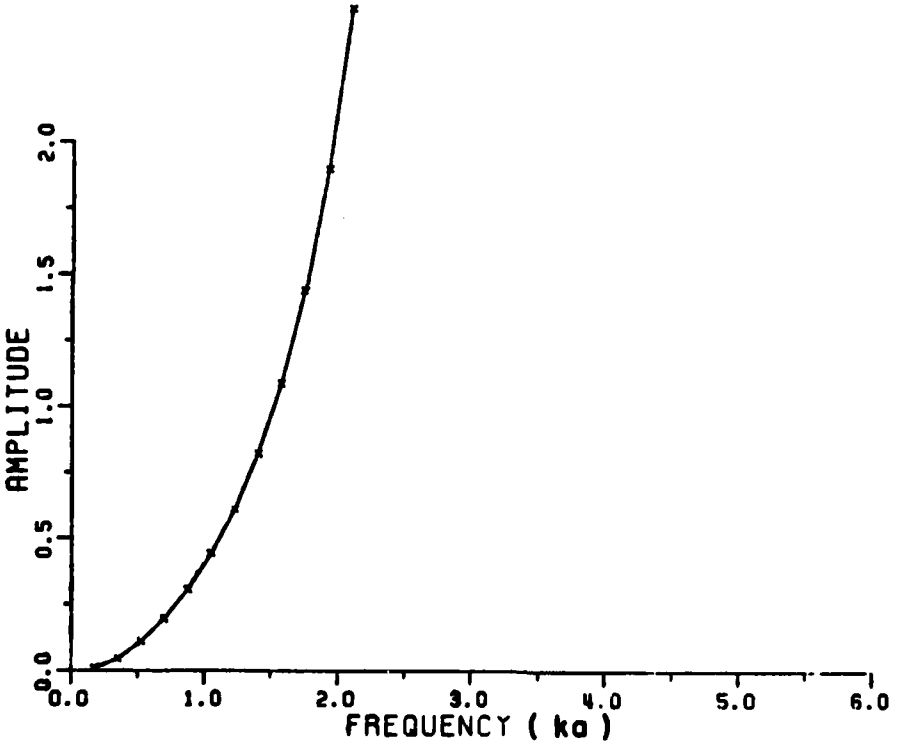

Figure 5-37. The RFA for (M,N) as (12,11) fit to the calculated backscattering data (solid line) for the F104 aircraft at θ of 0°, ϕ of 0° incidence and E_ϕ polarization. The x's are the data points used in the RFA (amplitude plot).

RESI.		MAG. OF RESI.
1.917371 X10^{-4}	-8.032050 X10^{-5}	2.078810 X10^{-4}
1.917216 X10^{-4}	8.036675 X10^{-5}	2.078845 X10^{-4}
-8.374995 X10^{-1}	-2.008180 X10^{0}	2.175820 X10^{0}
-8.374995 X10^{-1}	2.008180 X10^{0}	2.175820 X10^{0}
-5.282340 X10^{-2}	6.765098 X10^{-2}	8.583103 X10^{-2}
-5.282343 X10^{-2}	-6.765101 X10^{-2}	8.583108 X10^{-2}
-1.842414 X10^{-4}	9.897473 X10^{-5}	2.091433 X10^{-4}
-1.842426 X10^{-4}	-9.897077 X10^{-5}	2.091424 X10^{-4}
-1.512233 X10^{0}	1.526751 X10^{-8}	1.512233 X10^{0}
1.345950 X10^{-3}	0.000000 X10^{0}	1.345950 X10^{-3}
4.072582 X10^{-4}	1.538104 X10^{-4}	4.353354 X10^{-4}
4.072582 X10^{-4}	-1.538104 X10^{-4}	4.353354 X10^{-4}

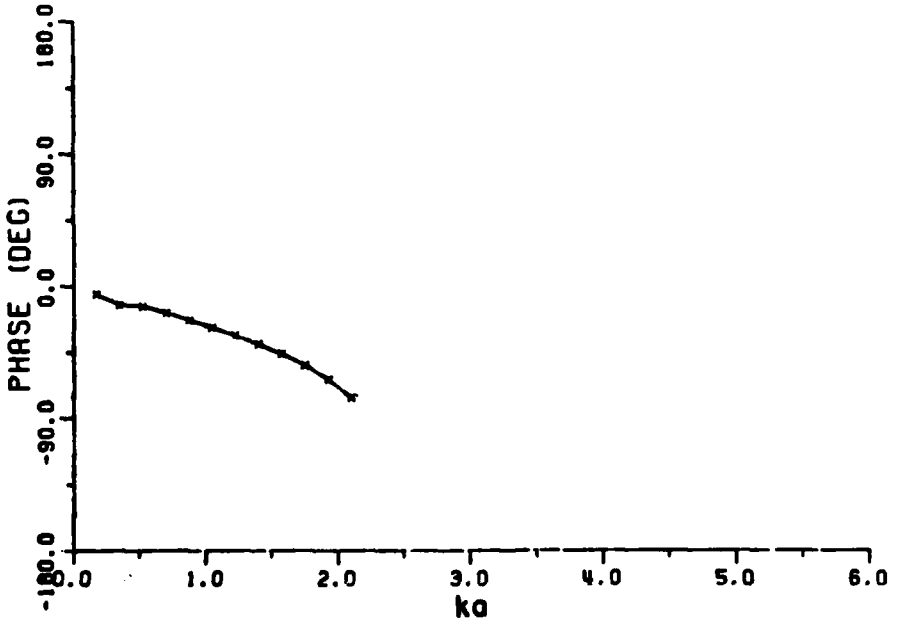

Figure 5-38. The RFA for (M,N) as (12,11) fit to the calculated backscattering (solid line) for the F104 aircraft at θ of 0°, ϕ of 0° incidence and E_ϕ polarization. The x's are the data points used in the RFA (phase plot).

CHAPTER VI

EXTRACTING COMPLEX NATURAL RESONANCES FROM MEASURED DATA

A. INTRODUCTION

The primary goal in this chapter is to describe in some detail a relatively general method for extracting complex natural resonances by applying the RFA to measured scattering data*. Because of the complexity of the target geometry for objects such as aircraft or ships, it is difficult (if not impossible) to formulate and solve the scattering problem even approximately using analytical methods. Thus measured data on some complex targets are necessary, particularly if broadband results are needed. In this chapter, measured data of two commercial passenger aircraft scale models are used. Sufficient detail

---

* The scattering data on complex targets were obtained from measurements being made on a noncooperative target recognition (NCTR) program in progress at the ElectroScience Laboratory. The targets are primarily fighter or other aircraft. Since no existing complex natural resonances are available for comparison for these targets, we shall only identify them by type, e.g., aircraft A, B etc. The analysis methods are adequately explained in applications to simple targets. This approach will circumvent any possible future classification problems while in no way diminishing the application results.

of RFA applications have been given on the simple targets, but it is important that the techniques developed herein be applied to measured data on real complex (geometry) targets. At the same time, classification problems are avoided by not specifically identifying the targets.

B. AMPLITUDE AND PHASE PLOTS

An advanced state-of-the-art broadband radar reflectivity measurement facility is under development at the ElectroScience Laboratory of the Ohio State University [42]. Detailed procedures for the measurement and data processing are not discussed here but it is helpful to present some of the scattering data as a function of frequency for the scale model targets. The coordinate system and the target orientation (aircraft shown in stick form only) which were used in the measurements are shown in Figure 6-1. The aircraft is aligned with wings and fuselage in the xy plane (nose in the positive x with direction and vertical stabilizer in the z direction). Vertical polarization is identified as measurements with the electric field polarized in the z direction and horizontal polarization as measurements with the electric field polarized in the xy plane.

For horizontal polarization, the complex data were taken in the frequency band of 1.5 GHZ to 6.5 GHZ in 500 steps for aircraft A. Also measured data in 1-2 GHz, 2-4 GHz, and 4-6 GHz bands (200 steps in each band) were taken for vertical polarization for aircraft A and 1.0 to 6.5

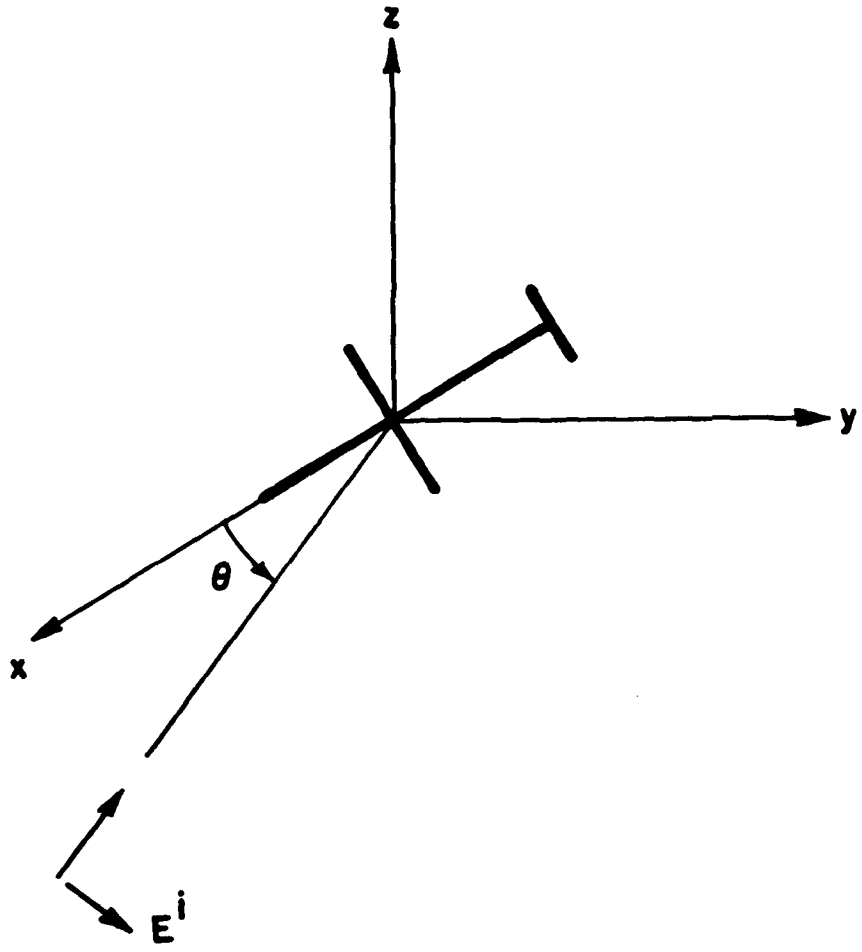

Figure 6-1. The scattering coordinate system of a transportation aircraft aligned with the fuselage along the x axis (nose in the x direction) with wings in xy plane.

GHz (550 steps) for aircraft B. Figures 6-2 and 6-3 (amplitude plots) and Figures 6-4 and 6-5 (phase plots) are the spectrum at aspect angles of 0°, 20°, 30°, 45°, 50° off the nose for horizontal polarization for aircraft A. Figures 6-6 and 6-7 are amplitude and phase plots for vertical polarization at aspect angles of 0°, 15°, and 30° off nose-on for aircraft A, and Figures 6-8 to Figure 6-11 are plots (Figure 6-8 and 6-9 amplitude, Figure 6-10 and 6-11 phase) for vertical polarization at 0°, 30°, 60°, 90°, 135°, 180° off nose-on for aircraft B. The amplitude is $\sqrt{\sigma}$ and is in the units of cm, where σ is the radar cross section (RCS) on a linear scale. (The RCS is in the units of cm^2.)

The plots of the spectra are shown here because the number of peaks in the amplitude plots are clues for determining the system order. Furthermore, as will be seen later, the imaginary part of the extracted poles are near most of those peaks. A comparison of the amplitude plots of the measured data for aircraft A at horizontal and vertical polarizations from nose-on is shown in Figure 6-12. All of these plots shown in this Chapter have been smoothed by the zero-phase-shift digital filter given in Appendix B.

It is difficult to smooth noisy data precisely (without any distortion of the signal) because the transient responses vary in length for various targets, aspects, and polarizations. However, strongly excited poles will not be influenced much as long as the cut-off frequency of the zero-phase low-pass digital filter is properly designed.

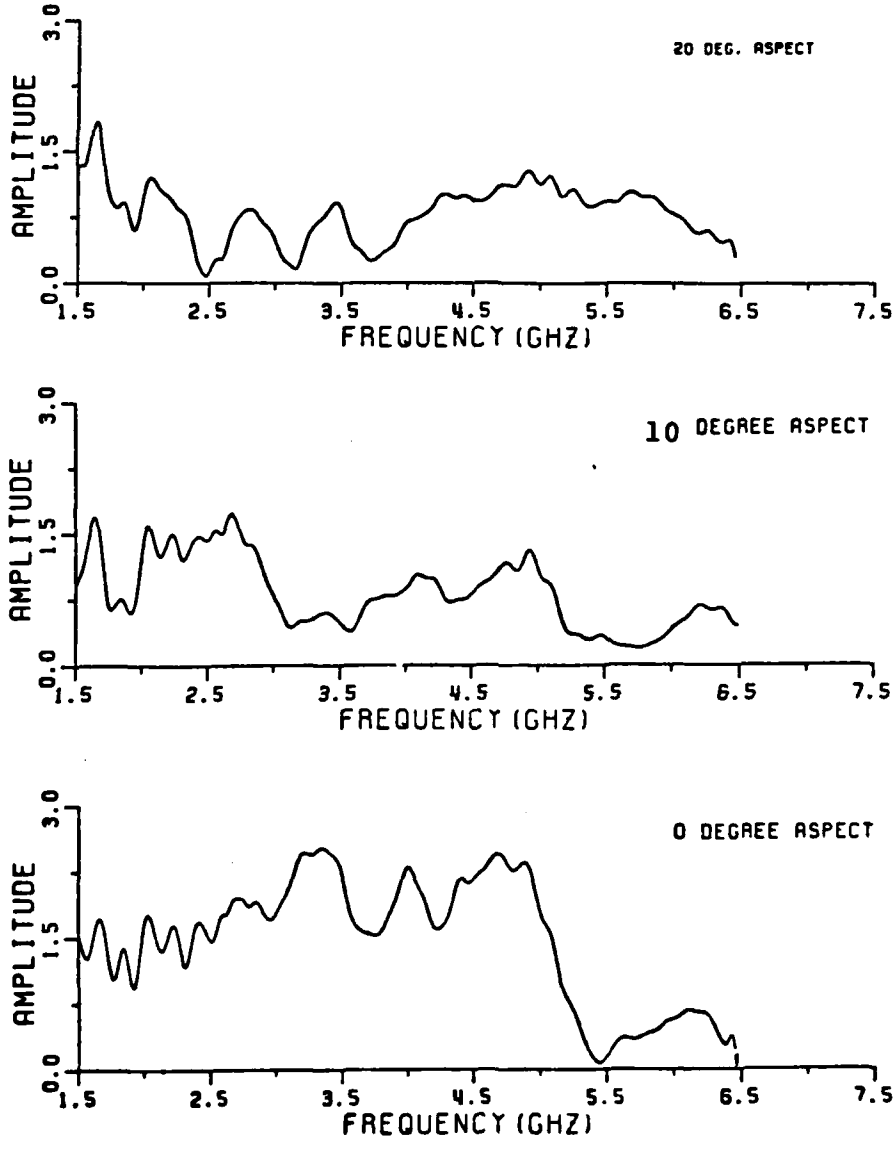

Figure 6-2. The backscattered amplitude for commercial transportation aircraft A at 0°, 10°, and 20° from nose-on for horizontal polarization.

AD-A143 913 APPROXIMATE METHODS FOR OBTAINING THE COMPLEX NATURAL ELECTROMAGNETIC OSC..(U) OHIO STATE UNIV COLUMBUS ELECTROSCIENCE LAB T C LEE ET AL. FEB 84 ESL-710016-16 3/4

UNCLASSIFIED N00014-78-C-0049 F/G 20/3 NL

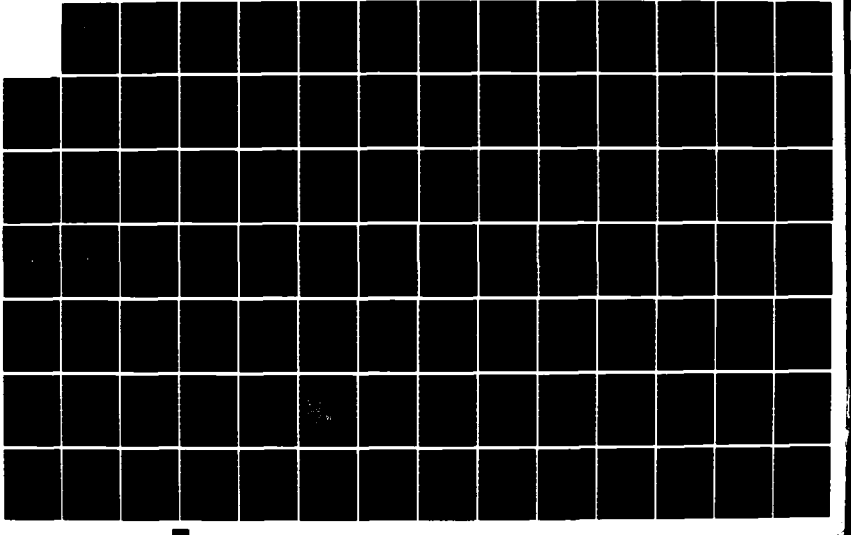

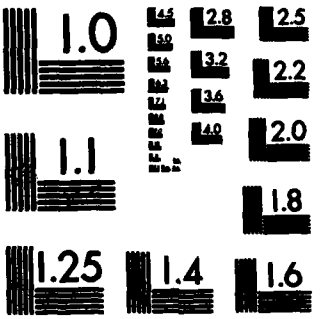

MICROCOPY RESOLUTION TEST CHART
NATIONAL BUREAU OF STANDARDS-1963-A

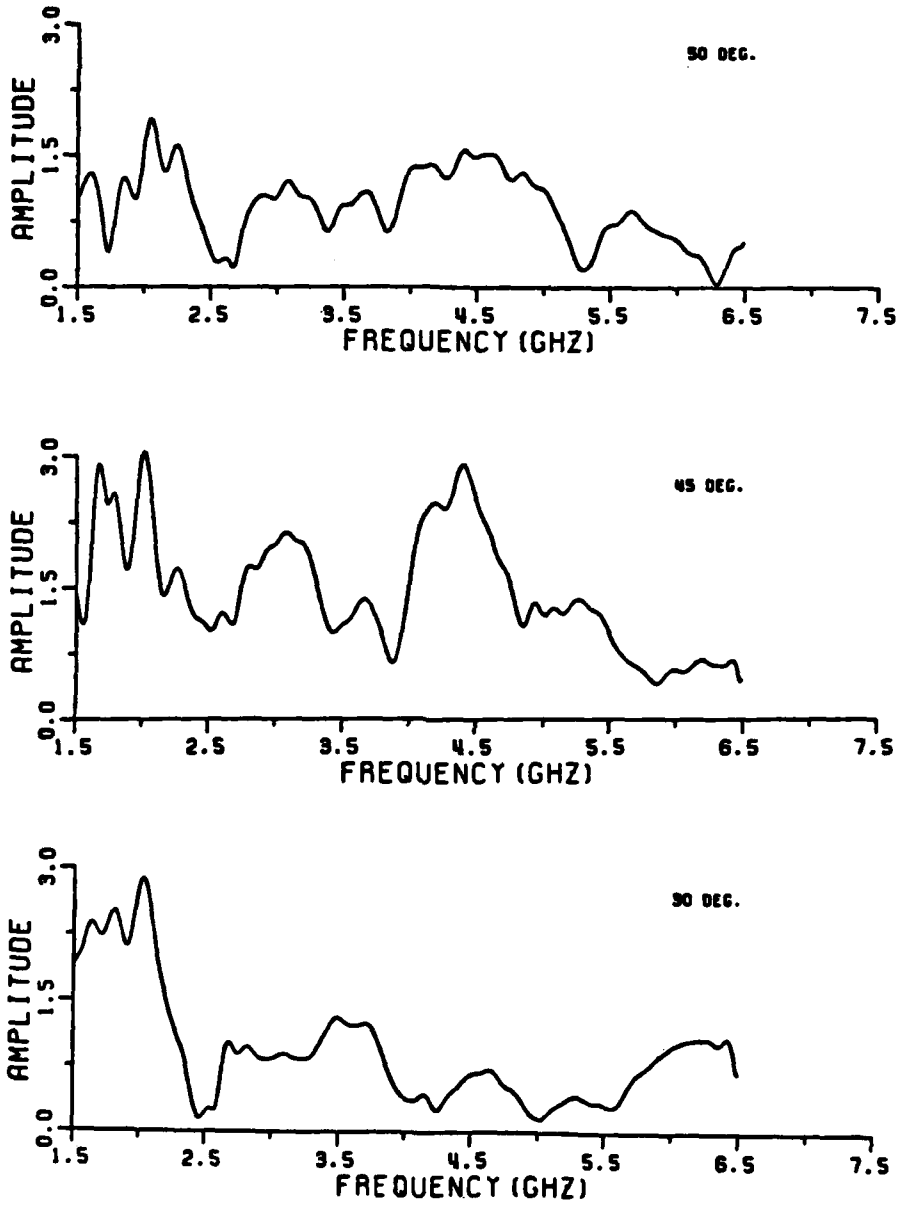

Figure 6-3. The backscattered amplitude for commercial transportation aircraft A at 30°, 45°, and 50° from nose-on for horizontal polarization.

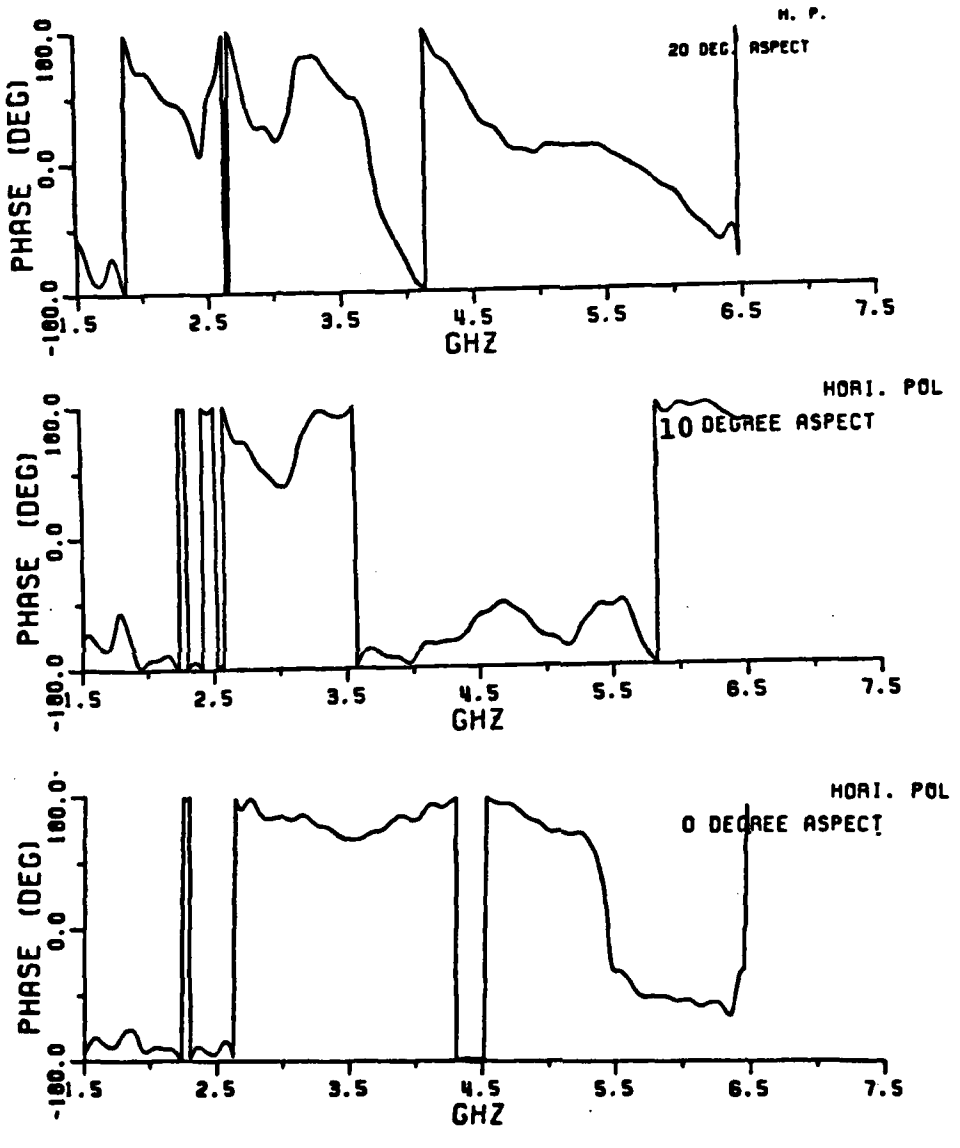

Figure 6-4. The backscattered phase for commercial transportation aircraft A at 0°, 10°, and 20° from nose-on for horizontal polarization.

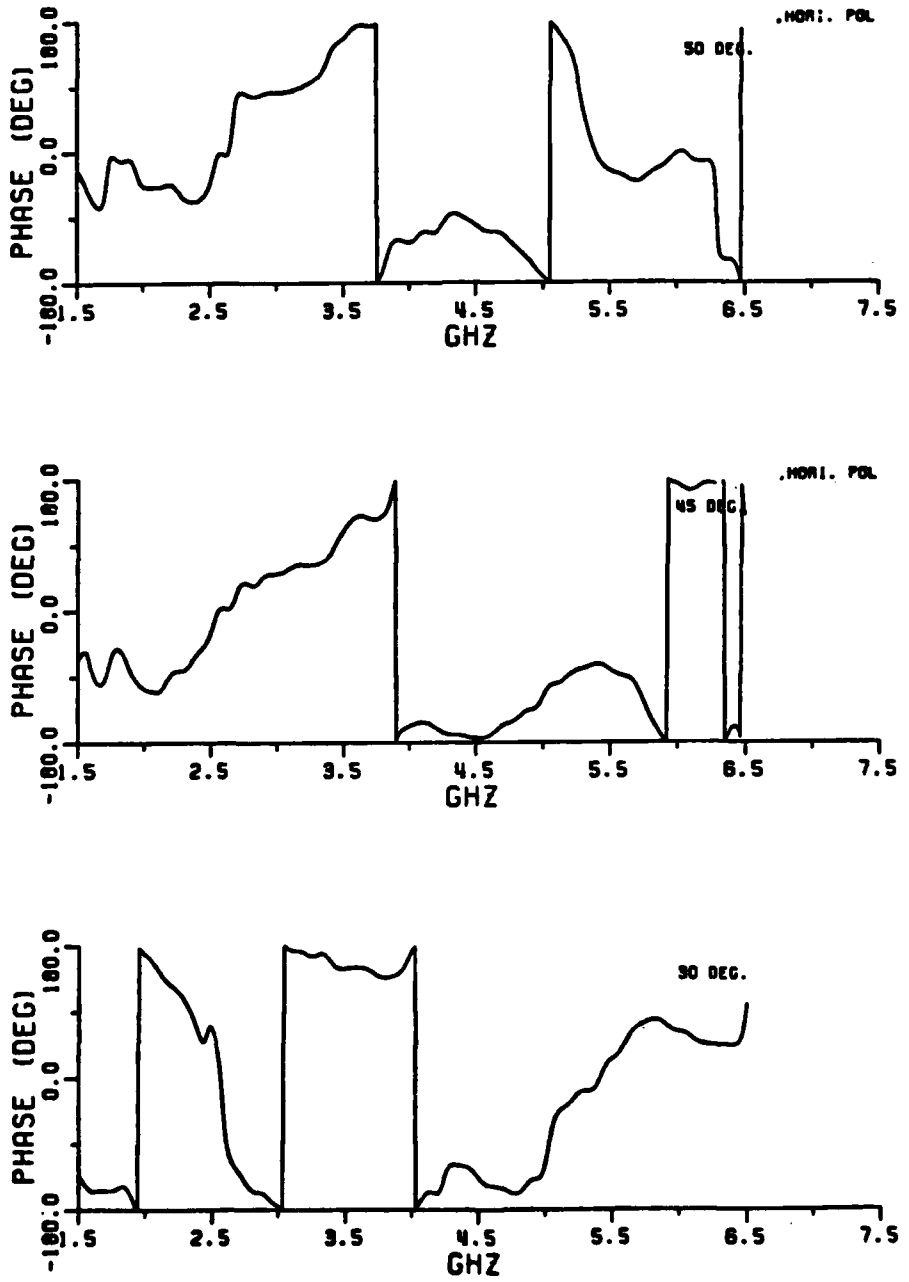

Figure 6-5. The backscattered phase for commercial transportation aircraft A at 30°, 45°, and 50° from nose-on for horizontal polarization.

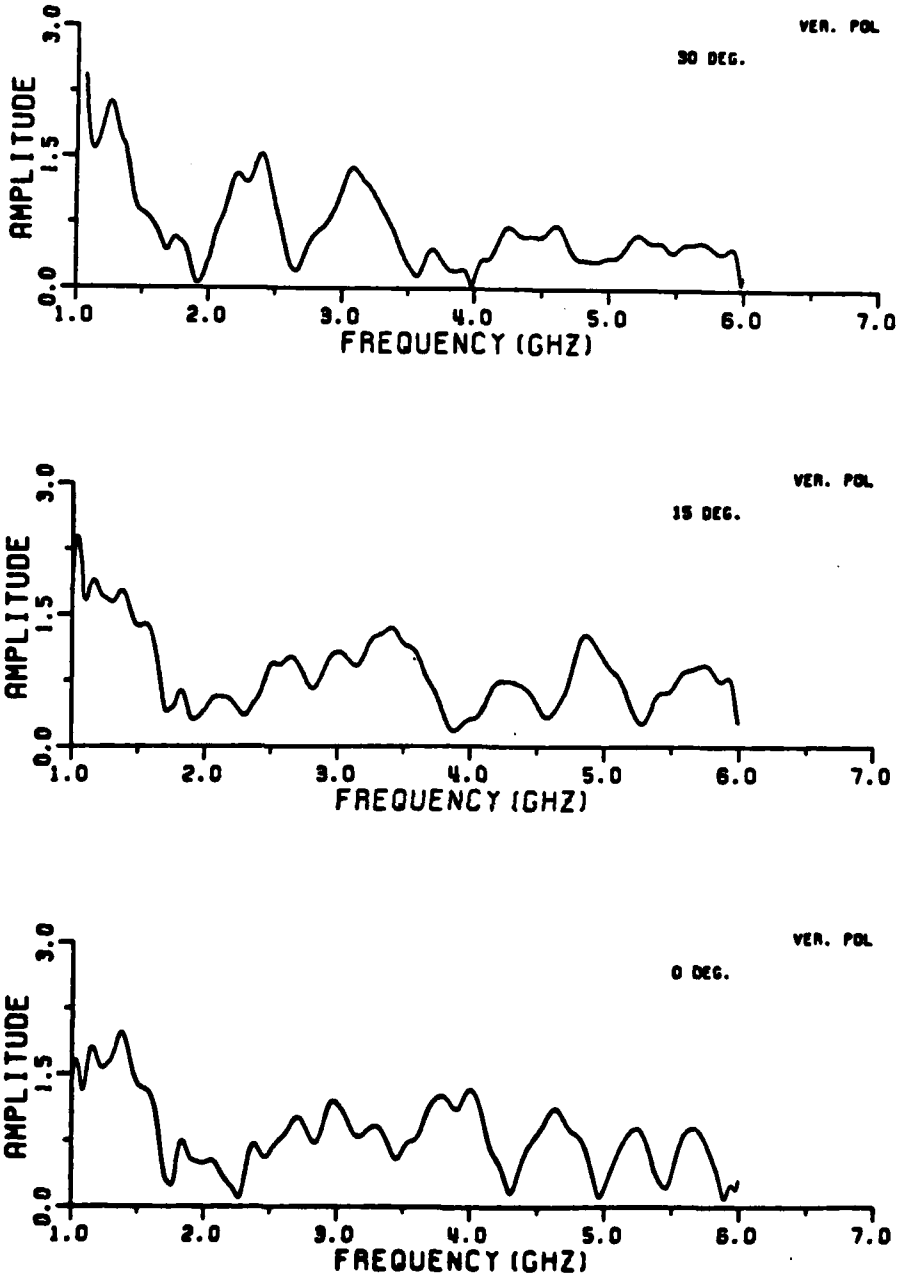

Figure 6-6. The backscattered amplitude for commercial transportation aircraft A at 0°, 15°, 30° from nose-on for vertical polarization.

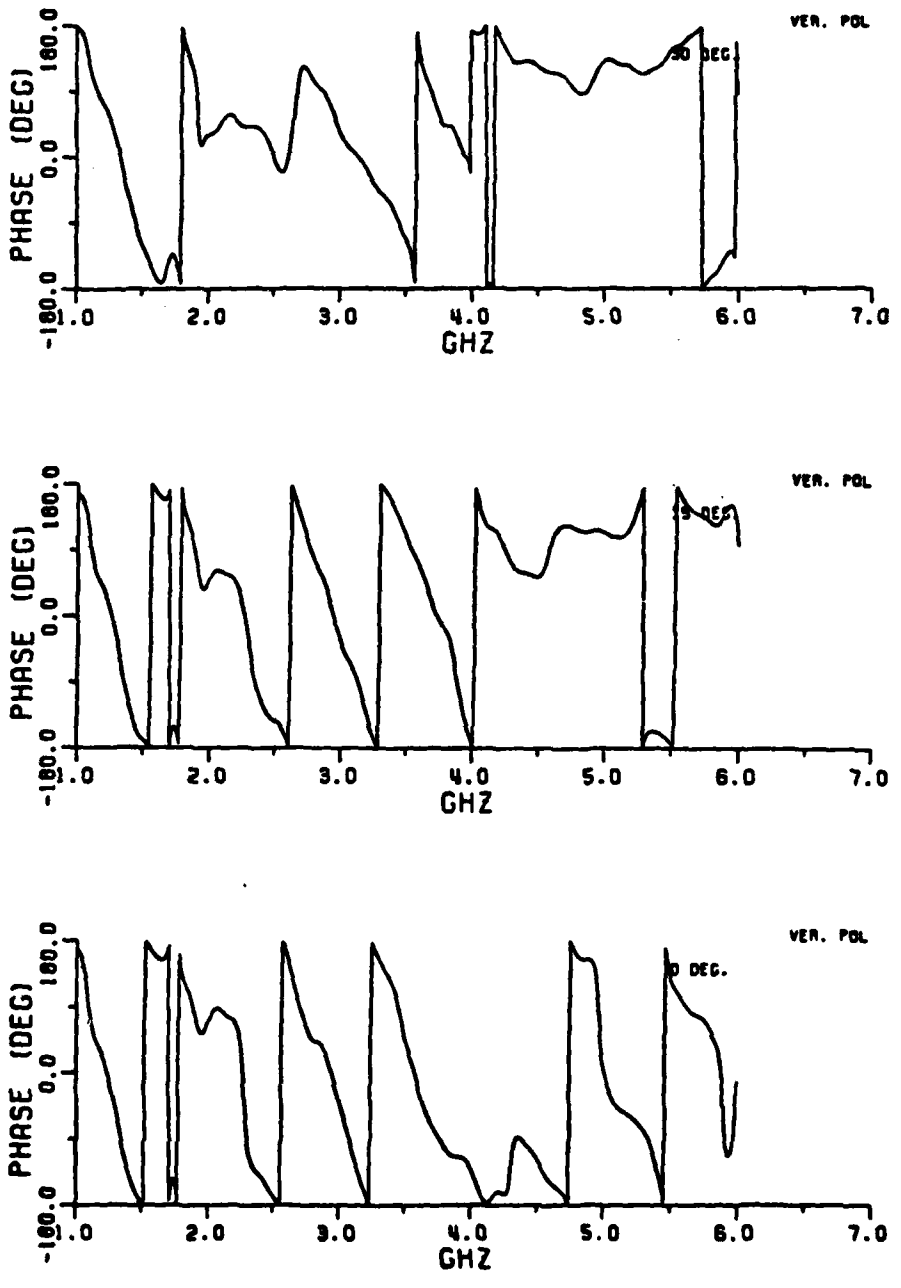

Figure 6-7. The backscattered phase for passenger transportaion aircraft A at 0°, 15°, and 30° from nose-on for vertical polarization.

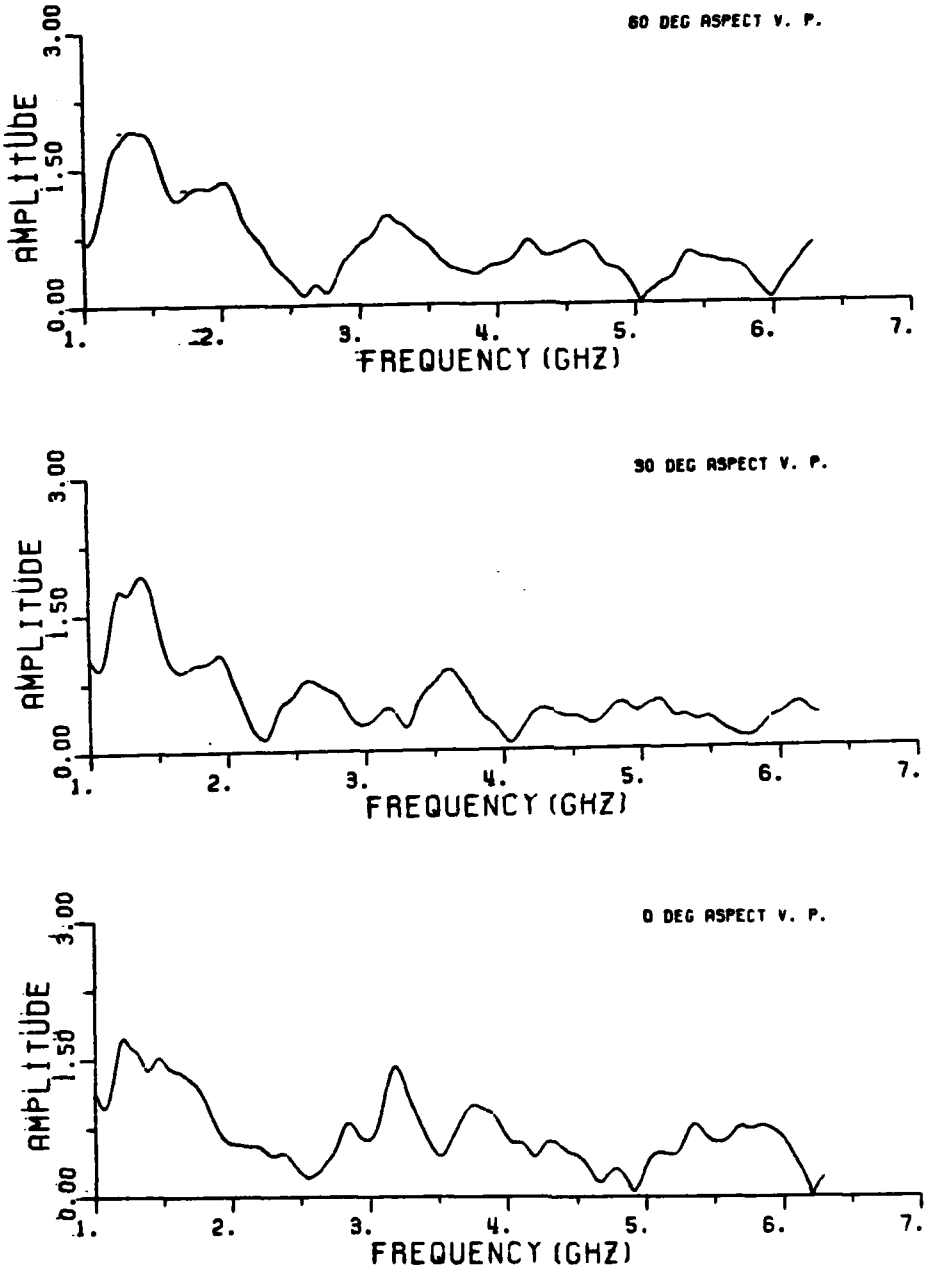

Figure 6-8. The backscattered amplitude for the commercial transportation aircraft B at 0^{o}, 30^{o}, and 60^{o} from nose-on for vertical polarization.

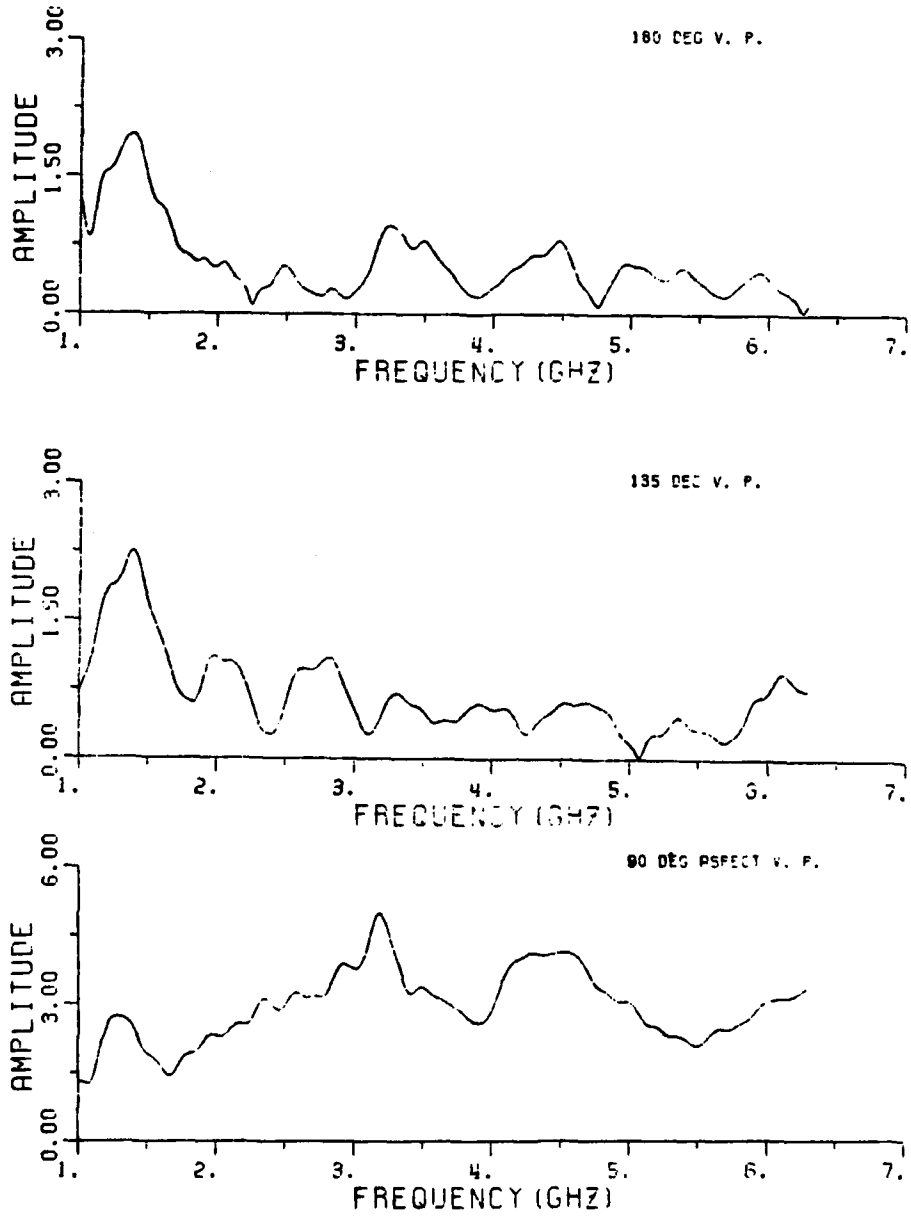

Figure 6-9. The backscattered amplitude for commercial transportation aircraft B at 90°, 135°, and 180° from nose-on for vertical polarization.

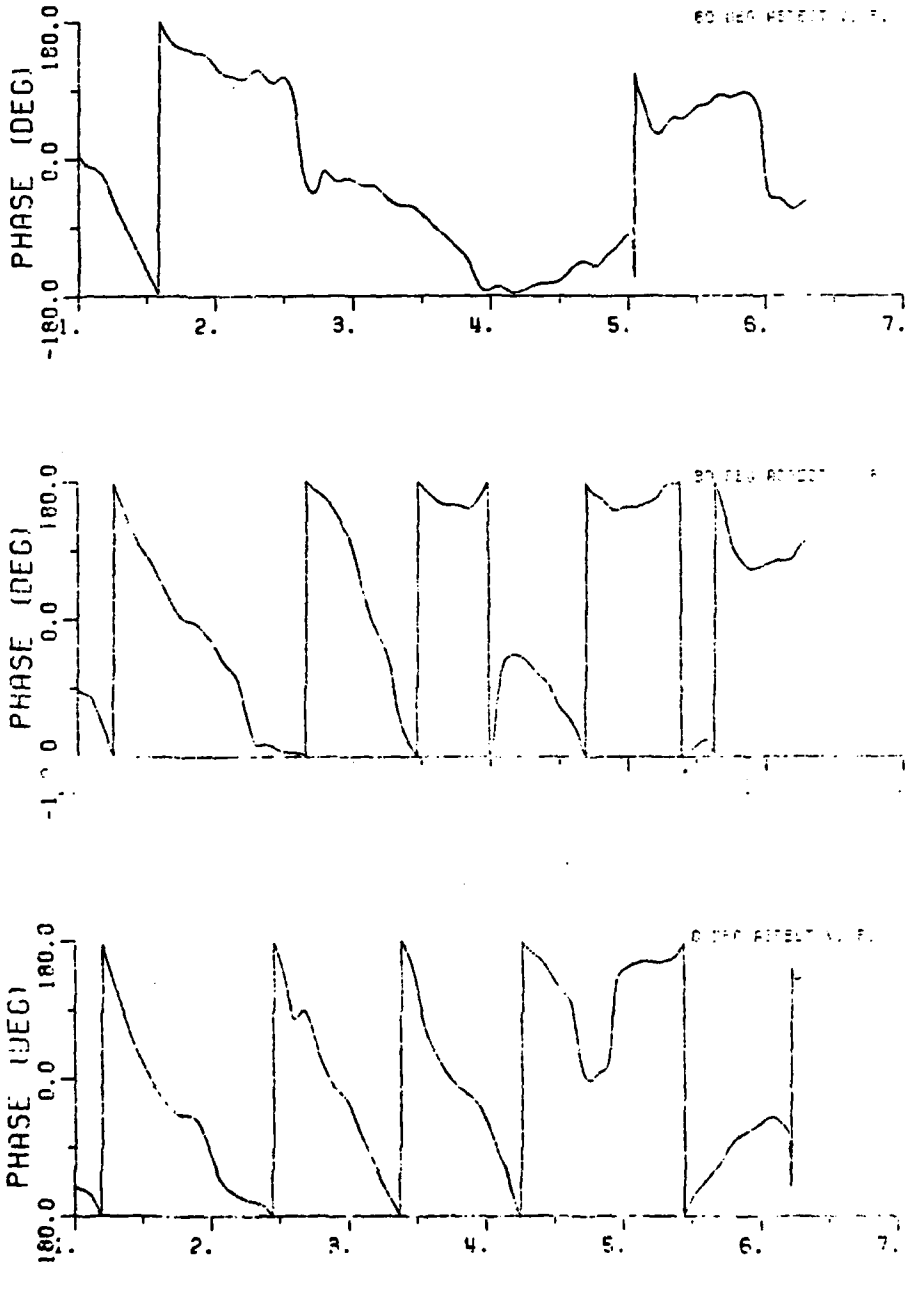

Figure 6-10. The backscattered phase for commercial transportation aircraft B at 0°, 30°, and 60° from nose-on for vertical polarization.

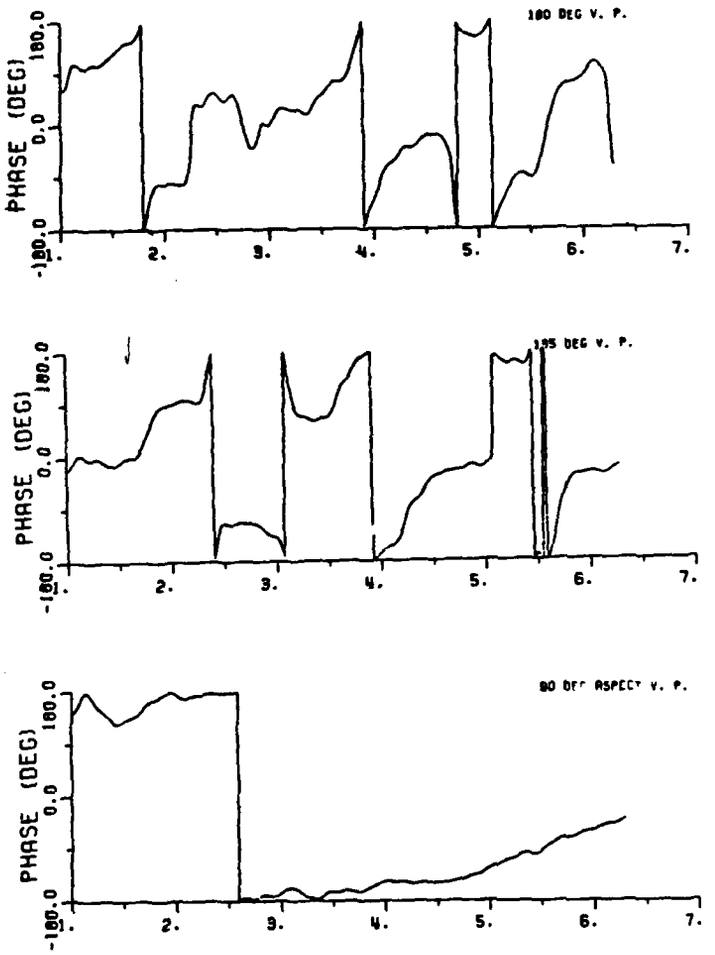

Figure 6-11. The backscattered phase for commercial transportation aircraft B at 90°, 135°, and 180° from nose-on for vertical polarization.

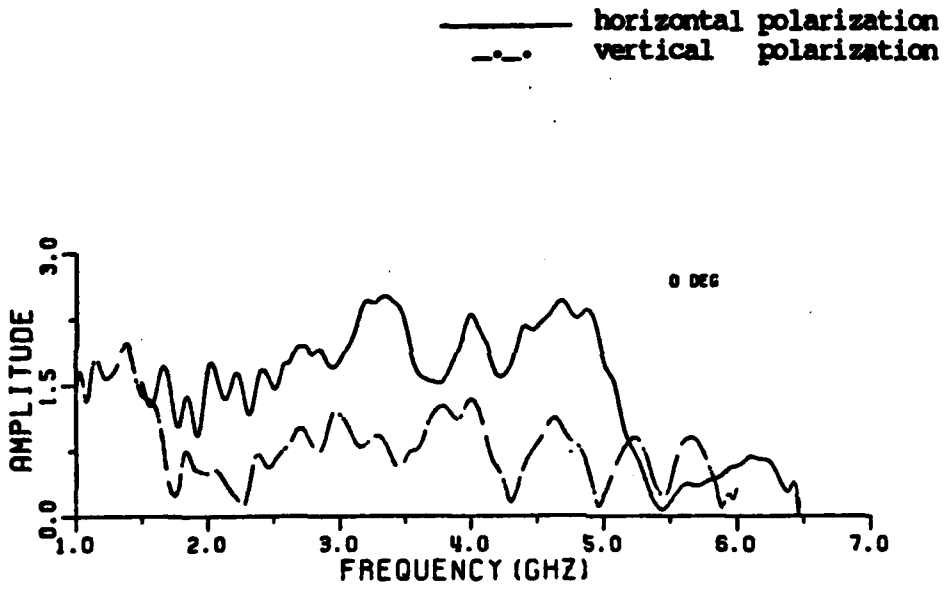

Figure 6-12. A comparison of the backscattering amplitude for the commercial transportation aircraft A at nose-on incidence for horizontal and vertical polarizations.

Normally 4 TAU width for the time-domain window (TAU is 2a/c, where a is a characteristic target length) is a good choice for most targets. Some targets however should have windows (the 3 dB cut-off frequency of the digital low-pass filter) wider than 4 TAU. Such targets have resonances with small damping such as, e.g., the circular loop. The cut-off frequency of the filter in the plots of Figures 6-2 to 6-8 is set to 23 Hz; and the sampling rate of the digital filter is assumed to be 500 Hz. The folding frequency is 250 Hz. The corresponding time-domain window width is therefore roughly 4 TAU for this cutoff frequency of 23 Hz. The sampling intervals in the spectra are 10 MHz. Typical examples of oversmoothing using zero-phase-shift digital filters are shown in Figures 6-13 to 6-16. The 3dB cut-off frequency is set to f_c of 11.5 Hz, i.e., 2 TAU lengths in the time domain. It has been found that some of the true poles were missed if oversmoothed data are used in the rational function approximation. Typical plots of the oversmoothed data for aircraft A are shown in Figures 6-13 and 6-14 (horizontal polarization), and in Figures 6-15 and 6-16 (vertical polarization) at nose on incidence. Obviously, these plots show that higher order scattering was filtered out. Oversmoothing results in loss of some weak resonances. To filter out noise and clutter, plots of the impulse response are necessary. The impulse response helps select f_c, the 3 dB cutoff frequency, of the digital filter as will be shown in section D of this chapter.

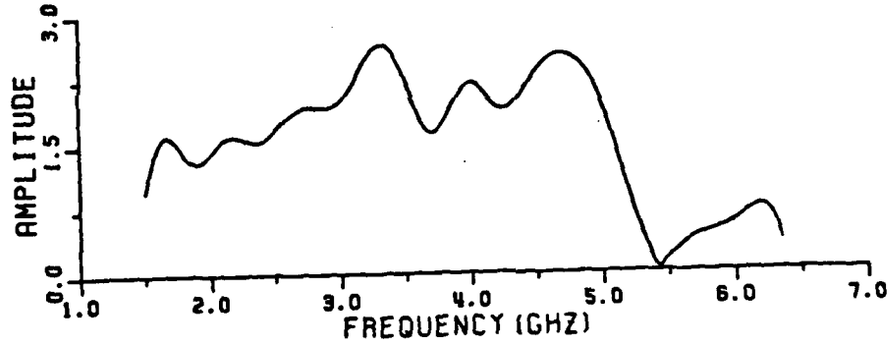

Figure 6-13. An amplitude plot of the backscattering data for commercial transportation aircraft A at nose-on. The measured data are oversmoothed by a zero-phase-shift digital filter.

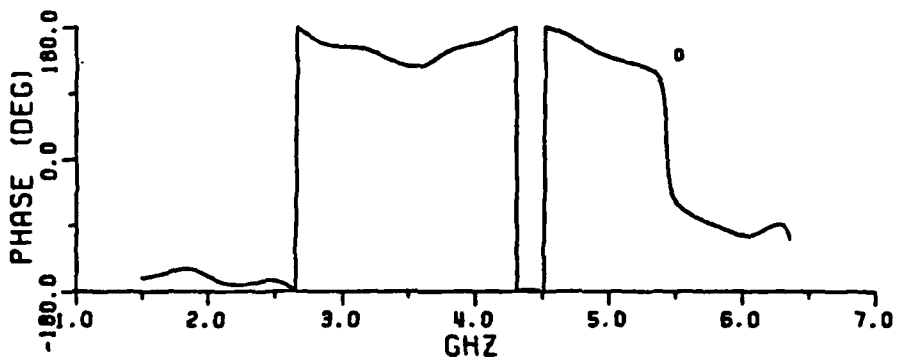

Figure 6-14. A phase plot of the backscattering data for commercial transportation aircraft A at nose-on. The measured data are oversmoothed by a zero-phase-shift digital filter.

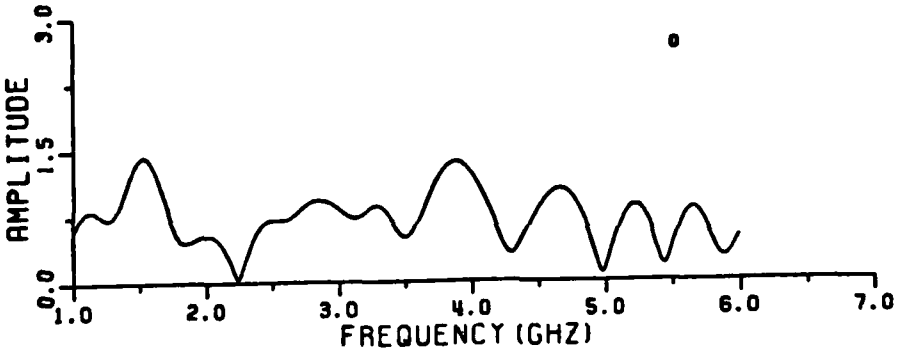

Figure 6-15. An Amplitude plot of the backscattering data for commercial transportation aircraft A at nose-on for vertical polarization. The data are oversmoothed by the zero-phase-shift digital filter.

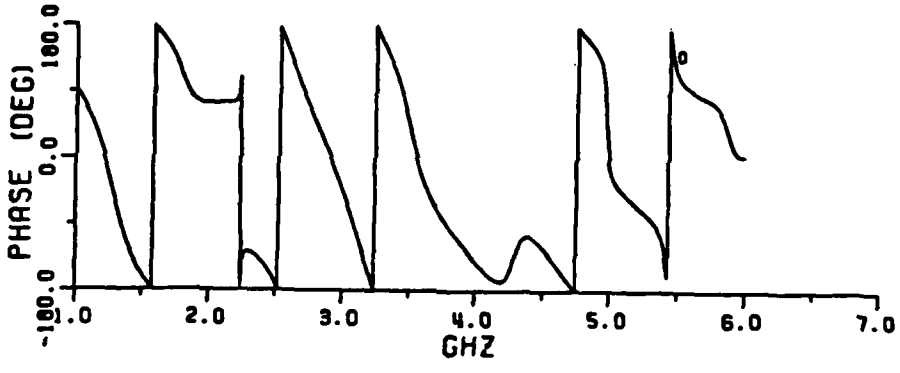

Figure 6-16. A phase plot of the backscattering data for commercial transportation aircraft A at nose-on for vertical polarization. The data are oversmoothed by the zero-phase-shift digital filter.

C. EXTRACTING THE COMPLEX NATURAL RESONANCE FROM THE MEASURED DATA

After RFA have been developed, it is relatively routine to apply the programs to measured data. The following features should be noted:

1. The measured data sets are smoothed by a low pass 10th order zero phase digital filter. The 3dB cutoff frequency of the low pass digital filter is movable.
2. The window technique is used with the RFA. This window is generated simply by taking sample points over a band limited region of the spectrum. The window used for the RFA is a very powerful tool for extracting the poles, because there are usually too many resonances within the spectrum to be covered by one RFA.
3. The system order is set at around twice the number of amplitude peaks in the spectrum covered by the window.
4. Several different sets of data points and system orders are tested at each window, and only the poles which are unchanged for more than two selected data sets are considered as candidate poles.
5. The window is chosen such that the magnitude of the fitted data lying outside the window is as small as possible. Thus, both end points of the window should be at relatively minimum amplitudes or at least on a portion of the negative slope.

1. Aircraft A

The complex natural resonances of the transportation aircraft A at 0°, 30°, 45°, 60°, 90°, 120°, 150°, 165°, and 180° aspect angles as extracted from the backscattering data in the 1-2 GHz band for horizontal polarization are given in Table 6-1. The 1-2 GHz and 2-4 GHz bands are treated individually because the measured data sets for these bands were taken separately. Table 6-2 lists the extracted poles from the backscattered data at 0°, 15°, 30°, 45°, 60°, 75°, 105°, 165°, and 180° aspect angles for the aircraft A and for the horizontal polarization in the 2-4 GHz band. However, the rational function approximation windows are set at 2-3 GHz only. The pole locations found are relatively aspect independent.

Table 6-3 shows the extracted poles for horizontal polarization at aspect angles of 0°, 10°, 20°, and 30° as found using 1.5 to 6 GHz band data. In order to compare with the other polarization (vertical polarization) only data in the 1.5 GHz to 3.0 GHz band were used. The extracted poles are relatively aspect independent. Note that more poles are excited for horizontal polarization than for vertical polarization.

2. Aircraft B

The complex natural resonances of aircraft B were extracted using the RFA and window techniques for data at 0°, 90°, and 135° from nose-on in the 1 to 2 GHz band. The extracted poles are listed in Table 6-4. The poles are relatively aspect independent and the pole sets for the

TABLE 6-1

THE COMPLEX NATURAL RESONANCES* FOR COMMERCIAL AIRCRAFT A OBTAINED FROM THE RATIONAL FUNCTION APPROXIMATION TO THE MEASURED DATA (BACKSCATTER, VERTICAL POLARIZATION, 1-2 GHz).

1-2 GHz

0°.	30°	45°
-0.082 +/-j1.082	-0.104+/-j1.034	-0.05+/-j1.07
not located	-0.093+/-j1.16	-0.06+/-j1.18
-0.092 +/-j1.318	-0.116+/-j1.338	-0.10+/-j1.33
-0.783 +/-j1.588	-0.085+/-j1.554	-0.07+/-j1.52
-0.645 +/-j1.765	-0.045+/-j1.73	-0.09+/-j1.71
-0.0755+/-j1.915	-0.05 +/-j2.06	-0.14+/-j1.95
60°	**90°**	**120°**
-0.068+/-j1.077	-0.035+/-j1.057	-0.039+/-j1.03
-0.082+/-j1.187	-0.031+/-j1.171	-0.06 +/-j1.11
-0.102+/-j1.34	-0.11 +/-j1.39	-0.10 +/-j1.33
-0.082+/-j1.53	-0.15 +/-j1.574	-0.07 +/-j1.54
-0.056+/-j1.71	-0.063+/-j1.775	-0.08 +/-j1.77
-0.091+/-j1.956	-0.11 +/-j1.95	-0.073+/-j1.934
150°	**165°**	**180°**
-0.051 +/-j1.053	-0.53 +/-j1.036	-0.058+/-j1.05
-0.052 +/-j1.18	-0.057+/-j1.141	-0.062+/-j1.161
-0.092 +/-j1.351	-0.056+/-j1.383	-0.084+/-j1.324
-0.09 +/-j1.559	-0.057+/-j1.572	-0.057+/-j1.512
-0.0936+/-j1.72	-0.055+/-j1.726	-0.040+/-j1.749
-0.093 +/-j1.959	-0.11 +/-j1.94	-0.029+/-j1.905

* The units of the poles are in GHz.

TABLE 6-2

THE COMPLEX NATURAL RESONANCES* FOR COMMERCIAL AIRCRAFT A OBTAINED FROM THE RATIONAL FUNCTION APPROXIMATION TO THE MEASURED DATA (BACKSCATTER, VERTICAL POLARIZATION, 2-3 GHz).

2-3 GHz

Aspect Angle 0°	Aspect Angle 15°	Aspect Angle 30°
-0.02 +/-j1.996		-0.008+/-j2.019
-0.108+/-j2.328	-0.146+/-j2.291	-0.068+/-j2.20
-0.07 +/-j2.681	-0.107+/-j2.665	-0.10 +/-j2.51
-0.068+/-j2.974	-0.100+/-j2.967	-0.08 +/-j2.72
		-0.192+/-j3.00
45°	60°	75°
-0.05 +/-j2.13	-0.047+/-j1.94	-0.053+/-j2.109
-0.09 +/-j2.37	-0.091+/-j2.22	-0.127+/-j2.317
-0.027+/-j2.65	-0.09 +/-j2.49	-0.08 +/-j2.593
-0.047+/-j2.94	-0.12 +/-j2.79	-0.097+/-j2.922
	-0.10 +/-j2.93	
105°	165°	180°
-0.051+/-j2.019	-0.099+/-j2.089	-0.117+/-j2.16
-0.079+/-j2.36	-0.128+/-j2.21	-0.105+/-j2.29
-0.07 +/-j2.61	-0.016+/-j2.362	-0.09 +/-j2.47
-0.047+/-j2.86	-0.037+/-j2.62	-0.09 +/-j2.88
-0.06 +/-j2.97	-0.032+/-j2.97	-0.16 +/-j3.00

* The units of the poles are in GHz.

TABLE 6-3

THE COMPLEX NATURAL RESONANCES* FOR COMMERCIAL AIRCRAFT A OBTAINED FROM THE RATIONAL FUNCTION APPROXIMATIONS TO THE MEASURED DATA (BACKSCATTER, HORIZONTAL POLARIZATION, 1.5-3 GHz).

0°	10°	20°	30°
(-0.12,1.55)	(-0.13,1.58)	(-0.057,1.513)	(-0.08,1.52)
(-0.14,1.69)	(-0.12,1.69)	(-0.12,1.67)	(-0.056,1.65)
(-0.11,1.75)	(-0.12,1.73)	(-0.11,1.79)	(-0.086,1.78)
(-0.10,1.81)	(-0.13,1.801)	(-0.14,1.85)	(-0.095,1.88)
(-0.08,1.93)	(-0.12,1.95)	(-0.10,1.93)	(-0.052,1.93)
(-0.24,2.00)	(-0.14,2.02)	(-0.10,2.06)	(-0.046,2.03)
(-0.08,2.16)	(-0.09,2.18)	(-0.07,2.17)	(-0.098,2.15)
(-0.15,2.22)	(-0.10,2.27)	(-0.57,2.21)	(-0.063,2.23)
(-0.10,2.34)	(-0.13,2.34)	(-0.11,2.36)	(-0.16,2.37)
(-0.07,2.57)	(-0.16,2.52)	(-0.05,2.54)	(-0.123,2.55)
(-0.09,2.63)	(-0.23,2.62)	(-0.19,2.67)	(-0.03,2.66)
(-0.10,2.76)	(-0.104,2.80)	(-0.57,2.86)	(-0.06,2.79)
(-0.14,2.99)	(-0.13,2.98)	(-0.14,2.94)	(-0.03,3.04)

* The poles are in the units of GHz

TABLE 6-4

THE COMPLEX NATURAL RESONANCES* OF AIRCRAFT B AT 0°, 90°, and 135° FROM NOSE-ON INCIDENCE FOR VERTICAL POLARIZATION

0°	90°	135°
-0.073+/-j1.095	-0.21+/-j1.097	-0.165+/-j1.023
-0.19+/-j1.232	-0.26+/-j1.25	-0.183+/-j1.214
-0.24+/-j1.450	-0.19+/-j1.47	-0.129+/-j1.437
-0.48+/-j1.628	-0.19+/-j1.66	-0.51+/-j1.65
		-0.07+/-j1.88
-0.21+/-j1.956		-0.18+/-j1.953

* The poles are in the units of GHz. The RFA fit in the 1-2 GHz band.

two aircraft are not the same. Therefore, it would appear that the pole sets could be used for the purpose of classification.

One of the characteristics of the complex natural resonances, polarization invariance, can be tested by comparing Table 6-1 to 6-3. It is well-known that the complete set of complex natural resonances of an object may not be optimally excited for one polarization or for one aspect angle. For example, a wire for broadside incidence has only even modes excited; at other aspects both even and odd modes are excited. But the total resonances of the wire include both even and odd resonances. Similarly, if the target has poles which are more strongly excited with horizontal polarization than with vertical polarization then more poles are extracted from the measured aircraft data for horizontal polarization. Portions of the extracted poles are nearly the same for both polarizations.

D. IMPULSE RESPONSES OF THE AIRCRAFT

Our purpose here is to plot some of the band limited impulse response waveforms of the aircraft using Fourier synthesis. We use an inverse Fast Fourier Transform (IFFT) to implement the Fourier synthesis and a smoothing window is used to eliminate the Gibbs' phenomenon. The window (W(n)) used here is

$$W(n) = \begin{cases} \dfrac{\sin\frac{2\pi n}{N}}{\frac{2\pi n}{N}} \cdot \dfrac{\left(\frac{N}{2}\right)^2}{\left(\frac{N}{2}\right)^2 - n^2} & \text{for } n \text{ not equal } N/2 \\ 1/2 & \text{for } n \text{ of } N/2 \end{cases} , \quad (6\text{-}1)$$

where N is the total number of samples. Study of the transient response waveforms for the aircraft is not for the purpose of target identification but rather for deciding the 3 dB cutoff frequency for the digital filter. Then, the noise and clutter can be reduced from the frequency domain measured data using a digital filter with proper cutoff frequency. Typical impulse responses for a transportation aircraft at some different aspect angles and for both polarizations are shown at the end of this section. The rough geometry of the aircraft is sketched indicating aircraft orientation and incident wave polarization for each impulse response waveform.

E. BRIEF SUMMARY AND DISCUSSION

In this dissertation no effort is made to relate features of the impulse response waveforms shown to geometrical features of the aircraft. To do so might compromise the actual identity of the targets and is not essential for any purpose. Both aircraft show response waveforms which ring for relatively long times, indicating that signals are bouncing between various structures. Given the actual size and shape of the aircraft, most of the dominant scattering mechanisms can be identified. For our purpose, it is also clear that an

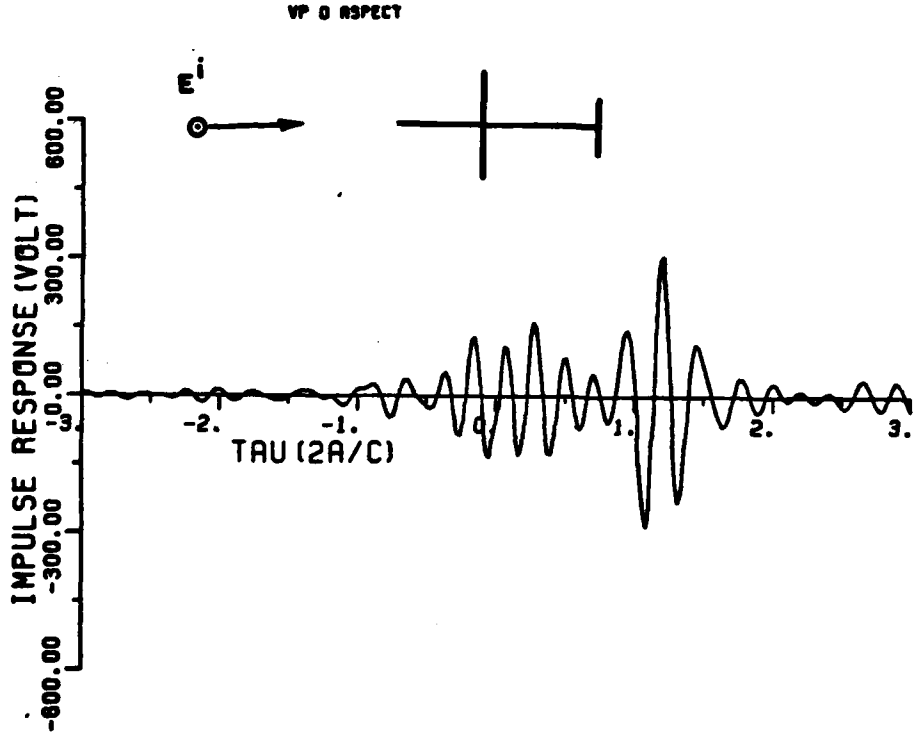

Figure 6-17. Backscattered impulse response waveform of commercial transportation aircraft A at nose-on incidence for vertical polarization.

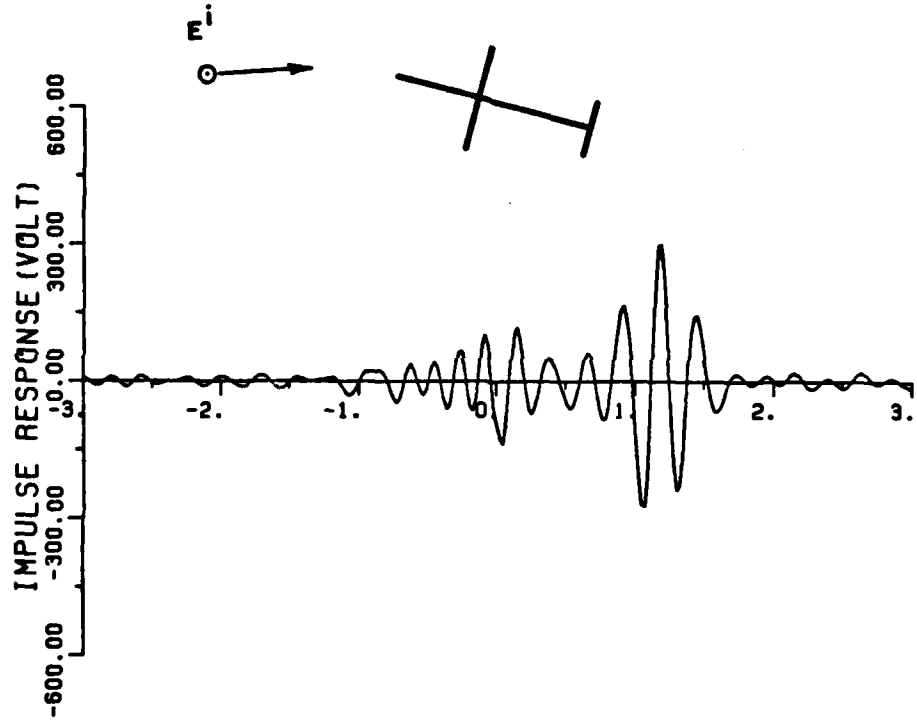

Figure 6-18. Backscattered impulse response waveform of commercial transportation aircraft A at 15° from nose-on for vertical polarization.

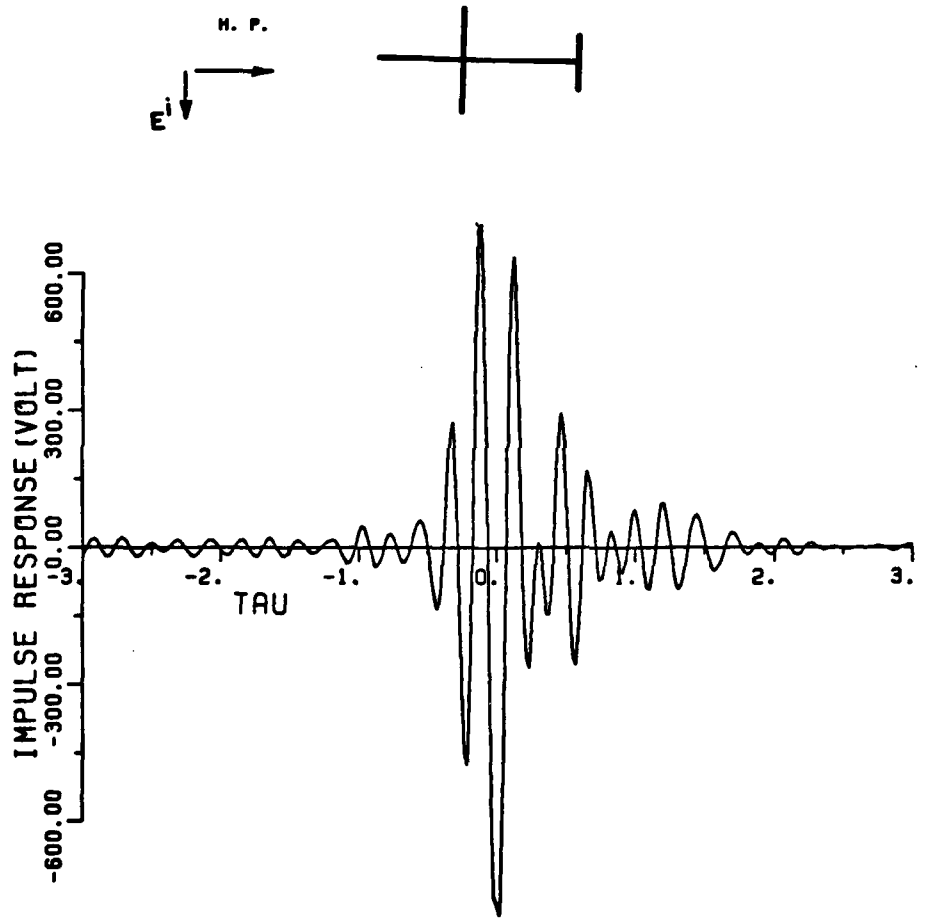

Figure 6-19. Backscattered impulse response waveform of commercial transportation aircraft A at nose-on for horizontal polarization.

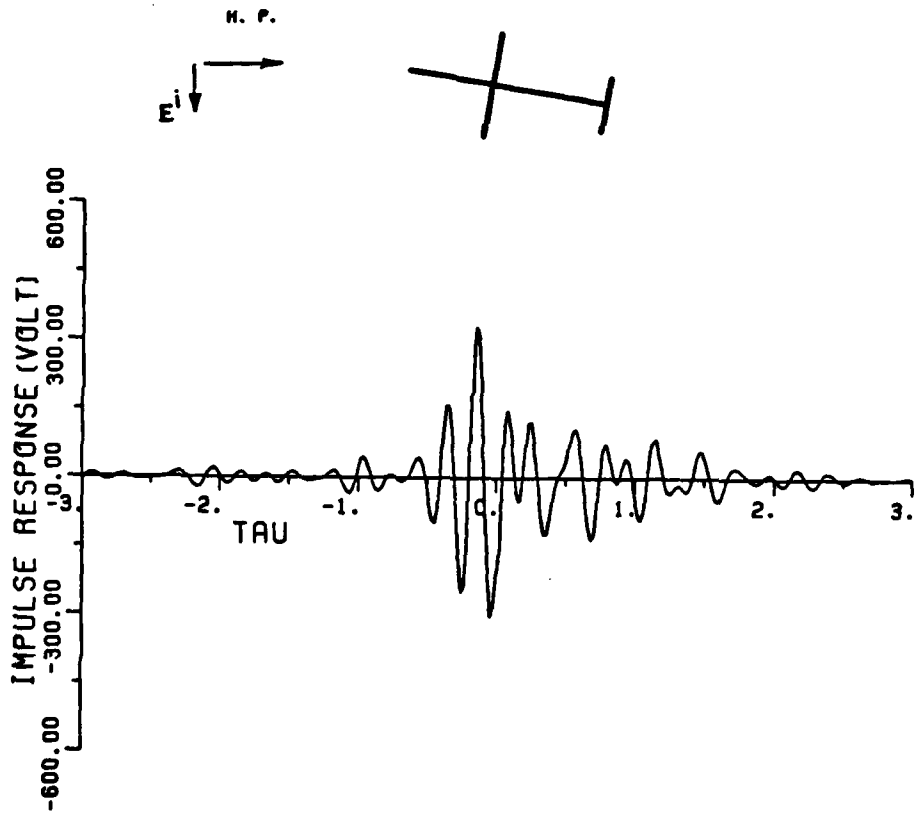

Figure 6-20. Backscattered impulse response waveform of commercial transportation aircraft A at 10° from nose-on for horizontal polarization.

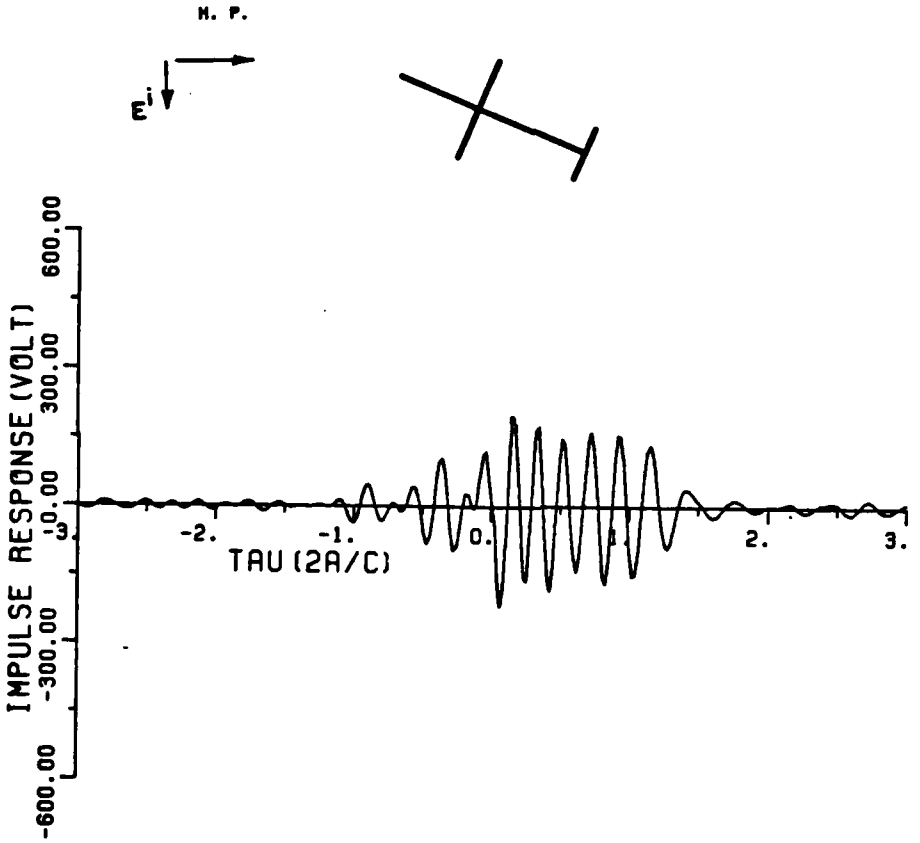

Figure 6-21. Backscattered impulse response waveform of commercial transportation aircraft A at 20° from nose-on for horizontal polarization.

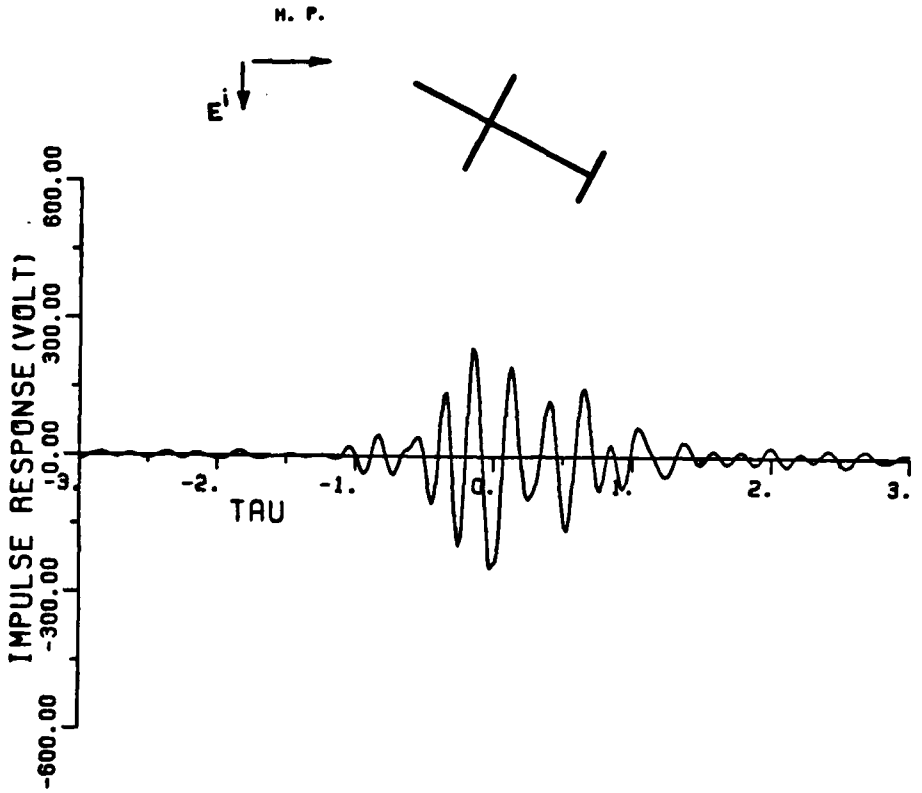

Figure 6-22. Backscattered impulse response waveform of commercial transportation aircraft A at 30° from nose-on for horizontal polarization.

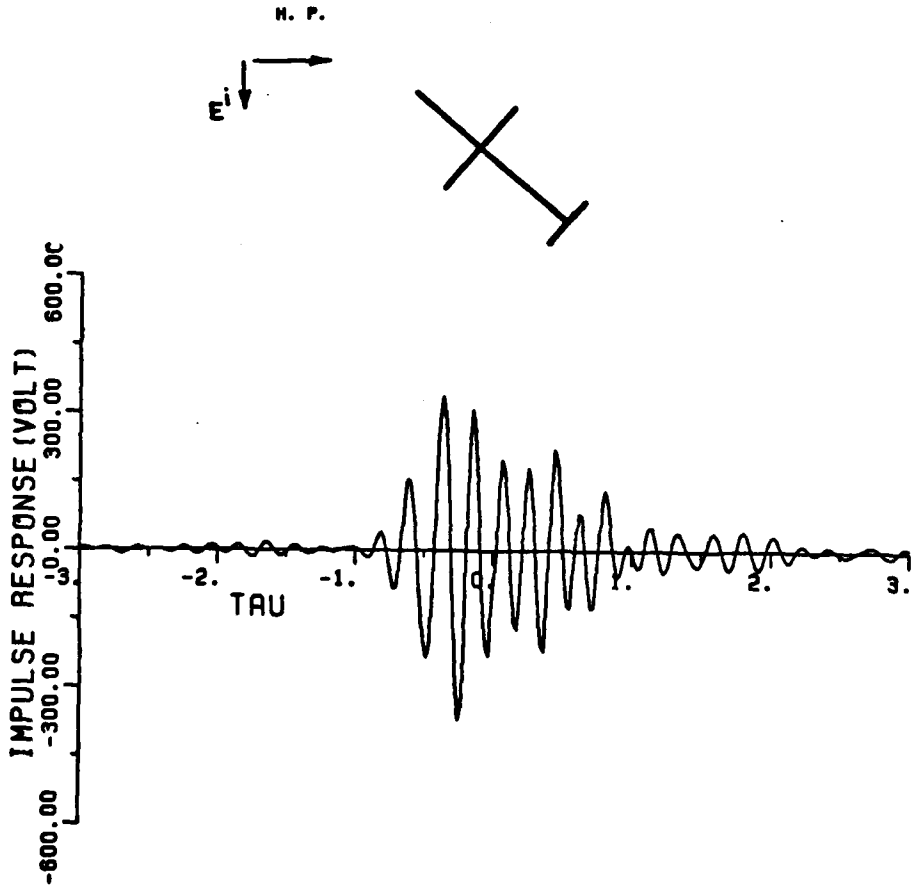

Figure 6-23. Backscattered impulse response waveform of commercial transportation aircraft A at 50° from nose-on for horizontal polarization.

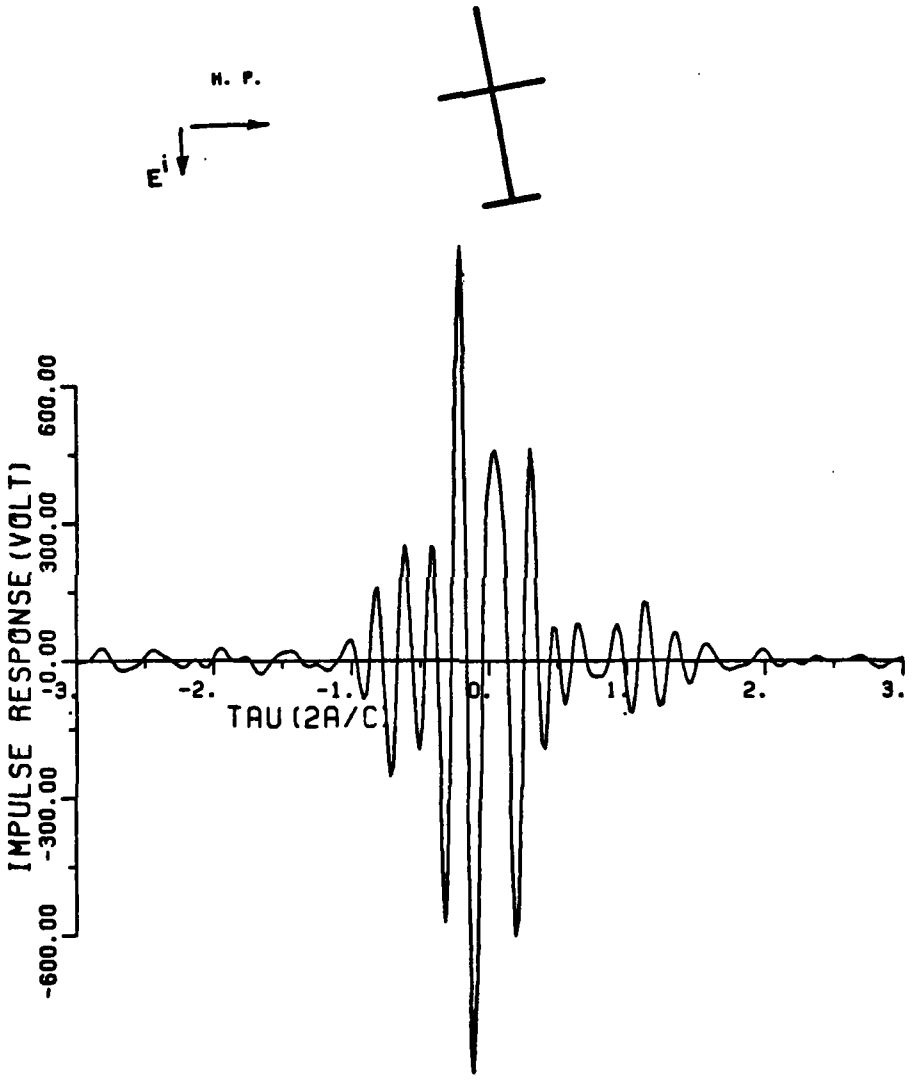

Figure 6-24. Backscattered impulse response waveform of commercial transportation aircraft A at 80° from nose-on for horizontal polarization.

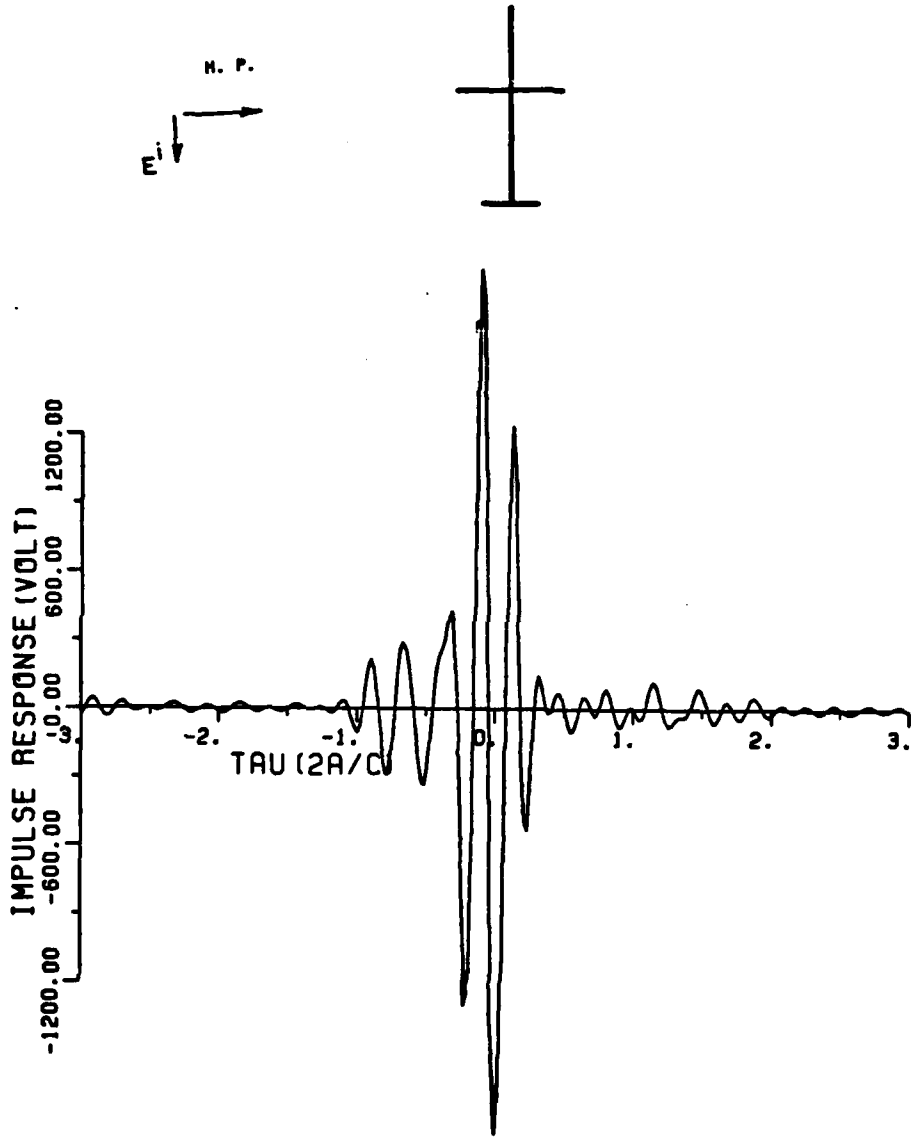

Figure 6-25. Backscattered impulse response waveform of commercial transportation aircraft A at 90° from nose-on for horizontal polarization.

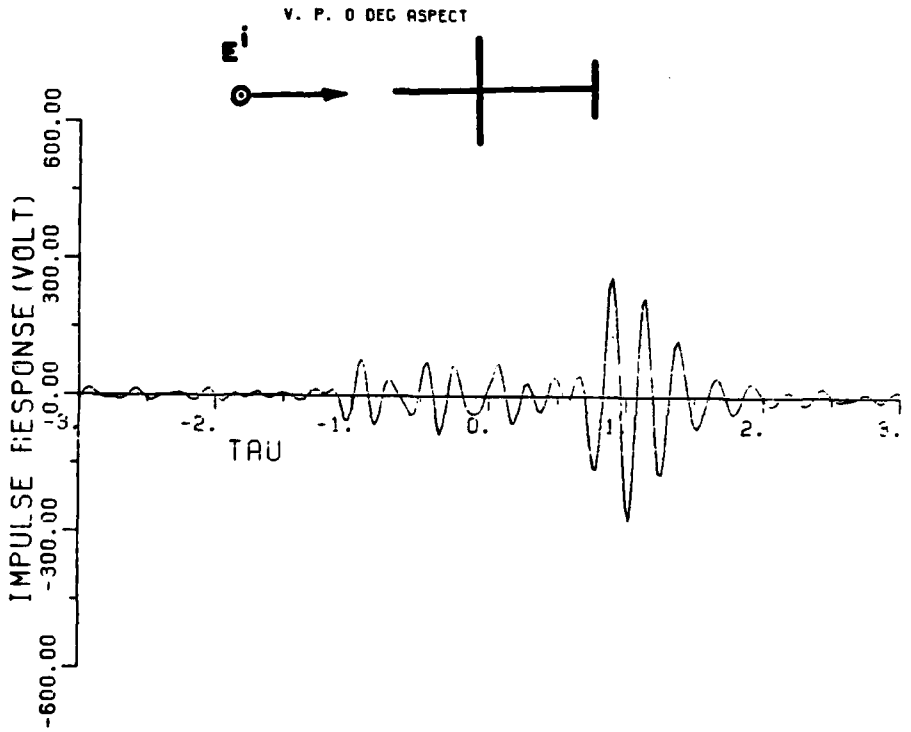

Figure 6-26. Backscattered impulse response waveform of commercial transportation aircraft B at nose-on for vertical polarization.

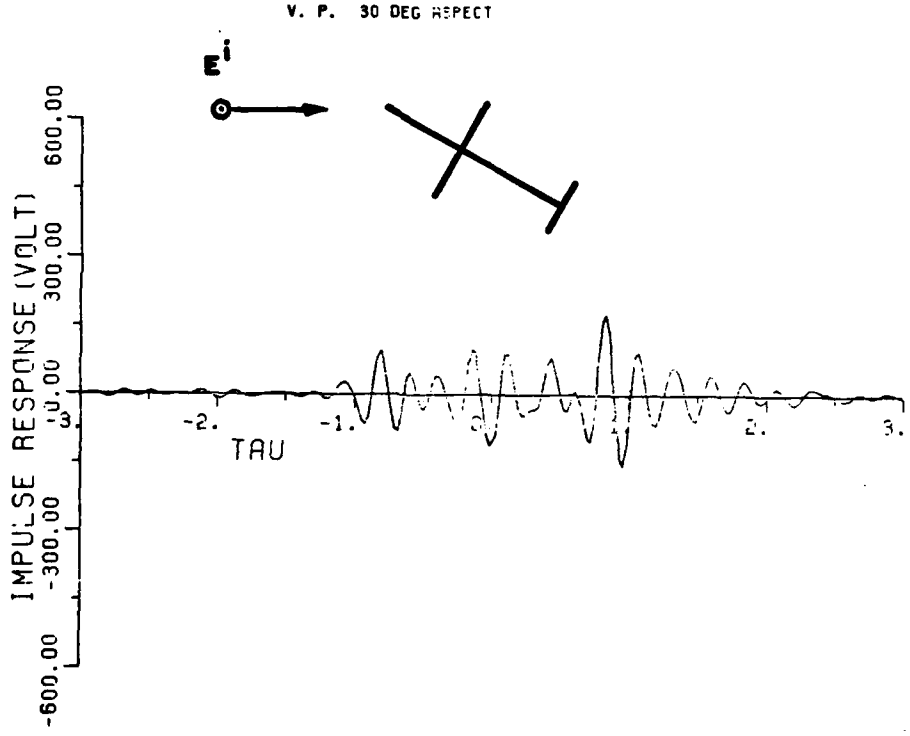

Figure 6-27. Backscattered impulse response waveform of commercial transportation aircraft B at 30° from nose-on for vertical polarization.

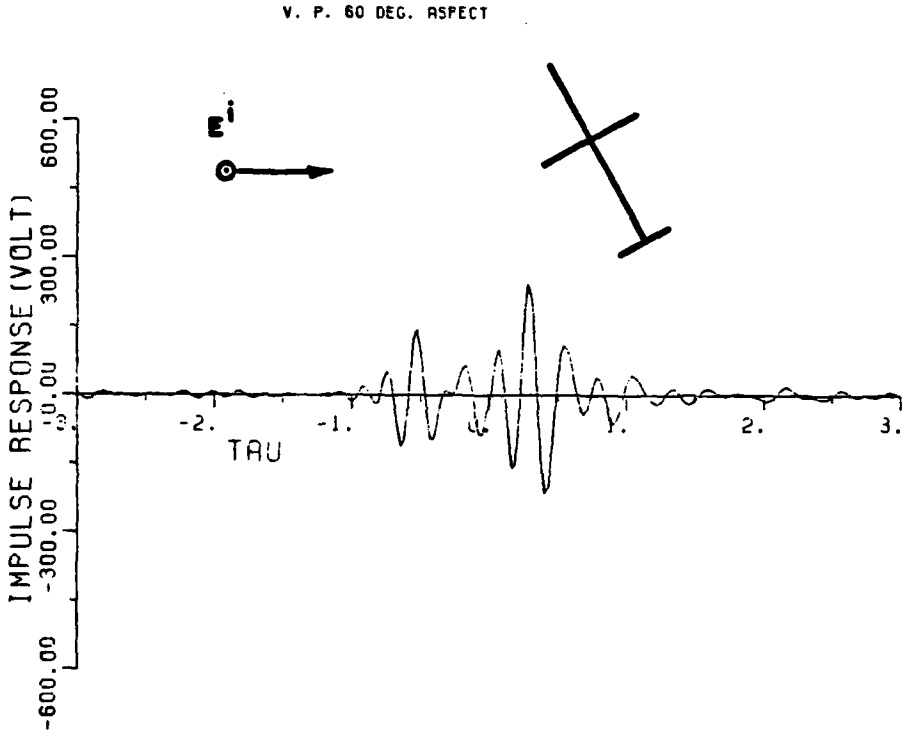

Figure 6-28. Backscattered impulse response waveform of commercial transportation aircraft B at 60° from nose-on for vertical polarization.

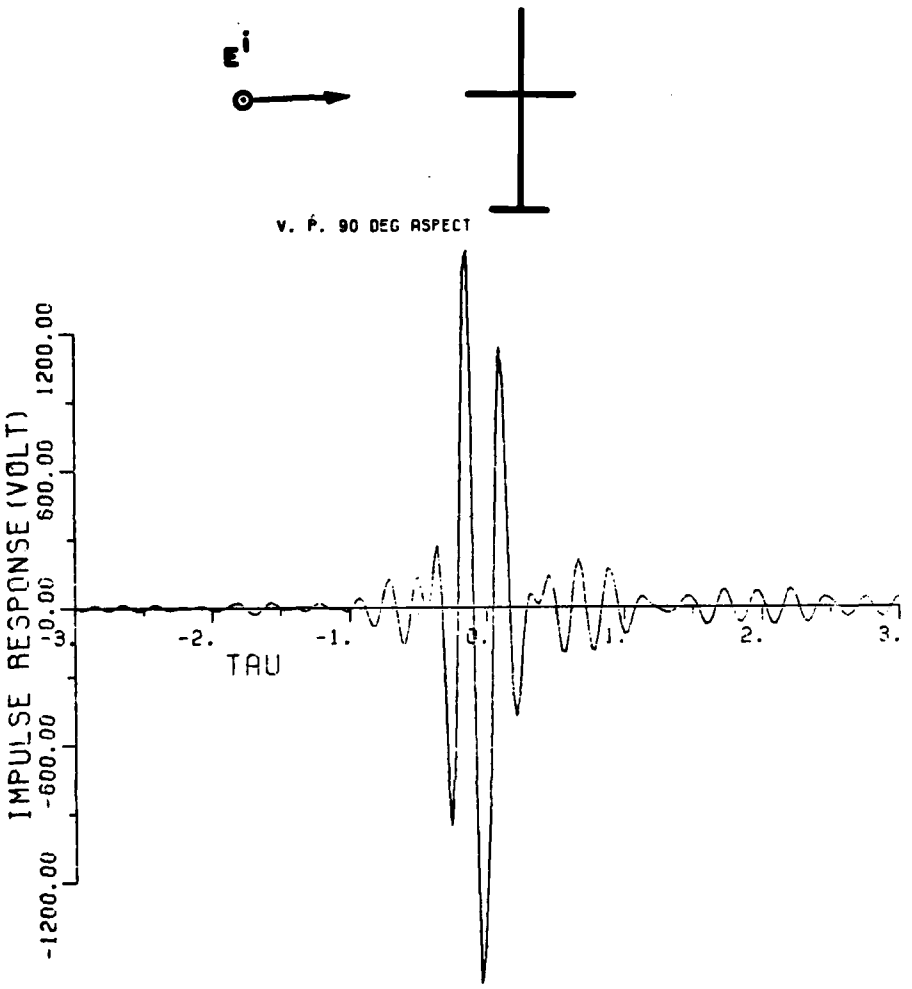

Figure 6-29. Backscattered impulse response waveform of commercial transportation aircraft B at 90° from nose-on for vertical polarization.

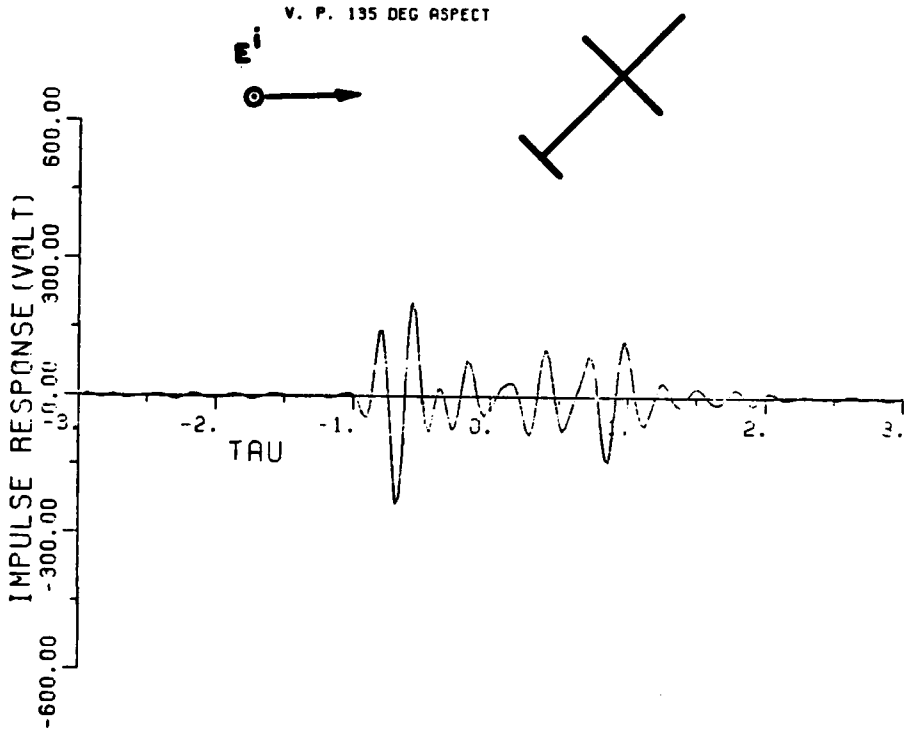

Figure 6-30. Backscattered impulse response waveform of commercial transportation aircraft B at 135° from nose-on for vertical polarization.

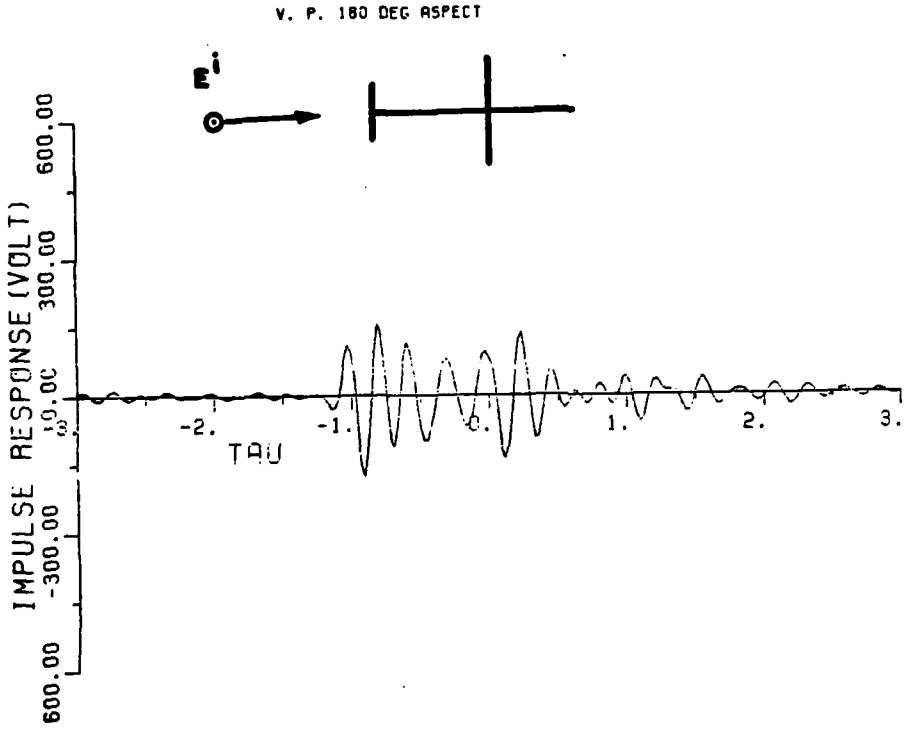

Figure 6-31. Backscattered impulse response waveform of commercial transportation aircraft B at 180° from nose-on for vertical polarization.

examination of the response waveforms is essential for selection of the best digital filter.

The ultimate goal in the chapter - extracting the complex natural resonances from the measured complex shape targets - has been accomplished for two passenger transportation aircraft. The applications of the RFA were limited to 1 to 3 GHz in order that the poles for many aspect angles and two polarizations could be extracted and compared easily. The number of complex natural resonances extracted is somewhat influenced by the 3 dB cut-off frequency of the digital filter. It is for this reason that the impulse response waveforms for the two aircraft were synthesized. The impulse response waveform with zero-phase-shift digital filter is shown in Figure 6-32. The horn antenna coupling, long path multiple scattering, target return reflector, system noise, and back wall are also displayed and clearly seen. The result of filtering the measured data using a zero phase low-pass digital filter (f_c of 15 Hz) is shown in Figure 6-33. One of the advantages of using the digital filter directly in the frequency domain is an inverse Fourier transform is not required. Therefore possible distortion due to the transformation can be avoided.

The exact 3 dB cut-off frequency of the lowpass filter should be different for various targets, aspect angles, and polarizations. The impulse responses for the aircraft are valuable in the determination of the 3 dB lowpass filter.

The RFA and the preprocessing techniques developed in this study can be applied to obtain the complex natural resonances of a complex

shape using measured data. The complex natural resonances obtained from the measured data are relatively aspect and polarization independent.

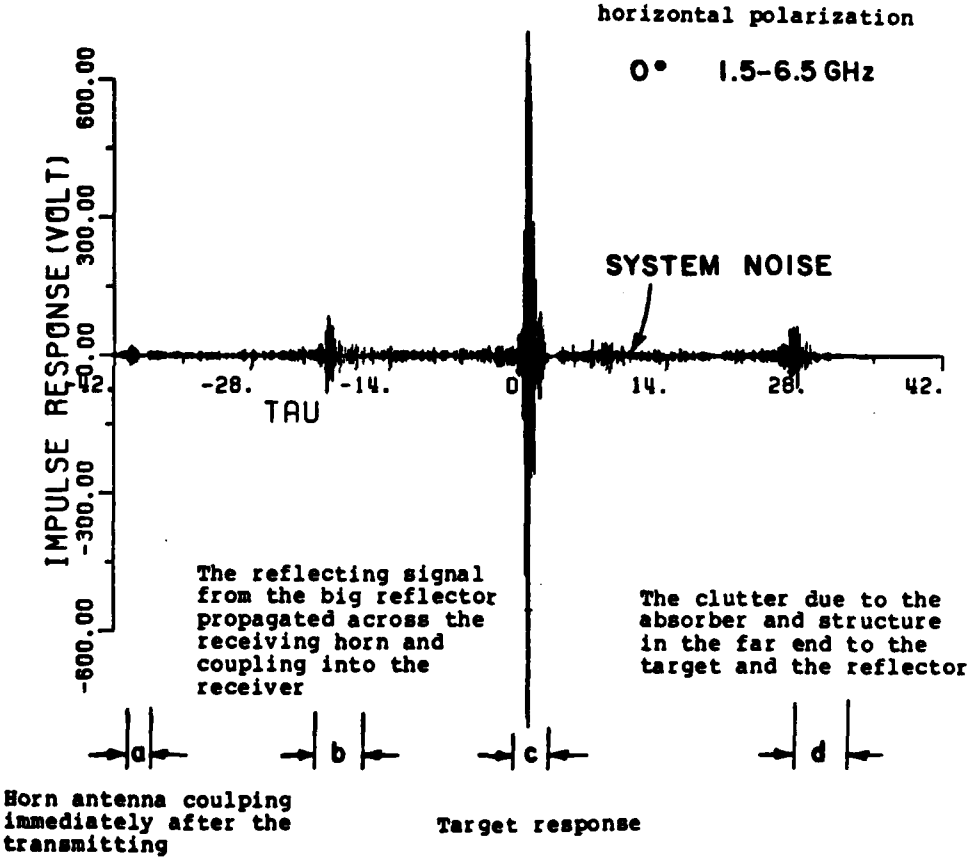

Figure 6-32. The impulse response of aircraft A at nose-on for horizontal polarization. The whole range is shown here.

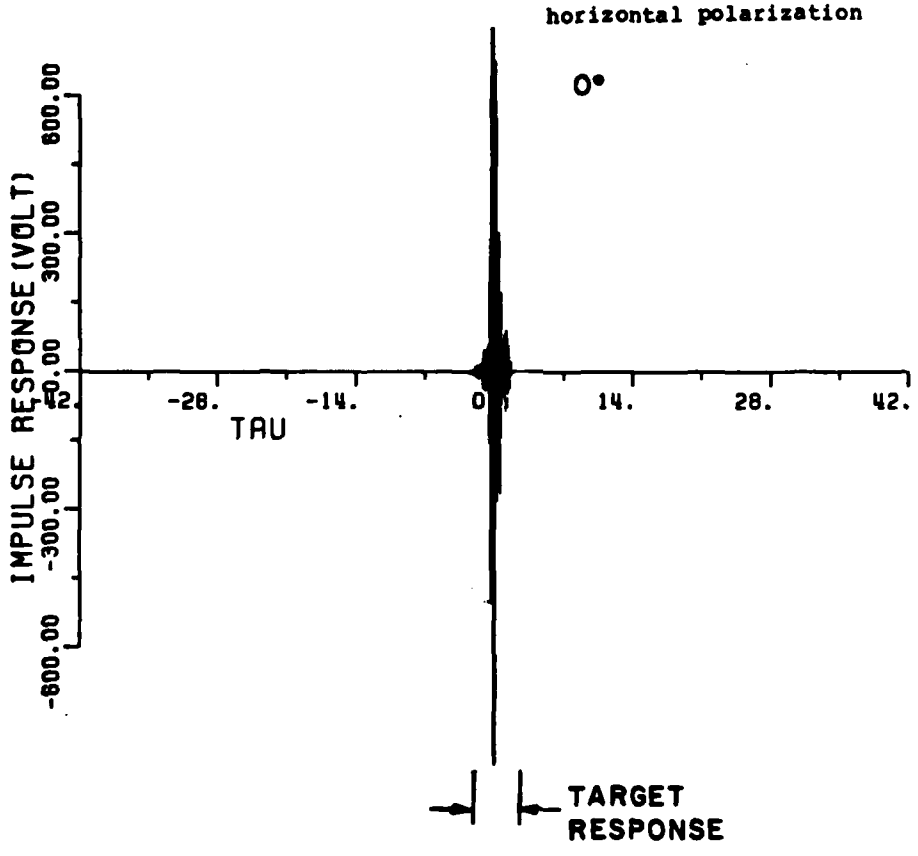

Figure 6-33. The impulse response of aircraft A at 0° aspect angle and horizontal polarization. Note the noise and clutter were filtered out by a lowpass zero-phase-shift digital filter (f_c of 15 Hz).

CHAPTER VII

CONCLUSIONS

An analytical model in the form of a rational function approximation (RFA) for fitting available complex spectral data has been developed. The available data which may be measured or calculated correspond, in principle, to any portion of the spectrum. The interest in this study is in scattered electromagnetic signals and in the extraction of complex natural oscillations (poles) from the fitted model.* The methods developed could have much wider applicability--to radiated as well as to scattered signals, for example, and to seismic and acoustic as well as to electromagnetic data.

Other methods for extracting complex natural resonances from data have been briefly reviewed, and the differences and advantages of the present technique explored. It is also demonstrated that rational function models can be used to supplement and complete an analytical

---

* The rational function approximation developed here is also an excellent tool for complex data interpolation. The application of the RFA to data interpolation has been made for thin wires and thick wires. The results have been shown to be very accurate when compared with the calculated data. A typical example can be seen in Figure 5-12, where the first resonances is not shown in the original data, but is plotted in the RFA (dotted line).

model (the K-pulse [6]) useful for relatively simple objects at high frequencies.

The RFA developed here has three main features: low-pass filtering to combat noise and clutter effects, windowing procedures to eliminate so-called curve fitting poles, and a sum operator which permits most of the available data to be used and is usually more effective than least squared error techniques (at least against an additive Gaussian white noise). There is, admittedly, little original in the generation of a system of linear, simultaneous equations for fitting complex, multiple frequency data. Yet the method of solution of the main data points and in the preprocessing of the data (fitting, sum operator) before pole extraction are new. Although the final step, i.e., pole extraction via of the zeros of the denominator of the rational function approximant is routine, it requires using double precision on a digital computer to illuminate near pole-zero cancellations.

Application of the RFA has been demonstrated for a variety of simple and complex objects, and, where possible, the results (complex natural resonances) have been compared to those obtained by other methods. Included here are spheres, discs, loops, thin wires, and finite and semi-infinite circular waveguides. Numerous tests of applications to a conducting spherical scatterer have been made. It must be stressed, however, that these methods have been tested against true poles with true residues (but finite in number) in an additive Gaussian white noise model. Tests of a parameter extraction procedure where equal excitation of parameters is assumed, albeit in noise, are

relatively meaningless. The RFA has also been applied to measured wide-band scattering data obtained using a new reflectivity facility being developed at the ElectroScience Laboratory [42]. The targets in this case are of complex geometry and of sufficient tactical importance to warrant classification (security) problems. Stressed, therefore, is the stability of results of RFA, and neglected is the precise identification of the scatterers for these cases. Excellent pole extraction has been demonstrated for both simple and complex geometries. Certain far-reaching conclusions can be drawn from the results of the research reported in this study.

1. Complex natural resonances can be successfully extracted from additive noise contaminated data with signal-to-noise ratios as low as 15.0 dB or lower.
2. For signal-to-noise ratios significantly lower than 15 dB, it does not appear that reliable pole extraction methods are feasible. Unless, of course, some new breakthrough is made.
3. From 2 above it has been concluded that pole extraction procedures from full scale, field-measured data are generally not feasible and should not be attempted. Roughly, signal-to-noise ratios of 13 to 15 dB are necessary for successful pole extraction. This does mean that pole extraction from controlled data, i.e., from laboratory measurements is feasible. The new ElectroScience Laboratory

reflectivity measurement facility or other careful measurements easily satisfy this requirement.

4. While this study does not explore target recognition, it must be stressed that pole extraction from real time radar data is not necessary for target recognition using prediction-correlation processing. The nearest neighbor decision rule [43] using the complex natural resonances can also be used. The rule is to identify a set of extracted poles $\{P_j\}$, as a member of the pole set of the known targets in a library, C^r, to which its nearest neighbor belongs. Therefore, noise and clutter problems do not negate this form of target recognition at least as far as pole extraction is concerned.
5. Parameter extraction for the complex natural resonances is not, at this stage, an exact science using the procedures of this study. Experience, in processing and in realizing what is and what is not reasonable in terms of electromagnetic reverberations, is indispensable. A completely foolproof automatic procedure cannot be devised at this time.

Using both RFA and asymptotic estimates, new and significant results have been obtained for the complex natural resonances of the thin circular loop. Of particular importance is the fact that poles from RFA which are most precise at lower frequencies show a region of overlap with poles obtained from asymptotic methods. Therefore, from a

combination of the two methods relatively lengthy (>30 or 40) pole-pair strings can be obtained. Such long pole strings are precisely what are needed to obtain a K-pulse waveform using one particular approach [44].

A thin-wire circular loop has also been used to test RFA for complex natural resonances extraction. In this case, comparisons are made with existing poles obtained from an integral equation formulation and numerical search; good agreement is obtained. A K-pulse for the circular loop using just those poles corresponding to creeping wave type modes is obtained, and the backscatter response of the loop to this K-pulse for edge-on incidence has been derived. Derivation of K-pulse-response waveform pairs for a particular target is beyond the scope of this study but these initial results do show the utility of RFA. In the course of this study, new canonical response waveforms have been shown for the thin-wire loop and for cross-polarized responses of the circular disc.

As noted above, RFA has been used to extracted complex natural resonances of several relatively complex target geometries. The broadband scattering data for these applications were measured on the new compact reflectivity measurement facility at the ElectroScience Laboratory. In this dissertation a number of band-limited impulse response waveforms, generated from these measured data, have been shown. These waveforms vividly demonstrate the tremendous diagnostic potential of time domain response waveforms. The response from various geometrical features of the targets as well as possible reverberations between various features are easily seen. This aspect of the response

waveforms has not been stressed here for obvious reasons but one must perceive the future significance of what might be termed "scattering reflectometry."

The most immediate application of the tools developed in this dissertation is to extract complex target poles for target recognition using prediction-correlation [45]. In this regard it is noted that the poles of complex target geometries as extracted using RFA do not show precise excitation invariance, particularly with respect to the damping of a given pole. The reason--weak excitation of a particular resonances at a given aspect or polarization--is obvious. As a practical matter, however, it is clear that a single complex geometry target will have to be treated as several targets (somewhat different pole damping) in prediction-correlation processing. Research on this aspect of the problem using the RFA tools developed here has already been initiated.

REFERENCES

[1] E.M. Kennaugh and R.L. Cosgriff, "The Use of Impulse Response in Electromagnetic Scattering Problems," 1958 IRE Nat'l Conv. Rec., Pt.1, pp. 72-77.

[2] E.M. Kennaugh and D.L. Moffatt, "Transient and Impulse Approximations," IEEE Proceedings, Vol. 53, No. 8, August 1965, pp. 893-901.

[3] C.E. Baum, "Electromagnetic Transient Interaction With Objects With Emphasis on Finite Size Objects, and Some Aspects of Transient Pulse Production," Presented at 1972 Spring URSI Meeting, Washington D. C.

[4] Charles L. Dolph and Soon K. Cho, "On the Relationship Between the Singularity Expansion Method and Mathematical Theory of Scattering," IEEE Trans. Antennas Propagation, Vol. AP-28, No. 6, November, 1980.

[5] Alexander G. Ramm, "Theoretical and Practical Aspects of Singuarity and Eigenmode Expansion Methods," IEEE Trans. Antennas Propagation, Vol. AP-28, No. 6, November, 1980.

[6] E.M. Kennaugh, "The K-Pulse Concept," IEEE Trans. Antennas Propagation, Vol. AP-29, No. 2, March, 1981.

[7] J.A. Stratton, Electromagnetic Theory, McGraw-Hill Book Co., New York, 1941, pp. 554-560.

[8] D.P. Mithouard and D.B. Hodge, "Electromagnetic Scattering by a Disk," Report 710816-3, The Ohio State University ElectroScience Laboratory, Department of Electrical Engineering; prepared under Contract N00014-78-C-0049, Department of the Navy, Office of Naval Research, Arlington, Virginia, Sep. 1979.

[9] D.L. Moffatt, R.K. Mains, "Detection and Discrimination of Radar Targets," IEEE Trans. Antennas Propagation, Vol. AP-23, No. 3, May 1975.

[10] Jonathan S. Bagby, "Natural Electromagnetic Oscillations: A Geometrical Theory," Master's Thesis, Department of Electrical Engineering, The Ohio State University, 1981.

[11] R. Kouyoumjian and P.H. Pathak, "A Uniform Geometrical Theory of Diffraction for an edge in a Perfectly Conducting Surface," Proceedings of the IEEE, Vol. 62, No. 11, November, 1974, pp. 1448-61.

[12] P.H. Pathak and R.G. Kouyoumjian, "An Analysis of the Radiation from Aperatures in Curved Surfaces by the Geometrical Theory of Diffraction," Proceedings of IEEE, Vol. 62, No. 11, p. 1438, November, 1974.

[13] Prony, R., "Essai Experimental et Analytique sur les lois de la Dilatabilite de Fluides Elastiques et sur Celles de la Force Expansive de la Vaperu de l'Alkool, a Differentes Temperatures," J. l'Ecole Polytech. (Paris), Vol. 1, No. 2, pp. 24-76, 1795.

[14] M.L. Van Blaricum, "Techniques for Extracting the Complex Natural Resonances of a System Directly from its Transient Response," Ph. D. Dissertation, Department of Electrical Electrical Engineering, University of Illinois at Urbana-Champaign, 1976.

[15] F.M. Tesche, "On the Analysis of Scattering and Antenna Problems Using the Singulaity Expansion Technique," IEEE Trans. Antennas and Propagation, Vol. AP-21, No. 1, January, 1981, pp. 53-62.

[16] D.L. Moffatt, J.D. Young, A.A. Ksienski, H.C. Lin, C.M. Rhoads, "Transient Response Characteristics in Identification and Imaging," IEEE Trans. on Antennas and Propagation, Vol. AP-29, No. 2, March, 1981.

[17] J.R. Auton and M.L. Van Blaricum, "Investigation of Procedures for Automatic Resonance Extraction from Noisy Transient Electromagnetics Data," Vol I-III, Final Report for Contract #N00014-80-C-0299, Effects Technology, Inc., Aug., 1981.

[18] J. Makhoul, "Linear Prediction: A Tutorial Review," Proceedings of the IEEE, Vol. 63, No. 4, pp. 561-580, April, 1975.

[19] H. Akaike, "A New Look at Statistical Model Identification," IEEE Transactions on Automatic Control, Vol. AC-19, pp. 716-723, Dec., 1974.

[20] J.T. Cordaro and W.A. Davis, "Time Domain Techniques in the Singularity Expansion Method," IEEE Trans. on Antennas and Propagation, Vol. AP-29, No. 4, May, 1981, pp. 534-538.

[21] L. Marin, "Natural-Mode Representation of Transient Scattering from Rotational Symmetric Bodies," IEEE Trans. Antennas and Propagation, Vol. AP-22, No. 2, March, 1974.

[22] R.R. Blackburn and D.R. Wilton, "Analysis and Synthesis of an Impedance-Loaded Loop Antenna Using the Singularity Expansion Method," IEEE Trans. on Antennas and Propagation, Vol AP-26, No. 1, January, 1978, pp. 136-140.

[23] D.L. Moffatt, "Time Domain Electromagnetic Scattering from Highly Conducting Objects," ElectroScience Laboratory Report, Department of Electrical Engineering, The Ohio State University, Columbus, Ohio, May, 1971.

[24] J.N. Brittingham, E. K. Miller, J. L. Willows, "Poles Extraction From Real-Frequency Information," IEEE Proceeding, pp. 263-273, Vol. 68, No. 2, Feb., 1980.

[25] T.B.A. Senior, J.M. Pond,"Poles Extraction in the Frequency Domain," Interaction notes, note 411, Radiation Lab., Department of Electrical and Computer Engineering, The University of Michigan, Ann Arbor, Michigan, July, 1981.

[26] E.M. Kennaugh and D.L. Moffatt,"Comments on Impulse Response of a Conducting Sphere Based on Singularity Expansion Method," Proceedings of IEEE, Vol. 70, No. 3, March, 1982.

[27] Marley E. Bechtel, "Scattering Coefficients for the Backscatteirng of Electromagnetic Waves from Perfectly Conducting Spheres," CAL Report No. AP/RIS-1, Cornell Aeronautical Laboratory, Inc. of Cornell University, Buffalo, N.Y., Dec., 1962.

[28] R.W. Kulp, "An Optimum Sampling Procedure for Use with Prony Method," IEEE Transactions on Electromagnectic Compatibility, Vol. EMC-23, No. 2, May, 1978.

[29] C.L. Ryan and L. Peters, Jr., "Evaluation of Edge-Diffracted Fields Including Equivalent Currents for the Caustic Regions," IEEE Trans. Antennas and Propagation, Vol. AP-17, No. 3, pp. 292-299, May 1969.

[30] W. Andrejewski, "Die Beugung Elektromagnetischer Wellen an der Leitenden Kreisscheibe und an der Kreisformigen Offnung im Leitenden Ebenen Schieum," Dissertation for Rheinich-Westfalichen Technischen Hochschule, Aachen, Germany, 1952.

[31] C. Flammer, "The Vector Wave Function Solution of the Diffraction of Electromagnetic Waves by Circular Disks and Aperatures," J. Applied Physics, Vol. 24, pp. 1218-1231, 1953.

[32] D.B. Hodge, "The Calculation of Far Field Scattering by a Circular Metallic Disk," Technical Report 710816-2, The Ohio State University ElectroScience Laboratory, Department of Electrical Engineering, Columbus, Ohio, Feb., 1979.

[33] D.B. Hodge, "Spectral and Transient Response of a Circular Disk to Plane Electromagnetic Waves," Scientific Report No. 5, The Ohio State University, ElectroScience Laboratory, Columbus, Ohio, May 28, 1970.

[34] T.B.A. Senior, "Disk Scattering at Edge-On Incidence," IEEE Tans. on Antennas and Propagation, Vol. AP-17, No. 6, Nov., 1969.

[35] C.E. Ryan, Jr. and L. Peters, Jr., "A Creeping-Wave Analysis of the Edge-On Echo Area of Disks," IEEE Trans. on Antennas and Propagation, p. 274, March, 1968.

[36] J.A. Landt and E.K. Miller, "Short Pulse Response of a Circular Loop," IEEE Trans. Antennas Propagation, Vol. AP-22, No. 1, Jan., 1974.

[37] T.W. Johnson, "Electromagnetic Scattering by Open Circular Waveguides," Ph.D. Dissertation, Department of Electrical Engineering, The Ohio State University, Dec., 1980.

[38] "Analysis of Electromagnetic Backscatter from an Inlet Cavity Configuration," The Ohio State University ElectroScience Laboratory, Report 712661-4, Oct., 1982.

[39] Chuang, C.W., The Ohio State University, Electroscience Laboratory, Personal Communication.

[40] Y.T. Lin, "Computation of Low Frequency Scattering from Airplanes," Report 2768-9, Sept., 1972, The Ohio State University ElectroScience Laboratory, Department of Electrical Engineering, Prepared Under Grant AFOSR-69-1710 for Air Force Office of Scientific Research.

[41] C.W. Chuang and D.L. Moffatt, "Natural Resonances of Radar Targets Via Prony's Method and Target Discrimination," IEEE Transactions on Aerospace and Electronic Systems, Vol. AES-12, No. 5, Sept., 1976.

[42] J.S. Chen and E.K. Walton, "The Ohio State Universty NCTR Data Base File Structure," Department of Electrical Engineering, The Ohio State University, ElectroScience Laboratory, Technical Report 714190-1.

[43] D.L. Moffatt, A.A. Ksienski, J.H. Richmond, et al., "Radar Target Identification," Short Course, Class Note Vols. I and II, Department of Electrical Engineering, The Ohio State University, Columbus, Ohio 43210.

[44] I. Gerst and J. Diamond, "The Elimination of Intersymbol Interference by Input Signal Shaping," Proc. IRE, Vol. 19, No. 7, pp. 1195-1203, 1961.

[45] R.K. Mains and D.L. Moffatt, "Complex Natural Resonances of an Object in Detection and Discrimination," The Ohio State University ElectroScience Laboratory, Department of Electrical Engineering, Report 3424-1, June, 1974.

[46] W.D. Stanley, Digital Signal Processing, Reston Publishing Company, Inc., Reston, Virginia, Prentice-Hall, 1975.

[47] J.J. Bowman, T.B.A. Senior, and P.L.E. Uslenghi, Electromagnetic and Acoustic Scattering by Simple Shape, North-Holland Publishing Co., Amsterdam, 1969, Sole Distributor: Wiley Interscience Division, John Wiley & Sons, Inc., New York.

ADDITIONAL REFERENCES

A.A. Ksienski, L.J. White and A.G. Repjar, "Object Identification From Multifrequency Radar Returns," Report, The Ohio State University ElectroScience Laboratory, Department of Electrical Engineering, Columbus, Ohio May 21, 1974.

G.R. Mattson, "Electromagnetic Plane Wave Scattering by a Perfectly Conducting Disk," Ph.D. Dissertation, University of Michigan, Ann Arbor, Michgan.

K.R. Umashankar and D.R. Wilton, "Transient Characterization of Circular Loop Using Singularity Expansion Method," Interaction Notes, Note 259, University of Mississippi, Mississippi, Aug., 1974.

J.D. Markel and A.H. Gray, Jr., Linear Prediction of Speech, Communication and Cybernetics 12, Springer-Verlag Berlin heidelberg New York, 1976.

R.S. Anderssen and M.R. Osborne, Least Squares Methods in Data Analysis, University of Queensland Press, Australia, 1969.

C.L. Lawson and R.J. Hanson, Solving Least Squares Problems, Prentice-Hall Series in Automatic Computation, Prentice-Hall, Inc., Englewood Cliffs, New Jersey, 1974.

Hildebrand, Introduction to Numerical Analysis, McGraw-Hill Book Company, New york, 1974.

David F. Findley, Applied Time Series Analysis, Academic Press, 1978.

A.V. Oppenheim and R.W.Schafer, Digital Signal Processing, Prentice-Hall, Inc., 1975.

E.F. Knott, T.B.A. Senior, P.L.E. Uslenghi, "High-Frequency Backscattering From a Metallic Disc," Proc. IEE, Vol. 118, No. 12, Dec., 1971.

C.E. Ryan and L. Peters, Jr., "A Creeping-Wave Analysis of the Edge-On Echo Area of Discs," IEEE Trans., AP-16, pp. 274-275, 1968.

R.R. Blackburn and D.R. Wilton, "Analysis and Synthesis of an Impedance-Loaded Loop Antenna Using the Singularity Expansion Method," IEEE Trans. on Antennas and Propagation, Vol. AP-26, No. 1, January, 1978, pp. 136-140.

T.W. Johnson and D.L. Moffatt, "Electromagnetic Scattering by an Open Circular Waveguide," Radio Science, Vol 17, Nov.-Dec., 1982.

P.D. Lax and R.S. Phillips, Scattering Theory, Academic Press, 1967.

J.B. Keller, "The Field of an Antenna Near the Center of a Large Circular Disk," J. Soc. Indust. Appl. Math., Vol. 11, No. 4, Dec., 1963.

A.Q. Howard, Jr., "A Geometrical Theory of Natural Oscillation Frequencies in Exterior Scattering Problems," Interaction Notes, Note 378, Department of Electrical Engineering, University of Arizona, Oct. 1, 1979.

V.K. Jain and R.D. Gupter, "Identification of Linear System Through a Grammian Technique," International Journal of Control, pp. 421-431, Vol. 12, 1970.

Haroid J. Price, "An Improved Prony Algorithm for Exponential Analysis," Mission Research Corporation, Mathematics Note, Note 59, Albuquerque, New Mexico 87108, Nov., 1978.

Roger F. Harrington, Field Computation by Moment Method, New York, Macmillan, 1968.

J.R. Auton and L.W. Pearson, "Some Numerical Methods for Exponential Analysis with Connection to a General Identification Scheme for Linear System," Mathematics Notes, Note 69, Department of Electrical Engineeing, University of Kentucky, November, 1980.

Chen-To Tai, Dyadic Green's Functions in Electromagnetic Theory, Intext Educational Publishers, College Division of Intext, San Francisco, 1971.

R.H. Schafer and R.G. Kouyoumjian, "Transient Currents on a Cylinder Illuminated by an Impulsive Plane Wave," IEEE Trans. Antennas and Propagation, Vol. AP-23, No. 5, pp. 627-638, September, 1975.

E. Heyman and L.B. Felsen, "Creeping Waves and Resonances in Transient Scattering by Smooth Convex Objects," IEEE Trans. Antennas Propagation, Vol. AP-31, No. 3, pp. 426-437, May, 1983.

Y. Lin and J.H. Richmond, "EM Modeling of Aircraft at Low Frequencies," IEEE Trans. Antennas Propagation, Vol. AP-23, No. 1, January, 1975.

N. Wang, "Self-Consistent GTD Formulation for Conducting Cylinders with Arbitrary Convex Cross Section," IEEE Trans. Antennas Propagation, Vol. AP-24, July, 1976.

R.P. DE Figueiredo and C.L. Hu, "Waveform Feature Extraction Based on Tauberian Approximation," IEEE Trans. on Pattern Analysis and Machine Intellignece, Vol. PAMI-4, No. 2, March, 1982.

H. Lin and K.S. Fu, "A Syntatic Approach to Seismic Pattern Recognition," IEEE Trans. on Pattern Analysis and Machine Intelligence, Vol. PAMI-4, No. 2, March, 1982.

W. Boerner, C. Ho, and B. Foo, "Use of Randon's Projection Theory in Electromagnetic Inverse Scattering," IEEE Trans. on Antennas and Propagation, Vol. AP-29, No. 2, pp. 336-341, March, 1981.

K.J. Langenberg, "Transient Fields of Small Loop Antennas," IEEE Trans. on Antennas and Propagation, Vol. AP-24, No. 2, pp. 236-239, March, 1976.

L. Peters, Jr., "Two Dimensional Applications for Bodies with Edges," The Modern Geometrical Theory of Diffraction, Vol. 1, GTD Short Course, Department of Electrical Engineering, The Ohio State University, Columbus, Ohio 43210, 1981.

APPENDIX A

A ZERO PHASE SHIFT LOWPASS DIGITAL FILTER

The goal in this Appendix is to design a 10th order zero-phase-shift lowpass digital filter. The first step here is to design a 5th order lowpass Butterworth digital filter in terms of a 5th order analog filter [46]. Then, two 5th order filters, H(z) and H*(z) (H*(z) is the complex conjugate of H(z)) are cascaded to make a 10th order zero-phase-shift digital filter. A block diagram of 5th order digital filter is shown in Figure A-1. The transfer function of the 5th order Butterworth analog filter [46] with a 3 dB cutoff frequency at 1 radian/second is given by

$$G(s) = \frac{A_0}{B_0 + B_1 s + B_2 s^2 + B_3 s^3 + B_4 s^4 + B_5 s^5} \quad , \qquad \text{(A-1)}$$

where

$$A_0 = B_0 = 1 \quad , \qquad \text{(A-2.1)}$$

$$B_1 = 3.236068 \quad , \qquad \text{(A-2.2)}$$

$$B_2 = 5.236068 \quad , \qquad \text{(A-2.3)}$$

$$B_3 = 5.236068 \quad , \qquad \text{(A-2.4)}$$

$$B_4 = 3.236068 \quad , \qquad \text{(A-2.5)}$$

and

$$B_5 = 1 \quad , \tag{A-2.6}$$

If the transfer function of the digital filter is written as

$$H(z) = \frac{a_0 + a_1 z^{-1} + a_2 z^{-2} + a3 z^{-3} + a_4 z^{-4} + a_5 z^{-5}}{1 + b_1 z^{-1} + b_2 z^{-2} + b_3 z^{-3} + b_4 z^{-4} + a_5 z^{-5}} \quad , \tag{A-3}$$

the following relationships are true [45].

$$A = B_0 + B_1 C + B_2 C^2 + B_3 C^3 + B_4 C^4 + B_5 C^5 \quad , \tag{A-4.1}$$

$$a_0 = A_0/A \quad , \tag{A-4.2}$$

$$a_1 = 5A_0/A \quad , \tag{A-4.3}$$

$$a_2 = 10A_0/A \quad , \tag{A-4.4}$$

$$a_3 = 10A_0/A \quad , \tag{A-4.5}$$

$$a_4 = 5A_0/A \quad , \tag{A-4.6}$$

$$a5 = A_0/A \quad , \tag{A-4.7}$$

$$b_1 = (5B_0 + 3B_1 C + B_2 C^2 - B_3 C^3 - 3B_4 C^4 - 5B_5 C^5)/A \quad , \tag{A-4.8}$$

$$b_2 = (10B_0 + 2B_1 C + 2B_2 C^2 - 2B_3 C^3 + 2B_4 C^4 + 10B_5 C^5)/A \quad , \tag{A-4.9}$$

$$b_3 = (10B_0 + 2B_1 C + 2B_2 C^2 + 2B_3 C^3 + 2B_4 C^4 - 10B_5 C^5)/A \quad , \tag{A-4.10}$$

$$b_4 = (5B_0 - 3B_1 C + B_2 C^2 + B_3 C^3 - 3B_4 C^4 + 5B_5 C^5)/A \quad , \tag{A-4.11}$$

$$b_5 = (B_0 - B_1 C + B_2 C^2 - B_3 C^3 + B_4 C^4 - B_5 C^5)/A \quad , \tag{A-4.12}$$

and

$$C = \lambda_r \cot\left(\frac{\pi}{2} \frac{f_c}{f_0} \right) \quad . \tag{A-4.13}$$

The remaining undefined parameters are:

λ_r is the 3 dB cutoff frequency for the analog filter (assuming that λ_r is 1 rad/sec for the analog filter given by Equation (A-1)), f_0 is the folding frequency, i.e., one half of the sampling frequency, f_c is the 3 dB cutoff frequency for the digital filter.

Assuming that the sampling frequency is fixed at 500 Hz, i.e., f_0 of 250 Hz, the only variable that still has to be determined is the 3 dB cut-off frequency f_c. Then all of the unknown coefficients in Equation (A.3) can be obtained using Equations (A-4.1) to (A-4.13). The implementation for the transfer function of the fifth order digital filter is shown in Figure A-1. The implementation of $H^*(z)$ is to input the data backward through the filter H(z) and reverse the output sequence.

In the application of the 10th order zero-phase-shift digital filter to the noisy data, the 3 dB bandwidth of the filter is chosen to cover the target size and transient response. The transient response waveforms are aspect and target dependent. However, a plot of the impulse response may help to decode the effective transient length. Normally, 4 to 5 TAU (target length transit time) is a good choice of the 3 dB bandwidth for most targets.

An example of the determination of the 3 dB cut-off frequency f_c for the calculated data for the sphere (Δka of 0.02) is shown here. Since the data for the sphere are sampled in the frequency domain, the corresponding impulse response is periodic with a period t_p given by

$$tp = 1/\Delta f^{*} = 157.25\ (TAU) \quad , \tag{A-5}$$

where Δf is the frequency increment between successive samples, TAU is $2a/c$, a is the radius of the sphere, and c is the speed of light in a free space. The corresponding 3 dB cutoff frequency f_c (in terms of target length transit time) for the digital filter is

$$f_c = 157.25 \frac{BW}{250} (TAU). \tag{A-6}$$

where BW is the desired 3 dB beamwidth for the digital filter in Hz.

---

* Δf is $(0.02/\pi) \frac{c}{2a}$ for Δka of 0.02.

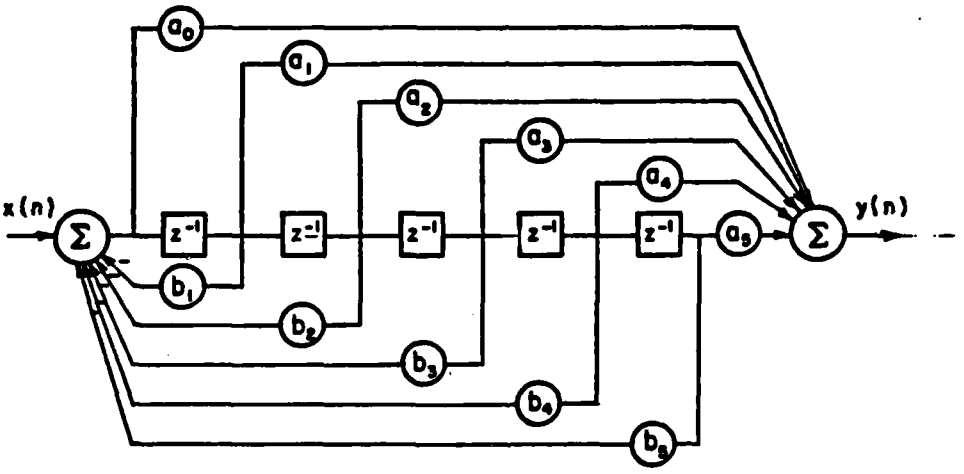

Figure A-1. A block diagram of the 5th order digital filter.

APPENDIX B

A SUM OPERATOR

As mentioned in Chapter III, an overdetermined system of linear equations is obtained after some manipulation of the rational function approximation (Equation (3.2)). Assuming the RFA has a system order of for (M,N) as (3,2), a system of linear equations can be written as

$$AX = B \quad , \tag{B-1}$$

where A is an 18x6 data matrix (assuming that 9 complex data points are used) and X and B are 6 row column vectors, i.e., 6 unknown coefficients. Thus

$$A = \begin{bmatrix} j\beta_1 X_1 & \alpha_1 X_1^2 & j\beta_1 X_1^3 & -X_1^2 & 0 & -X_1^4 \\ \alpha_1 X_1 & j\beta_1 X_1^2 & \alpha_1 X_1^3 & 0 & -X_1^3 & 0 \\ j\beta_2 X_2 & \alpha_2 X_2^2 & j\beta_2 X_2^3 & -X_2^2 & 0 & -X_2^4 \\ \alpha_2 X_2 & j\beta_2 X_2^2 & \alpha_2 X_2^3 & 0 & -X_2^3 & 0 \\ \vdots & & \vdots & & & \vdots \\ j\beta_9 X_9 & \alpha_9 X_9 & j\beta_9 X_9^3 & -X_9^2 & 0 & -X_9^4 \\ \alpha_9 X_9 & j\beta_9 X_9^2 & \alpha_9 X_9^3 & 0 & -X_9^3 & 0 \end{bmatrix}_{18 \times 6}, \qquad \text{(B-2)}$$

$$X = \begin{bmatrix} b_1 \\ b_2 \\ b_3 \\ a_0 \\ a_1 \\ a_2 \end{bmatrix}_{6 \times 1}, \qquad \text{(B.3)}$$

and

$$B = \begin{bmatrix} -\alpha_1 \\ -j\beta_1 \\ -\alpha_2 \\ -j\beta_2 \\ -\alpha_3 \\ -j\beta_3 \\ \vdots \\ -\alpha_9 \\ -j\beta_9 \end{bmatrix}_{18 \times 1} , \qquad (B.4)$$

where x_i is jk_ia, α_i are the real part of the known input data and β_i are the imaginary part of the input data. Given the noisy data at the ith frequency

$$E_i = (\alpha_{iR} + \tilde{\ell}_{iR}) + j(\beta_{iI} + \tilde{\ell}_{iI}) \quad , \qquad (B.5)$$

where $\tilde{\ell}_{iR}$ and $\tilde{\ell}_{iI}$ are two Gaussianly distributed pseudo random noise processes with zero mean and standard deviation σ. α_{iR} and β_{iI} are the real part and imaginary part of the noiseless data.

The matrix equation for additive noise is

$$A'X = B' \quad , \qquad (B-6)$$

where

$$
A' = \begin{bmatrix}
j\beta_1 X_1 + j\tilde{\ell}_{iI} X_1 & \alpha_1 X_1^2 + \tilde{\ell}_{iR} X_1^2 & j\beta_1 X_1^3 + j\tilde{\ell}_{iI} X_1^3 & -X_1^2 & 0 & -X_1^4 \\
\alpha_1 X_1 + \tilde{\ell}_{iR} X_1 & j\beta_1 X_1^2 + j\tilde{\ell}_{iI} X_1^2 & \alpha_1 X_1^3 + \tilde{\ell}_{iR} X_1^3 & 0 & -X_1^3 & 0 \\
j\beta_2 X_2 + j\tilde{\ell}_{iI} X_2 & \alpha_2 X_2^2 + \tilde{\ell}_{iR} X_2^2 & j\beta_2 X_2^3 + j\tilde{\ell}_{iI} X_2^3 & -X_2^2 & 0 & -X_2^4 \\
\alpha_2 X_2 + \tilde{\ell}_{iR} X_2 & j\beta_2 X_2^2 + j\tilde{\ell}_{iI} X_2^2 & \alpha_2 X_2^3 + \tilde{\ell}_{iR} X_2^3 & 0 & -X_2^3 & 0 \\
\vdots & \vdots & \vdots & \vdots & & \\
j\beta_9 X_9 + j\tilde{\ell}_{iI} X_9 & \alpha_9 X_9 + \tilde{\ell}_{iR} X_9 & j\beta_9 X_9^3 + j\tilde{\ell}_{iI} X_9^3 & -X_9^2 & 0 & -X_9^4 \\
\alpha_9 X_9 + \tilde{\ell}_{iR} X_9 & j\beta_9 X_9^2 + j\tilde{\ell}_{iI} X_9^2 & \alpha_9 X_9^3 + \tilde{\ell}_{iR} X_9^3 & 0 & -X_9^3 & 0
\end{bmatrix}_{18 \times 6}, \quad \text{(B-7)}
$$

and

$$
X = \begin{bmatrix} b_1 \\ b_2 \\ b_3 \\ a_0 \\ a_1 \\ a_2 \end{bmatrix}_{b \times 1}, \quad \text{(B-8)}
$$

$$B' = \begin{bmatrix} -\alpha_1 - \tilde{\ell}_{iR} \\ -j\beta_1 - j\tilde{\ell}_{iI} \\ -\alpha_2 - \tilde{\ell}_{iR} \\ -j\beta_2 - j\tilde{\ell}_{iI} \\ -\alpha_3 - \tilde{\ell}_{iR} \\ -j\beta_3 - j\tilde{\ell}_{iI} \\ \vdots \\ -\alpha_9 - \tilde{\ell}_{iR} \\ -j\beta_9 - \tilde{\ell}_{iI} \end{bmatrix}_{18 \times 1} . \qquad \text{(B-9)}$$

In order to reduce the additive noise in each element of the matrix A' and B', a sum operation is used. Each element of matrix A' and matrix B' in the same column of rows 1, 3 and 5* are added and then divided by 3. Thus, a new row is obtained. The same procedure is applied to rows 7, 9, and 11, rows 13, 15 and 17, rows 2, 4,and 6, . . . and rows 14, 16 and 18. The following new matrix equation results from the above procedure

$$A''X = B'' \quad , \qquad \text{(B-10)}$$

---

* Choosing the odd rows to be a group and the even rows to be a group, then the summation will be limited to the real part domain and imaginary part domain respectively.

where A" is a 6x6 data matrix and X and B" are 6x1 column vectors in this example. The matrix equation in Equation (B-10) is exactly determined. Thus, this matrix equation can be solved in the exact sense. The variance of the noise is reduced by a factor of about 3 in this example. Similarly, the sum operation can be applied to a higher order system that utilizes more data points. The basic reason for the noise reduction is an averaging as shown in Equations (3-18) and (3-19).

It should be noted that there is a limitation on the number of samples (N) used for the sum operation, because the noise in each element of the matrix A' has been magnified by a factor of X_i^n (see Equation (B-7)), where $X_i = jk_i a$ and n is an integer. For small N and small frequency increments $(x_i - x_{(i-1)})$, it is true that

$$\tilde{X}_1 = \tilde{X}_2 = \tilde{X}_3 = \ldots = \tilde{X}_N \qquad \text{(B-11)}$$

so that the reduction factor is N. However, for larger N, the assumption is no longer even approximately true. Therefore, the noise reduction factor is less than N. Considering the sum operation in the above section of this Appendix, it is possible to define a sum operator, S, in general for a matrix equation. Given a matrix equation

$$CX = D \quad , \qquad \text{(B-12)}$$

where

$$C = \begin{bmatrix} C_{11} & C_{12} & C_{13} & \cdots & C_{1n} \\ C_{21} & C_{22} & C_{23} & \cdots & C_{2n} \\ \vdots & & & & \\ C_{m1} & C_{m2} & C_{m3} & \cdots & C_{mn} \end{bmatrix}_{mxn} , \qquad \text{(B-13)}$$

$$X = \begin{bmatrix} x_1 \\ x_2 \\ \vdots \\ x_n \end{bmatrix}_{n \times 1} , \qquad \text{(B-14)}$$

and

$$D = \begin{bmatrix} d_1 \\ d_2 \\ \vdots \\ d_m \end{bmatrix}_{m \times 1} . \qquad \text{(B-15)}$$

The sum operator S is defined as an average of I elements in the same column but in I different rows. Basically, there is no limitation in the selection of those I rows needed in group summation. However, in the application of a sum operator to a matrix equation that results from a RFA, the I group of rows are the ones nearest to the new desired row.

Moreover, the S operator can be applied repeatedly. Thus, in general, the new matrix equation using one S operator is

$$C'X = D' \quad , \tag{B-16}$$

where

$$C' = \begin{bmatrix} SC_{11} & SC_{12} & SC_{13} & \cdots & SC_{1n} \\ SC_{21} & SC_{22} & SC_{23} & \cdots & SC_{2n} \\ \vdots & & & & \\ SC_{m1} & SC_{m2} & SC_{m3} & \cdots & SC_{mn} \end{bmatrix}_{mxn} \quad , \tag{B-17}$$

and

$$D' = \begin{bmatrix} Sd_1 \\ Sd_2 \\ \vdots \\ Sd_m \end{bmatrix}_{m \times 1} \quad . \tag{B-18}$$

Note again here that the sum operator is manipulated in the matrix equation; and the sum operation in the matrix equation is basically similar to row echelon algorithms used in the Gauss elimination, i.e., any row can be multiplied by a constant and can be added to other rows.

The sum operator itself does not filter out any of the signal*; however, the noise is indeed reduced by using the sum operator.

* When the sum operator and the RFA are applied together to a set of noiseless data, the result is exactly the same as that using only the RFA to the noiseless data.

APPENDIX C

A COMPARISON OF THE RAYLEIGH-STEVENSON EXPANSION AND THE EXPANSION FROM RFA FOR A DISC AT BROADSIDE

In this Appendix, a list of the unknown coefficients for the rational function approximation with system order for (M,N) as (14,13) to the backscattered data for the disc at broadside excitation is shown in Table C-1. The corresponding poles, zeros and residues are listed in Table C-2. A synthetic division of the rational function approximation (Equation C-1)) using the coefficients listed in Table C-1 agrees closely with the low ferequency power series expansion (Equation (C-2)) for the disc at broadside given by Boersma [47] in powers of X(jka) up to the 10th order. The rational function yields

$$E_n(X) = .8486751X^2 + 0.000437X^3 - 0.4542859X^4 + .2433949X^5$$
$$- .1253862X^6 - .2085668X^7 + .0445261X^8 + .0943268X^9$$
$$- 0.0782452X^{10} + \ldots \quad . \qquad \text{(C-1)}$$

Compared to Boersma's result of

$$E_n(X) = .84882636X^2 + 0X^3 - .45270739X^4 + .24016873X^5$$

$$+ .12934497X^6 - .21134848X^7 + .04495919X^8$$

$$+ .09588391X^9 - 0.07943693X^{10} + \ldots \quad . \qquad \text{(C-2)}$$

Thus, it seems that the RFA is a fairly accurate model for the spectrum data in the low frequency range.

TABLE C-1

A LIST OF THE COEFFICIENTS OF RFA FITTED TO THE CALCULATED BACKSCATTERING DATA FOR THE DISC AT BROADSIDE FOR (M,N) as (14,13) (ka of 0.2(0.2)15.2)

b1	1.320147094030905	0.0000000E+00
b2	1.357353646716751	0.0000000E+00
b3	0.7226181666170916	0.0000000E+00
b4	0.2757995040340761	0.0000000E+00
b5	6.384684484384773E-02	0.0000000E+00
b6	1.393516660154239E-02	0.0000000E+00
b7	1.776953002411417E-03	0.0000000E+00
b8	2.537849963300935E-04	0.0000000E+00
b9	1.945935410225849E-05	0.0000000E+00
b10	1.915758234240143E-06	0.0000000E+00
b11	8.676931321086627E-08	0.0000000E+00
b12	5.894096535908268E-09	0.0000000E+00
b13	1.290482523274168E-10	0.0000000E+00
b14	5.660624815012401E-12	0.0000000E+00
a0	0.8486743429354422	180.0000
a1	1.120820652271342	180.0000
a2	0.6982300296585792	180.0000
a3	0.2575860119100928	180.0000
a4	6.439681695523009E-02	180.0000
a5	1.341247689272333E-02	180.0000
a6	1.807907714189658E-03	180.0000
a7	2.473083576985542E-04	180.0000
a8	1.983476677625886E-05	180.0000
a9	1.879157725046216E-06	180.0000
a10	8.845994331552881E-08	180.0000
a11	5.805497654194576E-09	180.0000
a12	1.315546076443300E-10	180.0000
a13	5.593956887722427E-12	180.0000

TABLE C-2

A LIST OF POLES, ZEROS, AND RESIDUES* WHICH CORRESPOND TO THE RFA COEFFICIENTS IN TABLE C-1.

ZERO	
(-4.4236853311705000,-19.2850137855124900)	
(-4.4236855770208895,19.2850134147279800)	
(-1.2694472074508670,-14.3574438095092800)	
(-1.2694464921951290,14.3574371337880600)	
(-1.2428040504455570,-11.1990489959716800)	
(-1.2428052425384520,11.1980613937377900)	
(-1.1630043963459470,-7.9819722175598140)	
(-1.1630030870437620,7.9819669723510740)	
(-1.0335289239883420,-4.6665477752685550)	
(-1.0335292816162110,4.6665477752685550)	
(-1.5517776012420650,-1.4805915355682370)	
(-1.5517777204513550,1.4805916547775270)	
(-2.1487789154052730,-7.3575705696197249E-20)	
(0.0000000000000000E+00,0.0000000000000000E+00)	
(0.0000000000000000E+00,0.0000000000000000E+00)	

POLE	RESIDUE
(-4.5509216889669120,19.5300442973305000)	(-1.3574670471030232E-02,-2.6027321831730036E-03)
(-4.5509240523050610,-19.5300451007855510)	(-1.3574738076051711E-02,2.6028251299968531E-03)
(-1.2702333927154540,14.4197406768779880)	(-4.2411289530884857E-03,5.0483649520162132E-04)
(-1.2702273130416870,-14.4197435379028300)	(-4.2412526096687346E-03,-5.0527048240107889E-04)
(-1.2423505768308105,11.2876806259155300)	(-7.5976620692366828E-03,1.5636508040546024E-03)
(-1.2423545122146610,-11.2876720428466810)	(-7.5970085358471856E-03,-1.5631593647531584E-03)
(-1.1645487546920780,8.1058416366577150)	(-1.4522798852815856E-02,3.7634124907381915E-03)
(-1.1645493507385250,-8.1058483123779300)	(-1.4523605682120583E-02,-3.7635658529653062E-03)
(-1.0443925857543950,4.8724513053894040)	(-3.8068529450704954E-02,1.4498705899993531E-02)
(-1.0443918704986570,-4.8724498748779300)	(-3.8068193050171631E-02,-1.4498718155096962E-02)
(-1.6355692148208620,-1.6990646259307860)	(-8.4212858934880469E-03,-8.2351453037297361E-02)
(-1.6355690956115720,1.6990641490936280)	(-8.4212342761281710E-03,8.2351287952638226E-02)
(-0.4907488418983459,1.2302992343902590)	(-0.4076851655181451,0.3853218341053265)
(-0.4907490015029907,-1.2302991151180969)	(-0.4076852409537003,-0.3853216537022632)

* The units are in ka, where k is the wavenumber and a is the disc radius.

APPENDIX D

THE COMPLEX NATURAL RESONANCES OF THE DISC

Keller's scalar diffraction coefficients [11] for the edge at normal incidence are given by

$$D_{\substack{s \\ h}} = (\psi,\psi') = \frac{-e^{-j\,\pi/4}}{2\sqrt{2\pi k}} \left[\sec\left(\frac{\psi-\psi'}{2}\right) \mp \sec\left(\frac{\psi+\psi'}{2}\right)\right] , \qquad (D\text{-}1\cdot1)$$

Where D_s is edge diffraction coefficient associated with the soft (Dirichlet) boundary conditions, D_h is the edge diffraction associated with the hard (Neumann) boundary condition, ψ' is the incident wave angle and ψ is the diffracted wave angle as shown in Figure D-1. It should be noted that Keller's formula is good if the field point is not close to a shadow or reflection boundary.

As the field point is close to the shadow or reflection boundary (transition regions), the Uniform Theory of Diffraction (UTD) derived by Kouyoumjian and Pathak [11] should be used instead of Keller's formula. The UTD edge diffraction coefficients for curved edge or straight edge in a plane screen at normal incidence are

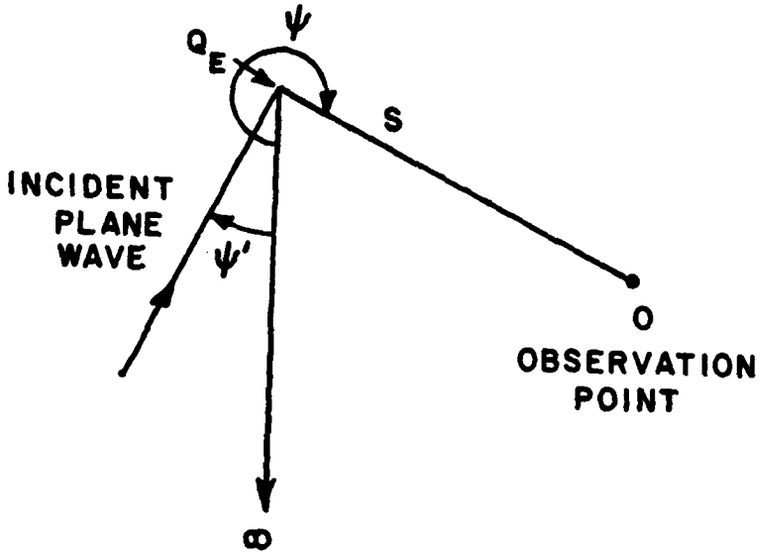

Figure D-1. The coordinate system for the incident wave diffracted by a half plane.

$$D_{\substack{s\\h}} = \frac{e^{-jk/4}}{2\sqrt{2\pi k}} \left\{ \frac{F[2kL\cos^2(\psi-\psi')/2]}{\cos\left(\frac{\psi-\psi'}{2}\right)} \mp \frac{F[2kL\cos^2(\psi+\psi')/2]}{\cos\left(\frac{\psi+\psi'}{2}\right)} \right\}, \quad \text{(D-1.2)}$$

where

$$F(x) = 2j\sqrt{x}\, e^{-jx} \int_{\sqrt{x}}^{\infty} e^{-j\tau^2}\, d\tau \quad , \quad \text{(D-1.3)}$$

A Fresnel integral, and

$$L = \frac{s(\rho_e^i + s)\,\rho_1^i\,\rho_2^i}{\rho_e^i(\rho_1^i + s)(\rho_2^i + s)} \quad , \quad \text{(D-1.4)}$$

a distance parameter, where ρ_1^i, ρ_2^i are the principal radii of curvature of the incident wavefront at the point of reflection, ρ_e^i is the radius of curvature of the incident waveform at the diffraction point taken in the plane containing the incident ray and the edge, and s is the distance from the diffraction point to the observation point.

The equivalent edge currents concept was proposed in [29] to solve the field in the caustic direction using the available diffraction coefficients. The equivalent electric and magnetic edge current I_1 and M_1, respectively are positioned on the circular edge of the disc. They are given by [29].

$$I_1(\phi') = -Y_0\sqrt{\frac{8\pi}{jk}}\, D_s(\psi,\psi')(\bar{E}^i\cdot\hat{\phi}') \quad , \quad \text{(D-2)}$$

$$M_1(\phi') = -Z_0\sqrt{\frac{8\pi}{jk}}\, D_h(\psi,\psi')(\bar{H}^i\cdot\hat{\phi}') \quad , \quad \text{(D-3)}$$

where $\hat{\phi}$ is the unit tangent vector to the circular edge of the disc, ψ' and ψ are interpreted as the incident and diffracted ray angles as shown in Figure D-2 and D-3. It follows that

$$\bar{H}^{bs1}(\theta=0) = \frac{jka}{4\pi} Y_o \frac{e^{-jkR}}{R} \int_0^{2\pi} (\hat{x}\sin\phi' - \hat{y}\cos\phi')M_1 d\phi' \quad , \qquad (D\text{-}4)$$

where

$$M_1 = \frac{-\hat{\phi}\cdot\bar{H}^i}{Y_o} D_h(\psi' = \frac{\pi}{2}, \psi = \frac{\pi}{2}) \cdot \sqrt{\frac{8\pi}{k}} \cdot e^{-j\,\pi/4} \quad . \qquad (D\text{-}5)$$

Note D_h in Equation (D.1-b) should be used for Equation (D.5) due to the field point at the reflection boundary. Similar first order scattering electric field using the equivalent electric current concept can be obtained. Furthermore, the doubly and triply diffracted field (only exist for hard case in this example) can be formulated.

$$H^{bs2}(\theta=0) = \frac{jka}{4\pi} Y_o \frac{e^{-jkR}}{R} \int_0^{2\pi} (\hat{x}\sin\phi' - \hat{y}\cos\phi')\, M_2\, d\phi' \quad , \qquad (D\text{-}6)$$

where

$$M_2 = \frac{-\hat{\phi}'\cdot\bar{H}_2^i}{Y_o} \cdot D_h(\psi' = 0, \psi = \frac{\pi}{2}) \sqrt{\frac{8\pi}{k}} e^{-j\,\pi/4} \quad , \qquad (D\text{-}7)$$

$$\bar{H}_2^i = \hat{\phi}' H_o \cdot \sin\phi' \cdot D_h(\psi' = \frac{\pi}{2}, \psi = 0) \sqrt{\frac{\rho}{2a(\rho+2a)}}\, e^{-2jka} \quad , \qquad (D\text{-}8)$$

and

ρ is $-a$.

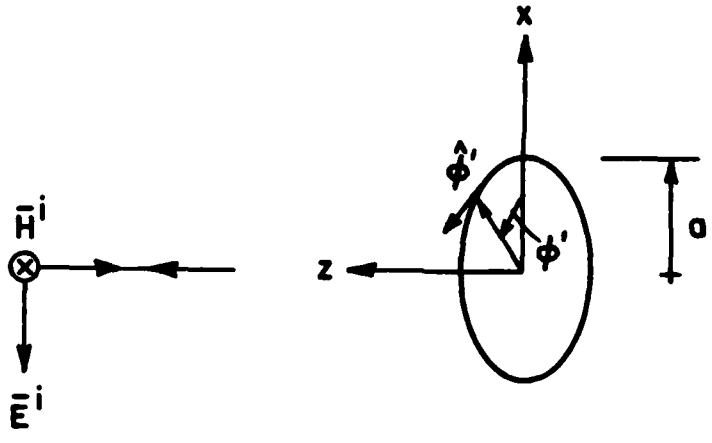

$$\bar{E}^i = -\hat{x}\, E_0\, e^{jkz}$$

Figure D-2. On-axis backscattering from the circular metallic disc.

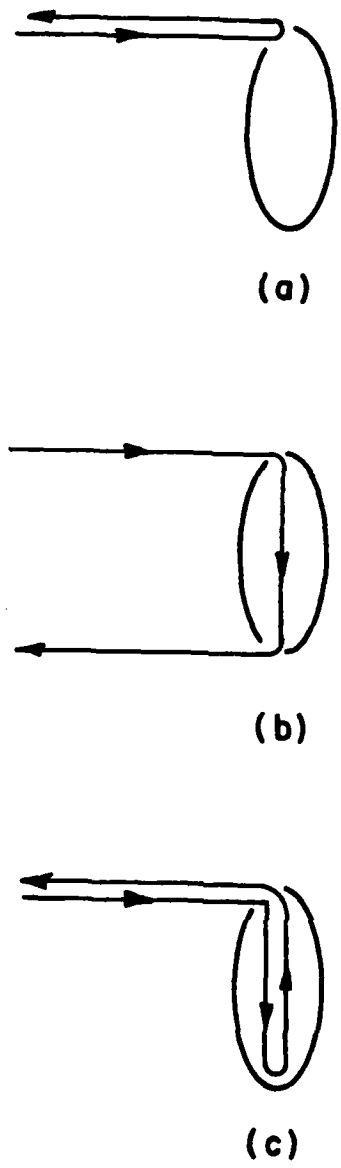

Figure D-3. The singly, doubly and triply diffracted mechanisms of the the backscattering from the circular metallic disc.

Furthermore,

$$H^{bs3}(\theta=0) = \frac{jka}{4\pi} Y_o \frac{e^{-jkR}}{R} \int_0^{2\pi} (\hat{x} \sin\phi' - \hat{y} \cos\phi') M_3 d\phi' , \quad \text{(D-9)}$$

where

$$M_3 = \frac{-\hat{\phi} \cdot \bar{H}_3^i}{Y_o} \cdot D_h(\psi' = 0, \psi = \frac{\pi}{2}) \sqrt{\frac{8\pi}{k}} e^{-j\pi/4} , \quad \text{(D-10)}$$

$$\bar{H}_3^i = \hat{\phi}' \cdot H_2^i \cdot D_h(\psi' = 0, \psi = 0) \cdot \sqrt{\frac{\rho}{2a(\rho+2a)}} e^{-2jka} , \quad \text{(D-11)}$$

and

$$\rho = -a.$$

Therefore, it is clearly here that

$$M_3 = D_h(\psi' = 0, \psi = 0) \cdot \sqrt{\frac{\rho}{2a(\rho+2a)}} \cdot e^{-2jka} \cdot M_2 . \quad \text{(D-12)}$$

$$M_4 = D_h(\psi' = 0, \psi = 0) \cdot \sqrt{\frac{\rho}{2a(\rho+2a)}} \cdot e^{-2jka} \cdot M_3 . \quad \text{(D-13)}$$

$$M_5 = D_h(\psi' = 0, \psi = 0) \cdot \sqrt{\frac{\rho}{2a(\rho+2a)}} \cdot e^{-2jka} \cdot M_4 . \quad \text{(D-14)}$$

$$\vdots$$

Thus, the total high order backscattered field is

$$H^{bst}(\theta=0) = \frac{jka}{4\pi} Y_o \frac{e^{-jkR}}{R} \int_0^{2\pi} (\hat{x} \sin\phi' - \hat{y} \cos\phi') M_t d\phi' , \quad \text{(D-15)}$$

where

$$M_t = M_2 + M_3 + M_4 + \ldots$$

$$= M_2 \, (1 + \gamma + \gamma^2 + \ldots)$$

$$= M_2/1-\gamma \quad , \tag{D-16}$$

and

$$\gamma = D_h^*(\psi' = 0, \; \psi = 0) \cdot \sqrt{\frac{\rho}{2a(\rho+2a)}} \cdot e^{-2jka}\Big|_{(\rho=-a)}$$

$$= \frac{-e^{-j\,\pi/4}}{\sqrt{2\pi k}} \cdot \frac{j}{\sqrt{2a}} \cdot e^{-2jka}$$

$$= -\frac{e^{j\,\pi/4}}{2\sqrt{\pi k a}} \cdot e^{-2jka} \quad . \tag{D-17}$$

Consequently,

$$1 - \gamma = 1 + \frac{e^{j\,\pi/4}}{2\sqrt{\pi k a}} \, e^{-2jka}$$

$$= 1 + \frac{e^{j\,\pi/2}}{2\sqrt{\pi z}} \, e^{-2z}$$

$$= 1 + j \, \exp(-2z)/(4\pi z)^{1/2} \quad , \tag{D-18}$$

where $z = jka$.

---

* Keller's formula.

Equation (D-18) is the charasteristic equation for the edge diffraction mode for the disc at broadside excitation. The 26 pairs of poles have been extracted using a zero searching routine for this equation. They are listed in Table D-1. Note the first 3 pole-pairs listed are from the RFA to the backscattering data for the disc for broadside excitation because the GTD is not accurate in the low-frequencies. Also the induced current on the rim due to the singly diffracted field (see Figure D-3) corresponds to the lowest frequency pole-pairs of the creeping wave mode because the variation of the current along the rim is exactly one period. For the off-axis illumination, the higher order diffracted field is due to the multiple diffractions at Q_1 and Q_2 (see Figure D-4). Several efforts have been made to find a closed form for the resonances similar to the one derived for the broadside incidence but without success. Once again Keller's edge diffraction coefficients are used here. And the following formula is introduced for the calculation of the caustic distance.

$$\frac{1}{\rho} = \frac{1}{\rho_e^i} - \frac{\hat{n}_e \cdot (\hat{s}' - \hat{s})}{a_e} \quad , \tag{D-19}$$

where ρ_e^i is the radius of curvature of the incident waveform at Q_E taken in the plane containing the incident ray and the edge; $\hat{n}_e$ is the associated unit normal vector to the edge directed away from the center of the curvature, the unit vector $\hat{s}'$ is in the direction of incidence at

TABLE D-1

A LIST OF 26 POLE*-PAIRS FOR THE A DISC FOR BROADSIDE EXCITATION (BACKSCATTER)

Pole Number	Real part	(+/-)Imaginary Part
1	-0.49069	1.23103
2	-1.04579	4.87347
3	-1.16349	8.10608
4	-1.24179	11.36106
5	-1.30243	14.50748
6	-1.35120	17.65236
7	-1.39201	20.79634
8	-1.42709	23.93976
9	-1.45784	27.08279
10	-1.48523	30.22556
11	-1.50991	33.36812
12	-1.53238	36.51053
13	-1.55299	39.65282
14	-1.57203	42.79502
15	-1.58972	45.93715
16	-1.60625	49.07920
17	-1.62175	52.22122
18	-1.63634	55.36318
19	-1.65013	58.50512
20	-1.66320	61.64701
21	-1.67562	64.78889
22	-1.68746	67.93073
23	-1.69875	71.07256
24	-1.70956	74.21437
25	-1.71992	77.35616
26	-1.72987	80.49794

* The unit of poles is ka, where k is the propagation constant a is the radius of the disc.

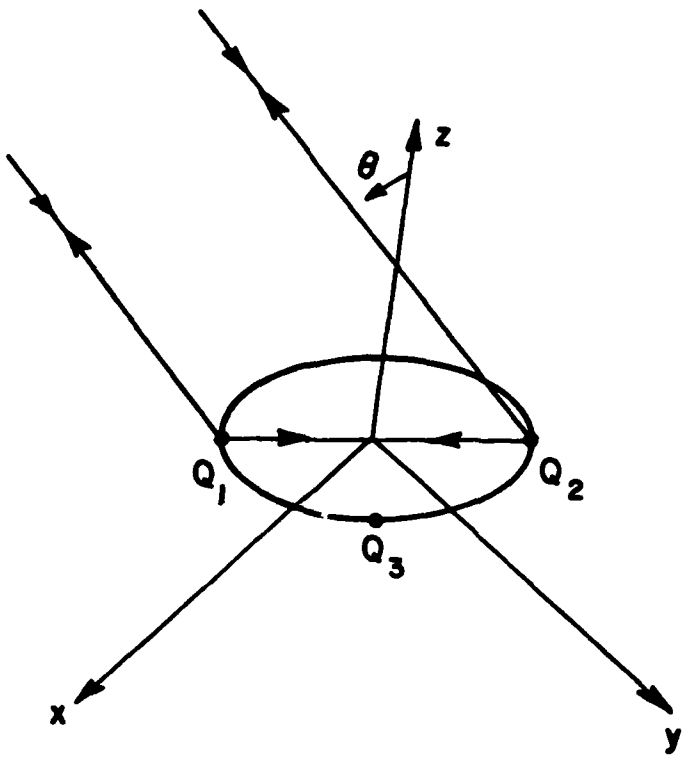

Figure D-4. The coordinate system and the higher order ray paths for the disc at angles off broadside excitation.

the edge and $\hat{s}$ is the direction of diffraction, a_e is the radius of curvature of the edge at Q_E.

The following caustic distances are obtained using Equation (D-19) the multiple diffraction at Q_1 and Q_2 shown in Figure D-4.

$$\rho^0 = \rho_{0-2} = \frac{-a}{1+\sin\theta} \quad . \tag{D-20}$$

$$\rho^1 = \rho_{0-2-1} = \frac{-a[1+2\sin\theta]}{1+3\sin\theta} \quad . \tag{D-21}$$

$$\rho^2 = \rho_{0-2-1-2} = \frac{-a[1+4\sin\theta]}{1+5\sin\theta} \quad . \tag{D-22}$$

$$\rho^3 = \rho_{0-2-1-2-1} = \frac{-a[1+6\sin\theta]}{1+7\sin\theta} \quad . \tag{D-23}$$

$$\vdots$$

$$\rho^N = \rho_{0-2-1-2-1-2} = \frac{-a[1+2N\sin\theta]}{1+(2N+1)\sin\theta} \quad . \tag{D-24}$$

Although the diffraction coefficients are the same in each order, the caustic distance ρ associated with each diffraction is not the same. Consequently, the factor $D_h \cdot \frac{\rho}{2a(\rho+2a)}$ is different in each order of diffraction. Therefore, there appears to be no way to form a geometrical series similar to that for the broadside case.

APPENDIX E

THE POLES FOR A CIRCULAR METALLIC DISC AT EDGE-ON INCIDENCE

The analytic form for the creeping wave around the circumference of a disc at edge-on incidence is given by Senior [34] as follows:

$$S^{CW} \cong \left(1 - \frac{\gamma}{\pi}\right)^{-1/2} e^{-i0.068\pi(ka)^{2/3}} e^{-j2ka+j3\pi/4} \qquad \text{(E-1)}$$

$$\cdot \exp\{-i\pi ka(1 - \frac{1}{2}(ka)^{-2/3} e^{-j\pi/3})\} \quad ,$$

where S^{CW} is the scattering amplitude defined in [34], γ is a trial value, for example, γ may equal 0.8*PI. In terms of S^{CW}, the normalized scattering amplitude is given as

$$E_n^{CW1} = 2\, S^{CW}/ka \quad , \qquad \text{(E-2)}$$

or

$$E_n^{CW1} = \frac{2}{ka}\left(1 - \frac{\gamma}{\pi}\right)^{-1/2} e^{-i0.068\pi(ka)^{2/3}} e^{-j2ka+j3\pi/4}$$

$$\cdot \exp\{-i\pi ka(1 - \frac{1}{2}(ka)^{-2/3} e^{-j\pi/3})\} \quad , \qquad \text{(E-3)}$$

or substituting u for jka

$$E_n^{CW1} = 2(1-\frac{\gamma}{\pi})^{-1/2}\, u^{-1/3} e^{-2\mu}\, e^{j5\pi/6}\, \exp[-\pi\mu + \frac{\pi}{2}\,\mu^{1/3}] \quad . \tag{E-4}$$

If the phase reference point is shifted from the front end of the disc to the center of the disc

$$E_n^{CW} = 2(1-\frac{\gamma}{\pi})^{-1/2}\, u^{-1/3}\, e^{j\frac{5\pi}{6}}\, \exp[-\pi\mu + \frac{\pi}{2}\,\mu^{1/3}] \quad . \tag{E-5}$$

If we also consider the creeping wave due to an additional time around the disc, then,

$$E_n^{CW} = 2(1-\frac{\gamma}{\pi})^{-1/2}\, \mu^{-1/3} e^{j\frac{5\pi}{6}}\, \exp[-\pi\mu + \frac{\pi}{2}\,\mu^{1/3}]$$

$$\cdot\, \exp[-2\pi\mu + \pi\mu^{1/3}] \quad . \tag{E-6}$$

Obviously, successive contributions need an additional phase form of

$$P(u)=\exp[-2\pi\mu + {}_{\pi}\mu^{1/3}] \quad . \tag{E-7}$$

The complex natural resonances are obtained by imposing the phase coherence at the starting points after one or more revolutions.

In order to obtain a pole string for the creeping wave at edge on incidence, set

$$-2\pi\mu + \pi\mu^{1/3} = \pm j2n\pi \quad . \tag{E-8}$$

then

$$\mu^{1/3} - 2\mu = \pm j2n \quad . \tag{E-9}$$

Let

$$z = ka \quad , \tag{E-10}$$

and

$$z = Y^3 \quad . \tag{E-11}$$

Then,

$$j^{1/3}Z^{1/3} - 2jZ = \pm j2n \quad , \tag{E-12}$$

or

$$j^{1/3}Y - 2jY^3 = \pm j2n \quad . \tag{E-13}$$

Since

$$j^{1/3} = e^{\left[\frac{j\pi}{2} \pm 2n\pi\right]^{1/3}} \quad , \tag{E-14}$$

The principle values of $(j)^{1/3}$ are obtained from (E-14) at n=0,1,2

i.e., $e^{j\pi/6}$, $e^{j5\pi/6}$, $e^{j9\pi/6}$

or $e^{j\pi/6}$, $e^{j5\pi/6}$, $-j$

Any of the three principle values can satisfy (E-14). We choose

$$(j)^{\frac{1}{3}} = -j \quad . \tag{E-15}$$

Then,

$$-jY - 2jY^3 = \pm j2n \quad . \tag{E-16}$$

or

$$Y^3 + \frac{Y}{Z} \pm n = 0 \quad . \tag{E-17}$$

The zeros of Equation (E-17) are related to the poles of the disc due to the creeping wave mode by Equation (E-8). The zeros of Equation (E-17) can be found by using the DPOLYRT Routine (a zero searching routine for a polynomial) for any integer n. A pair of complex conjugate zeros and one real zero are obtained. However, only the complex conjugate poles are meaningful when they are substituted into Equation (E-10) and (E-11). Pure imaginary resonances could imply internal resonances. A list of the first thirty pole-pairs using Equation (E-17) at n = 1, 2, . . . 30 are listed in Table 5-6.

APPENDIX F

A COMPARISON OF EXACT AND APPROXIMATE BACKSCATTERED FIELDS FOR THE CIRCULAR DISK FOR EDGE-ON INCIDENCE

The backscattered field for the disc at edge-on incidence using exact calculated data from Hodge [32] and Senior's Geometrical theory of diffraction (GTD) result [34] are compared in amplitude and phase in Figures F-1 and F-2 respectively. The GTD result is not good at low frequencies due to the asymptotic nature of the GTD approximation. However, the amplitude plots at high frequencies, as shown in Figure F-1, agree well except that there is a phase lag in the GTD result. Figure F-2 is a comparison of the phase plots both from GTD and the exact result. There is a phase difference between the calculated data and Senior's approximation. The comparison made here suggests that additional improvement could be made in the asymptotic model.

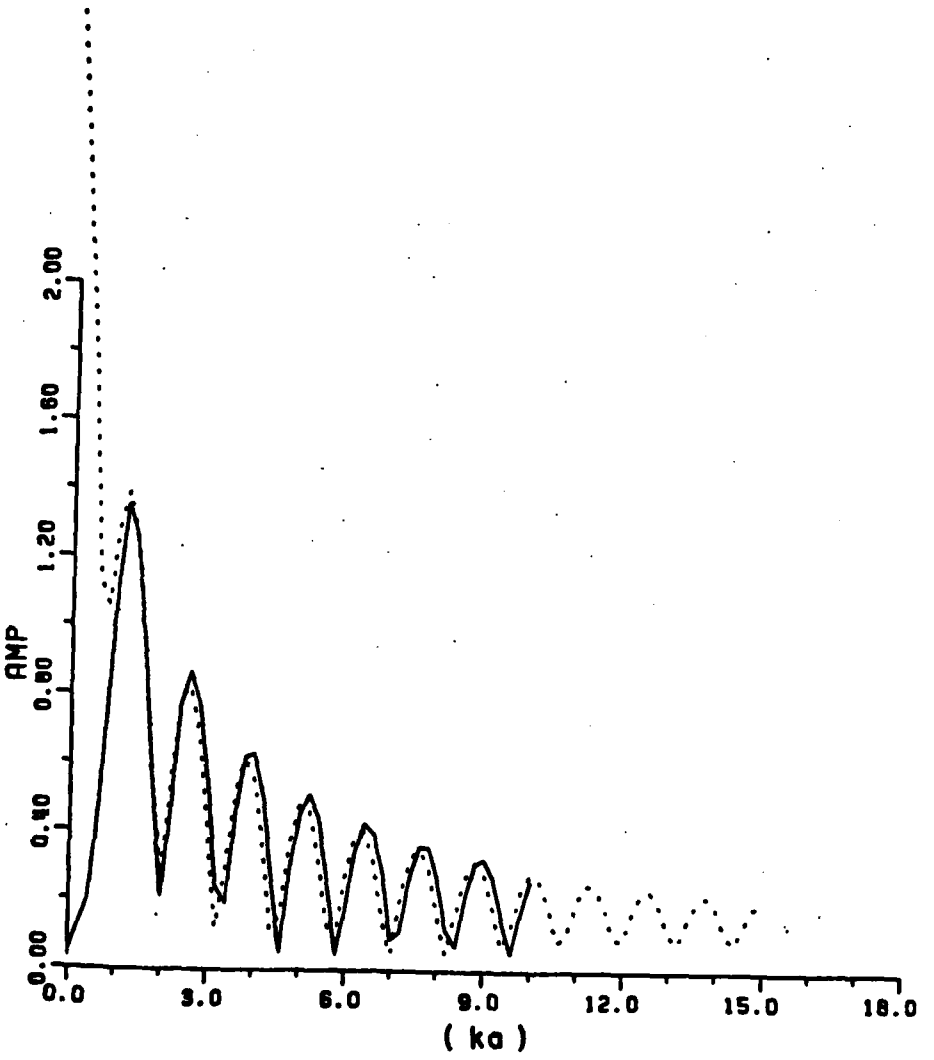

Figure F-1. A comparison for the backscattering data for the disc at edge-on incidence (amplitude plot), dotted line--Senior's GTD mode, solid line--Hodge's calculation.

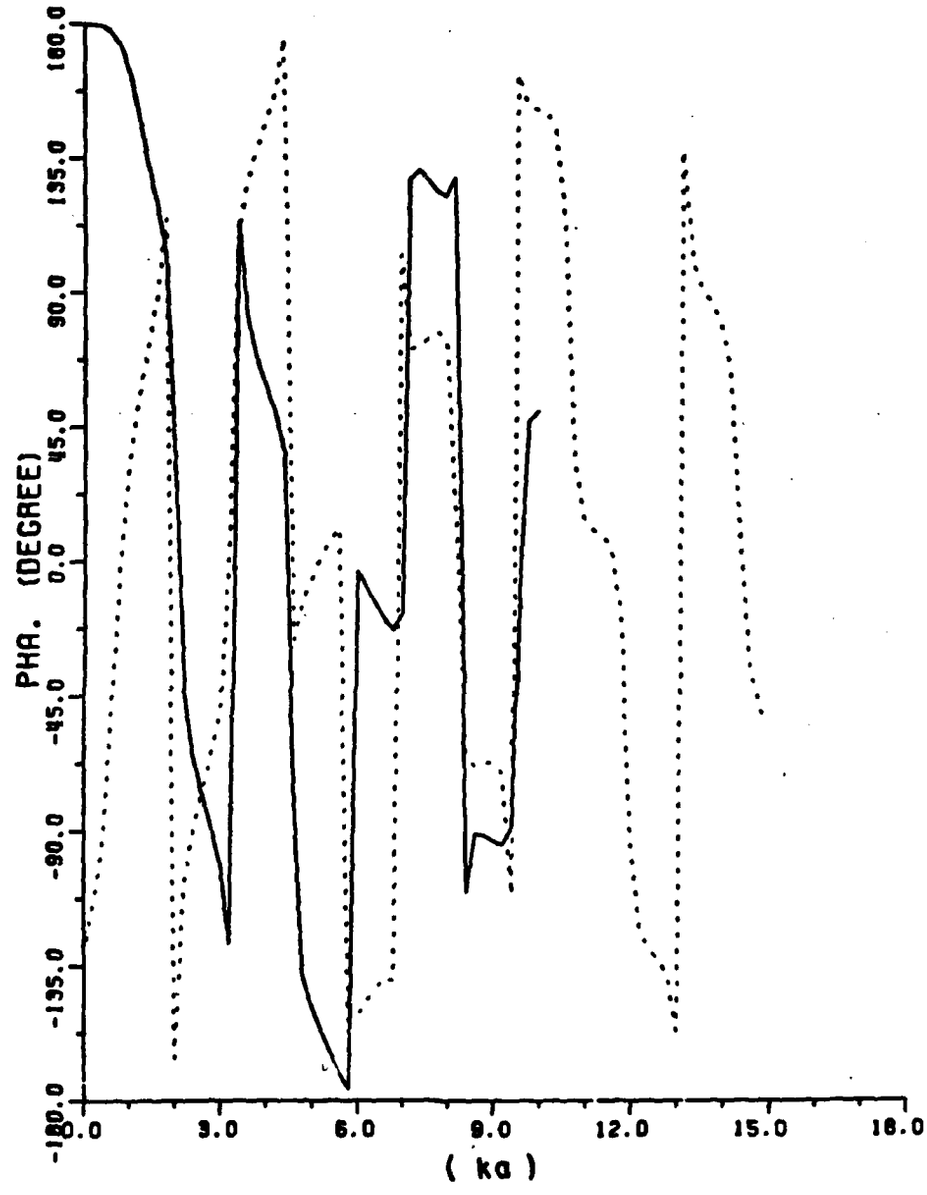

Figure F-2. A comparison for the backscattering data for the disc at edge-on incidence (phase plot), dotted line--Senior's analytic mode, solid line--Hodge's calculation.

APPENDIX G

A REPRODUCTION OF ANDREJEWSKI'S NEAR FIELD DATA OF THE DISC

The normalized magnetic scattered near field for the disc is reproduced using Andrejewski's formula. From Andrejewski, the normalized magnetic near field (H) is calculated as

$$H = 1 + \frac{1}{\gamma^2} \frac{Wo(0,\gamma,0)\psi_0(1,\gamma)}{\psi_0(0,\gamma)+\psi_2(0,\gamma)} - W_0(1,\gamma,0) \quad , \qquad (G\text{-}1)$$

where γ is ka, and the parameters are listed in the following Table (Table G-1). Using Equation (G-1) and Table G-1, 14 data points (ka of 0.5(0.5)4. and ka of 4.(1.),10.) are reproduced. The data points are then approximated by a rational function in Chapter V.

TABLE G-1

THE W_0, ψ_0, ψ_2 LISTED IN ANDREJEWSKI'S DISSERTATION.

411. $W_0(0;r;0)$, $W_0(1;r;0)$, $W_0(\eta;r;0)$.

r	$\frac{i\pi}{2r} W_0(0;r,0)$
0,5	1,024 + i 0,3169
1	1,097 + i 0,6238
1,5	1,220 + i 0,9037
2	1,381 + i 1,134
2,5	1,594 + i 1,304
3	1,691 + i 1,425
3,5	1,73 + i 1,53
4	1,883 + i 1,644
5	2,067 + i 1,894
6	2,204 + i 2,091
7	2,431 + i 2,254
8	2,555 + i 2,491
9	2,739 + i 2,592
10	2,875 + i 2,727

r	$W_0(1;r;0)$
0,5	0,105 - i 0,286
1	0,469 - i 0,384
1,5	1,25 - i 0,137
2	2,71 + i 0,494
2,5	5,13 + i 1,35
3	8,63 + i 2,08
3,5	13,0 + i 2,63
4	18,1 + i 1,89
5	28,4 - i 0,910
6	37,3 - i 4,85
7	45,8 - i 3,80
8	58,3 + i 0,576
9	78,3 + i 5,81
10	104 + i 6,19

r	$\frac{i\pi}{2r} \Psi_2(0;r)$
0,5	-0,0805 - i 0,0000
1	-0,2091 - i 0,0018
1,5	-0,5383 - i 0,0203
1.6	-0.5841 - i 0.0259
2	-0,7361 - i 0,0896
2,5	-0,8169 - i 0,2224
3	-0,7652 - i 0,3938
3,5	-0,5790 - i 0,5499
4	-0,1998 - i 0,6199
5	0,4157 - i 0,4692
6	0,7701 + i 0,0025
7	0,4665 + i 0,5742
8	-0,2327 + i 0,5893
9	-0,7474 + i 0,0933
10	-0,576 - i 0,4907

r	$\frac{i\pi}{2r} \Psi_0(0;r)$
0,5	0,9805 + i 0,3039
1	0,6232 + i 0,5268
1,5	0,2279 + i 0,6106
2	-0,1976 + i 0,5365
2,5	-0,5546 + i 0,3266
3	-0,7587 + i 0,0336
3,5	-0,789 - i 0,273
4	-0,5769 - i 0,5177
5	0,1387 - i 0,6067
6	0,7375 - i 0,1393
7	0,6165 + i 0,4613
8	-0,0443 + i 0,6449
9	-0,6625 + i 0,2381
10	-0,6608 - i 0,3913

r	$\Psi_0(1;r)$
0,5	0,1008 - i 0,3285
1	0,3971 - i 0,6982
1,5	0,8631 - i 1,162
2	1,445 - i 1,758
2,5	2,075 - i 2,465
3	2,72 - i 3,231
3,5	3,40 - i 3,87
4	4,185 - i 4,797
5	6,028 - i 6,581
6	7,988 - i 8,419
7	10,05 - i10,65
8	12,33 - i13,01
9	14,85 - i15,69
10	17,35 -i18,30

APPENDIX H

SOME TRANSIENT RESPONSES

In this Appendix, several transient response waveforms are presented. The impulse response and the ramp response of the loop at edge-on incidence are presented in Figure H-1 and Figure H-2. The ramp response of the loop for broadside* excitation is shown in Figure H-3. All of these plots are obtained using Fourier synthesis of the calculated spectral data for the loop at edge on and broadside excitation. All of the plots shown in this Appendix are limited to 30 transit times for the loop diameter. The actual waveform durations are somewhat longer than those. Singly stated that circular loop (like the wire) is a high Q scatterer.

Figure H-4 shows ramp response waveforms for the circular disc at several aspect angles (cross polarization) where 10 harmonics have been used in the synthesis of the ramp response.

---

* The impulse response of the loop for broadside excitation has also been shown in Chapter V.

AD-A143 913 APPROXIMATE METHODS FOR OBTAINING THE COMPLEX NATURAL ELECTROMAGNETIC OSC..(U) OHIO STATE UNIV COLUMBUS ELECTROSCIENCE LAB T C LEE ET AL. FEB 84 ESL-710816-16 4/4

UNCLASSIFIED N00014-78-C-0049 F/G 20/3 NL

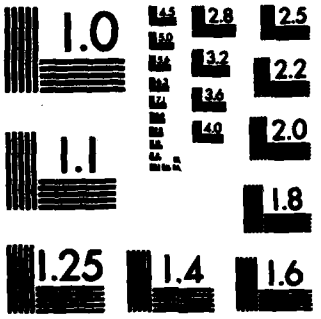

MICROCOPY RESOLUTION TEST CHART
NATIONAL BUREAU OF STANDARDS-1963-A

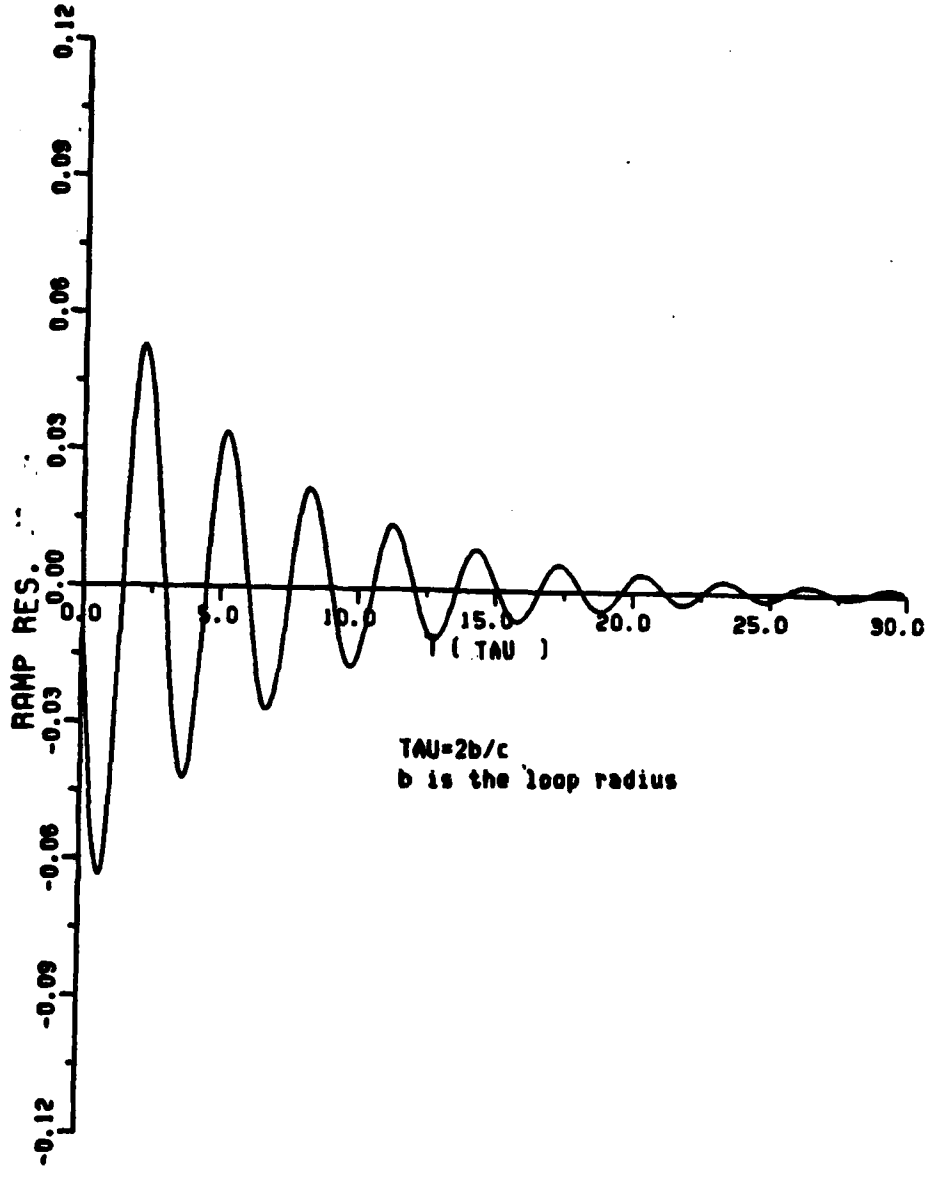

Figure H-3. The ramp response for a loop for broadside excitation.

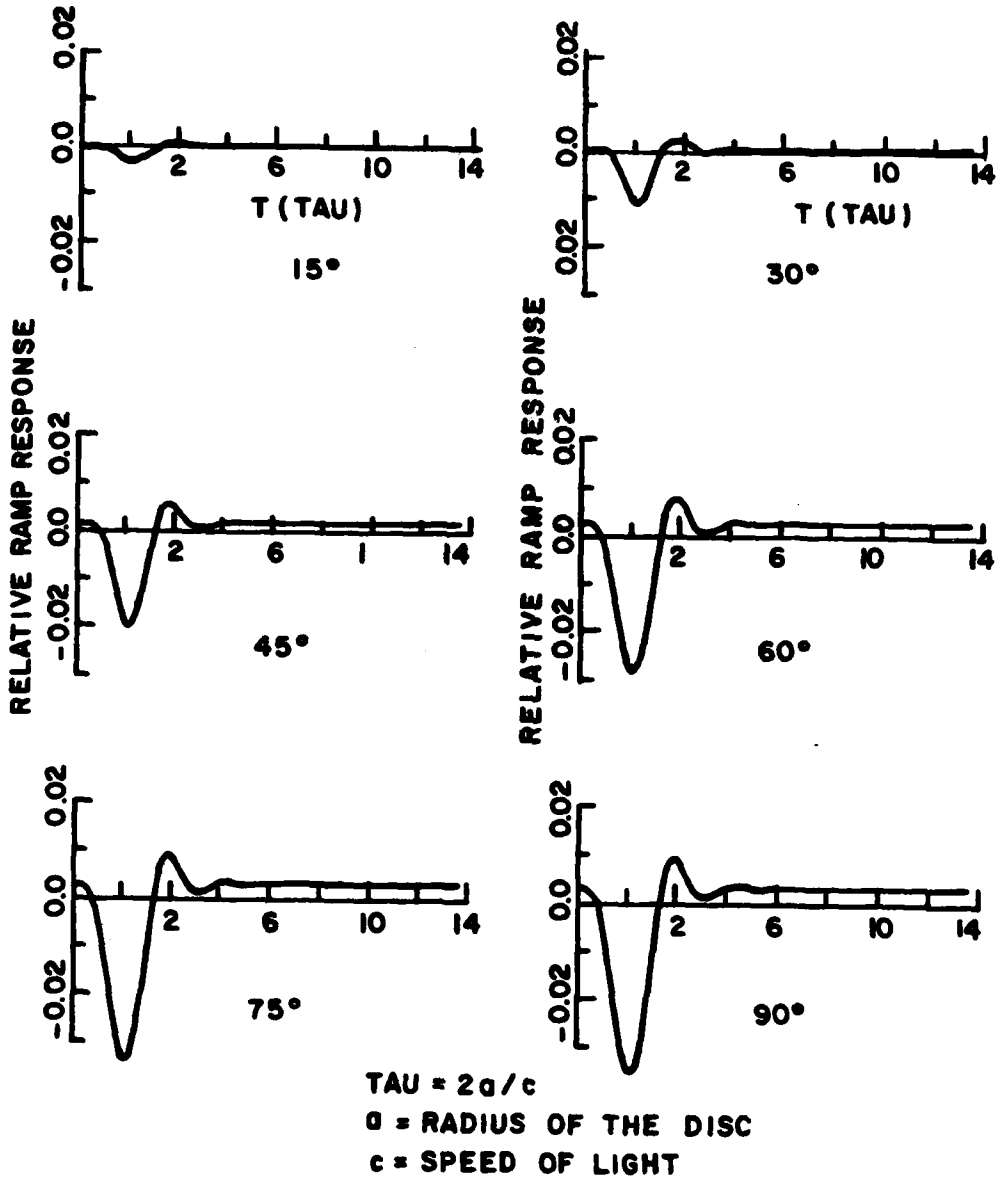

Figure H-4. The ramp response waveforms for the disc at 15°, 30°, 45° 60°, 75°, and 90° off broadside incidence (cross polarization).

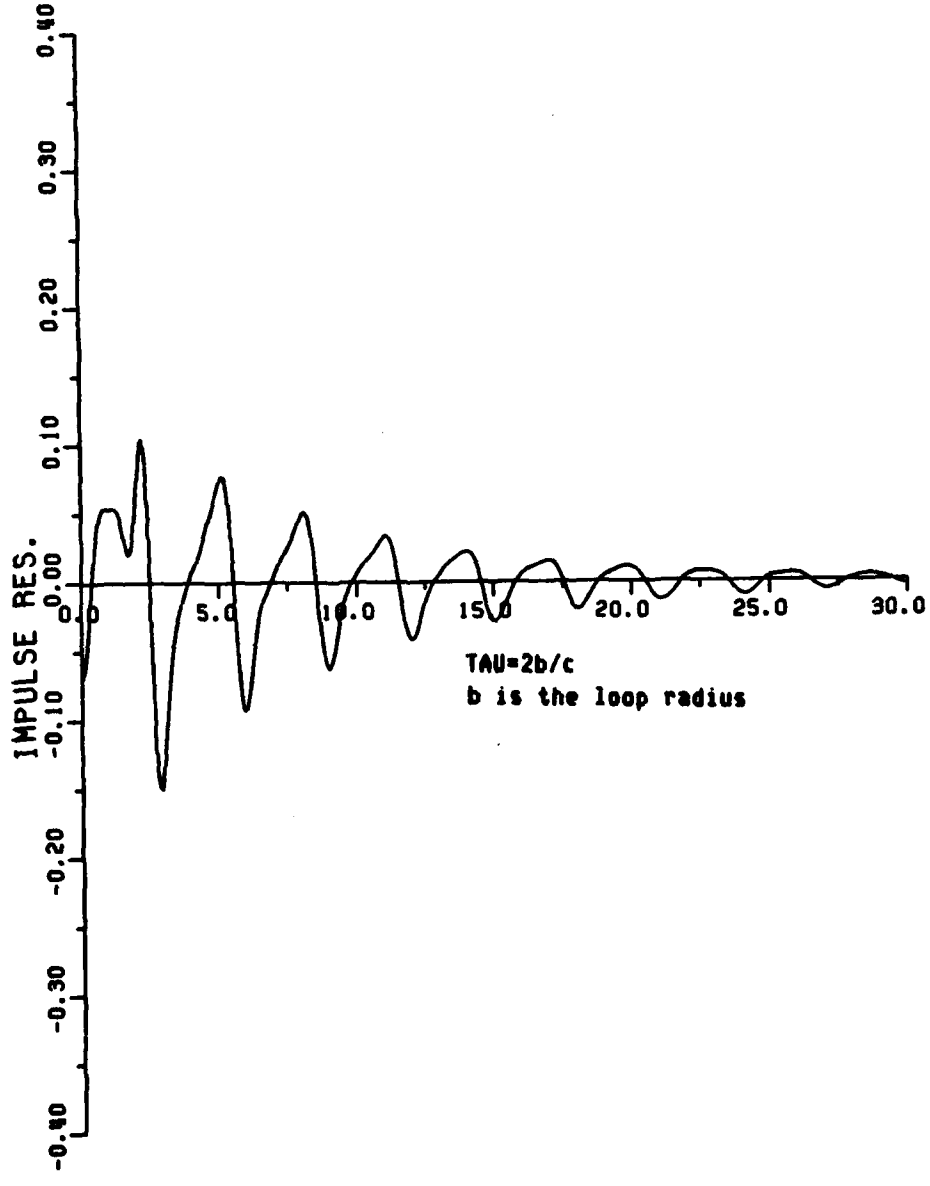

Figure H-1. Impulse response for a loop for edge-on incidence.

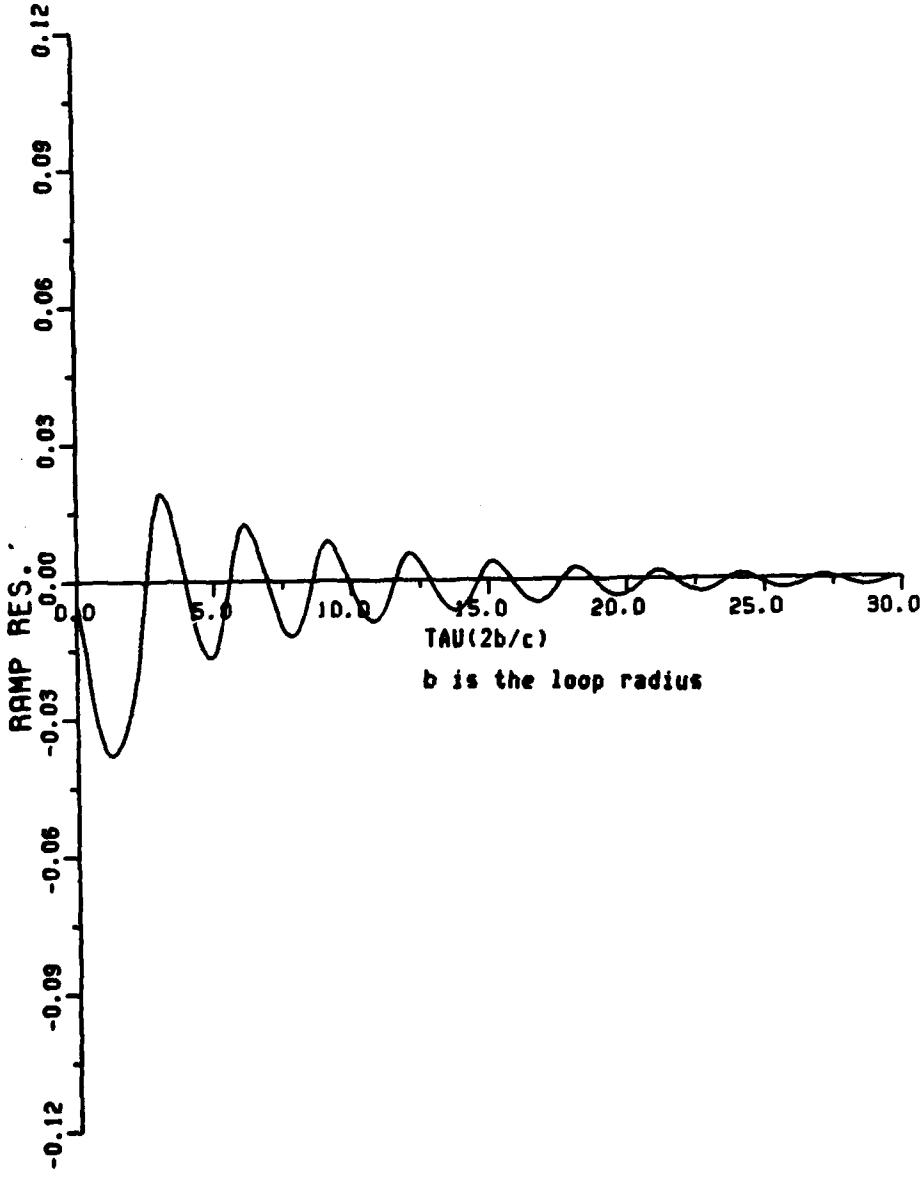

Figure H-2. The ramp response for a loop for edge-on incidence.

APPENDIX I

K-PULSE WAVEFORM FOR THE THIN CIRCULAR LOOP

The K-pulse waveform for an object, as defined by Kennaugh [6], is a single time-limited excitation waveform which will elicit unique time limited response waveforms from the object at arbitrary aspects. One method for generating the K-pulse involves a weighted product of the complex natural resonances of the object [44], i.e.,

$$E^{i}(s) = \frac{1-e^{-\varepsilon s}}{s} \prod_{j=1}^{n} [1 - e^{-\varepsilon(s-P_j)}] \quad , \tag{I-1}$$

where ε is an arbitrary positive number, and P_j are the poles of the object. Then, $E^{i}(s)$ has a finite duration inverse Laplace transformation of length $(n + 1)\varepsilon$. Having formulated the K-pulse input spectrum, the K-pulse input waveform is generated by the Fourier synthesis of the spectrum. Note the weighting function,

$$W(n)^{*} = \frac{\sin 2\pi n/N}{2\pi n/N} \cdot \frac{(N/2)^2}{(N/2)^2-n^2} \quad , \tag{I-2}$$

where N is the number of sampled data, is used to avoid Gibbs

---

* If n is N/2, W(n) is 1/2.

phenomenon. Since the K-pulse and response waveforms must be time limited, the K-pulse actually should have exactly maximum time length of $(n + 1)\varepsilon$ as specified, these waveforms are an excellent test of complex natural resonances locations (poles) deduced using approximate methods. That is, the generated K-pulse and response waveforms will indeed be time-limited if the pole locations are accurate. Some allowance must be made of course for truncated pole products used to obtain the K-pulse.

The most simple application of these ideas involves a single string of poles (one resonant-type mode). If more than one type of resonance is possible the K-pulse becomes more complicated. For the loop at edge-on incidence, resonance is confined to the creeping wave mode and represents an excellent test.

The first 10 pole-pairs listed in Table 5-6 (creeping wave poles for circular loop) were used to obtain the K-pulse spectrum (amplitude and phase) and waveform for the loop shown in Figure I-1, I-2 and Figure I-3 respectively. Figure I-1 (amplitude) and Figure I-2 (phase) are the K-pulse input spectrum. Figure I-3 is the K-pulse input waveform. Note the K-pulse length is assumed arbitrarily to be π TAU (loop diameter transit time). The ringing shown is primarily associated with truncation, and not inaccuracies of the poles.* Response to the K-pulse shown in Figure I-3 is shown in Figure I-4. Clearly there is some slight ringing and the response waveform is not precisely time-limited.

---

* Unpublished results by Kennaugh confirm this postulate. Using 20 pole-pairs deleted most of the ringing.

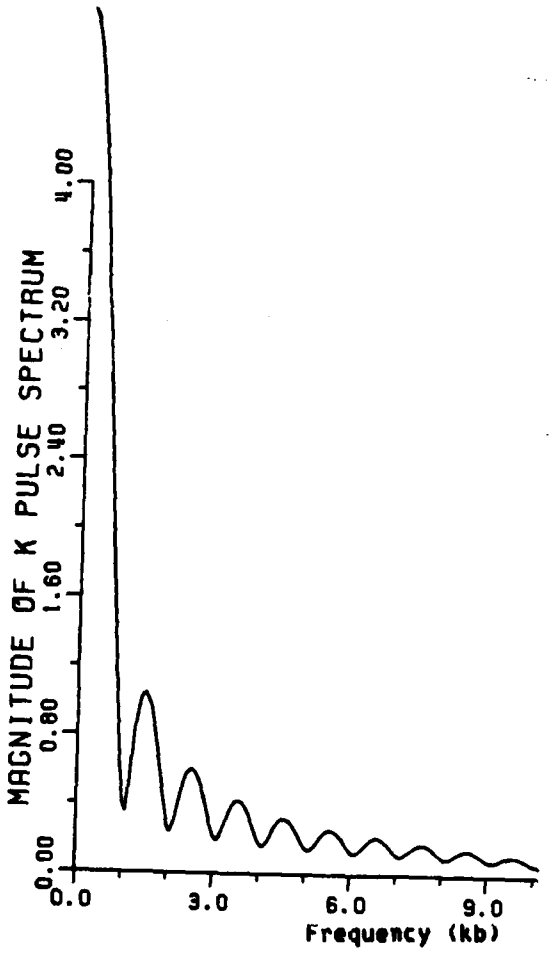

Figure I-1. The K-pulse input spectrum (amplitude plot) generated from Equation (I-1) using the first 10 pole-pairs of the circular loop at edge of incidence (TE mode). The pulse duration is confined to π TAU, where π = 3.14159 and TAU is the loop diameter transit time. Note the spectrum is spread over all the frequency, however, as shown above, the amplitude is small for kb greater than 10.

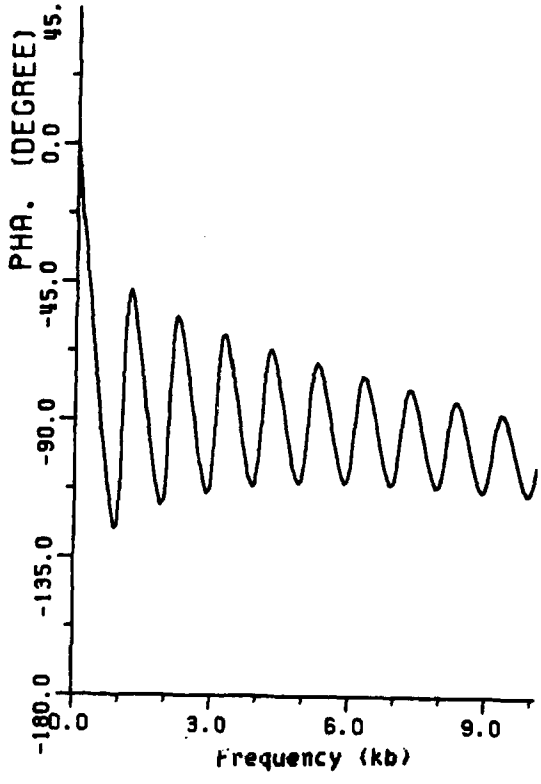

Figure I-2. The K-pulse input spectrum (phase plot) generated from (I-1) using 10 pole-pairs for the circular loop (TE mode). The pulse duration at edge-on is confined to π TAU, where π = 3.14159 and TAU is the loop diameter transit time. The data are truncated at ka of 10 because the corresponding amplitude is small for kb greater than 10.

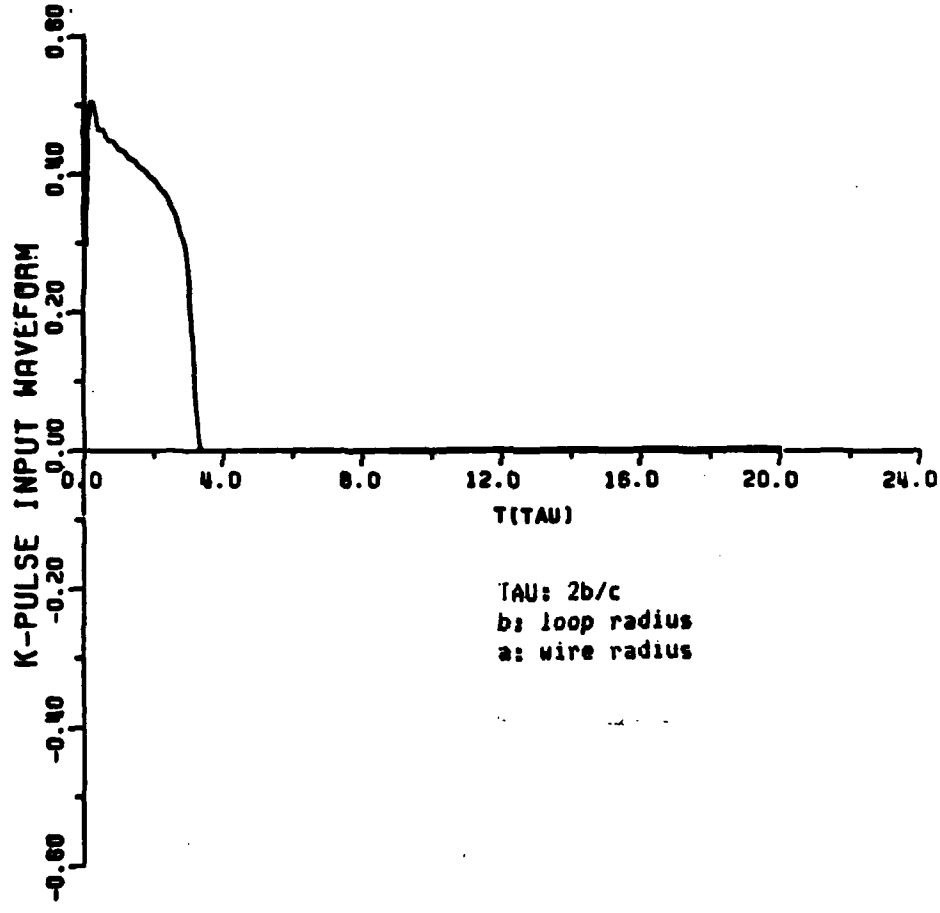

Figure I-3. A K-pulse input waveform for a loop for edge-on incidence (TE mode). The ringing is due to the truncation of poles (10 pole-pairs used here). The duration is confined to π TAU, where π is 3.14159.

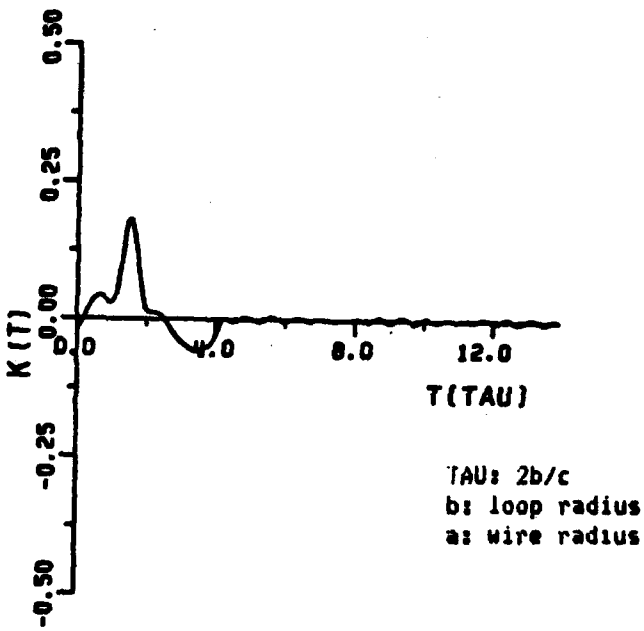

Figure I-4. A K-pulse output waveform for a loop for edge-on incidence. The duration is longer than π TAU, where π is 3.14159. This is due to both the truncation of poles and spectrum.

Figure I-4 is generated using Fourier synthesis of the K-pulse output spectrum, which is the product of the K-pulse input spectrum and the transfer function of the target. All the spectra are generated in the region up to kb of 10, where b is the loop radius. The result shown in Figure I-4 is similar to the result shown by Kennaugh [6] for a finite thin-wire scatterer. Also the K-pulse response is about π TAU lengths as expected. Therefore, the pole locations found from RFA or integral equation formulation and numerical search are reasonably accurate. More importantly, it would appear that it is feasible to obtain K-pulse waveforms from pole locations found from measured data.

At this stage we are admittedly not in a position to discuss the K-pulse and response waveforms for the loop (edge-on incidence) in the same fashion as could be done, for example, for the transmission line by Kennaugh [6]. The cancellation ideas are less direct, but still occur. A more detailed study of the loop, involving general aspects and diffraction as well as creeping wave resonances, would appear to be a fruitful area for future study.

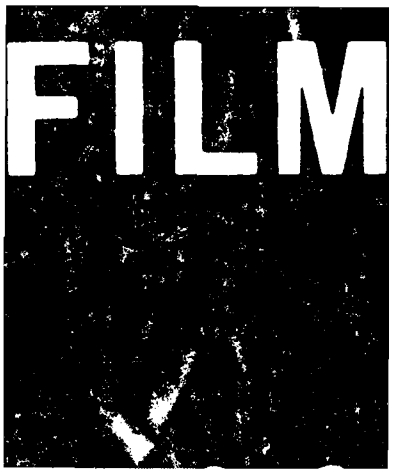
FILM